Institute of Geosciences

Photogrammetry and distinct element geomechanical modelling of sinkholes and large-scale karstic depressions

Djamil Al-Halbouni

Cumulative dissertation

to obtain the academic degree "doctor rerum naturalium" (Dr. rer. nat.)
in the scientific discipline Geophysics.

Submitted to the
Faculty of Mathematics and Natural Sciences
at the University of Potsdam, Germany.

Prepared at Section 2.1 - Physics of Earthquakes and Volcanoes,
Department of Geophysics, Helmholtz Centre Potsdam -
GFZ German Research Centre for Geosciences.
&
Institute of Geosciences, University of Potsdam, Germany.

Date of disputation: 19 June 2019

Academic advisor:
Prof. Dr. Torsten Dahm, University of Potsdam, Germany.
Academic mentor:
Associate Prof. Dr. Eoghan P. Holohan, University College Dublin, Ireland.

Reviewers:
Prof. Dr. Torsten Dahm
Prof. Dr. Francisco Gutiérrez
Associate Prof. Dr. Eoghan P. Holohan

Examining committee:
Prof. Dr. Jens Tronicke
Prof. Dr. Torsten Dahm
Prof. Dr. Charlotte Krawczyk
Associate Prof. Dr. Eoghan P. Holohan
Prof. Dr. Niels Hovius

https://doi.org/10.25932/publishup-43215
https://nbn-resolving.org/urn:nbn:de:kobv:517-opus4-432159

Statement of Originality

I hereby declare that this thesis is the product of my own work. All the assistance received in preparing this thesis and the sources used have been acknowledged. The work contained in this thesis has not been previously submitted for a PhD degree at any other higher education institution.

Djamil Al-Halbouni

29 July 2019

Table of Contents

Abstract

Sinkholes and depressions are typical landforms of karst regions. They pose a considerable natural hazard to infrastructure, agriculture, economy and human life in affected areas worldwide. The physio-chemical processes of sinkholes and depression formation are manifold, ranging from dissolution and material erosion in the subsurface to mechanical subsidence/failure of the overburden. This thesis addresses the mechanisms leading to the development of sinkholes and depressions by using complementary methods: remote sensing, distinct element modelling and near-surface geophysics.

In the first part, detailed information about the (hydro)-geological background, ground structures, morphologies and spatio-temporal development of sinkholes and depressions at a very active karst area at the Dead Sea are derived from satellite image analysis, photogrammetry and geologic field surveys. There, clusters of an increasing number of sinkholes have been developing since the 1980s within large-scale depressions and are distributed over different kinds of surface materials: clayey mud, sandy-gravel alluvium and lacustrine evaporites (salt). The morphology of sinkholes differs depending in which material they form: Sinkholes in sandy-gravel alluvium and salt are generally deeper and narrower than sinkholes in the interbedded evaporite and mud deposits. From repeated aerial surveys, collapse precursory features like small-scale subsidence, individual holes and cracks are identified in all materials. The analysis sheds light on the ongoing hazardous subsidence process, which is driven by the base-level fall of the Dead Sea and by the dynamic formation of subsurface water channels.

In the second part of this thesis, a novel, 2D distinct element geomechanical modelling approach with the software PFC2D-V5 to simulating individual and multiple cavity growth and sinkhole and large-scale depression development is presented. The approach involves a stepwise material removal technique in void spaces of arbitrarily shaped geometries and is benchmarked by analytical and boundary element method solutions for circular cavities. Simulated compression and tension tests are used to calibrate model parameters with bulk rock properties for the materials of the field site. The simulations show that cavity and sinkhole evolution is controlled by material strength of both overburden and cavity host material, the depth and relative speed of the cavity growth and the developed stress pattern in the subsurface. Major findings are: (1) A progressively deepening differential subrosion with variable growth speed yields a more fragmented stress pattern with stress interaction between the cavities. It favours multiple sinkhole collapses and nesting within large-scale depressions. (2) Low-strength materials do not support large cavities in the material removal zone, and subsidence is mainly characterised by gradual sagging into the material removal zone with synclinal bending. (3) High-strength materials support large cavity formation, leading to sinkhole formation by sudden collapse of the overburden. (4) Large-scale depression formation happens either by coalescence of collapsing holes, block-wise brittle failure, or gradual sagging and lateral widening.

The distinct element based approach is compared to results from remote sensing and geophysics at the field site. The numerical simulation outcomes are generally in good agreement with derived morphometrics, documented surface and subsurface structures as well as seismic velocities. Complementary findings on the subrosion process are provided from electric and seismic measurements in the area.

Based on the novel combination of methods in this thesis, a generic model of karst landform evolution with focus on sinkhole and depression formation is developed. A deepening subrosion system related to preferential flow paths evolves and creates void spaces and subsurface conduits. This subsequently leads to hazardous subsidence, and the formation of sinkholes within large-scale depressions. Finally, a monitoring system for shallow natural hazard phenomena consisting of geodetic and geophysical observations is proposed for similarly affected areas.

List of Figures

CHAPTER 1

Introduction

1.1 Sinkholes in karst dominated regions

Humanity dedicates a large effort to understand the natural processes in order to mitigate the effects of any kind of prominent natural hazards and desasters, i.e. earthquakes, volcano eruptions, storms, floodings and landslides, just to name a few very well known examples. Sinkholes, however, are an until recently rather unknown and underestimated natural hazard. These circular to elliptical, closed depressions of the Earth's surface can cause considerable damage to infrastructure, agriculture, economy and human life in affected areas worldwide (Waltham et al., 2005)). Prominent examples (Fig. 1.1) can be found in Florida (US) (Tihansky, 1999; Brinkmann et al., 2008), Italy (Intrieri et al., 2018; Parise and Vennari, 2013), the Ebro valley in Spain (Gutiérrez et al., 2011), China (Pan et al., 2018), all along the Dead Sea shore (Abelson et al., 2017), in the German Kyffhäuser mountains (Wadas et al., 2016) and northern sediment plains (Kaufmann et al., 2018), as well as in many large cities of the world, e.g. in Guatemala, (Hermosilla, 2012).

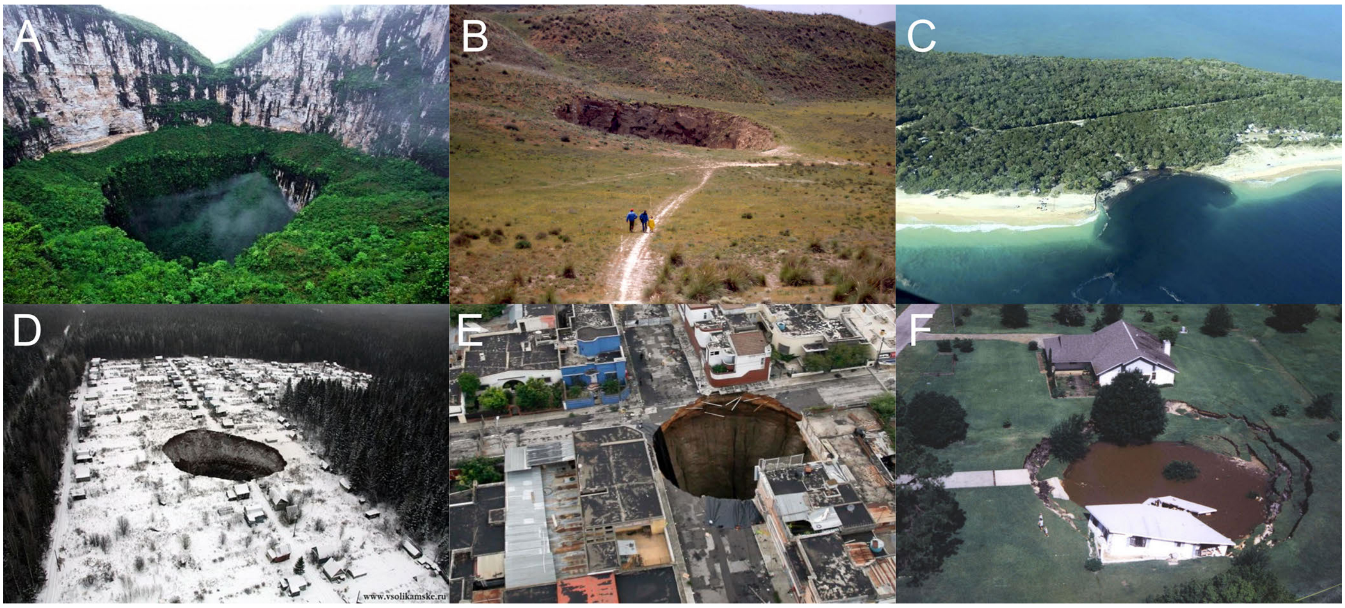

Figure 1.1: Media covered prominent sinkholes. Typical examples of natural (top row) and man-made sinkholes (bottom row): (**A**) in the mountain province of Fengjie, Chongquing, China, (**B**) the Chinchòn doline, Spain, (**C**) at a campsite at rainbow beach, Queensland, Australia, (**D**) due to Potash mining at Solikamsk-2 in Perm, Russia, (**E**) due to a broken water channel in Guatemala city, Guatemala and (**G**) due to water extraction at Crooked Lake, Florida, USA. Credits are listed in MediaSH (2019).

The physio-chemical processes leading to the development of sinkholes are manifold and often not yet fully understood, but in most natural cases linked to the development of a karst system, hydrologically complex geological units that consist of interconnected cavities, cracks, tubes, fissures and other secondary void spaces with fluid flow. Karst aquifers consist of carbonate or evaporitic rocks and cover approximately 10 % of the Earth's surface (cf. World Karst Map BGR et al., 2017), providing fresh water for a quarter of the world's population (USGS, 2000). The primary processes of karst formation are:

- Chemical dissolution (leaching) by undersaturated water with respect to the mineral composition of the surrounding material. This concerns usually limestones, dolomites, chalk and any kind of evaporitic deposits that are rich in soluble minerals like calcite, gypsum, anhydrite, aragonite or halite (Warren, 2006).
- Physical erosion, i.e. mechanical mobilization of unconsolidated materials of the subsurface of any grain sizes.

The term 'subrosion' is often used for both leaching and physical erosion of the subsurface. In this study it is used to distinguish the mobilisation by leaching and transport from pure dissolution. Subrosion leads to material removal in the underground with possible subsequent ground subsidence or collapse. Such a collapse, termed either sinkhole formation or sinkhole collapse in the following, happens generally when the critical mechanical strength of the overburden is surpassed. This may happen slowly, due to continuous material removal and progressive failure of the overburden, or relatively fast, due to sudden failure and potentially triggered by external processes like earthquakes, storms or human interference (constructions, mining, pumping), that may cause a collapse due to short-term changes of the physical conditions of the subsurface. In either case, the mechanical constitution of the subsurface and overburden, whether it can sustain large voids or not, is essential for the type of sinkhole developed at the surface. There are several classifications of sinkhole types available in literature (Gutiérrez et al., 2014; Waltham et al., 2005). In this work the generic classification by Gutiérrez et al. (2014) based on collapse styles (morphology) and type of cover and basement rock is used.

A simple conceptual model of sinkhole formation is shown in Fig. 1.2. A subrosion zone is sketched in the subsurface and is of general interest for geophysical investigation, to assess the hazard potential and possible collapse precursors.

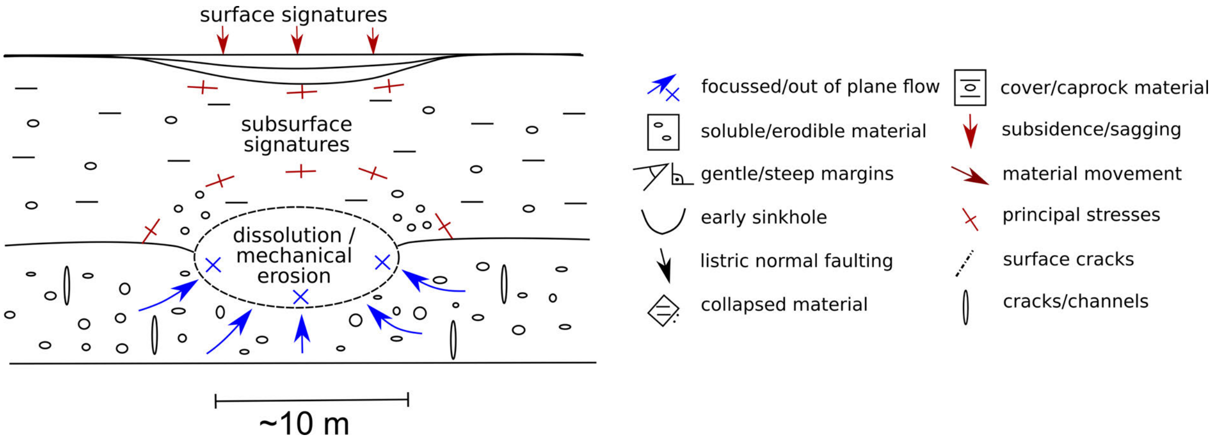

Figure 1.2: Simple conceptual model of sinkhole formation. Indicated are typical surface and subsurface features the principal stress system around a subsurface void space.

Due to material removal, small subsidence may appear before collapse. In nature, generally mixtures of different types of sinkholes are widespread (cf. Gutiérrez et al., 2014) and the detailed steps of formation in the subsurface are still unknown. In an evolved karst system one finds typically large depression landforms into which the sinkholes are embeded. Coalescence of holes into larger groups or clusters and alignements are common. In karst terminology, more complex shaped, large-scale depressions with lower slope-inclinations are called uvalas and elongated, flat valley like depressions are commonly referred to as poljes (Waltham et al., 2005).

Since the last two decades only, a large effort has been undertaken to investigate the physical background of sinkholes and subsidence, culminating into recent interdisciplinary projects (Kottmeier et al., 2016; Krawczyk, 2018), into which this thesis is embedded. The Dead Sea has been chosen as the focus area to compare modelling results of this study because of its unique setting as a natural laboratory.

1.2 The Dead Sea sinkhole hazard

Tectonically the Dead Sea pull-apart basin forms part of the Dead Sea transform fault (DSTF), an active left-lateral rift system between the Arabian and African plate running from the East Anatolian fault in the North to the Red Sea in the South (Bender, 1968; Garfunkel and Ben-Avraham, 1996). The Dead Sea hypersaline terminal lake is located in this basin and is mainly fed by the Jordan river and several Wadi systems (Siebert et al., 2014). This setting, together with the semi-arid to arid climatic conditions makes the region around the Dead Sea vulnerable to several natural hazards like droughts, flashfloods and severe storms, subsidence, landslides as well as sinkholes (Kottmeier et al., 2016; Vey et al., 2019). The development of the latter with more than six thousand sinkholes documented so far has steadily increased in the last decades (Abelson et al., 2017). It has been connected to the dramatic drop of the lake level from -393 mbsl in the 1950^{s} (Taqieddin et al., 2000) to -433.4 mbsl in Oct. 2018 and the subsequent base-level fall (Watson et al., 2019). As a result, a higher groundwater head gradient develops towards the Dead Sea. This recession is clearly seen in the increased exposure of the shore (Fig. 1.3), where the most active sinkhole areas on both sides of the lake are marked.

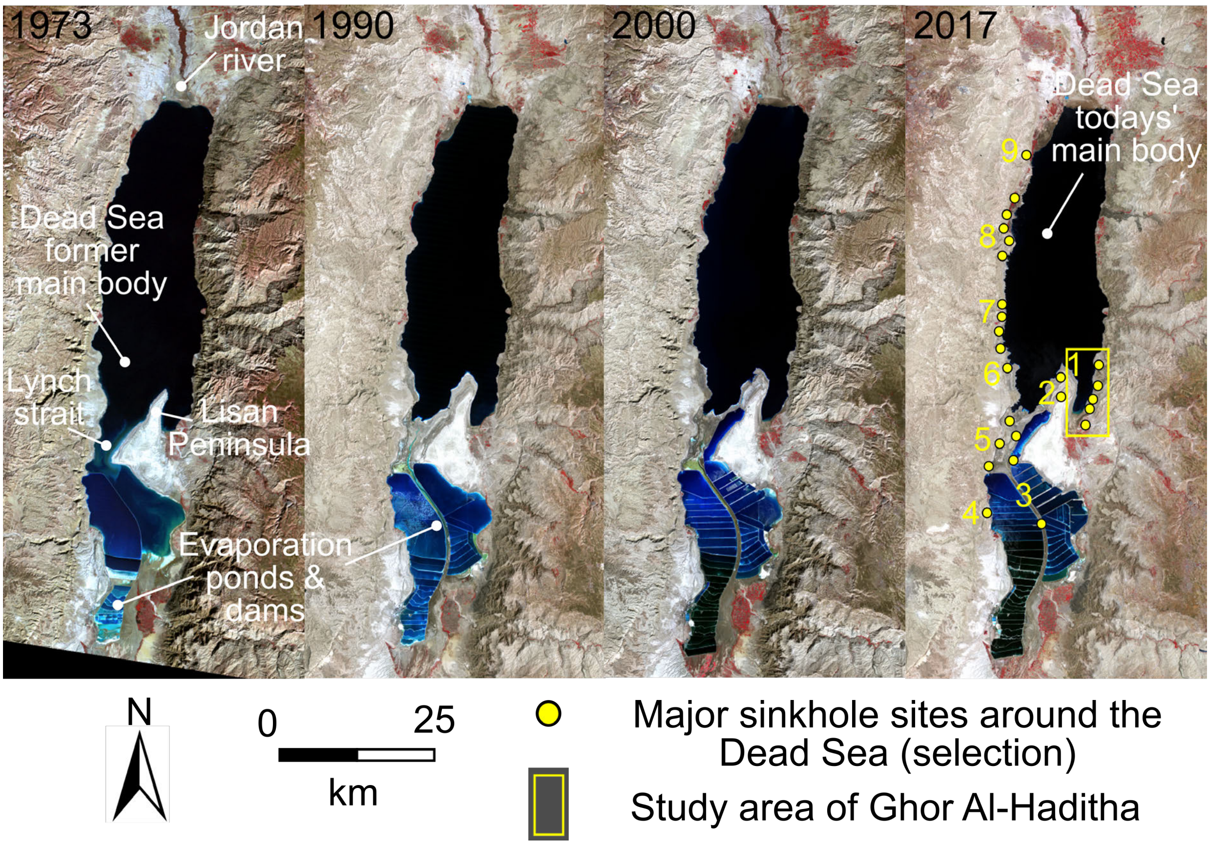

Figure 1.3: Landsat satellite images of the Dead Sea area. A recession of the shoreline and the separation into a Northern Dead Sea body and the evaporation pond body is clearly visible between 1973 and today. Yellow circles mark a selection of the most important sites with known sinkhole formation on both sides of the Dead Sea, based on Ezersky et al. (2017) and Abou Karaki et al. (2016) and this work. These are: 1) Ghor Al-Haditha, the study area of this work; 2) Lisan Peninsula; 3) Arab Potash company and Dead Sea works; 4) Newe Zohar and Ein Boqeq; 5) Lynch Strait; 6) Nahal Zeelim; 7) Ein Gedi to Nahal Hever; 8) Dragot to Mineral Beach and 9) Zikim. Satellite images are from USGS (2017) with spatial resolutions of 60 m before the year 2000 and 30 m thereafter.

The investigation area of this study is located near Ghor Al-Haditha in Jordan, on the southeastern shore of the main body of the Dead Sea, between the Lisan Peninsula and the Moab mountains (Fig. 1.4A). The area forms part of a piedmont of consolidated to semi-consolidated alluvial fan deposits of Pleistocene to recent age, and lies between several ephemeral streams as indicated in Fig. 1.4B. Different viewpoints of the area are shown in parts C-F of Fig. 1.4. Since 1970, the shoreline has retreated by 2.5 km exposing the former Dead Sea lakebed. It consists of silt-clay material (mud) interbedded with evaporites (halite, gypsum, aragonite, calcite) of the Lisan formation (see Chap. 3 and Taqieddin et al., 2000; Watson et al., 2019).

The first sinkholes formed in 1985 near the Wadi Ibn Hamad and since then, more than 1100 have appeared in the area, covering a stretch of approximately 25 km^2 (Fig. 1.4B). The main clusters of hazardous sinkholes formed around the former 'Numeira mixed salts and mud company', at the border between the alluvial cover and the mud-flat, and lead to the destruction of the factories infrastructure and neighboring agricultural fields and roads until 2009 (Watson et al., 2019; Closson and Abou Karaki, 2009, see Chap. 3). In the last decade, the majority of sinkholes started to appear in the northern part of the area and moved closer to the shoreline, although activity in the southern part has not ceased yet.

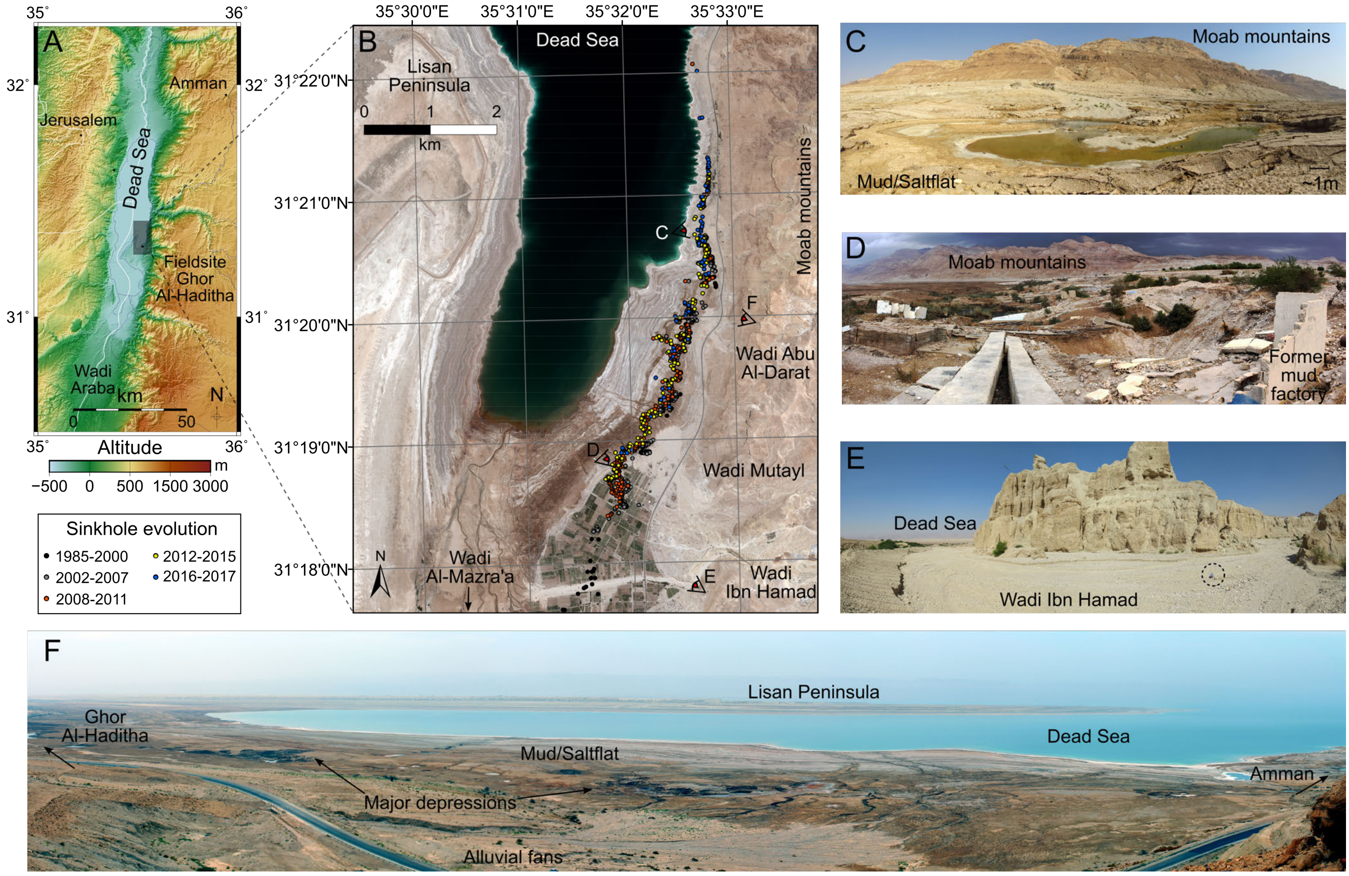

Figure 1.4: Overview of the sinkhole area of Ghor Al-Haditha. (**A**) map of the Dead Sea with location of the study area. (**B**) Pleiades satellite image from April 2018 with a resolution of 50 cm. Sinkhole evolution and migration since the year 1985 is depicted in coloured circles (modified after Watson et al. (2019)). The location of parts (C-F) is indicated by symbols. (**C**) exposed mud/salt-flat, the former lakebed of the Dead Sea. (**D**) former mud factory area which has been destroyed by subsidence, sinkhole and canyon formation. (**E**) view of the main Wadi Ibn Hamad. (**F**) overview from the Moab mountains with major canyons and geological materials. The length of the road section visible to the left of the image is 0.5 km.

Sinkhole types in the area follow generally two main morphological endmembers: flat and wide sinkholes in the mud/salt-flat and narrow and deep sinkholes in the alluvium or thick evaporite cover (Fig. 1.5). While this distinction generally holds for individual sinkhole endmembers, mixtures of both types, lateral widening, soil piping structures and coalesced/nested multiple sinkholes developed over time in this area (Fig. 1.5B and C). This development is related to the above described maturation of the karst system and goes along with the formation of large depression zones and uvalas. Furthermore, sinkholes may be associated to individual relatively fresh water springs and may lie adjacent to active canyons (see Chap. 3 and Watson et al., 2019).

Despite several geophysical studies (cf. e.g. Ezersky et al., 2017; Ezersky and Frumkin, 2013; Frumkin et al., 2011; Sawarieh et al., 2000; Diabat, 2005; El-Isa et al., 1995) sinkhole occurrence, morphology and development at Ghor Al-Haditha remain incompletely understood and a topic of high relevance, not only for the local authorities. For this study, Ghor Al-Haditha was therefore chosen as the suitable field-site and remote sensing was used to enlight the spatio-temporal development of karst landforms.

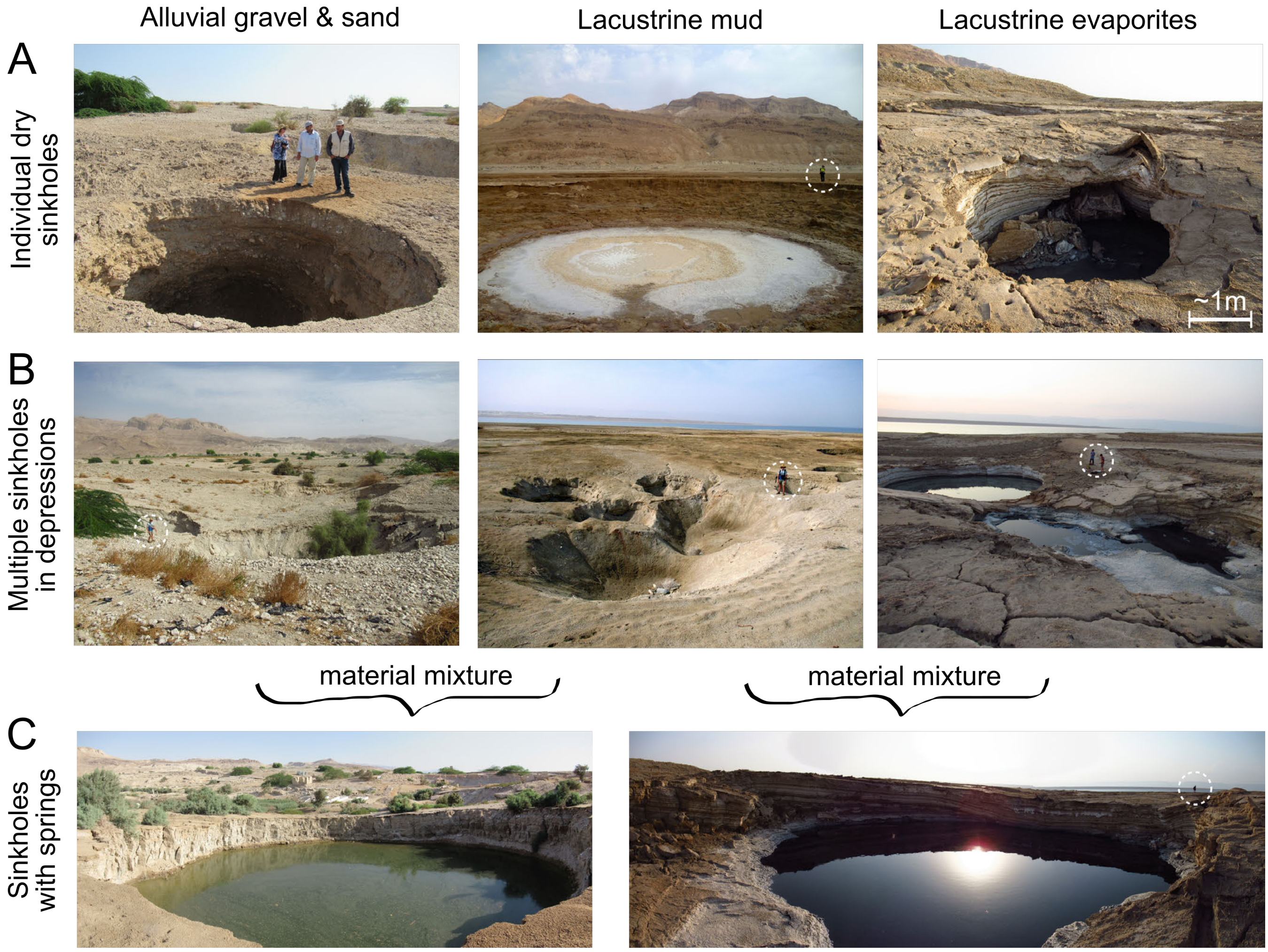

Figure 1.5: Different forms of sinkholes at the Dead Sea shoreline. (**A**) examples of individual sinkholes in the three typical cover materials (alluvium, mud and salt). (**B**) multiple sinkholes and larger depression structures in the same materials. (**C**) sinkholes with active springs with typical mixtures of the materials observable at the margin outcrops. Note persons/infrastructure for scale.

1.3 Geomechanical numerical modelling of collapse processes

Numerical modelling is widely used for a further understanding of the physio-chemical processes that involve material removal and fracturing of rock mass with subsequent, potentially hazardous, ground collapse or subsidence. Numerical simulation of a dynamic karst system is generally complex due to the discontinuities, heterogeneities and complex porosities of carbonate rocks (Andriani and Parise, 2015). Continuum mechanics based numerical simulation methods are widely used to investigate both the process of rock dissolution and karst evolution (cf. overview from Parise et al., 2018) and the stability of single cavity systems for specific applications (Fazio et al., 2017; Carranza-Torres et al., 2016; Fuenkajorn and Archeeploha, 2010; Parise and Lollino, 2011; Rawal et al., 2016; Salmi et al., 2017). Recent promising advances have been made with viscoelastic modelling of sinkhole formation, partly with application to the Dead Sea area (Shalev and Lyakhovsky, 2012; Baer et al., 2018; Souley et al., 2011), and three-dimensional finite element modelling (FEM) of caves (Sainsbury, 2012).

However, three major drawbacks are identified in these approaches considering geomechanical simulation of collapse processes and sinkhole formation: Firstly, rotation, fracturing and non-elastic deformation subject to large and highly localised strains are difficult to simulate with FEM (Jing and Stephansson, 2007). Secondly, past continuum-based approaches have often neglected the mechanical growth of void spaces and the explicit simulation of sinkhole collapse. And thirdly, the geometries of voids involved in sinkhole development are often non-singular, irregular and distributed over lots of scales (see Chap. 3 and Abelson et al., 2017; Ezersky et al., 2017; Gutiérrez et al., 2016; Yizhaq et al., 2017), and most present studies do not account for this.

For addressing these drawbacks related to rock mechanics, discontinuous medium simulation methods are more suitable, where the intrinsic heterogeneity of the particle assembly allows for complex mechanical behaviour and spontaneous crack formation. The main advantage is its ability to simulate rock samples or rock masses as an assemblage of discrete particles or blocks, which can undergo large displacements and rotations. A member of the family of such discrete element methods which uses undeformable particles is called the distinct element method (DEM, cf. Cundall and Strack, 1979; Potyondy and Cundall, 2004; Fakhimi and Villegas, 2007).

While DEM has been developed and used since several decades for small-scale modelling, the application to large-scale geological problems has only been rising recently due to the increase of computer power. Recent successful large-scale numerical simulation of rock failure processes with DEM address the topics of caldera subsidence and volcano deflation (Holohan et al., 2011, 2015, 2017; Gudmundsson et al., 2016), structures and growth of normal fault systems (Schöpfer et al., 2007a,b, 2016, 2017), as well as slope, mine and tunnel stability (Bonilla-Sierra et al., 2015; Thompson et al., 2010). The latter is generally linked to the topic of sinkhole formation due to the basic approach to simulate a void space in the underground with observation of the surface displacements. For modelling sinkhole collapse and surface deformation, Baryakh et al. (2008, 2009) and Bym et al. (2013) used DEM for single void space analysis, Hatzor et al. (2010) used predefined discrete fracture networks and Mercerat (2007) used DEM limited to a single rock layer in a FEM coupled model of a salt-cavern. However, the explicit simulation of the growth and mechanical interaction of single and multiple void spaces is essential for understanding sinkhole and subsidence formation and has not been presented so far.

This thesis is embedded in the above elaborated framework. The software Particle Flow Code (PFC-V5) from Itasca (Potyondy and Cundall, 2004; Potyondy, 2014) is used to develop a 2D DEM approach of large-scale mechanical collapse processes modelling and comparison with results obtained by remote sensing and geophysics.

1.4 Structure of this cumulative thesis

An introduction to the structure of this thesis is given in the following. Chapter 2 highlights the main research questions of this work and summarises the methods used in all main authored publications. Chapter 3 deals specifically with the analysis of the sinkhole formation at the field site via an up-to-date high resolution photogrammetric survey and satellite image analysis. It provides essential findings on sinkhole development and morphology important both for process understanding and comparison with numerical modelling. In Chap. 4, after benchmarking and calibration of rock mechanical parameters, a sophisticated geomechanical numerical modelling approach to simulate individual sinkhole formation is presented. In Chap. 5, a more generic version of this approach is presented to investigate subsurface failure processes and morphologies of more complex karstic landforms. Finally, the implications for the sinkhole formation process in the field area and the potential of further advanced numerical modelling and geophysical monitoring is discussed in Chap. 6. In the following, the main highlights of all main author and co-author publications part of or relevant for this thesis and the broader perspective are summarised.

1.4.1 Publications as chapters of this thesis

Statement of contribution: As the main author of these publications the contribution ranged from scientific literature research, collecting and analysing the data, programming the model codes and analysing the model outputs, to writing the text and putting together the figures as well as final correction of the revised manuscripts.

Publication 1 (Chap. 3): **Al-Halbouni, D.**, Holohan, E. P.Saberi, L., Alrshdan, H., Sawarieh, A., Closson, D., Walter, T. R., & Dahm, T., Sinkholes, subsidence and subrosion on the eastern shore of the Dead Sea as revealed by a close-range photogrammetric survey. *Geomorphology, 285*, 305-324. https://doi.org/10.1016/j.geomorph.2017.02.006, 2017

Publication one is included as Chap. 3 in this thesis. This work builds the basis for the numerical modelling as it reveals important information about the strong physical component of the material removal based on subsurface stream flows and its relation to sinkhole morphologies in the former Dead Sea mud-flat and alluvial fan sediments. Structural, morphological and hydrological features of the Ghor Al-Haditha sinkhole area in Jordan are analysed by close-range photogrammetry, GIS and (hydro)-geological fieldwork. Important quantitative parameters (sinkhole circularities, depth/diameter (De/Di) ratios, slope steepness) and erosion rates for the southern part of the area are estimated based on high resolution and high accuracy orthophotos (OF) and digital surface models (DSM).

Publication 2 (Chap. 4): **Al-Halbouni, D.**, Holohan, E. P., Taheri, A., Schöpfer, M. P. J., Emam, S., & Dahm, T.: Geomechanical modelling of sinkhole development using distinct elements: Model verification for a single void space and application to the Dead Sea area. *Solid Earth, 9, Environmental Changes and Hazards in the Dead Sea Region* ,1341-1373. https://doi.org/10.5194/se-2018-62, 2018

Publications two is included as Chap. 4. A new technical and methodological development using 2D distinct elements for modelling individual sinkhole collapse based on the growth of single void spaces in the underground is presented. A detailed numerical benchmarking of the methods with analytical solutions and calibration of rock parameters for the three typical sediment types at the Dead Sea is performed: lacustrine mud, alluvial sand-gravel and lacustrine rock salt. It reveals the high susceptibility of all materials to mechanical failure and sinkhole formation, and a dependency of morphological aspects on the mechanical strength of the overburden. Also, the collapse process itself differs, depending on the material in which the void space forms: large cavities may be sustained or the subsurface collapse zone may form a triangular area. The observed structures and quantitative measurements of morphological (De/Di ratios) parameters fit well to results from photogrammetry, revealing the evolution history of the sinkholes at Ghor Al-Haditha.

Publication 3 (Chap. 5): **Al-Halbouni, D.**, Holohan, E. P., Taheri, A., Watson, R., Polom, U., Schöpfer, M. P. J., Emam, S. and Dahm, T., Distinct element geomechanical modelling of the formation of sinkhole clusters within large-scale karstic depressions, *Solid Earth, 10, 1219-1241*, https://doi.org/10.5194/se-10-1219-2019, 2019.

Publications three is included as Chap. 5. An extended DEM approach is presented to simulate complex karstic landforms like clustered sinkholes and large-scale depressions, as observed in the field and by remote sensing (cf. publication 6). A comparison between different multiple cavity growth scenarios is provided. The importance of a differential velocity field in the material removal system to produce multiple sinkholes, rather than only block-wise subsidence, is highlighted. A deepening of the subrosion zone is necessary to simulate the correct appearance order of sinkholes within large-scale depressions. This deepening differential subrosion scheme mimics the driving background processes of base-level fall at the Dead Sea and preferential flow paths in a karstic system. Morphometric aspects of the sinkholes and depressions as well as structural and geophysical features (cf. publication 7) of the subsurface of the sinkhole field site Ghor Al-Haditha are well reproduced.

1.4.2 Further relevant publications

Publication 4: Kottmeier, C., Agnon, A., **Al-Halbouni, D.**, Alpert, P., Corsmeier, U., Dahm, T., Eshel, A., Geyer, S., Haas, M., Holohan, E. P., Kalthoff, N., Kishcha, P., Krawczyk, C. M., Lati, J., Laronne, J. B., Lott, F., Mallast, U., Merz, R., Metzger, J., Mohsen, A., Morin, E., Nied, M., Rödiger, T., Salameh, E., Sawarieh, A., Shannak, B., Siebert, C., & Weber, M., New perspectives on interdisciplinary earth science at the Dead Sea: the DESERVE project. *Science of the Total Environment, 544*, 1045-1058, https://doi.org/10.1016/j.scitotenv.2015.12.003, 2016

Publication four gives an overview of the international and interdisciplinary DESERVE project which deals with natural hazards at the Dead Sea region. Scientific investigation of meteorological, hydrological and tectonic hazards formed part of this Helmholtz Virtual Institute, into which the sinkhole topic and this thesis are embedded.

Publication 5: Vey, S., Alshawaf, F., **Al-Halbouni, D.**, Metzger, J., Güntner, A., Dick, G., Ramatschi, M., Wickert, J., & Weber, M., Interplay of climate, water and Solid Earth - Subsidence of the Dead Sea shore. *Scientific Reports*, in review, 2019.

Publication five shows the direct interplay between three different compartments, "Solid Earth", "hydrosphere" and "atmosphere", in their role regarding the Dead Sea subsidence phenomenon. From GNSS reflectometry derived subsidence rates of the surface are synchronous, with a time-lag of two months, to the Dead Sea lake drop and derived evaporation rates. This work describes the background processes of the Dead Sea regression and the related ground subsidence relevant for the sinkhole hazard adressed in this thesis.

Publication 6: Watson, R. A., Holohan, E. P., **Al-Halbouni, D.**, Saberi, L., Sawarieh, A., Closson, D., Alrshdan, H., Abou Karaki, N., Siebert, C., Walter, T.R., & Dahm, T., Sinkholes and uvalas in evaporite karst: spatio-temporal development with links to base-level fall on the eastern shore of the Dead Sea. *Solid Earth Discussions*, accepted, https://doi.org/10.5194/se-2018-105, 2019.

Publication six expands the remote sensing analysis of the sinkhole affected area in Jordan to nearly five decades. Sinkhole distribution and migration in space and time is analysed with the help of satellite and aerial images. Quantitative measurements of alluvial fan growth, stream channel incision, land subsidence and sinkhole morphologies in three different cover materials are provided. The relation between the hydrogeological system of the Wadis at Ghor Al-Haditha, the subsurface channels and sinkhole/depression formation is highlighted. This publication shows that sinkholes usually form before major depressions develop, probably related to the rapid base-level fall of the Dead Sea, and is an important link for comparison to our numerical models.

Publication 7: Polom, U., Alrshdan, H., **Al-Halbouni, D.**, Dahm, T., Sawarieh, A., Atallah, M. Y., & Krawczyk, C. M., Shear wave reflection seismics yields subsurface dissolution and subrosion patterns: application to the Ghor Al-Haditha sinkhole site, Dead Sea, Jordan. *Solid Earth, 9, Environmental Changes and Hazards in the Dead Sea Region*, 1079-1098, https://doi.org/10.5194/se-9-1079-2018, 2018.

Publication seven analyses the subsurface of Ghor Al-Haditha with the shear wave reflection method. This method has been applied several consecutive years in the main sinkhole affected area. A high resolution characterization of the subsurface into intercalated, dipping alluvial fan and mud-flat sediment layers is revealed. The structure of the subsurface is analysed and depressions, bowl-shaped zones, void space and subrosion areas with low reflectivity, stable areas as well as the depth of the main limestone-carbonate mud layer susceptible to subrosion are delineated. Interestingly, the analysis reveals the non-existence of a massive salt layer in this area, contrary to findings on the western side of the lake, which attribute this layer as the base to subsurface erosion and dissolution. Rather, interpretation of the seismic profiles together with photogrammetric analysis lead to conclusions about the importance of the physical erosion of chemically weakened mud and alluvial sediments containing thin evaporite layers. This work builds another important basis to which the numerical modelling results are compared to.

Publication 8: **Al-Halbouni, D.**, Holohan, E. P., Alrshdan, H., Sawarieh, A., & Dahm, T., Sinkhole morphologies from photogrammetry and distinct element modelling - an example from the Dead Sea. In: Recent Advances in Environmental Science from the Euro-Mediterranean and Surrounding Regions. Proceedings of the CAJG conference 12-15 November, Hammamet, Tunesia, Springer, 2019.

Publication eight summarises the use of the distinct element modelling method to reproduce morphological features of the mud-flat and alluvium sinkholes at the Dead Sea shoreline. It highlights the complementary use of field methods and numerical modelling for a broader readership interested in the hazard potential of sinkholes.

CHAPTER 2

Objectives and methods

In this chapter, the research questions and methods used to address the topic of sinkhole and large-scale depression formation are highlighted and the link to each corresponding part of this cumulative thesis is given. The questions can generally be transferred to any area affected by rapid sinkhole growth. The answers to these questions are discussed in a broader perspective in Chap. 6.

2.1 Research questions

① **What are the typical morphologies and ground features that develop in an active karst area? How do sinkholes develop in space and time?**

- Background: Sinkhole morphologies give important hints about their dimensions (depth and diameter) and ellipticities. They are dependent on the material distribution involved in the collapse. Recognition of structural features like large depression zones, uvalas, sinkhole alignment and clustering, canyon slumps, bowl-shaped formations, faults, cracks, crevasses and fissures in the surface and subsurface gives indications about their origin and may help to define hazardous areas. The (hydro)-geological background here forms an important integral part to understand the formation process.
- Data/methods used: Literature research, field survey, aerial images from drones and balloons, photogrammetry and Geographical Information System (GIS) software.
- Chapter(s): 3 and 6.

② **How can large-scale ground subsidence and sinkhole formation be simulated with the particle-based distinct element method?**

- Background: DEM has not been used yet intensively to address the large-scale problem of subsidence and sinkhole formation (see Chap. 1). An approach using this computationally intensive particle-based method for large-scale simulation needs to be thoroughly benchmarked and calibrated before applying it to real cases. This involves comparison with analytical solutions for simple excavation shapes and calibration of real rock parameters.
- Data/methods used: Distinct element modelling with PFC2D-V5.
- Chapter(s): 4 and 6.

③ How does a void space develop mechanically in the subsurface and how does it translate to a sinkhole at the surface? How do sinkhole clusters and depressions develop mechanically?

- Background: This question concerns the general investigation of mechanical controls of sinkhole formation. It addresses the comparison of DEM outcomes with real field observations from the Dead Sea. This topic concerns the analysis of structural features, sinkhole collapse onset, morphologies and morphometrics, evolution and patterns, the mechanical interaction of voids in a karst system and the relation between large-scale depressions and sinkholes.
- Data/methods used: Distinct element modelling with PFC2D-V5, field survey, photogrammetry, GIS, and shear wave reflection seismics.
- Chapter(s): 4, 5 and 6.

④ What is the relation between subsurface geophysical parameters and the sinkhole/depression formation process?

- Background: Field data comparison with model results is essential for correct interpretation of geophysical data and established conceptual models for characterization of subsurface processes. Subject to implementation, with the help of DEM it is generally possible to track geodetic and geophysical parameters on a very high resolution scale. Knowing calibrated macroscopic rock parameters helps to derive e.g. apparent seismic velocity distribution with depth. Moreover, near-surface geophysical studies reveal essential information about subsurface processes.
- Data/methods used: Distinct element modelling with PFC2D-V5, photogrammetry and GIS, shear wave reflection seismics, electric resistivity tomography (ERT) and self-potential (SP).
- Chapter(s): 4, 5, 6 and 7.

2.2 Applied methods

The scientific questions of Sec. 2.1 are addressed by the most suitable method or by a combination of methods. These methods are highlighted in Fig. 2.1. Different complementary approaches from various perspectives are combined:

1. Remote: Aerial imagery from satellites, drones and balloons is analysed by near-field photogrammetry and GIS.
2. Ground based: Observations from geologic fieldwork and hydro(geo)logical measurements.
3. Subsurface: Geophysical imaging by shear wave reflection seismics and electrics.
4. Simulation: 2D geomechanical numerical modelling of sinkhole formation with the distinct element approach.

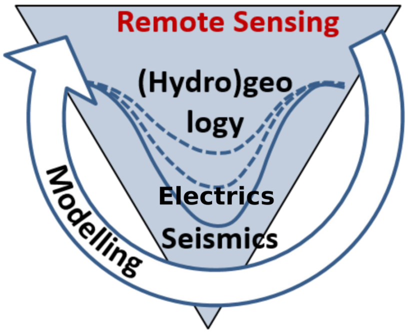

Figure 2.1: Overview of the different perspectives the sinkhole phenomenon is addressed.

The technical details of all methods can be found in the according publications and manuscripts of this cumulative thesis (see list in Chap. 1). Highlight, and main focus of this thesis, are the photogrammetric analysis (Chap. 3) and the numerical modelling of sinkhole formation with the distinct element method (Chapters 4, 5, and 6).

CHAPTER 3

Sinkholes, subsidence and subrosion on the eastern shore of the Dead Sea as revealed by a close-range photogrammetric survey

Published on 15th of May 2017 in *Geomorphology* vol. 285 pp. 305–324.
https://doi.org/10.1016/j.geomorph.2017.02.006

Geomorphology 285 (2017) 305–324

Contents lists available at ScienceDirect

Geomorphology

journal homepage: www.elsevier.com/locate/geomorph

Sinkholes, subsidence and subrosion on the eastern shore of the Dead Sea as revealed by a close-range photogrammetric survey

Djamil Al-Halbouni[a,*], Eoghan P. Holohan[a,d], Leila Saberi[a], Hussam Alrshdan[b], Ali Sawarieh[b], Damien Closson[c], Thomas R. Walter[a], Torsten Dahm[a]

[a] GFZ German Research Centre for Geosciences, Section 2.1, Telegrafenberg, Potsdam14473, Germany
[b] Ministry of Energy and Mineral Resources, Mahmoud Al Moussa Abaidat Street, Amman140027, Jordan
[c] Eurosense Belfotop, Remote Sensing Applications Department, Nerviërslaan 54, WemmelB-1780, Belgium
[d] UCD School of Earth Sciences, University College Dublin, Belfield, Dublin 4, Ireland

ARTICLE INFO

Article history:
Received 29 April 2016
Received in revised form 23 January 2017
Accepted 16 February 2017
Available online 22 February 2017

Keywords:
Photogrammetry
Sinkholes
Subsidence
Subrosion
Karst
Dead Sea
Ghor Al-Haditha

ABSTRACT

Ground subsidence and sinkhole collapse are phenomena affecting regions of karst geology worldwide. The rapid development of such phenomena around the Dead Sea in the last four decades poses a major geological hazard to the local population, agriculture and industry. Nonetheless many aspects of this hazard are still incompletely described and understood, especially on the eastern Dead Sea shore. In this work, we present a first low altitude ($<$ 150 m above ground) aerial photogrammetric survey with a Helikite Balloon at the sinkhole area of Ghor Al-Haditha, Jordan. We provide a detailed qualitative and quantitative analysis of a new, high resolution digital surface model (5 cm px^{-1}) and orthophoto of this area (2.1 km^2). We also outline the factors affecting the quality and accuracy of this approach.

Our analysis reveals a kilometer-scale sinuous depression bound partly by flexure and partly by non-tectonic faults. The estimated minimum volume loss of this subsided zone is $1.83 \cdot 10^6$ m^3 with an average subsidence rate of 0.21 m yr^{-1} over the last 25 years. Sinkholes in the surveyed area are localized mainly within this depression. The sinkholes are commonly elliptically shaped (mean eccentricity 1.31) and clustered (nearest neighbor ratio 0.69). Their morphologies and orientations depend on the type of sediment they form in: in mud, sinkholes have a low depth to diameter ratio (0.14) and a long-axis azimuth of NNE–NE. In alluvium, sinkholes have a higher ratio (0.4) and are orientated NNW–N. From field work, we identify actively evolving artesian springs and channelized, sediment-laden groundwater flows that appear locally in the main depression. Consequently, subrosion, i.e. subsurface mechanical erosion, is identified as a key physical process, in addition to dissolution, behind the subsidence and sinkhole hazard. Furthermore, satellite image analysis links the development of the sinuous depression and sinkhole formation at Ghor Al-Haditha to preferential groundwater flow paths along ancient and current wadi riverbeds.

1. Introduction

Ground subsidence phenomena occur all over the world due to both natural and anthropogenic causes (cf. e.g. Kohl, 2001; Denizman, 2003; Caramanna et al., 2008; Closson et al., 2009; Parise and Lollino, 2011; Dahm et al., 2011; Dreybrodt, 2012; Gutierréz et al., 2014; Kotyrba, 2015; Parise, 2015). Sinkholes in particular are enclosed depressions of the soil/rock surface caused by subsurface chemical dissolution (Waltham et al., 2005) or subsurface mechanical erosion (Parise, 2010), termed subrosion in the following as in e.g. Dahm et al. (2011). They typically span a submeter to hundreds of meters scale, both for depth and diameter (cf. e.g. Goldscheider and Drew, 2007; Filin et al., 2011; Gutierréz et al., 2014; Messerklinger, 2014). Sinkholes are genetically classified into two main groups: solution and subsidence sinkholes (Waltham and Fookes, 2005; Gutiérrez et al., 2008; Beck, 2012). Subsidence sinkhole end-member classification refers to the affected material (cover, caprock or bedrock) and the process of formation (collapse, sagging or suffosion) (cf. Gutierréz et al., 2014). In karst environments, collapse sinkholes are often related to subsurface void collapse (Hatzor et al., 2010; Parise and Lollino, 2011; Dreybrodt, 2012; Gutierréz et al., 2014; Waltham, 2016), where stress conditions exceed material strength in the surroundings, frequently related to sudden water-level changes

---

[*] Corresponding author.
E-mail address: halbouni@gfz-potsdam.de (D. Al-Halbouni).

http://dx.doi.org/10.1016/j.geomorph.2017.02.006
0169-555X/

(Tharp, 1999, 2002; Shalev and Lyakhovsky, 2012; Lollino et al., 2013) or seismic activity (e.g. L'Aquila earthquake, Kawashima et al., 2010; Parise et al., 2010). These phenomena are most hazardous due to the rapid cavity roof breakdown and include not only potential direct losses of life, but also damage to economically important buildings, land (Parise, 2010; Krawczyk and Dahm, 2011) and infrastructure (e.g. Brinkmann et al., 2008; Dahm et al., 2011; Gutierréz et al., 2014). The opposite, a slow subsidence process with long-term sinkhole growth, holds for sagging or suffosion sinkholes and is considered as less hazardous from an engineering point of view (Gutierréz et al., 2014).

The sinkhole formation at the Dead Sea (Fig. 1A) has increased sharply in the last decades (Arkin and Gilat, 2000; Yechieli et al., 2015). This development has been associated with the significant lake-level drop since the 1950s (Taqieddin et al., 2000) from ≈ 393 m to 430 m (20.10.2015) below sea level. Anthropogenic influence is considered to be the main reason for this decline, i.e. large water irrigation projects in the northern part along the Jordan river catchment (Gavrieli and Oren, 2004; Bowman et al., 2010), extensive use of Dead Sea brine for Potash production (Lensky et al., 2005; Abelson et al., 2006) as well as the increasing need for drinking and irrigation water due to a growing population (World Bank, 2016) and climatic changes (Menzel et al., 2007; MWI, 2013; Al-Omari et al., 2014; Odeh et al., 2015). Attention to the sinkhole phenomenon has increased, since touristic regions, highways, agricultural land as well as industries (e.g. Ein Gedi, Ghor Al-Haditha, Arab Potash factory) have become seriously affected (Nof et al., 2013; Closson et al., 2013; Closson and Abou Karaki, 2015).

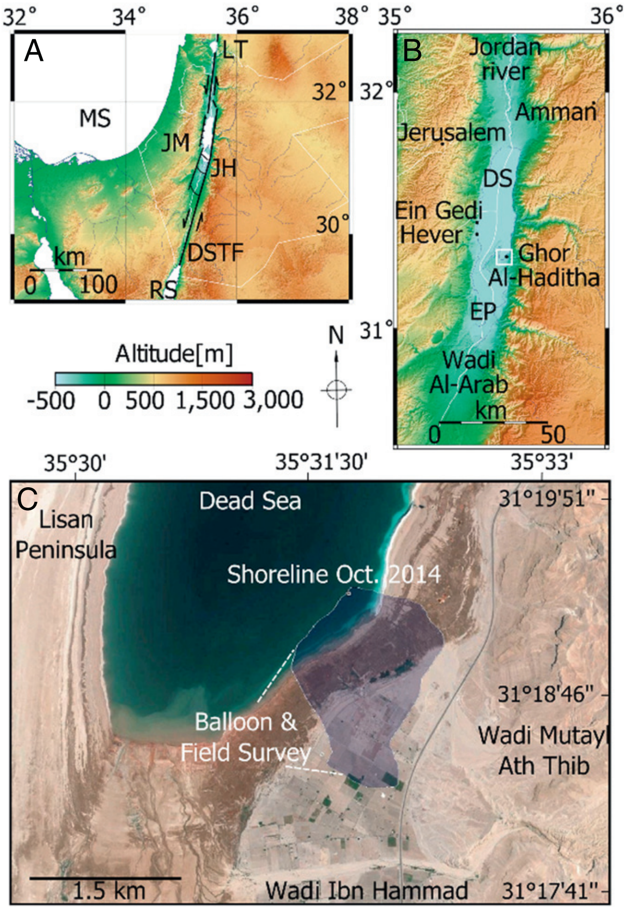

Fig. 1. Location of the Dead Sea and investigation area Ghor Al-Haditha: **A**: Schematic tectonic background of Dead Sea transform fault (DSTF) based on (Bender, 1968; Closson, 2004; Le Béon et al., 2012). MS: Mediterranean Sea, RS: Red Sea, JM: Judean Mountains, JH: Jordanian Highlands, LT: Lake Tiberias. Topographic data are based on SRTM3 databases (Farr et al., 2007). **B**: Dead Sea and surroundings. The survey area Ghor Al-Haditha in Jordan is located at the SE margin of the Dead Sea basin. DS: Dead Sea, EP: Evaporation Ponds. **C**: Detailed outline of the investigation area and the main wadis. A third river, Wadi Al Madbaa, discharges into the delta system in the southern bay and is located further south outside the shown area. Image is a publically available 2009 Digital Globe image from Google Earth.

An important scientific question concerns the mechanical and chemical processes of sinkholes formation: is the formation mechanism controlled by pure salt-dissolution (Frumkin et al., 2011; Oz et al., 2016), faults (Closson and Abou Karaki, 2009), both (Ezersky and Frumkin, 2013; Closson and Abou Karaki, 2013; Ezersky et al., 2014) or subrosion (Arkin and Gilat, 2000)? Hereby the role of rock properties and detailed material/(sub)surface water movement is essential for understanding sinkhole evolution and development of early-warning scenarios (Waltham et al., 2005; Parise, 2008; Lollino et al., 2013; Gutierréz et al., 2014).

In this context, we conducted a high resolution close-range photogrammetric (Burner et al., 1983; Luhmann et al., 2014) investigation of the active sinkhole area of Ghor Al-Haditha in Jordan (cf. DESERVE project in Kottmeier et al., 2016) in Oct. 2014 and 2015 (Fig. 1B,C). We used a cost-efficient and robust helium balloon technique for areas, such as this one, where legal permissions for other UAV based surveys and access to satellite images are difficult to attain.

Photogrammetry has been applied extensively on the western shore of the Dead Sea, e.g. for mapping stream channel incision (Bowman et al., 2010), ground-water flow paths (Mallast et al., 2011) and is currently used for spring discharge detection (Siebert et al., 2014a). However, rather cost-intensive LiDAR (Laser Imaging, Detection and Ranging) or low resolution satellite based InSAR (Interferometric Synthetic Aperture Radar) studies have been used for detailed sinkhole characterization (Filin et al., 2011; Nof et al., 2013; Atzori et al., 2015). Especially on the eastern side of the lake remote sensing studies are still under way (e.g. Al-Ruzouq et al., 2011; Tessari and Floris, 2014, unpublished reports). This is the first study to present a high resolution (5 cm px^{-1}) digital surface model (DSM) and orthophoto of the sinkholes in Jordan.

We firstly introduce the area (Section 2) and then detail the methods used (Section 3). In the results (Section 4) we demonstrate that at Ghor Al-Haditha a large-scale depression has developed in a zone of former surface water channels. In this main depression, at the boundary between two geological units, the alluvium and mud-flat, sediment-laden artesian springs and stream channels appear, continuing both on the surface and below. Furthermore, we provide an estimation of the minimum volume loss in this area and quantitative evidence for material control on sinkhole morphologies. Limitations of the method, implications and a detailed discussion on structural, lithological and groundwater control of subsidence and sinkhole formation are given (Section 5). Finally, we provide a conceptual model for subsidence and sinkhole formation at Ghor Al-Haditha. This study is hence important for the understanding of sinkhole formation processes both at the Dead Sea and in similar hydrogeological environments and may serve as a basis for future sinkhole hazard and risk assessment.

2. Ghor Al-Haditha sinkhole area

The investigation area is located at the SE shore of the northern Dead Sea basin (Fig. 1B,C), an orthorhombic pull-apart basin of 80 km length, between 5 and 17 km width and up to 10 km depth of the sediment infill (Ten Brink and Ben-Avraham, 1989; Garfunkel and Ben-Avraham, 1996; Smit et al., 2008). It forms part of the left-lateral Dead Sea Transform Fault System (DSTF, see Fig. 1A), running from the Red Sea to the East Anatolian Fault between the African and Arabian plates (Bender, 1968), with typically a N10–30° orientation of the main faults (cf. e.g. Yechieli et al., 2015). In this semi-arid to arid region, the Dead Sea is considered as a hyper-saline terminal lake of the Jordan river (Siebert et al., 2014b); the course of which follows the DSTF.

Marine and lacustrine sediment sequences cover the Dead Sea floor and surroundings (cf. e.g. Bender, 1968; Begin et al., 1974; Garfunkel and Ben-Avraham, 1996; Taqieddin et al., 2000; Frumkin et al., 2011). The most prominent is the late Miocene Usdom (Sedom) formation (2–4 km) of diapiric evaporites found by oil drillings beneath the Lisan Peninsula (Bentor, 1961). On top are the middle-late Pleistocene lacustrine-fluviatile Amora and Samra formations, up to 3 km thick. Exposed at the surface are lacustrine sediments of the late Pleistocene Lisan formation (10–40 m) and recent sediments with thickness of several tens of meters. Kilometer long flats of those lacustrine sediments are nowadays exposed by the Dead Sea regression on both sides of the lake.

The Ghor Al-Haditha sinkhole area lies partly on a piedmont of alluvial fan deposits of Pleistocene to recent age (Taqieddin et al., 2000). It is around 3 km wide and lies between three periodically active wadi systems, Wadi Ibn Hammad, Wadi Mutayl Ath Thib and Wadi Al-Madbaa in the South (Fig. 1C). In 1970, these wadis fed fertile alluvial fan-deltas that were largely used for agriculture; no sinkholes had formed at that time (Fig. 2).

The first sinkholes appeared at Ghor Al-Haditha, south of Wadi Ibn Hamad, in the 1980s, but were quickly filled in. At the beginning of the 1990s, more sinkholes opened north of the Wadi Ibn Hamad river. Following this development, local geological and geophysical studies were initiated to assess the sinkhole hazard (El-Isa et al., 1995). The ‘Numeira mixed salts and mud company’ started a factory in this area in 1997, but since sinkhole clusters were approaching the factory, more scientific research was undertaken (Taqieddin et al., 2000; Sawarieh et al., 2000; Diabat, 2005; Al-Zoubi et al., 2007; Frumkin et al., 2011; Alrshdan, 2012; Ezersky et al., 2013, partly unpublished reports).

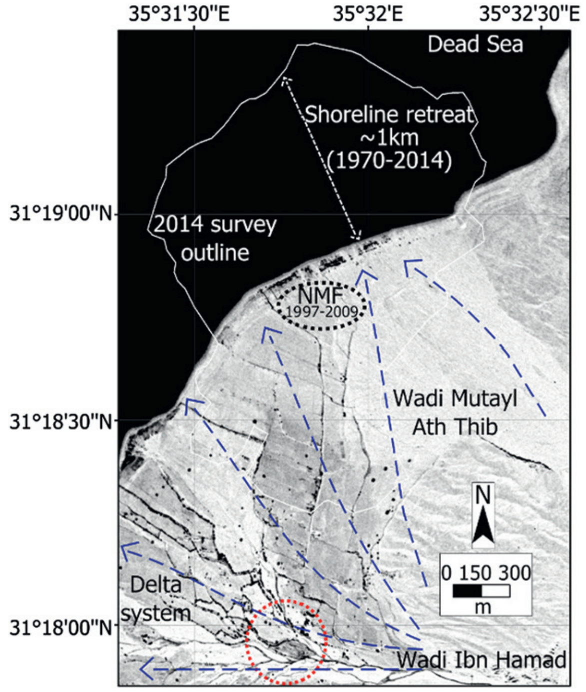

Fig. 2. Corona satellite image of Ghor Al-Haditha from 1970, with overlay of the survey outline. At that time the fan-deltas were strongly used by agriculture and no sinkholes were recorded yet. Since then, the Dead Sea has receded by around 1 km. The first sinkholes appeared in the 1980s near the Wadi Ibn Hamad (red circle), but then approached the Numeira Mud factory (NMF). Blue arrows show schematically the groundwater flow pattern in this area in the year 1999 based on water level measurements in wells and springs mentioned in the unpublished report of Sawarieh et al. (2000). The general trend was towards N–NW from the alluvial fans towards the Dead Sea (black coloured), with an estimated hydraulic gradient of $> 30\ \text{m km}^{-1}$.

Already in the late 1990s, the main recommendation for both the land farmers and factory was to leave the area, as it was, and is, considered a hazardous zone. In the early 2000s, the most hazardous zone shifted closer to the factory (Kottmeier et al., 2016). The agricultural area was partly abandoned and the factory had to be closed in 2009 (Fig. 3) (Closson et al., 2009, and personal communication by Eng. Emad Talafeha). Sinkholes still develop nowadays (cf. Fig. 3) in the alluvial fans as well as in the more and more exposed former lake bed.

Nontheless, sinkhole occurrence, morphology and development in Ghor Al-Haditha are incompletely understood and remain a topic of high relevance also for the local authorities. We therefore undertook a high resolution photogrammetric survey to provide a more detailed documentation of the sinkholes in the area surrounding the former factory site and to gain new insight into the factors controlling their formation (cf. Section 5).

3. Data acquisition and processing

3.1. Close-range photogrammetry

Aerial images of the area were acquired by a Ricoh GRII camera with 16.2 MP resolution, an angle of view of 28 mm and a focus

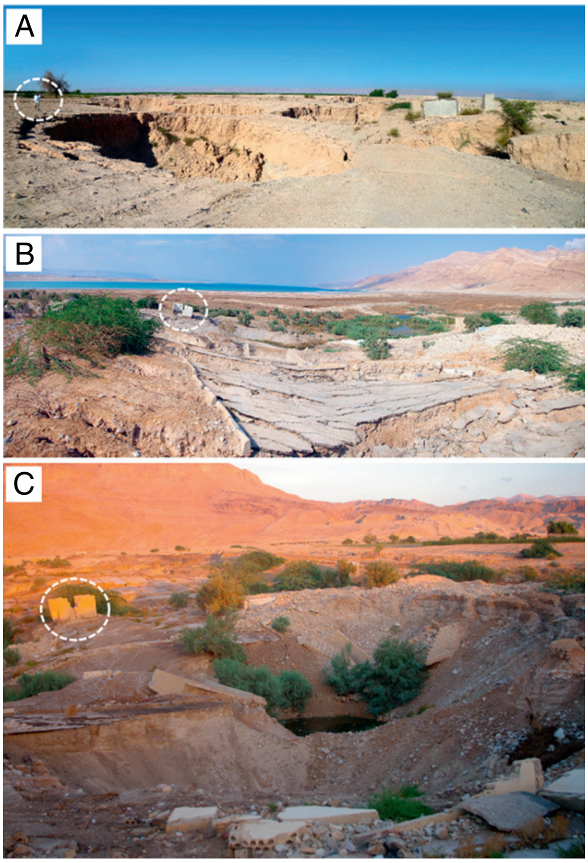

Fig. 3. Damage of infrastructure at Ghor Al-Haditha sinkhole site. **A**, **B**: Panorama views of deep cover-collapse sinkholes that destroyed agricultural buildings and roads. **C**: Sinkholes and subsidence destroyed the ‘Numeira mixed salts and mud company’ at the alluvium/mud-flat contact. Dashed circles mark scales (persons, buildings).

length of 13.7 mm. It was mounted on a kite-stabilised, helium-filled balloon (Helikite) of 4.5 m^3 size that flew at between 100 and 150 m altitude (Appendix Fig. A1A). For the requirements of the acquired near-field image pairs (see algorithm description below), the balloon offered the best possibilities (cf. Walter, 2014), as in windy areas like at the Dead Sea the kite stabilizes the azimuth and incidence angle. The photo footprint at 100 m flight height was about 125 × 180 m, leading to ≈ 3.6 cm px^{-1} ground resolution for an image at nadir. The calculated mean ground resolution for all processed images was 6.7 cm px^{-1}. For geo-referencing, over 60 ground control points (GCPs) were measured by a Differential Global Positioning System (DGPS) with up to 10 cm horizontal and vertical accuracy (Appendix Fig. A1B), using a real-time global satellite-based augmentation system (Trimble Omnistar XP.).

The aerial images of Oct. 2014 were used to build a 3D digital surface model and orthophoto. A Multiview Stereopsis technique (Furukawa and Ponce, 2010) of the structure-from-motion close-range photogrammetric method (Harwin and Lucieer, 2012; Luhmann et al., 2014) was applied, as implemented in the commercial software package PhotoScan Pro (Agisoft LLC). We followed mainly the processing scheme shown in Fig. 4 and described in detail in e.g. Agisoft (2013) and Leon et al. (2015).

Photogrammetry in general uses single or multi-image photographic recordings for the 3D reconstruction and interpretation of objects or areas of interest (Luhmann et al., 2014). The interior 2D image coordinate system (x', y') of each point (P), defined by the camera of the acquired photograph, is transformed by mathematical models into the exterior 3D object space (X, Y, Z) (Förstner and Wrobel, 2013), see bundle adjustment technique in Appendix A.1. For this purpose a record of a single image point needs to be available in at least two photographs, providing intersecting image rays. For a high accuracy in all coordinates, at least three to four photos are desirable (Luhmann et al., 2014). Therefore common aerial photo surveys with photogrammetric purpose tend to have 50–70 % overlap between each acquired image pair and recordings at different incidence angles.

Each point of the generated sparse point cloud is identified by its particular information about geometric position and radiometric data (Luhmann et al., 2014), like grey value, RGB, gradients and intensity. This requires ideally similar image acquisition conditions (light sources, shadow distribution and camera sensor), which in the field can be fulfilled by repeated measuring at the same time of the day or selection of appropriate time spans. In our case the light conditions are of special importance for the edge detection algorithm of structures in the field, therefore photos were taken mainly from late morning to early afternoon.

By using relative positions of the detected sets of overlapping image points, a multi-image triangulation and space resection (see Appendix A.1) is performed taking into account the camera calibration. In PhotoscanPro the camera position is determined after primary sparse point cloud image triangulation, by using information like camera type, focal length and resolution from the metadata of the images to determine distortions. When survey information on the object surface (geometries and reference points) exists, the normal equations are over determined and the bundle is transferred into a local or global (geo-referenced) coordinate system, building the Dense Point Cloud (Fig. 4). The final adjusted bundle contains 3D information of the measured object or area with a quality (coordinate residuals) mainly determined by the accuracy of the reference measurements, the correlation of physical parameters of the pixel comparison algorithm and systematic errors. An evaluation loop is applied and erroneous regions have been improved by carefully adding further images, manual point cloud editing, non-linear deformation removal (Agisoft, 2013) and model cropping and merging, so that the final optimized DSM is achieved.

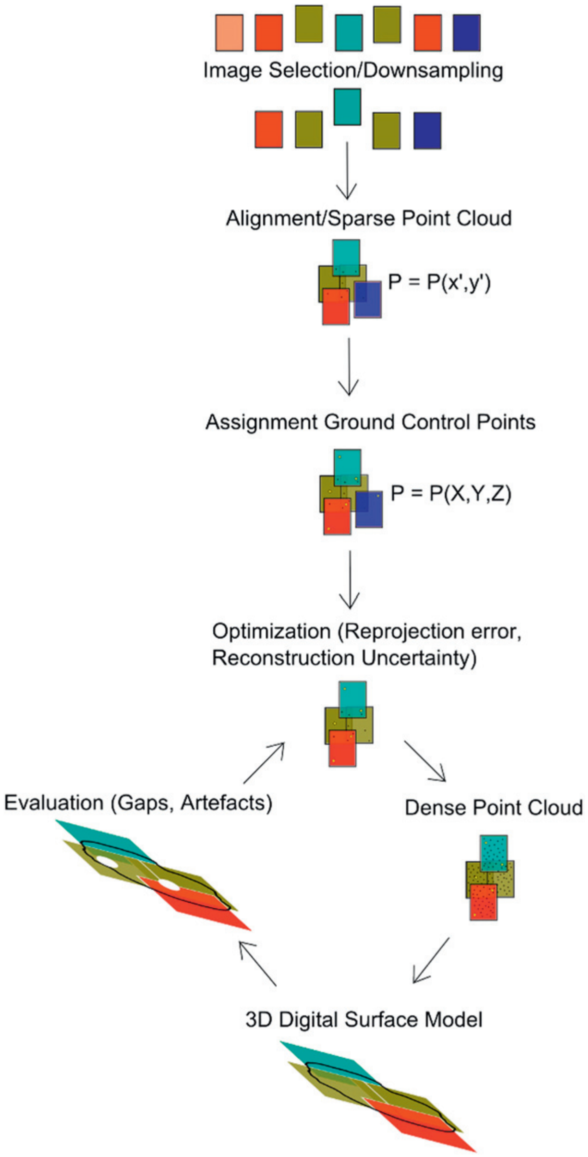

Fig. 4. Applied processing scheme of the structure-from-motion close-range photogrammetric method. See text for a detailed description.

To place the photogrammetric results into the geomorphological context, we also analysed a set of satellite images with 1.8 m px^{-1} resolution, acquired by the Corona (USGS, 2015) mission KH-4B 1111 from 1970-08-05. This represents the time when the shoreline was still stable, corresponding to the superficial limit between alluvium and mud-flat in our area (cf. Section 2). Additionally, we analysed satellite images from Quickbird-2 (0.6 m px^{-1}) and Worldview-2 (0.46 m px^{-1}) from 2012. For further analysis of the DSM, GIS has been used. It enabled a detailed mapping of structures and morphological features in the survey area. Details of the algorithms used can be found in Esri (2015) and De Smith et al. (2015). GIS and aerial photo analysis was complemented by field observations made in 2014 and 2015.

3.2. Accuracy and limitations

As a first step, a sensitivity study on the northern half of the surveyed area has been performed to investigate the role of reference marker selection. In general, at least three GCPs should exist in a survey area, while a higher accuracy and a more even distribution of GCPs increase the accuracy of the derived DSM (Harwin and Lucieer, 2012; Luhmann et al., 2014). Different GCP distributions have been tested and an elevation difference (reprojection error) of the individual Test-DSM with respect to the measured GCP values has been calculated (Figs. 5 and 6). The term elevation is used here and in the following with reference to the geoid equipotential surface of the Earth.

Gaps and artefacts generally occur due to downsampled image sets, significantly different light conditions in the overlapping regions, vegetation, or at the margins of the area. A crucial factor for the existence of gaps in the DSM is the number of image overlaps (Fig. 5A). Even large numbers of GCPs, which means a strong interpolation of elevation data, cannot counterbalance a low number of image tie points. A GCP selection orientated roughly perpendicular (NE–SW) to the overall topographic gradient shows the highest root mean square error ($\bar{R}$) values (Figs. 5B and 6B), while the same line simply orientated parallel (NW–SE) and hence spanning a large elevation gradient, performs much better (Figs. 5C and 6B). The lowest mismatch is achieved by using all GCPs in this area (33MHP), while the selection of 20, 12 or even only six well-distributed GCPs (20MDIS, 12MDIS and 6M-OR) still yields a very good result and shows similar mismatches (Figs. 5D-F and 6B). The most important criteria hence for DSM accuracy are the equal spatial distribution of the marker points and the accuracy of the GCP positions.

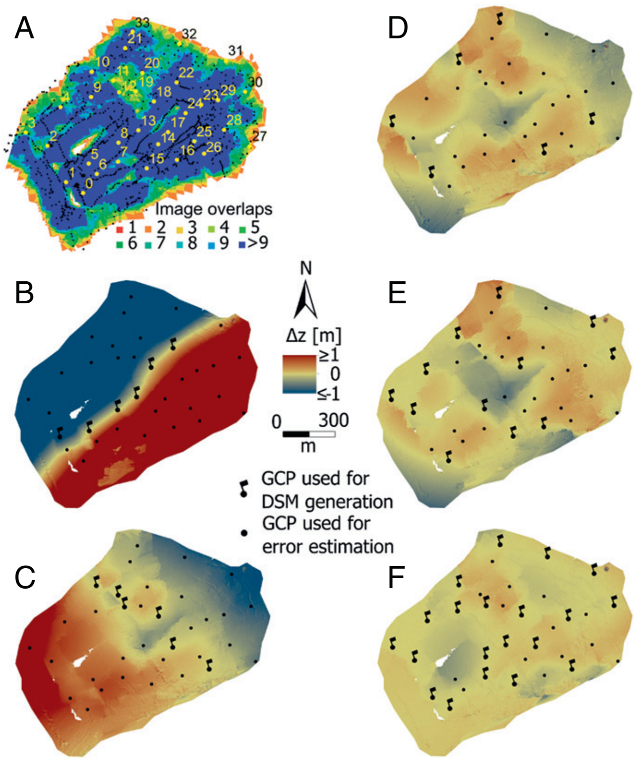

Fig. 5. DSM quality analysis for the northern half of the survey area. **A**: Agisoft image overlaps. Missing images lead to a lack of tie points, as seen nicely at the upper central part and the gap (white) areas. This hence will hinder the optimal referencing of the image pairs. Black circles refer to camera locations. Numbers indicate IDs of control points (yellow circles) used for error estimation. **B–F**: Elevation differences with reference to a DSM generated with all 33 ground control points, the lowest error DSM for this part (cf. Fig. 6B). Here, black circles indicate GCPs used for error estimation while circles with flags mark the control points used for georeferencing the individual DSM. **B**: Six NE–SW aligned GCPs. |Δz| is higher than 1 m as the GCPs tend to follow a topographic contour line. **C**: Six NW–SE aligned GCPs. |Δz| is lower than at **B**, because of the perpendicularity to topographic contour lines. **D**: Six GCPs approximately aligned as a rectangle. This distribution strongly improves the mismatch. **E**: Twelve well distributed GCPs. The overall mismatch is slightly lower while locally areas with high mismatch remain. **F**: Twenty well distributed GCPs.

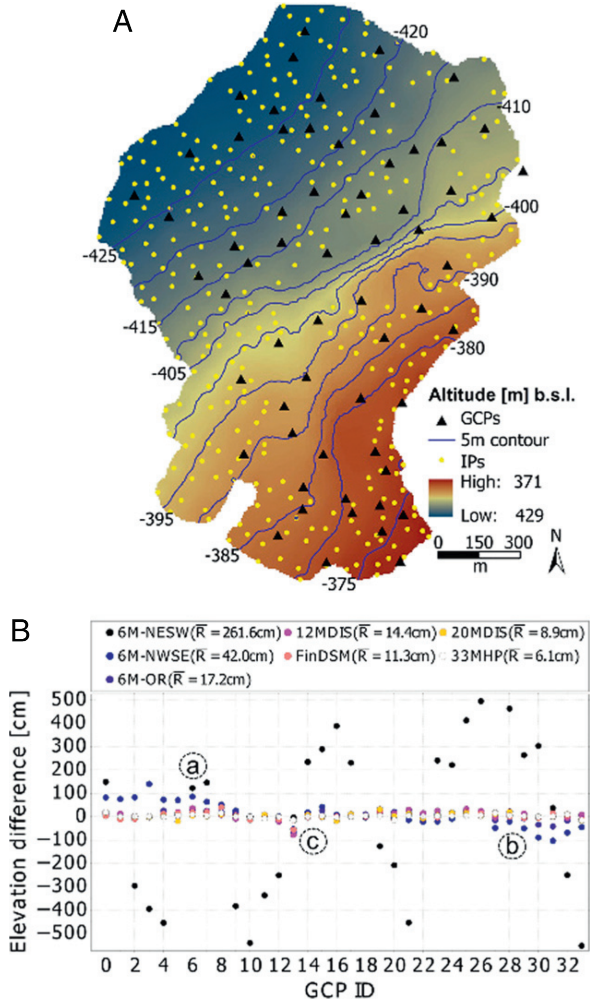

Fig. 6. Georeferencing and error analysis of the DSM. **A**: Position of all ground control points used for georeferencing the final DSM (black triangles). Note that the distribution is plotted before final optimization of the DSM, resulting in some GCPs outside the cutted margins. The background topography is an interpolated pre-subsidence DSM used for volume loss estimation of the Ghor Al-Haditha sinkhole area. The main depression and canyons have been omitted in the placement of the fixed boundary points (IP, yellowish circles). **B**: Reprojection error analysis for the northern half of the survey area. A comparison of the calculated DSMs of varying GCP selection with original in-field measured elevations is shown (cf. Fig. 5 and part A for GCP locations). Markers **a** and **b** emphasize the spatial distribution effect, where the DSM of six NE–SW aligned GCPs performs badly at the margins and well at the center (GCP ids 12-20). The behaviour of GCP id 13 at marker **c** highlights that even high numbers of image projections do not avoid errors in elevation estimation, if certain GCPs are not included.

4. Results

We present a high resolution orthophoto and digital surface model of the surveyed sinkhole area of Ghor Al-Haditha. This is followed by a detailed qualitative and quantitative analysis of structural and morphological aspects of the subsidence phenomena. Combining the photogrammetry with satellite image analysis we then describe evidence for surface and subsurface water flow and its relationship to the morphological and structural phenomena at Ghor Al-Haditha.

4.1. Orthophoto and digital surface model

From close-range photogrammetry, we generated a high resolution orthophoto (Fig. 7) and digital surface model (DSM, Fig. 8). Marked in both images for reference are the most important morphological features and the locations of aerial and ground-based photos. The total size of the surveyed area is ca. 2.1 km^2.

After the GCP selection procedure, a preliminary DSM, based on more than 3100 photos, was generated stepwise in three overlapping model areas due to computation limitations. Following corrections with the evaluation loop technique described above (Section 3), the final DSM is based on approximately 8400 photos. A modelling mesh of $6.56 \cdot 10^6$ vertices was used to produce a high resolution (6.7 cm px^{-1}) orthophoto (Fig. 7) and final 3D DSM (Fig. 8) of the area of interest. The reprojection error of the final DSM is higher than the optimal value calculated for the northern part (Fig. 6B). This is due to lower DGPS accuracy, more image-pairs and markers missing at the margins (cf. final GCP distribution in Fig. 6A). Nonetheless the final accuracy of the DSM is around 10/11/15.2 cm (x,y,z). The effective DSM resolution is 29.6 cm px^{-1} with a point density of 11.31 pt m^{-2}, while interpolation for smoother subsequent analysis leads to a feasible higher resolution of 5 cm px^{-1}.

In the orthophoto and DSM (Figs. 7 and 8) we distinguish the two principally affected surface materials: (1) the Dead Sea mud and salt sequences of the former Dead Sea lake bed (cf. Appendix Fig. A2C) and (2) the alluvial fan sediments of the Lisan formation (cf. Section 2). The mud appears dark reddish-brownish in the northern part of the area with individual whitish areas of exposed evaporites. A sharp boundary delimits the mud from the bright greyish alluvial sediments in the southern part.

The distinction between both main geological units is also very clearly visible in the DSM. The topographically high area (reddish) corresponds to the alluvial fans, while the low lying area (blueish) corresponds to the mud-flat. The observable and marked transition zone shows a relatively sharp drop in elevation between approximately −393 and −407 m. This corresponds to the old, long-term stable and vegetated shoreline of the Dead Sea.

4.2. A several hundred metre scale sinkhole-hosting depression

The DSM reveals a distinctive bright area marking a subtle, large-scale, sinuousoidal depression. The limits of this depression have been determined visually rather than by GIS tools following suggestions from Doctor and Young (2013). Meter-scale concentric faults

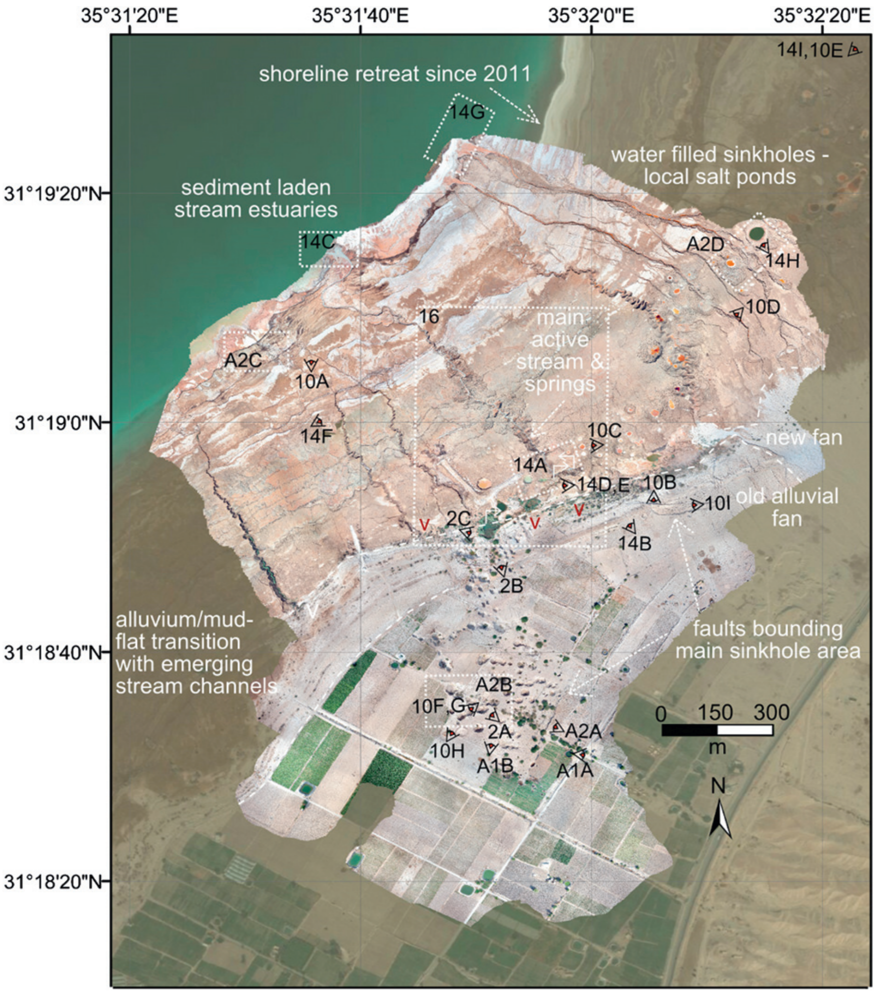

Fig. 7. High resolution (6.7 cm px^{-1}) orthophoto of Ghor Al-Haditha sinkhole area. The orthophoto lies upon a satellite image background from February 2011 provided by ArcGIS basemap source Digital Globe with 15 m px^{-1} resolution. Indicated are the most important large-scale morphological features as well as locations of field observation and aerial photos. This dynamically changing area contains very recently formed channels (center, N) and alluvial fans (center, E). Concentric normal faults partly bound the main sinkhole area. Streams and springs carry sediments into the lake. Sinkhole-related pools and salt ponds are observable in the mud-flat. Vegetation (v) and stream channels appear at the alluvium/mud-flat boundary.

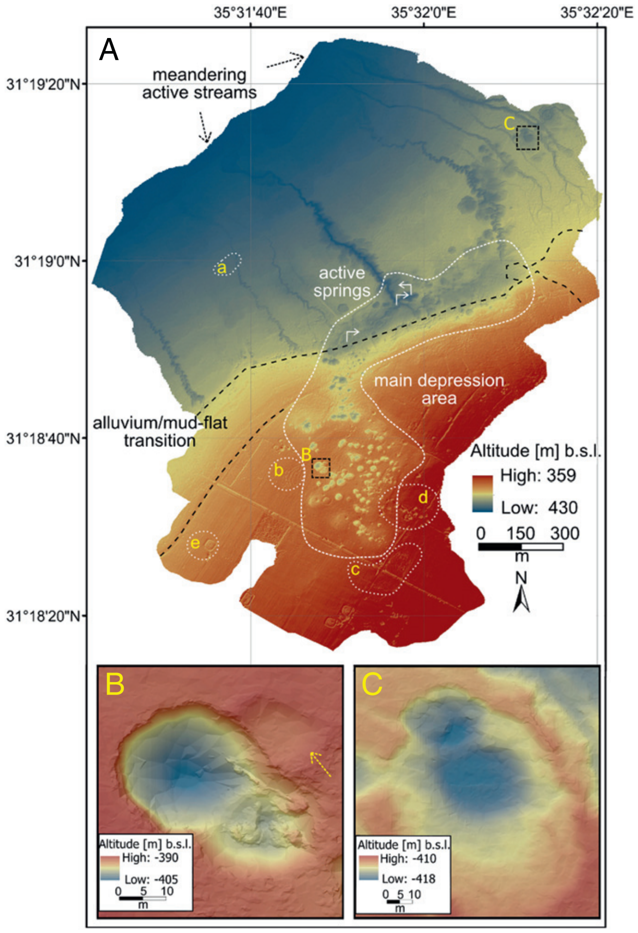

Fig. 8. High resolution (5 cm px^{-1}) digital surface model of Ghor Al-Haditha sinkhole area. **A**: Shaded relief image of topography within the surveyed part of the Ghor Al-Haditha sinkhole area resulting from the DSM. The main depression area, the alluvium/mud-flat boundary and the active groundwater springs are indicated. A further continuation of the main depression area to the NE can be inferred from the DSM. **B**: Closeup of a representative sinkhole in the alluvium. **C**: Closeup of a representative sinkhole in the mud. Dotted lines mark either data gaps (**a**), uncertain areas with higher error (**b**) and identified artefact zones (**c**), resulting from different light conditions or missing images. Trees may rarely be confounded with or hide sinkholes (**d** and closeup **B**) and artificial water ponds are recognizable due to their elevated rims (**e**, see also truncated irrigation pond marked with an arrow in **B**).

and ground cracks bound the area and are visible in the orthophoto; a ground based view is given in Appendix A.2 (Fig. A2A). The gentle main depression area covers roughly 0.34 km^2 and contains approximately 85 % of the identified sinkholes. The deepest point in the main depression lies at −424 m elevation, exactly at the spring point of an active stream that is described more in detail in Section 4.5.

4.3. *Sinkhole distribution and clustering*

The total number of sinkholes identified in the surveyed area is 298; in alluvium 193 and in mud 105. Closeup DSMs of representative sinkholes in these materials are shown in Fig. 8A,B. Twenty-four of those counted as in mud are at the vegetated transition between both surface material types. Eleven sinkholes are filled with water, most of them in the mud. The total area affected by sinkholes, including the northward possible continuation of the depression and marginal sinkholes, is approximately 0.45 km^2, leading to a density estimation of 6.6 sinkholes ha^{-1}.

The observed clustering is quantified via a GIS nearest neighbor comparison (Esri, 2015). A random distribution yields a nearest neighbor ratio (*NNR*) of 1. $NNR < 1$ means a clustered distribution, while $NNR >> 1$ means a dispersed distribution. With $NNR < 1$ the distribution for both mud- and alluvium-hosted sinkholes is significantly clustered with a mean intra-cluster distance of 18.7 m between two sinkholes (Table 1). According to the relative density map (Fig. 9), the majority of those clusters is inside the main depression.

Table 1
Nearest neighbor comparison of sinkholes for Ghor Al-Haditha sinkhole area. *NNR* is the nearest neighbor ratio, *P* the significance level and $\bar{d}$ the mean distance between sinkholes. As all $NNR < 1$, the distribution is significantly clustered.

	Alluvium	Mud	Total
NNR	0.64	0.83	0.69
P-value	< 0.01	< 0.01	< 0.01
$\bar{d}$[m]	16.18	24.03	18.66

4.4. *Material control on subsidence morphology and structure*

4.4.1. *Qualitative observations*

As identified in the DSM and orthophoto, the area contains two main geological units (Fig. 10A,B), covered by a few meters of topsoil: old to recent poorly consolidated, coarse to fine grained alluvial fan deposits (alluvium) and interbedded, lacustrine, fine grained clay and evaporites (mud-flat). The Dead Sea mud (Fig. 10A) comprises dark organic material (brownish-reddish to olive-greyish), greyish calcite and whitish aragonite laminae (cf. e.g. Khoury, 2002). It is also referred to as 'lime carbonates' (Frydman et al., 2008) because of the high content of carbonate minerals (Khlaifat et al., 2010). It even

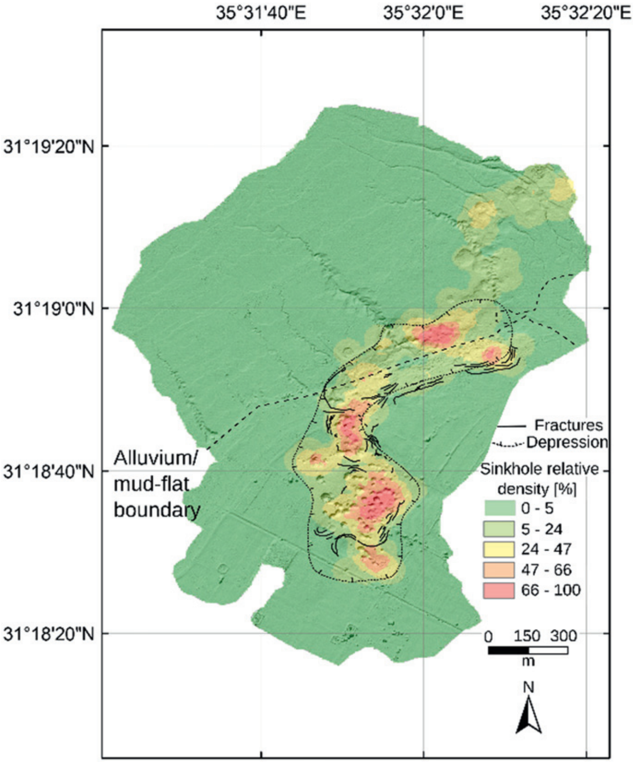

Fig. 9. Relative density distribution of sinkholes. Each sinkhole is represented by a uni-sized point at its center. The density is calculated via the kernel density calculation by GIS, using standard search radius and a smooth quadratic and tapered surface for each point (Esri, 2015). The resulting maximum number of 2496 pixels per unit area has been used for normalization of the colorscale. Clearly, a local clustering with changing bulk cluster orientation is observed (red areas). In alluvium the high density clusters tend to strike NNW–N, and in mud from NE–E. The main fractures bounding the depression area are indicated.

Fig. 10. Geology, structures and sinkhole morphologies at Ghor Al-Haditha. **A**: Mud-flat deposits, comprising laminated silt and clay, locally interbedded with evaporite layers up to 1.5 m thick (**a**) and ideomorphic halite crystals (**b**). **B**: Alluvial fan deposits, comprising poorly consolidated gravels (**a**), coarse to fine grained sand (**b**), with clayey topsoil (**c**). **C**: Typical shallow and wide sinkhole (depth to diameter ratio $D \approx 1.5\ \mathrm{m}/17\ \mathrm{m} = 0.09$) with gentle slopes in the mud-flat deposits about 100 m north of the alluvium/mud-flat contact (**a**). Note tripod for scale. **D**: Listric normal fault bounding outward-rotated blocks of a landslide or slump into a dry stream channel in the rheologically weak mud-flat deposits. **E**: Small overhanging sinkhole in a mud-salt sequence locally dominated by thin but strong evaporite layers. Highlighted by contrast stretching is the wet mud filling. A tunnel has been carved into the strong salt layer whose overhanging side points towards the Dead Sea. **F**: Typical deep sinkhole with high $D = 12\ \mathrm{m}/23\ \mathrm{m} = 0.52$ in the rheologically strong alluvium. **G**: Inward-tilted and overhanging faulted blocks at the margin of a sinkhole in the alluvium. Note person (circled) for scale. **H**: Overhanging side walls of sinkhole in the alluvium, here highlighted by contrast stretching. **I**: Up to 2 m high normal fault scarp (**a**) and ca. 4 m deep cracks (**b**) in the alluvium about 20 m from the alluvium/mud-flat transition (**c**).

contains idiomorphic halite (NaCl) crystals, in places up to 50 % by volume. Locally, individual evaporite layers (Fig. 10A and Appendix Fig. A2C) 1 cm to 1.5 m thick were observed in sections along the stream channels. The alluvial sediments comprise a mixture of clasts of sandstone, limestone, marl, chert and basalt, with grain sizes varying from fine grained sand to pebbles and even boulders (Fig. 10B). The material compound is partly to poorly cemented.

Important morphological differences have been observed between the subsidence phenomena of the mud-flat and alluvial fans, as highlighted in a slope distribution map (Fig. 11) and in Closeup DSMs for representative sinkholes in Fig. 8A,B. In the mud, sinkholes are generally wide but shallow (Figs. 8B and 10C), sometimes coalesced into uvala like structures. Slopes of the margins are more gentle (0° to 90°), similar to the slopes at canyon slumps. Nevertheless, some sinkholes in mud with relatively strong evaporitic cover show overhanging margins (Fig. 10E). Many sinkholes in mud display a wide peripheral zone of extensional fracturing and outward-rotated strata (Fig. 11F). This is structurally and morphologically similar to landslides or slumps found adjacent to the deeper stream channels (Fig. 11G); these slumps are bound by listric normal faults (Fig. 10D). Despite overprinting effects, a distinction between sinkholes and slumps is possible. Slumps are open on the streamward side and generally spatially connected to the outer-arc of the stream meanders (cf. DSM in Fig. 8). Finally, slump boundaries do not cross the associated stream channel, as would be so in the case of a sinkhole intersected by a stream.

In the alluvium, sinkholes generally show steeper internal slopes (between 45° and 90°) and in several places linear alignments or coalescence (Fig. 11C,D). Some of these deep and narrow sinkholes (Figs. 8A and 10F) display inward-tilted (toppled) sidewall blocks (Fig. 10G), or even partially overhanging side walls (Fig. 10H). More rarely, subsidence in the alluvium expresses locally as 'sag' structures with a wide 'halo' of concentric cracks (Fig. 11B). These non-collapsed depression areas may show compression ridges in the center. Within the alluvium numerous cracks, fault scarps of up to 2 m height and crevasses with depths of up to 4 m (Figs. 10I and 11A) adjoin the deeper points of the depression zone (Fig. 9).

4.4.2. Quantitative observations

Quantitative analysis of sinkhole geometries requires an error estimation for sinkhole depth and diameter. It is based on a manual determination of the standard deviation of long, short axis and depth. A randomly chosen sample set of 40 sinkholes has been used for this purpose. Considering the horizontal error of the DSM, the mean relative error for sinkhole diameter estimation is 17.6 % and for the depth 27.9 %. Those sinkholes filled with water and most of those in the transition zone between the cover materials are excluded from further detailed quantitative analysis.

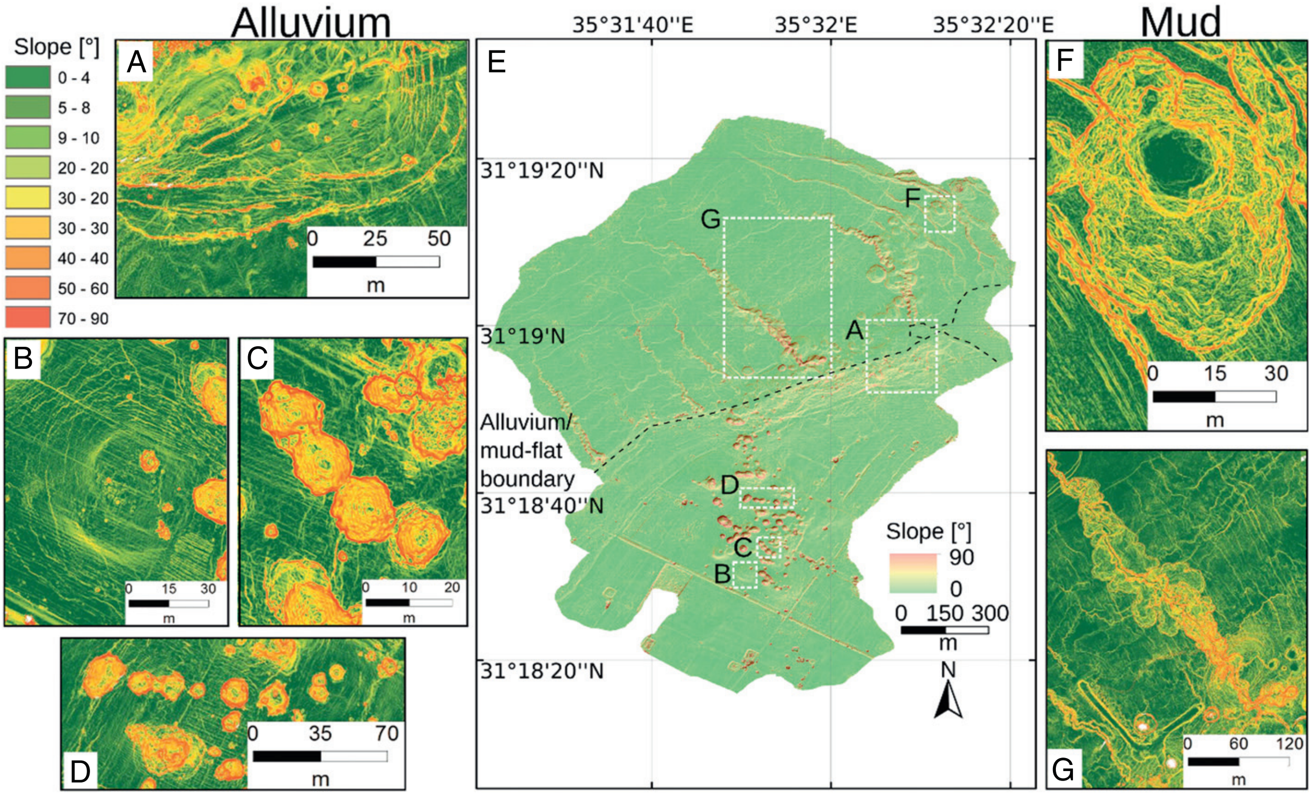

Fig. 11. Slope maps with hillshade background to visualize the morphological expressions of subsidence and depression structures at Ghor Al-Haditha. Slopes in alluvium sinkholes are generally much higher ($> 45^\circ$) than in mud. The specific morphological expressions for alluvium (**A–D**) and mud (**F–G**) are described in the text. Note the different colorscale to highlight the detailed structures.

The mode of sinkhole diameter distribution (Fig. 12A) in alluvium is between 4–12 m. In mud the value is slightly shifted to 8–16 m, with a longer tail due to larger diameters of up to 75 m in the surveyed area. Sinkholes in the alluvium deposits display a higher depth to diameter ratio, ($\bar{D}_a = 0.4 \pm 0.11$) than those in the mud layers ($\bar{D}_m = 0.14 \pm 0.04$; Fig. 12B). The surveyed sinkholes show a mean eccentricity value of $\bar{E} =$ long axis/short axis $= 1.3062 \pm 0.23$, with similar values for for mud $\bar{E}_m = 1.37 \pm 0.24$ and alluvium $\bar{E}_a = 1.28 \pm 0.225$ (Fig. 12C). E values larger than 2 are rarely observed, however.

Sinkholes with $E > 1.05$ on the alluvium display a main orientation of NNW–N, while those in the mud strike NNE–NE (Fig. 13). Nested or elongated sinkholes appear in both types of cover material (see DSM in Fig. 8 and Appendix Figs. A2B and D). Coalesced or nested sinkholes are considered as one entity if their margins partially overlap. The general trend of all sinkhole long axes is N to NNE. This is because those in the alluvium outnumber those in the mud.

4.5. Surface and subsurface groundwater flow

Typical erosional morphological features observed in the former lake bed are wave-cut steps, rills and both surface and sub-surface stream channels. Wave-cut steps up to 0.75 m high mark former shoreline limits. Erosional rills are generally orientated perpendicular to the mud-flat slope. Most stream channels dissecting the mud-flat (Fig. 7) were dry at the time of our survey. However, several active streams were also observed:

1. A main stream channel (canyon) emerges in the center of the ENE-WSW elongated section of the main depression (Fig. 8). The stream rises from several springs here within the mud-flat sediments at or near the contact with the alluvium. The main spring lies in the channel head at around 6.5 –7 m below the former lake bed (Fig. 14A,B). In addition, a spring rises under the now destroyed factory site and feeds a tributary stream that passes through several vegetated pools before joining the main stream. The main stream meanders, with slump related structures on the outer-arc bends and discharges into the Dead Sea. Both the stream channel depth and the marginal slumping gradually diminish lakeward. Aerial images and field observations show that is is carrying a substantial load of sediments already at the spring points (Fig. 14C,E). An artesian, periodically and rapidly location changing, sediment-laden new spring (Fig. 14D,E) formed in 2015, a few tens of meters SE of the main springs of 2014, as observed during a second field survey in October 2015. It disgorges pebbles of the alluvial sequence in the pressurized outflow (Fig. 14E), thus indicating subsurface flow through the alluvium or along the alluvium/mud boundary.
2. A small active stream channel in the North that carries reddish sediments into the lake (close to the location of Fig. 14G). The spring point must lie within the mud-flat as the heads of all channels from the more recent Wadi Mutayl fan were dry.
3. At least one small subsurface stream (Fig. 14F) has been observed at the base of a hole of around 1.5 m depth in the central area of the mud-flat. No directly obvious outflow of this channel into the Dead Sea could be seen at surface, nor could a surface inflow source be found.

The mud-flat also exhibits several slump-related seeps, as well as water-filled sinkholes that lack salt rims (Fig. 14A) and have no obvious channel connection (Fig. 14H,I). Whether active or dry, several

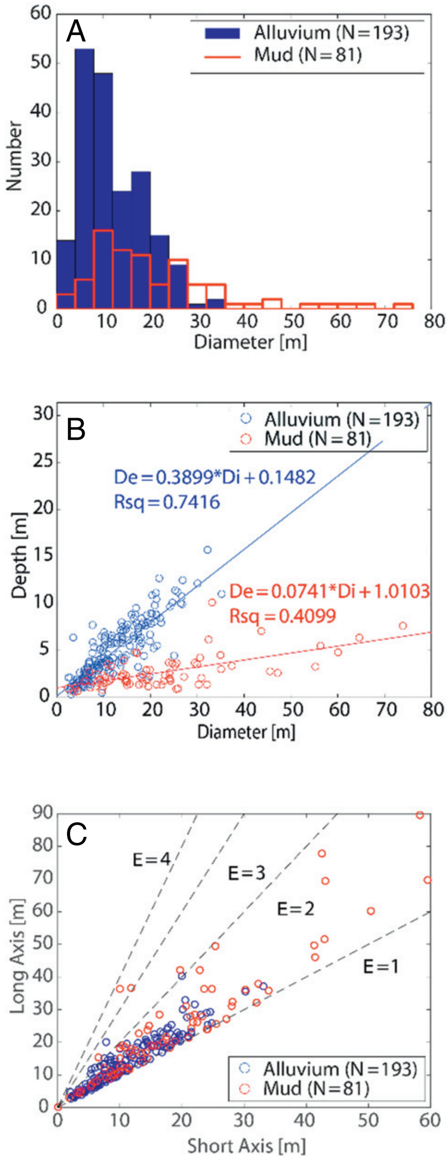

Fig. 12. Quantitative analysis of sinkhole geometries at Ghor Al-Haditha. **A**: Histogram (i.e. frequency- magnitude distribution) of sinkhole diameters in alluvium (blue) and mud (red). **B**: Sinkhole mean diameter to maximum depth. Sinkholes in alluvium material show higher depth/diameter (D) ratios between 0.05 and 1.8 with a mean of 0.4. Sinkholes in mud have values of D between 0.036 and 0.41 with a mean of 0.14. **C**: Plan-view long axis versus short axis plot of all sinkholes in the area. The mean eccentricity is $\bar{E} = 1.306$.

stream channels that cut the mud-flat do not continue onto the alluvium. Rather, the heads of these channels occur at or close to the alluvium/mud-flat boundary (Fig. 7). With the exeption of the Wadi Mutayl at the north-eastern-most edge, there are currently no natural stream channels on the alluvium in the surveyed area. A storm drain runs NW–SE at the SW edge of the surveyed area, but does not continue into any of the stream channels incised into the mud-flat.

Trees and bushes are preferentially found at the old shoreline, particularly where this coincides with the margin of the main depression. They are also found in dried streams on the mud or even inside many sinkholes on the alluvium (Fig. 7). Aerial photos of the current shoreline reveal dark, circular to sub-circular shaped features in clusters immediately off-shore (Fig. 14G), which elsewhere have been associated with submarine sinkholes and springs in coastal karst systems (Fleury et al., 2007; Boever et al., 2013).

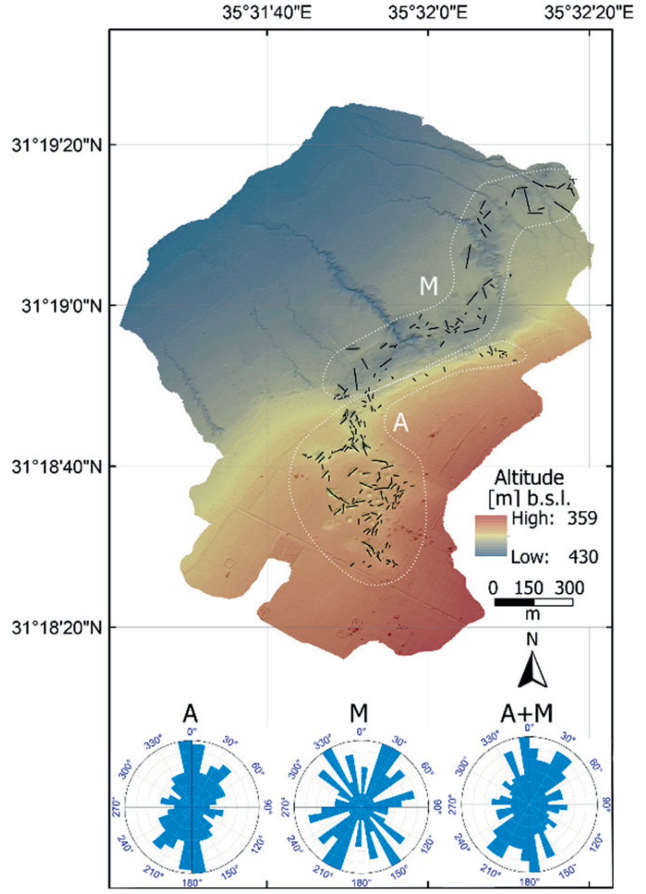

Fig. 13. Map showing the azimuths of the long axis of sinkholes with $E > 1.05$. The rose diagrams at the bottom are produced by a 9° binning for **A**, the alluvial sinkholes, **M** the mud sinkholes and **A+M** all sinkholes. The trends are discussed in the text.

4.6. Temporal evolution of surface and groundwater flow from satellite image analysis

Here we take a closer look at the 1970 satellite image presented in Section 2. To highlight vegetation and water channels, we used a coloured version of the image (Fig. 15). Although flow from the Wadi Ibn Hamad is constrained today by engineering works (Fig. 1c), in 1970 flow was dispersed within alluvial fan-deltas that extended both south of and inside todays' sinkhole affected area. In particular, one observes two individual water channels leading from the wadi to the present-day main depression zone. Interestingly, the currently most affected area around the destroyed 'Numeira mixed salts and mud company' factory was located at the outflow points of those two channels at that time.

Publically available satellite images (Google Earth) of the 2000s show the development of a lake of unsaturated water within the current main depression. This lake was separated from the Dead Sea base level by a NE-SW elongated natural dam made of salty mud (Closson and Abou Karaki, 2008), i.e. the NW margin of the main depression. The water accumulated exactly at the boundary between the alluvium and clay sequences.

The evolution of a wide canyon, related to the drainage of the lake, is seen in satellite images (Fig. 16). In an image from March 2012 a NW–SE stream channel terminating landward in a fork has developed from the Dead Sea shore to the middle of the mud-flat. This channel is not visible in an image from December 2011. There is also an outflow point from the lake in the centre of Closeup image (a in Fig. 16), but this cannot be traced with certainty to the fork in

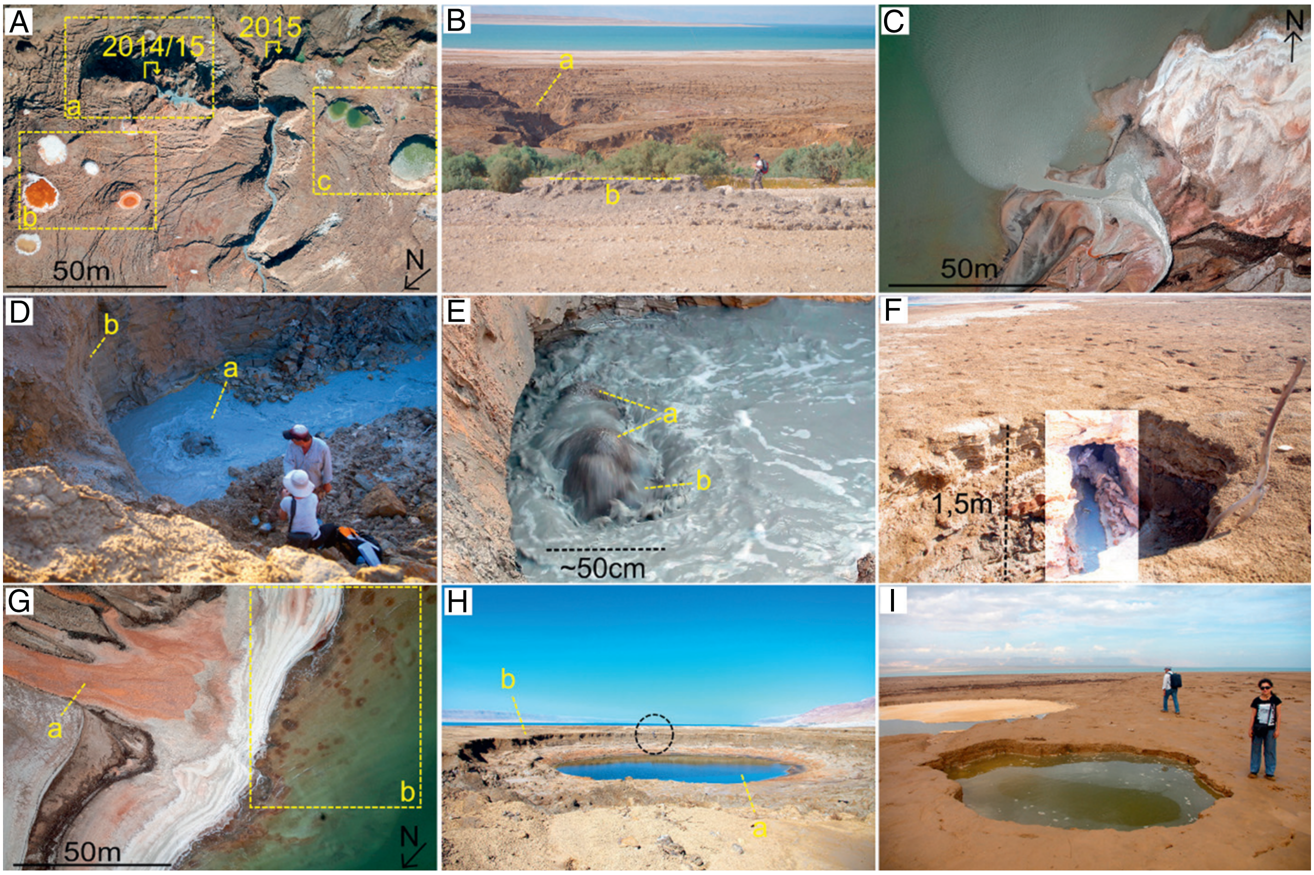

Fig. 14. Evidence of subsurface groundwater flow and subrosion in the mud-flat at Ghor Al-Haditha. **A**: A sediment-laden stream emerging from within the mud-flat sediments (**a**). Clearly distinguishable are sinkholes in the mud-flat filled by saturated salt-water (**b**, note white rims of salt) and fresh/brackish water (**c**). The main springs observed in 2014/15 and the newly formed artesian spring (part D and E) are marked. **B**: Vegetated contact between alluvial fan and mud-flat. The active stream channel in part A has dug a 6–7 m deep canyon into the mud-flat (**a**). Its spring point lies a few tens of meters north of the alluvium/mud-flat contact (**b**). **C**: Sediment plume at the outlet of the active main stream shown in A. **D**: New artesian, periodically location changing and sediment bearing spring (**a**) discovered in Oct. 2015 at the main canyon area. This outflow was observed to cause active upstream channel incision through collapse of overlying material (**b**). **E**: Spring of subfigure D carrying clearly visible sediments (**a**) and pebble-sized clasts (**b**) in the upwelling water. **F**: Channelized flow within the mud-flat sediments. Highlighted by contrast stretching, the water bearing channel has no onshore outflow, hence indicating a submarine point of emanation. **G**: Current Dead Sea shoreline at superficially dry canyon fan-deltas (**a**). Dark round shapes in the water are possibly related to submarine sinkholes and/or springs (**b**). **H**: Fresh-water filled mud-flat sinkhole (**a**) with no obvious surface channel connection, hence indicating subsurface recharge. Freshly collapsed rims show a continuing lateral sinkhole evolution (**b**). Note person circled for scale. **I**: New sinkhole on the mud-flat, formed after a storm event in Oct. 2015 and filled with relatively fresh water.

the image. It is thus possible that the connection was underground at this time. By retrogressive erosion, the NW–SE stream channel extended towards the lake, crossing the natural dam perpendicularly (b). The surface connection of the channel with the lake was established between May and June 2012 (b and c). Progressive with the development of the channel the reservoir drained, as seen in the receding lake shore line from March to June 2012. By August, the lake was almost completely drained (d). The NW–SE stream enlarged progressively owing to the springs located in the depression. The nearly dried out area comprised several nested depression structures with channels between them in August 2012. By the time of our survey in October 2014, only a few water-filled ponds remained around the factory site.

4.7. Estimation of volume loss due to sub-surface material removal

Under the assumption of stability around the areas obviously affected by subsidence, we are able to calculate an interpolated pre-subsidence DSM (Fig. 6A). From this, a minimum volume loss of the depression and sinkholes can be estimated by GIS volume subtraction algorithms for equally gridded datasets. Only minimum values can be determined by this approach because the margins around the areas of interest might have also subsided and sinkhole refillings are not considered. A compilation of the results for the depression zone in mud and alluvium separately and for the whole surveyed area is presented in Table 2.

The total minimum volume loss of this area including stream channels is estimated as roughly $\Delta V_{min,tot} = 2.5 \cdot 10^6$ m^3. Assuming, the strong Dead Sea recession started in 1955 (cf. Section 2 and Taqieddin et al., 2000) this would mean a minimum erosion rate of $r_{tot} = 41,670$ m^3 yr^{-1}. As sinkholes in the study area only appeared from the year 1990 on, 25 years of subsurface material removal ($\Delta V_{min,dep} = 1.83 \cdot 10^6$ m^3) leads to an estimation of the minimum erosion rate in the main depression area to $r_{dep} = 73,200$ m^3 yr^{-1}.

The minimum subsidence S_{min} is calculated by $S_{min} = \Delta V_{min}/A$ averaged over each area of interest. For the southern part of the depression area in the alluvium the calculation yields $S_{min} = 4.2$ m. For the northern part of the depression area in the mud-flat, including the boundary region to the alluvium with strong topographic gradient (Fig. 8), we have $S_{min} = 6.95$ m. Weighted by the area for alluvium and mud, the total value for the depression area is $S_{min,dep} = 5.36$ m. This yields an average minimum subsidence rate of $\dot{S} = \approx 0.21$ m yr^{-1} for the main depression in 25 years.

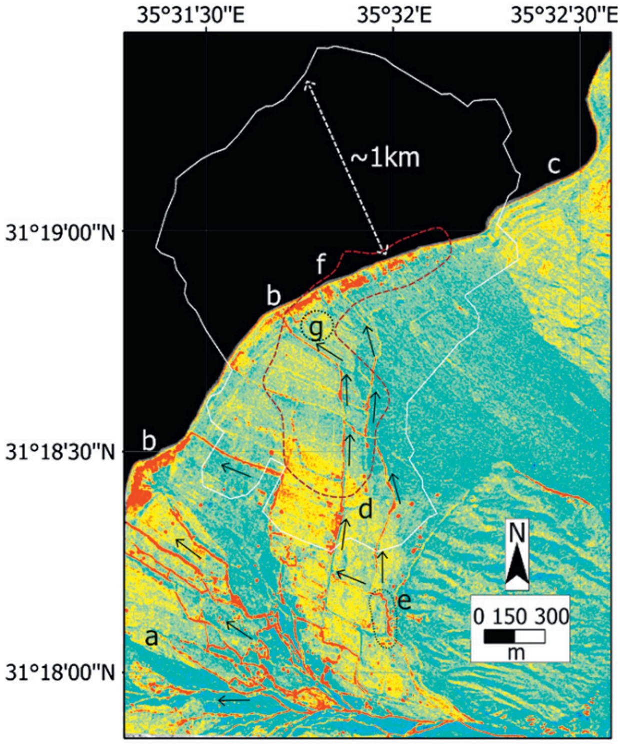

Fig. 15. Coloured Corona image (1970) with close-range photogrammetry outline (2014) highlighting water flow in the Wadi Ibn Hamad delta system (**a**). Vegetation (**b**) at the former Dead Sea shoreline (**c**) appears in red. Two identified main surface water channels (**d**) bifurcate at (**e**) from the Wadi Ibn Hamad. They flow into what is now the main depression zone (**f**) and pass the future Numeira mud factory location (**g**). Interpreted surface water flow is indicated by arrows.

5. Discussion

This qualitative and quantitative geomorphological analysis of the sinkhole affected area of Ghor Al-Haditha reveals several main new results. A NNW–NE orientated, 0.34 km^2 gentle depression straddling mud-flat and alluvial-fan sediments contains the majority of nearly 300 sinkholes in the surveyed area.

Sinkhole morphologies depend on the cover material in which they formed: In mud, the holes are elliptically shaped ($\bar{E}_m = 1.37 \pm 0.24$) with a long-axis strike of NNE-NE and a depth to diameter ratio of $\bar{D}_m = 0.14 \pm 0.04$. In alluvium, holes show a similar eccentricity ($\bar{E}_a = 1.28 \pm 0.255$), but with a long-axis strike of NNW–N and $\bar{D}_a = 0.4 \pm 0.11$. Sinkholes have a clustered distribution ($\overline{NNR} = 0.69$, $\bar{d} = 18.66$ m), with a bulk cluster orientation of NNW–N in alluvium and NE–E in mud and a density of 6.6 sinkholes ha^{-1} in the most affected zone in and around the main depression.

Dynamic, sediment-laden springs appear at the alluvial-fan/mud-flat contact. Channelized subsurface groundwater flow is seen within the salty mud evaporite sequence of the mud-flat. These flows discharge into the Dead Sea either through canyon-like channels or tunnels. Analysis of satellite images reveals the former existence of wadi riverbeds spatially coincident with the main depression on the alluvial fan. The satellite images also reveal that the section of the main depression along the mud-flat/alluvium boundary hosted a lake that drained in conjunction with the development of an upstream incision of a channel. This new canyon-like channel hosts the major active stream in the surveyed area and is fed from springs rising within the main depression.

The calculated minimum volume loss since 1955 in the main depression is $\Delta V_{dep} = 1.83 \cdot 10^6$ m^3, around 73 % of the volume loss of the whole survey area. The surface of the now main depression area lies on average at least 4.2 m in the alluvium and 6.95 m in the mud lower than 25 years ago. This leads to a minimum average subsidence rate of $\bar{S}_{min} \approx 0.21$ m yr^{-1}.

After a quality assessment of the DSM, we focus in this section on different aspects of the control of subsidence and sinkhole formation. We provide an overall interpretative scheme and highlight relevant implications for areas and studies of similar natural hazard phenomena.

5.1. Quality and relevance of the DSM and uncertainties in volume loss calculation

This study shows the feasibility of the cost-efficient Helikite aerial survey approach to address complex geomorphological phenomena like subsidence and sinkhole formation at the Dead Sea. It has been shown that the distribution, accuracy and orientation of GCPs rather than the quantity is essential for correct georeferencing. This is important for e.g. planning further photogrammetric surveys in terrains that are hard to access. As some of the GCPs were lost during the survey, their distribution across the area is not homogeneous, introducing a larger reprojection error especially at the margins of the area (cf. Figs. 5 and 6).

Two small artefacts (Fig. 8) are identified in the DSM by careful comparison with the orthophoto (Fig. 7). One artefact is a consecutive topography change that arises from vegetation cover. It is only visible at strong relief shading and is within the margin of error of the vertical accuracy of the DSM. Another artefact appears as an arc-like step and is due to different light conditions of surveys undertaken at different times of day. Data gaps due to missing images occur only at a small (60 × 30 m) spot in the mud-flat.

Sinkhole mapping has been done carefully with back and forth comparison of DSM and orthophoto to exclude features of human origin, such a irrigation ponds. The maximum depth of small sinkholes with overhanging sides is underestimated because of shadowing effects. This introduces a small error for the D ratio estimation for those holes, but since the number affected is small (4 out of 298), the error has negligible impact on our main conclusions.

The volume loss of the main depression has been calculated under the premise of non-subsided surroundings (Fig. 6A). We have currently no means of testing the validity of this premise, but there are no grounds to regard it as unreasonable. Nevertheless, such a surface-derived volume loss, for both individual holes and the main depression is likely to be less than the true sub-surface volume loss, because of material dilation during subsidence ('bulking', cf. Reddish and Whittaker, 2012) and possible sinkhole refilling by farmers. We provide a minimum value for the total volume loss and dependent erosion rate and subsidence estimation. This includes stream channels, springs, roads, vegetation and artificial water ponds, although the contribution from these factors is small. The contribution of the main stream channel incision to volume change in the mud-flat area of the main depression is likewise negligible (≈ 7 %).

Sinkhole hazard susceptibility models (cf. Galve et al., 2011) generally apply the here presented well-established GIS analysis. Our photogrammetric survey however provides a high resolution DSM for further detailed studies on sinkhole precursors. Subtle local subsidence and crack formation may precede sinkhole collapse processes (Tharp, 1999; Closson et al., 2009; Shalev and Lyakhovsky, 2012), and these are detectable by the InSAR technique (Nof et al., 2013; Intrieri et al., 2015). On a large scale, typical subsidence rates of mm–cm month^{-1} before sinkhole formation have been determined (Baer et al., 2002; Abelson et al., 2006; Yechieli et al., 2015), while on the local scale the low resolution (2.5 m px^{-1}) of the technique and the missing orthophoto for comparison prevents a more detailed analysis (cf. e.g. Intrieri et al., 2015). This gap can be filled by low-altitude UAV surveys such as performed here. Our approach can be used either as a stand-alone method, or in combination

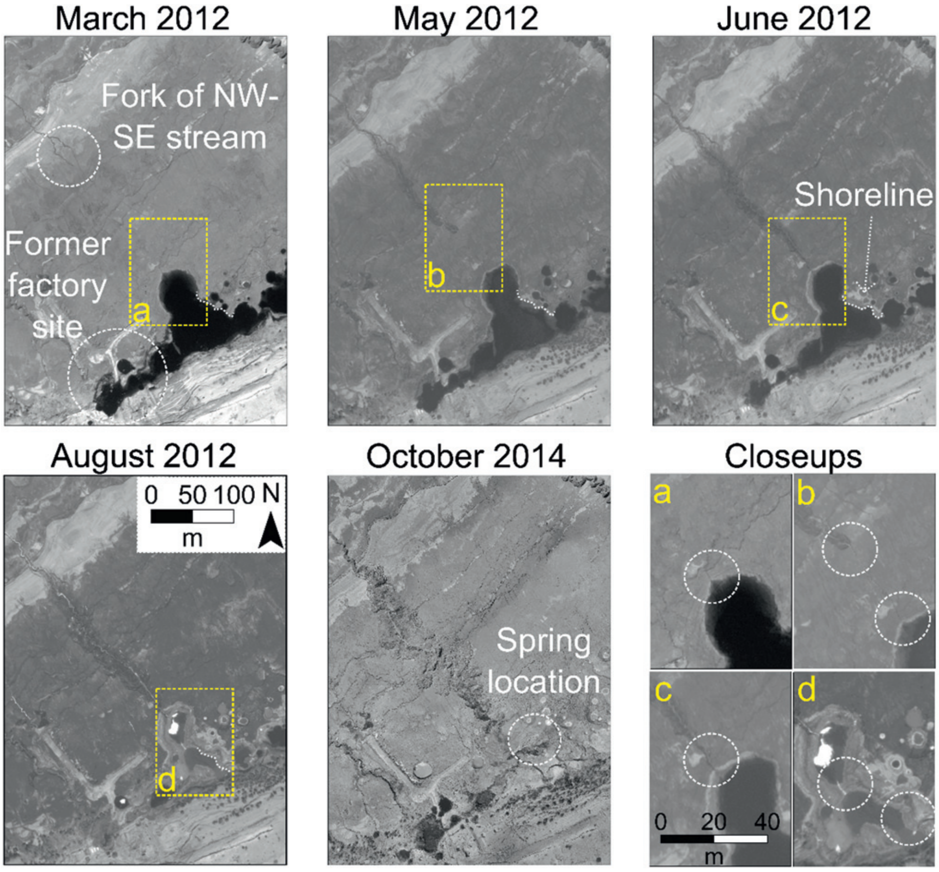

Fig. 16. Lake drainage and canyon development near the former mud factory site. Images were acquired in March (Quickbird-2 with 0.6 m px^{-1} resolution), May, June, August 2012 (Worldview-2 satellite with 0.46 m px^{-1}) and October 2014 (orthophoto from close-range photogrammetry). Visible channels (circled) exist already in March 2012 in the NW, where later the canyon develops. Note the shoreline retreat from May to August 2012 as indicated by the dashed line. Circles on closeup figures **a–c** show the lake outflow point and migrating channel head (nick-point) and channels interlinking the lake remnants in **d**.

with subsurface investigation via geophysical (e.g. Kaufmann et al., 2011; Margiotta et al., 2012; Kaufmann, 2014), hydrogeological (e.g. Caramanna et al., 2008; Panno et al., 2013) and numerical modelling methods (e.g. Shalev et al., 2006; Fuenkajorn and Archeeploha, 2010; Lollino et al., 2013). Given the high resolution, the simple application (especially in areas of complicated legal permissions) and the cost-efficiency both of the equipment and logistics, a similar approach may be appropiate for scientific research and early-warning analysis in other subsidence and sinkhole affected regions worldwide.

5.2. Lithological control on subsidence structure and morphology

Our quantitative sinkhole depth/diameter analysis confirms results of previous studies elsewhere around the Dead Sea, in that we also show that sinkhole morphology is strongly controlled by the differing mechanical properties of the sediments in which they form (e.g. Arkin and Gilat, 2000; Filin et al., 2011; Shalev and Lyakhovsky, 2012). The soft, cohesive clay sequence reveals a dominant 'sagging style' subsidence. This suggests the role of a mechanically weaker cover material in the depression formation (Holohan et al., 2011; Shalev and Lyakhovsky, 2012). A related brittle-ductile deformation leads to the formation of wide but shallow sinkholes which enlarge laterally by retrogressive slumps. As seen in numerical models (cf. Holohan et al., 2011), this process of lateral enlargement in the weak mud probabaly accounts for the observed wide periphal zones of fractured and outward-rotated blocks around many sinkholes in the mud. It may also explain both the low depth/diameter ratio and skew towards larger diameters seen for sinkholes in the mud (cf. Fig. 12).

The alluvial fan sediments show generally poor cementation and so are generally easily erodible (Taqieddin et al., 2000). Compared to the mud however, the alluvium is rheologically rather strong, and supports a more brittle deformation style. The older alluvium is locally sufficiently compacted/cemented to form vertical scarps of up to 2 m in height and cracks of up to 4 m deep, bordering the main depression. Moreover, the alluvium enables sinkholes within it to attain generally higher slopes and greater depths than the mud. In some cases alluvial-based sinkholes have overhanging sides and cavities have also been observed (Closson and Abou Karaki, 2009). Similar features also characterise sinkholes formed in salt-dominated deposits at the surface. These structural and morphological characteristics of subsidence are seen also in numerical models with high material strength (Holohan et al., 2011). The high

Table 2
Affected area A, minimum volume loss ΔV_{min} and corresponding minimum average subsidence S_{min} for the alluvium and mud zones of the main depression as well as the total survey area in 25 years.

	Alluvium	Mud	Total
A [km^2]	0.197	0.144	2.1
ΔV_{min} [m^3]	$0.83 \cdot 10^6$	$1 \cdot 10^6$	$2.5 \cdot 10^6$
S_{min} [m]	4.2	6.95	1.2

strength of the alluvium retards the lateral enlargement of the sinkholes, thus leading to the observed higher depth/diameter ratio (cf. Fig. 12).

5.3. Structural controls on sinkhole distribution and alignment

A structural control by NNE trending concealed neotectonic faults is suggested by Closson and Abou Karaki (2009) to be such a preferred groundwater flow and material dissolution path, responsible for the typically observed clustering and alignment of sinkholes along an en-echelon structure. We find a general northward trend of the sinkhole long-axis alignment, which only in the mud sinkholes partially matches the general major Dead Sea rift faults' N10−30° trend. On the other hand, long-axis azimuths (NNW–N) in the alluvium point towards the former mud factory. They are similar to regional fault strikes determined by Diabat (2005) in the hard rock areas around Ghor Al-Haditha.

No direct evidence of tectonic faults or fractures has been found in the surveyed area, although these may be concealed (Closson, 2004). Cracks, crevasses and faults adjacent to the main depression zone are spatially and temporally linked to it, and so are non-tectonic (i.e. local subsidence-related structures). With continuous base-level drop, the former surface water channels revealed by the satellite image analysis (Section 4.6), are very likely to still persist as preferential pathways deeper in the underground. The main depression, and hence the distribution of the sinkholes and their appearance in clusters, at least on the surveyed scale, depends strongly on the distribution of salty mud-flat deposits (bathymetry and shore-line geometry) and the subsurface-water channel flow directions from the main wadis Ibn Hamad and Mutayl.

Due to the limited size of the survey area, we cannot rule out that the groundwater flows reveal concealed tectonic faults at a regional scale, e.g. for the bulk cluster orientation (Closson and Abou Karaki, 2009). However, in light of our results we suggest for the local scale at the survey area in Ghor Hadith a sub-surface stream flow control on subsidence and clustered sinkhole distribution. Tectonic faults are not necessary to explain the observed groundwater flow when we consider a developing karst aquifer system, as we will illustrate in the following section.

5.4. Sinkhole formation by dissolution/subrosion in a karst aquifer

The clay sequence of the former Dead Sea lake bed is considered as an aquiclude (Bender, 1968; Frumkin et al., 2011; Mallast et al., 2011; Ezersky and Frumkin, 2013; Siebert et al., 2014c), sub-dividing the alluvium into several sub-aquifers (Shalev et al., 2006; Yechieli et al., 2015) and hence preventing direct groundwater flow except when subject to faulting. We have shown from field and satellite observations in Section 4.6, however, that the mud sequence allows direct groundwater penetration, as stated originally in Arkin and Gilat (2000). Our direct field observations include: (1) channelized subsurface water flow and seepage within the upper few meters of the inter-layered salt and mud succession; (2) sinkholes with fresh/brackish water in the mud-flat without any associated surface channel and (3) the emergence of partly artesian springs within the mud-flat (cf. Section 4.5). It is reasonable therefore to consider that a karst aquifer is developing inside the salt and mud deposits of the mud-flat area. We hence interpret the current behaviour of the Dead Sea mud at Ghor Al-Haditha in hydrogeologic terms as aquitard, i.e. hindering groundwater flow but not preventing it.

We propose that the combination of chemical dissolution/leaching of the carbonate and salt minerals in the mud (cf. Section 4.4) and mechanical mobilization (subrosion) of poorly consolidated lacustrine and alluvial sediments (cf. Section 4.5) increases the permeability of the subsurface. A layered interface model among fresh-water (7–20 m depth), a mixing zone (20–32 m), saline water (32–81 m) and Dead Sea water (from 81 m depth) has been established by Alrshdan (2012) based on transient electromagnetics and electric resistivity imaging results on the alluvium close to the former mud factory. Due to the decreased base-level by ca. 18 m since 1999, the hydraulic gradient from the Wadi Ibn Hamad to the Dead Sea is expected to be even stronger than >30 m km^{-1} as determined by Sawarieh et al. (2000) (Fig. 2). Such a hydrogeological setting of a strong base-level drop, radially flowing groundwater towards the Dead Sea, high evaporation rates (cf. e.g. Salameh and El-Naser, 2000; Salameh and Hammouri, 2008; Siebert et al., 2014b; Salameh, 2016), sudden potentiometric differences and transient hydraulic head (at Ghor Al-Haditha: periodic wadi flood events) offers ideal conditions for the development of a karst system of branchwork caves (cf. e.g. computer models by Kaufmann and Braun, 2000; Gabrovšek et al., 2014) and sinkhole clusters (Whitman et al., 1999; Denizman, 2003). Additionally the local existence of rheologically strong evaporite layers in the mud (cf. Section 4.4) supports tunnel and subsurface void formation (cf. Section 5.2). This enables a positive feedback loop between cavity/channel creation and focussed groundwater flow. Consequently, the salty-mud deposits of the former lake bed may undergo a transition from initial aquiclude behaviour to progressively less-effective aquitard behaviour.

Such a process of relatively fast karst formation is highlighted in a conceptual model for Ghor Al-Haditha in Fig. 17. It is based not only on findings of this study, but also on (hydro)-geological information (boreholes) from El-Isa et al. (1995), Sawarieh et al. (2000), Taqieddin et al. (2000) and recent studies from Krawczyk et al. (2015) and Polom et al. (2016), which delineate the subsurface mud/alluvium boundary via shear wave reflection seismics.

Our quantitative sinkhole results (*NNR*, depth/diameter, eccentricity) fit well with outcomes of GIS studies in limestone karst (e.g. Whitman et al., 1999; Denizman, 2003), evaporite karst (Galve et al., 2009; Gutiérrez et al., 2016; Gutiérrez and Lizaga, 2016) and previous studies at the Dead Sea (Filin et al., 2011). All have in common that sinkholes appear clustered, with a higher frequency of small diameter sinkholes and pronounced elongated geometry. Because of the high sinkhole density of 6.6 sinkholes ha^{-1} and high degree of clustering, the nearest neighbor distance is at the lower margin of the study of Denizman (2003). This possibly indicates a youthful to early mature stage of a salt karst according to the engineering classification (cf. e.g. Waltham, 2016).

On the western side of the Dead Sea, the documented sinkholes, subsidence, uvalas and submarine springs (cf. e.g. Siebert et al., 2014b; Yechieli et al., 2015) are typical earth surface expressions of such a developing karst system (cf. e.g. Benito et al., 1995; Goldscheider and Drew, 2007; Parise, 2010). A 2–20 m thick and 20–50 m deep salt-layer from the Holocene period is found on the western side of the Dead Sea at Ein Gedi, nearby Mineral Beach and Nahal Hever (Fig. 1B, cf. e.g. Abelson et al., 2006; Ezersky, 2008; Legchenko et al., 2008; Ezersky et al., 2009; Stein et al., 2010; Frumkin et al., 2011; Yechieli et al., 2015). Evidence of such a thick salt-layer at Ghor Al-Haditha (El-Isa et al., 1995; Taqieddin et al., 2000; Ezersky et al., 2013) is relatively weak (Polom et al., 2016), although we cannot rule out its existence. Hence the subsidence phenomena can be alternatively explained by the progressive kartification of the thinly-bedded salty mud deposits with subsequent or concurrent physical material removal (subrosion) in the alluvium (Fig. 17A).

A similar mechanism of sinkhole formation by subsurface drainage and flow is mentioned by Arkin and Gilat (2000), Filin et al. (2011) and Garfunkel and Ben-Avraham (1996) on the nearby Lisan peninsula and at several sites on the western side. Therefore this mechanism - the Dead Sea mud acting as an aquitard and later as an aquifer - poses also a scientific novelty for numerical modelling of sinkhole formation including groundwater flow (see Shalev et al., 2006; Ezersky et al., 2013), and should be considered in further studies at both sides of the Dead Sea.

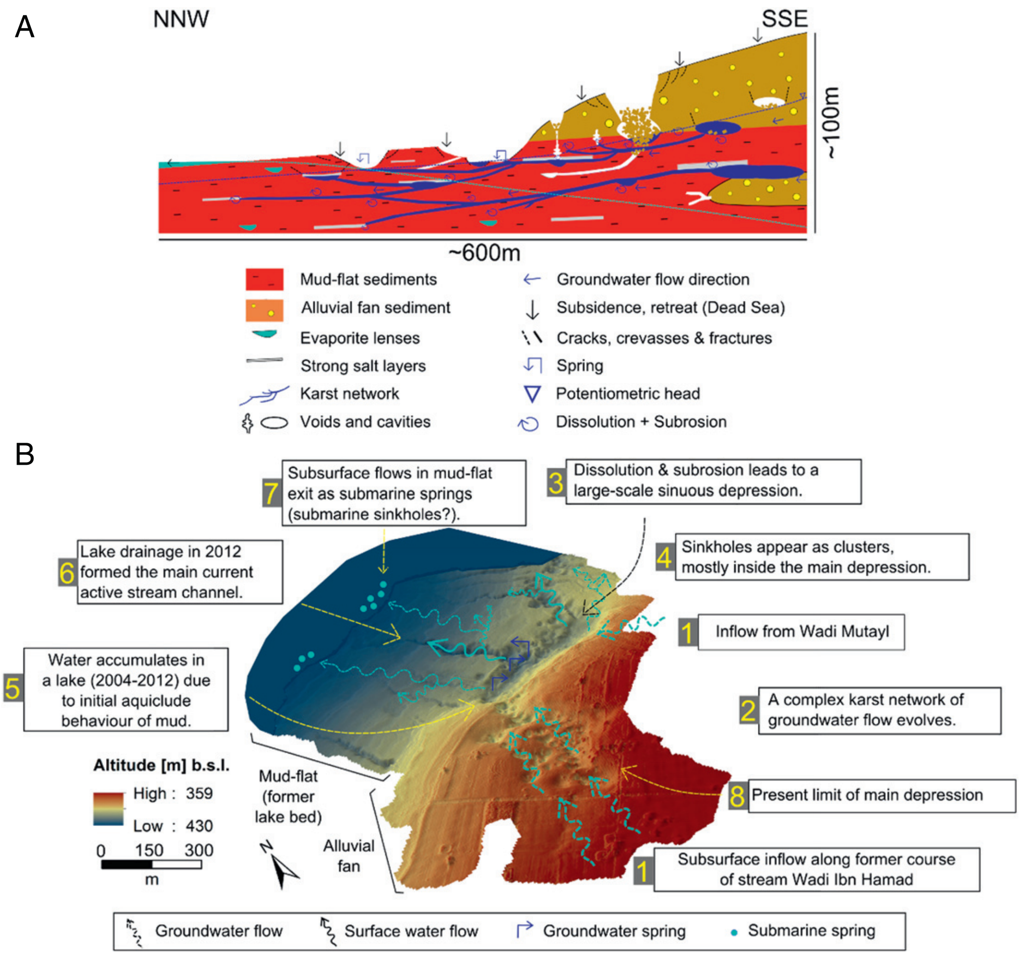

Fig. 17. Conceptual model of subsidence and sinkhole formation at Ghor Al-Haditha based on findings of this study and of previous investigations by (El-Isa et al., 1995; Sawarieh et al., 2000; Taqieddin et al., 2000; Krawczyk et al., 2015; Polom et al., 2016, partly unpublished reports). **A**: Development of a karst aquifer in the alluvium and clay-sequence along a roughly SSE–NNW cross-section. The geologic sequence consists of interbedded alluvial fan sediments and the lacustrine, evaporite rich mud-flat with strong salt-layers that support tunnels. Dissolution of local evaporitic lenses/layers and salt minerals weakens the material compound. The Dead Sea base-level drop forces strong mechanical mobilization (subrosion) of both mud and alluvial sediments by fresh-water flow and progressive karstification and consequent subsidence/sinkhole formation. Note that subrosion may act even below the salt-water table (light blue line) which is constrained by calculations from Salameh and El-Naser (2000). **B**: Interpretative scheme of subsidence and sinkhole formation processes at the study area, using a 3D Raster topographic image to highlight the main central sinuous depression. See text for a detailed description.

5.5. Overall interpretation of land subsidence at Ghor Al-Haditha

Our overall interpretation of the development of land subsidence and sinkhole formation processes at Ghor Al-Haditha is depicted graphically in part **B** of the conceptual model of Fig. 17.

Groundwater flows lakeward beneath the alluvial cover, following the old stream paths of waters from Wadi Ibn Hamad and Wadi Mutayl, seen in the satellite image from 1970 (Fig. 15). The subsurface sequences of intercalated alluvial fans and mud-flat sediments containing thin evaporite layers can easily be chemically and mechanically removed by the undersaturated water flow, which is driven by the high hydraulic gradient due to the continuous base-level drop. Sinkhole clusters appear initially on the alluvium but also later on the mud-flat (cf. Section 4.1). At the confluence of the groundwater flows and at the boundary between alluvium and mud-flat, a large depression formed with concentric cracks around it. The mud-flat sediments here act as an aquitard, leading to an accumulation of water in the depression to form major lakes and appearance of partially artesian springs (Fig. 17A). The lake drains, as a large canyon is formed via surface and subsurface flow in the exposed mud-flat on a timescale of a few months (cf. Section 4.5). The mud progressively develops into a karst aquifer system depending on the distribution of evaporites. Sinkholes nowadays appear more and more in the N–NE of the main depression, hence indicating a direction of the hydraulic gradient with the clayey layers as initial limiting boundary conditions. Subsurface channels without observed outflow into the Dead Sea are found and are likely to terminate as submarine springs. This system of preferential subterranean groundwater flow paths, involving dissolution of evaporitic minerals and subrosion of unconsolidated material, has to be considered as a complex karst water flow network.

Considering the complexity of the subsidence and sinkhole formation process around the Dead Sea, it is clear that a simple interpretative scheme does not explain every single feature or the complete time development in this area. We have studied in detail about 1.5 km of a 6 km long sinkhole lineament, hence our findings concern only about 25 % of the longest sinkholes' lineament in the whole Dead Sea area. In general the hydrogeological conditions, for example the aquicludal behaviour of the Dead Sea mud, the role of the salt-fresh water boundary in a context of such a complex flow network and the existence or removal of a salt-layer, need to be investigated more in detail as they are beyond the scope of this work.

Nevertheless, our results provide a new perspective on the ongoing processes of land subsidence at Ghor Al-Haditha. Importantly, the high resolution DSM and orthophoto, combined with future survey repetitions, will lead to an estimation of short-term subsidence rates (cf. Section 5.1), changes in morphology and the time evolution of sinkhole formation. This will in turn help to delineate zones prone to future collapse inside this actively subsiding area on a very detailed scale.

6. Conclusions

In this work we presented a first high resolution (5 cm px^{-1}) digital surface model and orthophoto (6.7 cm px^{-1}) for the sinkhole area of Ghor Al-Haditha in the SE part of the Dead Sea. We showed that the equal dispersed distribution of ground control points in the survey area is of crucial importance for correct georeferencing and reliable subsequent DSM analysis. The high resolution DSM and geomorphological analysis are of high relevance for subsidence and sinkhole hazard and precursor assessment on the eastern coast of the Dead Sea. This photogrammetric study, combined with field and satellite image analysis, reveals new quantative and qualitative aspects of the subsidence and sinkhole formation. We summarize the main outcomes here as follows:

1. A subtle, large-scale (length 1.5 km, width 0.15 –0.4 km), sinuousoidal depression bound partly by non-tectonic faults and orientated NNW with a shift to NE at the mud/alluvium contact has been identified at Ghor Al-Haditha. This depression contains around 85 % of the almost 300 identified sinkholes spread over 0.45 km^2 of the 2.1 km^2 survey area. Sinkhole density in the most affected zone is 6.6 sinkholes ha^{-1}.
2. The estimated minimum volume loss of the surveyed area is $2.5 \cdot 10^6$ m^3, the main depression alone counts for $1.83 \cdot 10^6$ m^3. The estimated minimum erosion rates are 41,670 m^3 yr^{-1} and 73,200 m^3 yr^{-1} respectively. The minimum subsidence of the depression lies between 4.2 m (alluvium) and 6.95 m (mud-flat), with an average subsidence rate of 0.21 m yr^{-1} since the beginning of sinkhole formation.
3. Sinkholes in the depression area show different morphologies related to the mechanical strength of the materials they formed in. In mud, wide and shallow sinkholes develop with low depth to diameter values (0.14); in alluvium, deep and narrow sinkholes develop (0.4).
4. Sinkholes are mostly elliptical with eccentricities of 1.31. The sinkhole sequence shows a significantly clustered distribution with a nearest neighbor ratio 0.69. Long-axis strike of the individual sinkholes in alluvium is between NNW–N, in mud NNE–NE.
5. Springs and highly mobile channelized groundwater flow appear at or near the contact between the mud and alluvium sequences. Observations of entrainment of unsoluble sediments of up to pebble size at the partially artesian springs adjacent this contact suggest that subrosion acts as a significant driving physical process for subsurface material depletion. The Dead Sea mud acts as an aquitard, locally penetrated by solution-driven water channels, which dynamically form new canyon systems and generally follow preferential flow paths.
6. Interbedded evaporite layers of observed 1.5 m maximum thickness facilitate groundwater penetration and dissolution processes within the salty mud sediments of the former Dead Sea lake bed. The voids and conduits form an actively evolving, complex karst system with sinkholes, subsidence and uvalas as typical morphological expressions.
7. A satellite image from 1970 reveals formerly existing surface water streams from the Wadi Ibn Hamad into todays' most affected sinkhole zone. Despite engineering diversion of the river, inferred continued existence of such a preferential subsurface flow provides a basis for chemical and mechanical material removal in the surveyed area.

In conclusion, sinkhole formation and subsidence at Ghor Al-Haditha is related to karstification by both chemical dissolution and mechanical subrosion along a channelized subterranean flow network in thinly interbedded salt and mud deposits. This constitutes an alternative to the massive salt layer dissolution models as proposed formerly for both sides of the Dead Sea.

Acknowledgements

We thank the Helmholtz Virtual Institute DESERVE and all involved institutions, especially the Ministry of Energy and Mineral Resources in Amman, Jordan, and the Leibnitz Institute of Applied Geophysics in Hannover, Germany. Special thanks also go to Ulrich Polom, Khalil Abu Ayyash, Emad Talafeha, Kayyed Aljbour, Showqi, Anas Maitah, Ali, Jaseed and Rshud for their kind support of the field campaign, logistic issues and scientific discussions. We also thank two anonymous reviewers and the editor for their fruitful comments and suggestions.

Appendix A

A.1. Bundle adjustment algorithm

We summarize here the mathematical fundamentals of the bundle adjustment algorithm used for multi-image triangulation in close-range photogrammetry based on detailed descriptions in Förstner and Wrobel (2013) and Luhmann et al. (2014).

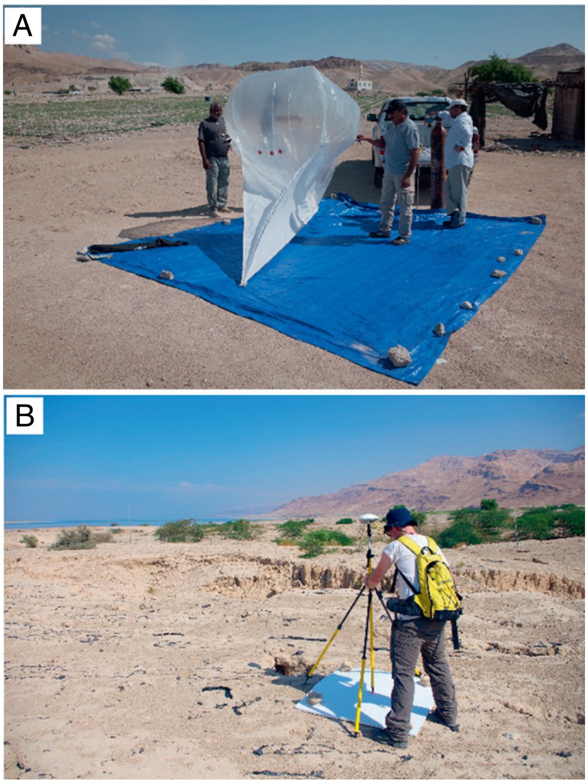

Fig. A1. Field equipment used for the photogrammetric survey. **A**: Filling and reeling out the camera bearing Helikite balloon. **B**: Measuring the ground control points with a high accuracy Differential GPS.

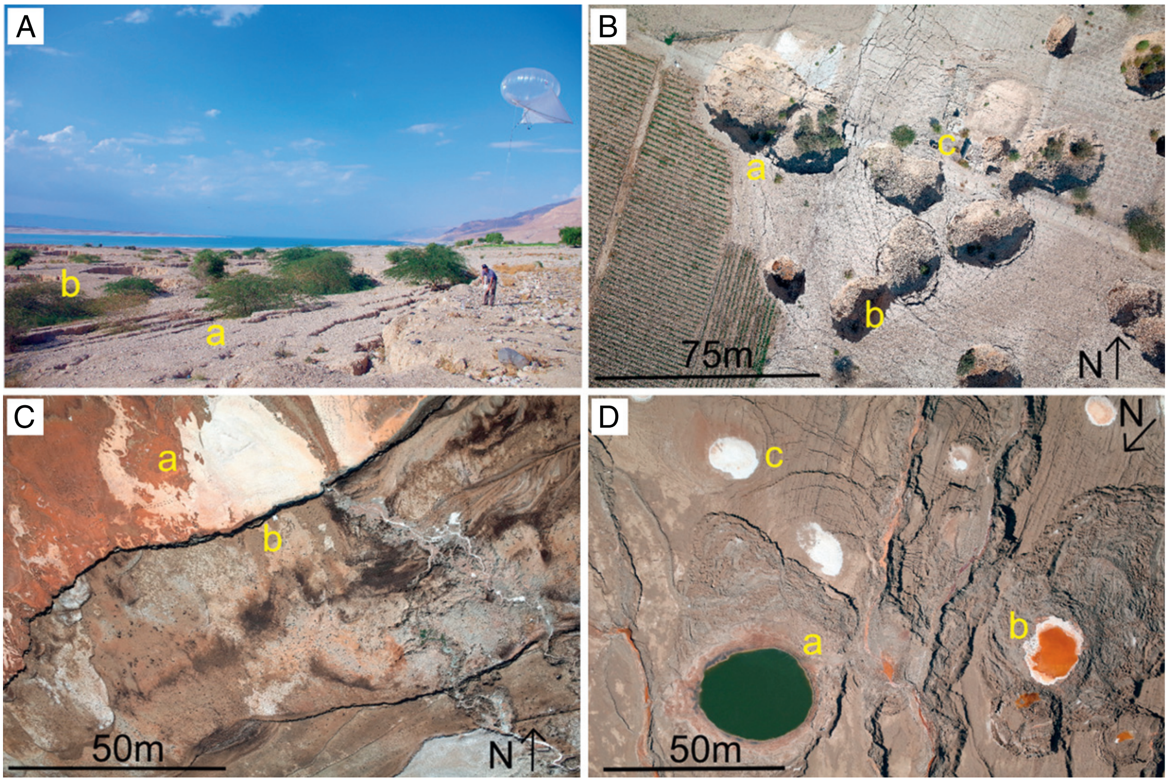

Fig. A2. Geomorphological structures in alluvium and mud. **A**: Major cracks (**a**) bounding the main depression zone at the fractured edge of the sinkhole area in the alluvium (**b**). **B**: Sinkhole cluster in the alluvium. Indicated are nested sinkholes (**a, b**) and a destroyed farm building (**c**). **C**: The retreat of the shoreline and the existence of individual salt pans (**a**), built by evaporation of closed salt-water ponds. Marker point a the edge of an old shoreline (**b**). **D**: Heterogeneous water filling of mud-flat sinkholes: Fresh-water (**a**), salt-water with high iron-oxide content (**b**) and dried out former salt-water sinkhole (**c**). Several older sinkholes of the nest zone are nowadays dry (**b**).

A.1.1. Collinearity equations

Looking at one single image first, the interior coordinate system (image frame, (x', y', z')) of the camera is known, including the offset z' of its perspective center (X_0) in relation to the origin of the reference exterior coordinate frame (global or object coordinate system, (X,Y,Z)).

The angular orientation ($\Phi = \omega, \varphi, \kappa$) in space of the image coordinate system is defined by a rotation matrix $\boldsymbol{R}$ about the global coordinate system:

$$\boldsymbol{R} = \begin{pmatrix} r_{11} & r_{12} & r_{13} \\ r_{21} & r_{22} & r_{23} \\ r_{31} & r_{32} & r_{33} \end{pmatrix} \qquad \text{(A1)}$$

Using a Helmert coordinate system transformation any point of the image (x') can now be translated from camera coordinates into the global coordinates, denoting the vector from the perspective center to the image point within the object coordinate system with X^*, so that $\boldsymbol{X} = X_0 + X^*$. The image vector can be expressed by scaling (m) and rotation as $X^* = m\boldsymbol{R}\cdot x'$. The projection of an image point into the object point is therefore:

$$\boldsymbol{X} = \boldsymbol{X_0} + m\boldsymbol{R}\cdot\boldsymbol{x'} = \boldsymbol{X_0} + \boldsymbol{X^*} \qquad \text{(A2)}$$

For a 3D inversion of this problem for one image point more information is needed in the form of intersection with additional image ray paths or surfaces. With x_0' as a principal point in the camera coordinate system and $\Delta x'$ as internal image distortion parameters, the inversion equation reads as:

$$\boldsymbol{x'} - \boldsymbol{x'_0} - \Delta x' = \frac{1}{m}\boldsymbol{R^{-1}}\cdot(\boldsymbol{X} + \boldsymbol{X_0}) \qquad \text{(A3)}$$

The scaling factor is eliminated by internal division of the first two rows by the third in Eq. (A3). This leads to the general collinearity equations for transformation of object (exterior) coordinates into image (interior) coordinates as function of the orientation parameters stated above, expressed here in vector entries notation:

$$\begin{aligned} x' &= x'_0 + \Delta x' + z'\frac{r_{11}(X - X_0) + r_{21}(Y - Y_0) + r_{31}(Z - Z_0)}{r_{13}(X - X_0) + r_{23}(Y - Y_0) + r_{33}(Z - Z_0)} \\ y' &= y'_0 + \Delta y' + z'\frac{r_{12}(X - X_0) + r_{22}(Y - Y_0) + r_{32}(Z - Z_0)}{r_{13}(X - X_0) + r_{23}(Y - Y_0) + r_{33}(Z - Z_0)} \end{aligned} \qquad \text{(A4)}$$

A.1.2. Space resection

In the case of a fixed interior coordinate system of e.g. a metric digital camera, at minimum three reference points in the object frame providing the position and orientation parameters are needed for the non-linear solution of the collinearity Eq. (A4) with approximate starting values. A unique solution will be achieved with four reference points and each 3D reference point provides three correction equations. A Taylor-series expansion linearisation and a least-squares fit is used for solving the resulting normal correction equations. For multi-image processing it has the general form:

$$\boldsymbol{X'_i} + v\boldsymbol{X'_i} = F\left(\boldsymbol{X_i}, \boldsymbol{X_{0j}}, \Delta\boldsymbol{x'_k}, \boldsymbol{X'_{0k}}, \boldsymbol{\Phi_j}\right) \qquad \text{(A5)}$$

with indices: i: image point, j: image and k: camera

The number of unknowns (u) in this set of equations can be calculated using reference points via:

$$u = u_I \, n_{\text{images}} + u_P \, n_{\text{points}} + u_C \, n_{\text{cameras}} \tag{A6}$$

with u_I = six parameters of exterior orientation, u_P = three parameters for the position of each point and u_C = zero to more than three parameters of the interior orientation per camera. Additional constraints, e.g. measured distances or object surfaces can be included in the correction equations leading to less degrees of freedom. In the case of a non-fixed interior coordinate system at minimum five reference points are needed to apply a Direct Linear Transformation method that does not need approximate initial values. For further reading and the mathematical details of these procedures refer to Luhmann et al. (2014).

A.2. Additional field and aerial photo evidence

We present the main equipment used in this study, namely the Helikite balloon used for acquisition of the aerial images (Fig. A1A) and the differential GPS device used for ground referencing (Fig. A1B). Finally, we provide an assemblage of further field and aerial photo evidence of the structures, sinkholes and streams/springs in the measurement area referred to in the main text (Section 4). A ground-based view of the non-tectonic faults bounding the main depression area is given in Fig. A2A. The detailed aerial photos highlight a sinkhole cluster sequence (B), individual salt accumulations (C) and the range of water infilling of the sinkholes (D).

References

Abelson, M., Yechieli, Y., Crouvi, O., Baer, G., Wachs, D., Bein, A., Shtivelman, V., 2006. Evolution of the Dead Sea Sinkholes. In: Enzel, Y., Agnon, A., Stein, M. (Eds.), New Front. Dead Sea Paleoenviron. Res. Geol. Soc. Am. Spec. Pap. 401. Geological Society of America., pp. 241–253.

Agisoft, 2013. Agisoft PhotoScan User Manual. Professional edition, version 1.0.0.

Al-Omari, A., Salman, A., Karablieh, E., 2014. The Red Dead Canal project: an adaptation option to climate change in Jordan. Desalin. Water Treat. 52 (13–15), 2833–2840.

Al-Ruzouq, R., Al-Zoubi, A., Abueladas, A., Akkawi, E., 2011. Hazard Mapping Along the Dead Sea Shoreline. FIG Work. Week - Bridg. Gap between Cult.. (Marrakech, Morocco).

Al-Zoubi, A.S., Abueladas, A.E.-R.a., Al-Rzouq, R.I., Camerlynck, C., Akkawi, E., Ezersky, M.G., Z.S.H, A.-H., Ali, W., Rawashdeh, S.A., 2007. Use of 2D Multi electrodes resistivity imaging for sinkholes hazard assessment along the Eastern Part of the Dead Sea, Jordan. Am. J. Environ. Sci. 3 (4), 230–234.

Alrshdan, H., 2012. Geophysical Investigations of Ghor Haditha Sinkholes, Jordan. 74th EAGE Work. Dead Sea Sink. - Causes, Eff. Solut.. (Copenhagen, Denmark).

Arkin, A., Gilat, Y., 2000. Dead Sea sinkholes an ever-developing hazard. Environ. Geol. 39 (7).

Atzori, S., Antonioli, A., Salvi, S., Baer, G., 2015. InSAR-based modeling and analysis of sinkholes along the Dead Sea coastline. Geophys. Res. Lett. 42, 8383–8390.

Baer, G., Schattner, U., Wachs, D., Sandwell, D., Wdowinski, S., Frydman, S., 2002. The lowest place on Earth is subsiding - an InSAR (interferometric synthetic aperture radar) perspective. Geol. Soc. Am. Bull. 114 (1), 12–23.

Beck, B., 2012. Soil Piping and Sinkhole Failures. In: White, W.B., Culver, D. (Eds.), Encycl. caves. Elsevier, New York, pp. 718–723.

Begin, Z.B., Ehrlich, A., Nathan, Y., 1974. Lake Lisan: the Pleistocene precursor of the Dead Sea. Geol. Surv. Isr. Bull. 63, (30 pp).

Bender, F., 1968. Geologie von Jordanien. Gebrüder Bornträger, Berlin - Stuttgart.

Benito, G., del Campo, P.P., Gutiérrez-Elorza, M., Sancho, C., 1995. Natural and human-induced sinkholes in gypsum terrain and associated environmental problems in NE Spain. Environ. Geol. 25 (3), 156–164.

Bentor, Y., 1961. Some geochemical aspects of the Dead Sea and the question of its age. Geochim. Cosmochim. Acta 25, 239–260.

Boever, M.D., Khlosi, M., Delbecque, N., Pue, J.D., Ryken, N., 2013. Desertification and Land Degradation - Processes and Mitigation. UNESCO Chair of Eremology, Ghent, Belgium.

Bowman, D., Svoray, T., Devora, S., Shapira, I., Laronne, J.B., 2010. Extreme rates of channel incision and shape evolution in response to a continuous, rapid base-level fall, the Dead Sea, Israel. Geomorphology 114 (3), 227–237.

Brinkmann, R., Parise, M., Dye, D., 2008. Sinkhole distribution in a rapidly developing urban environment: Hillsborough County, Tampa Bay area, Florida. Eng. Geol. 99 (3–4), 169–184.

Burner, A., Snow, W., Goad, W., 1983. Close-Range Photogrammetry with Video Cameras. . NASA Langley Research Center, Hampton, VA, United States.

Caramanna, G., Ciotoli, G., Nisio, S., 2008. A review of natural sinkhole phenomena in Italian plain areas. Nat. Hazards 45 (2), 145–172.

Closson, D., 2004. Structural control of sinkholes and subsidence hazards along the Jordanian Dead Sea coast. Environ. Geol. 47 (2), 290–301.

Closson, D., Abou Karaki, N., 2008. Human-induced geological hazards along the Dead Sea coast. Environ. Geol. 58 (2), 371–380.

Closson, D., Abou Karaki, N., 2009. Salt karst and tectonics: sinkholes development along tension cracks between parallel strike-slip faults, Dead Sea, Jordan. Earth Surf. Process. Landforms 34, 1408–1421.

Closson, D., Abou Karaki, N., 2013. Sinkhole hazards prediction at Ghor Al Haditha, Dead Sea, Jordan: “Salt Edge” and “Tectonic” models contribution - a rebuttal to Geophysical prediction and following development sinkholes in two Dead Sea areas, Israel and Jordan”, by: Ezersky et al., 201. Environ. Earth Sci. 70 (6), 2919–2922.

Closson, D., Abou Karaki, N., 2015. Earthen Dike Leakage at the Dead Sea. In: Lollino, G., Manconi, A., Guzzetti, F., Culshaw, M., Bobrowsky, P., Luino, F. (Eds.), Eng. Geol. Soc. Territ. - Vol. 5. Springer International Publishing., pp. 461–464.

Closson, D., Abou Karaki, N., Hallot, F., 2009. Landslides along the Jordanian Dead Sea coast triggered by the lake level lowering. Environ. Earth Sci. 59 (7), 1417–1430.

Closson, D., Abou Karaki, N., Pasquali, P., Riccardi, P., 2013. A 300m-width sinkhole threatens the stability of the embankment of a saltpan in Jordan, Dead Sea Region. Geophys. Res. Abstr. 15, 2363.

Dahm, T., Heimann, S., Bialowons, W., 2011. A seismological study of shallow weak micro-earthquakes in the urban area of Hamburg city, Germany, and its possible relation to salt dissolution. Nat. Hazards 58 (3), 1111–1134.

De Smith, M.J., Goodchild, M.F., Longley, P., 2015. Geospatial analysis: a comprehensive guide to principles, techniques and software tools. http://www.spatialanalysisonline.com.

Denizman, C., 2003. Morphometric and spatial distribution parameters of karstic depressions, lower Suwanee River basin, Florida. J. Cave Karst Stud. 65 (1), 29–35.

Diabat, A.A., 2005. Sinkholes related to tectonic factor at Ghor Al Haditha Area, Dead Sea/Jordan. Hydrogeol. und Umwelt 33 (17), 4.

Doctor, D.H., Young, J.A., 2013. An evaluation of automated GIS tools for delineating karst sinkholes and closed depressions from 1-meter LiDAR-derived digital elevation data. Thirteen. Multidiscip. Conf. Sink. Eng. Environ. Impacts Karst. pp. 449–458.

Dreybrodt, W., 2012. Processes in Karst Systems: Physics, Chemistry and Geology. 4. Springer Science & Business Media.

El-Isa, Z., Rimawi, O., Jarrar, G., Abou Karaki, N., Taqieddin, S., Atallah, M., Seif El-Din, N., Al Saed, A., 1995. Assessment of the Hazard of Subsidence and Sinkholes in Ghor Al-Haditha Area. Tech. rep.. University of Jordan, Center for consultation, technical services and studies.,

Esri, 2015. ArcGIS Version 10.2 online resource. date accessed 2015-08-13. https://doc.arcgis.com/en/arcgis-online.

Ezersky, M., 2008. Geoelectric structure of the Ein Gedi sinkhole occurrence site at the Dead Sea shore in Israel. J. Appl. Geophys. 64 (3–4), 56–69.

Ezersky, M., Frumkin, A., 2013. Fault - Dissolution front relations and the Dead Sea sinkhole problem. Geomorphology 201, 35–44.

Ezersky, M., Legchenko, A., Camerlynck, C., Al-Zoubi, A., 2009. Identification of sinkhole development mechanism based on a combined geophysical study in Nahal Hever South area (Dead Sea coast of Israel). Environ. Geol. 58 (5), 1123–1141.

Ezersky, M.G., Eppelbaum, L.V., Al-Zoubi, A., Keydar, S., Abueladas, A., Akkawi, E., Medvedev, B., 2013. Geophysical prediction and following development sinkholes in two Dead Sea areas, Israel and Jordan. Environ. Earth Sci. 70 (4), 1463–1478.

Ezersky, M.G., Eppelbaum, L.V., Al-Zoubi, A., Keydar, S., Abueladas, A.-R., Akkawi, E., Medvedev, B., 2014. Comments to publication of D. Closson and N. Abu Karaki “Sinkhole hazards prediction at Ghor Al Haditha, Dead Sea, Jordan: “Salt Edge” and “Tectonic” models contribution - a rebuttal to ”Geophysical prediction and following development .”. Environ. Earth Sci. 71 (4), 1989–1993.

Farr, T.G., Rosen, P.A., Caro, E., Crippen, R., Duren, R., Hensley, S., Kobrick, M., Paller, M., Rodriguez, E., Roth, L., Seal, D., Shaffer, S., Shimada, J., Umland, J., Werner, M., Oskin, M., Burbank, D., Alsdorf, D.E., 2007. The shuttle radar topography mission. Rev. Geophys. 45 (2), 1–43.

Filin, S., Baruch, A., Avni, Y., Marco, S., 2011. Sinkhole characterization in the Dead Sea area using airborne laser scanning. Nat. Hazards 58 (3), 1135–1154.

Fleury, P., Bakalowicz, M., de Marsily, G., 2007. Submarine springs and coastal karst aquifers: a review. J. Hydrol. 339 (1–2), 79–92.

Förstner, W., Wrobel, B., 2013. Mathematical concepts in photogrammetry. In: McGlone (Ed.), Man. Photogramm. American Society of Photogrammetry and Remote Sensing, Bethesda, MD, USA, pp. 63–233.

Frumkin, A., Ezersky, M., Al-Zoubi, A., Akkawi, E., Abueladas, A.-R., 2011. The Dead Sea sinkhole hazard: geophysical assessment of salt dissolution and collapse. Geomorphology 134 (1–2), 102–117.

Frydman, S., Charrach, J., Goretsky, I., 2008. Geotechnical properties of evaporite soils of the Dead Sea area. Eng. Geol. 101 (3–4), 236–244.

Fuenkajorn, K., Archeeploha, S., 2010. Prediction of cavern configurations from subsidence data. Eng. Geol. 110 (1–2), 21–29.

Furukawa, Y., Ponce, J., 2010. Accurate, dense, and robust multiview stereopsis. IEEE Trans. Pattern Anal. Mach. Intell. 32 (8), 1362–1376.

Gabrovšek, F., Häuselmann, P., Audra, P., 2014. ‘Looping caves’ versus ‘water table caves’: the role of base-level changes and recharge variations in cave development. Geomorphology 204, 683–691.

Galve, J., Gutiérrez, F., Remondo, J., Bonachea, J., Lucha, P., Cendrero, A., 2009. Evaluating and comparing methods of sinkhole susceptibility mapping in the Ebro Valley evaporite karst (NE Spain). Geomorphology 111 (3–4), 160–172.

Galve, J.P., Remondo, J., Gutiérrez, F., 2011. Improving sinkhole hazard models incorporating magnitude-frequency relationships and nearest neighbor analysis. Geomorphology 134 (1–2), 157–170.

Garfunkel, Z., Ben-Avraham, Z., 1996. The structure of the Dead Sea basin. Tectonophysics 266, 155–176.

Gavrieli, I., Oren, A., 2004. The Dead Sea as a Dying Lake. In: Nihoul, J.C.J., Zavialov, P.O., Micklin, P.P. (Eds.), Dying Dead Seas Clim. Versus Anthr. Causes SE - 11. NATO Science Series IV: Earth and Environmental Sciences 36. Springer Netherlands., pp. 287–305.

Goldscheider, N., Drew, D., 2007. Methods in Karst Hydrogeology. Taylor and Francis, London, UK.

Gutiérrez, F., Fabregat, I., Roqué, C., Carbonel, D., Guerrero, J., García-Hermoso, F., Zarroca, M., Linares, R., 2016. Sinkholes and caves related to evaporite dissolution in a stratigraphically and structurally complex setting, Fluvia Valley, eastern Spanish Pyrenees. Geological, geomorphological and environmental implications. Geomorphology 267, 76–97.

Gutiérrez, F., Guerrero, J., Lucha, P., 2008. A genetic classification of sinkholes illustrated from evaporite paleokarst exposures in Spain. Environ. Geol. 53 (5), 993–1006.

Gutiérrez, F., Lizaga, I., 2016. Sinkholes, collapse structures and large landslides in an active salt dome submerged by a reservoir: The unique case of the Ambal ridge in the Karun River, Zagros Mountains, Iran. Geomorphology 254, 88–103.

Gutierréz, F., Parise, M., De Waele, J., Jourde, H., 2014. A review on natural and human-induced geohazards and impacts in karst. Earth-Science Rev. 138, 61–88.

Harwin, S., Lucieer, A., 2012. Assessing the accuracy of georeferenced point clouds produced via multi-view stereopsis from Unmanned Aerial Vehicle (UAV) imagery. Remote Sens. 4, 1573–1599.

Hatzor, Y.H., Wainshtein, I., Bakun Mazor, D., 2010. Stability of shallow karstic caverns in blocky rock masses. Int. J. Rock Mech. Min. Sci. 47 (8), 1289–1303.

Holohan, E.P., Schöpfer, M.P.J., Walsh, J.J., 2011. Mechanical and geometric controls on the structural evolution of pit crater and caldera subsidence. J. Geophys. Res. 116 (B07202).

Intrieri, E., Gigli, G., Nocentini, M., Lombardi, L., Mugnai, F., Fidolini, F., Casagli, N., 2015. Sinkhole monitoring and early warning: An experimental and successful GB-InSAR application. Geomorphology 241, 304–314.

Kaufmann, G., 2014. Geophysical mapping of solution and collapse sinkholes. J. Appl. Geophys. 111, 271–288.

Kaufmann, G., Braun, J., 2000. Karst Aquifer evolution in fractured, porous rocks. Water Resour. Res. 36 (6), 1381–1391.

Kaufmann, G., Romanov, D., Nielbock, R., 2011. Cave detection using multiple geophysical methods: Unicorn cave, Harz Mountains, Germany. Geophysics 76 (3), B71–B77.

Kawashima, K., Aydan, Ö., Aoki, T., Kishimoto, I., Konagai, K., Matsui, T., Sakuta, J., Takahashi, N., Teodori, S.-P., Yashima, A., 2010. Reconnaissance investigation on the damage of the 2009 L'Aquila, Central Italy Earthquake. J. Earthq. Eng. 14 (6), 817–841.

Khlaifat, A., Al-Khashman, O., Qutob, H., 2010. Physical and chemical characterization of Dead Sea mud. Mater. Charact. 61 (5), 564–568.

Khoury, H.N., 2002. Clays and Clay Minerals in Jordan. Tech. rep.. Jordan University, Amman, Jordan.

Kohl, M., 2001. Subsidence and Sinkholes in East Tennessee. Tech. rep.. State of Tennessee, Department of Environment and Conservation, Division of Geology, Tennessee.

Kottmeier, C., Agnon, A., Al-Halbouni, D., Alpert, P., Corsmeier, U., Dahm, T., Eshel, A., Geyer, S., Haas, M., Holohan, E.P., Kalthoff, N., Kishcha, P., Krawczyk, C.M., Lati, J., Laronne, J.B., Lott, F., Mallast, U., Merz, R., Metzger, J., Mohsen, A., Morin, E., Nied, M., Rödiger, T., Salameh, E., Sawarieh, A., Shannak, B., Siebert, C., Weber, M., 2016. New perspectives on interdisciplinary earth science at the Dead Sea: the DESERVE project. Sci. Total Environ. 544, 1045–1058.

Kotyrba, A., 2015. A study of sinkhole hazard at area of Locked Colliery. Post-Mining. (Nancy).

Krawczyk, C., Dahm, T., 2011. Charakterisierung und Überwachung von Salz-bezogenen Erdfällen in urbanen Gebieten. Tech. rep.. Leibnitz Institute of Applied Geophysics, Hannover, Germany.

Krawczyk, C.M., Polom, U., Alrshdan, H., Al-Halbouni, D., Sawarieh, A., Dahm, T., 2015. New process model for the Dead Sea sinkholes at Ghor Al Haditha, Jordan, derived from shear-wave reflection seismics. EGU Gen. Assem. 2015. (Vienna, Austria).

Le Béon, M., Klinger, Y., Mériaux, A.S., Al-Qaryouti, M., Finkel, R.C., Mayyas, O., Tapponnier, P., 2012. Quaternary morphotectonic mapping of the Wadi Araba and implications for the tectonic activity of the southern Dead Sea fault. Tectonics 31 (5), 1–25.

Legchenko, A., Ezersky, M.G., Boucher, M., Camerlynck, C., Al-Zoubi, A., Chalikakis, K., 2008. Pre-existing caverns in salt formations could be the major cause of sinkhole hazards along the coast of the Dead Sea. Geophys. Res. Lett. 35 (19), 1–5.

Lensky, N.G., Dvorkin, Y., Lyakhovsky, V., Gertman, I., Gavrieli, I., 2005. Water, salt, and energy balances of the Dead Sea. Water Resour. Res. 41 (12), 1–13.

Leon, J., Roelfsema, C.M., Saunders, M.I., Phinn, S.R., 2015. Measuring coral reef terrain roughness using "Structure-from-Motion" close-range photogrammetry. Geomorphology 242, 21–28.

Lollino, P., Martimucci, V., Parise, M., 2013. Geological survey and numerical modeling of the potential failure mechanisms of underground caves. Geosystem Eng. 16 (1), 37–41.

Luhmann, T., Robson, S., Kyle, S., Boehm, J., 2014. Close-range photogrammetry and 3D imaging. second, Walter De Gruyter.

Mallast, U., Gloaguen, R., Geyer, S., Rödiger, T., Siebert, C., 2011. Derivation of groundwater flow-paths based on semi-automatic extraction of lineaments from remote sensing data. Hydrol. Earth Syst. Sci. 15 (8), 2665–2678.

Margiotta, S., Negri, S., Parise, M., Valloni, R., 2012. Mapping the susceptibility to sinkholes in coastal areas, based on stratigraphy, geomorphology and geophysics. Nat. Hazards 62 (2), 657–676.

Menzel, L., Teichert, E., Weiss, M., 2007. Climate Change Impact on the Water Resources of the Semi-arid Jordan Region. Proc. 3rd Int. Conf. Clim. Water, Helsinki. pp. 320–325.

Messerklinger, S., 2014. Formation mechanism of large subsidence sinkholes in the Lar valley in Iran. Q. J. Eng. Geol. Hydrogeol. 47, 237–250.

MWI, 2013. Jordan Water Sector Facts and Figures. . Ministry of Water and Irrigation, Amman, Jordan.

Nof, R.N., Baer, G., Ziv, A., Raz, E., Atzori, S., Salvi, S., 2013. Sinkhole precursors along the Dead Sea, Israel, revealed by SAR interferometry. Geology 41 (9), 1019–1022.

Odeh, T., Rödiger, T., Geyer, S., Schirmer, M., 2015. Hydrological modelling of a heterogeneous catchment using an integrated approach of remote sensing, a geographic information system and hydrologic response units: the case study of Wadi Zerka Ma'in catchment area, north east of the Dead Sea. Environ. Earth Sci. 73 (7), 3309–3326.

Oz, I., Eyal, S., Yoseph, Y., Ittai, G., Elad, L., Haim, G., 2016. Salt dissolution and sinkhole formation: results of laboratory experiments. J. Geophys. Res. Earth Surf. 1–17.

Panno, S.V., Kelly, W.R., Angel, J.C., Luman, D.E., 2013. Hydrogeologic and topographic controls on evolution of karst features in Illinois' sinkhole plain. Carbonates and Evaporites 28 (1–2), 13–21.

Parise, M., 2008. Rock Failures in Karst. Proc. 10th Int. Symp. landslides, Xi'an. 1. pp. 275–280.

Parise, M., 2010. Hazards in Karst. Sustain. Karst Environ. Dinaric Karst Other Karst Reg. Series on Groundwater, IHP-UNESCO, Plitvice Lakes, Croatia, pp. 155–162.

Parise, M., 2015. A procedure for evaluating the susceptibility to natural and anthropogenic sinkholes. Georisk Assess. Manag. Risk Eng. Syst. Geohazards 9 (4), 272–285.

Parise, M., Lollino, P., 2011. A preliminary analysis of failure mechanisms in karst and man-made underground caves in Southern Italy. Geomorphology 134 (1–2), 132–143.

Parise, M., Perrone, A., Violante, C., Stewart, J.P., Simonelli, A., Guzzetti, F., 2010. Activity of the Italian National Research Council in the aftermath of the 6 April 2009 Abruzzo earthquake: the Sinizzo Lake case study. Proc. 2nd Int. Work. Catastrophic Sink. Nat. Anthropog. Environ. Rome. pp. 623–641.

Polom, U., Alrshdan, H., Al-Halbouni, D., Sawarieh, A., Dahm, T., Krawczyk, C., 2016. Improved Dead Sea sinkhole site characterization at Ghor Al Haditha, Jordan, based on repeated shear wave reflection seismic profiling. EGU Gen. Assem. 2016. (Vienna, Austria).

Reddish, D.J., Whittaker, B.N., 2012. Subsidence: occurrence, prediction and control. 56. Elsevier.

Salameh, E., 2016. Effects of climatic changes on surface and groundwater resources in the northwestern part of Jordan. Int. J. Environ. Agric. Res. 2 (1).

Salameh, E., El-Naser, H., 2000. Changes in the Dead Sea level and their impacts on the surrounding groundwater bodies. Acta Hydrochim. Hydrobiol. 28 (1), 24–33.

Salameh, E., Hammouri, R., 2008. Sources of groundwater salinity along the flow path, Disi - Dead Sea/Jordan. Environ. Geol. 55, 1039–1053.

Sawarieh, A., Al Adas, A., Al Bashish, A., Al Seba'i, E., 2000. Sinkholes Phenomena At Ghor Al Haditha Area - Internal Report No. 12. Tech. rep.. Natural Resources Authority, Amman, Jordan.

Shalev, E., Lyakhovsky, V., 2012. Viscoelastic damage modeling of sinkhole formation. J. Struct. Geol. 42, 163–170.

Shalev, E., Lyakhovsky, V., Yechieli, Y., 2006. Salt dissolution and sinkhole formation along the Dead Sea shore. J. Geophys. Res. 111 (B3102).

Siebert, C., Mallast, U., Rödiger, T., Ionescu, D., Schwonke, F., Hall, J., Sade, A., Pohl, T., Merkel, B., 2014. Multiple sensor tracking of submarine groundwater discharge: concept study along the Dead Sea.. EGU Gen. Assem.. 16. European Geoscience Union, Vienna, Austria, pp. 11217..

Siebert, C., Rödiger, T., Mallast, U., Gräbe, A., Guttman, J., Laronne, J.B., Storz-Peretz, Y., Greenman, A., Salameh, E., Al-Raggad, M., Vachtman, D., Zvi, A.B., Ionescu, D., Brenner, A., Merz, R., Geyer, S., 2014. Challenges to estimate surface- and groundwater flow in arid regions: The Dead Sea catchment. Sci. Total Environ. 485–486, 828–841.

Siebert, C., Mallast, U., Rödiger, T., Strey, M., Ionescu, D., Häusler, S., Noriega, B., 2014. Submarine groundwater discharge at the Dead Sea. 23rd Water Intrusion Meet. Husum, Ger. 366–370.

Smit, J., Brun, J.-P., Fort, X., Cloetingh, S., Ben-Avraham, Z., 2008. Salt tectonics in pull-apart basins with application to the Dead Sea Basin. Tectonophysics 449, 1–16.

Stein, M., Torfstein, A., Gavrieli, I., Yechieli, Y., 2010. Abrupt aridities and salt deposition in the post-glacial Dead Sea and their North Atlantic connection. Quat. Sci. Rev. 29, 567–575.

Taqieddin, S. a., Abderahman, N.S., Atallah, M., 2000. Sinkhole hazards along the eastern Dead Sea shoreline area, Jordan: a geological and geotechnical consideration. Environ. Geol. 39 (11), 1237–1253.

Ten Brink, U., Ben-Avraham, Z., 1989. The anatomy of a pull-apart basin; seismic reflection observations of the Dead Sea basin. Tectonics 8 (2), 333–350.

Tessari, G., Floris, M., 2014. Characterization and Modelling of Geological Instabilities Through Remote Sensing Techniques and Numerical Simulations. Tech. rep.. Università degli Studi di Padova, Padua, Italy.

Tharp, T., 2002. Poroelastic analysis of cover-collapse sinkhole formation by piezometric surface drawdown. Environ. Geol. 42 (5), 447–456.

Tharp, T.M., 1999. Mechanics of upward propagation of cover-collapse sinkholes. Eng. Geol. 52 (1–2), 23–33.

USGS, 2015. Corona declassified satellite imagery, url=https://lta.cr.usgs.gov/declass_1, date accessed 2015-08-13.

Walter, T., 2014. Cost Effective Aero-photogrammetry Toys at Active Volcanoes: On the Use of Drones, Balloons and Kites. EGU Gen. Assem. Conf. Abstr.. 16. European Geoscience Union, Vienna, Austria, pp. 6427..

Waltham, A., Fookes, P., 2005. Engineering classification of karst ground conditions. Q. J. Eng. Geol. Hydrogeol. 3 (1), 1–20.

Waltham, T., 2016. Control the drainage: the gospel accorded to sinkholes. Q. J. Eng. Geol. Hydrogeol. 49 (1), 5–20.

Waltham, T., Bell, F., Culshaw, M.G., 2005. Sinkholes and Subsidence: Karst and Cavernous Rocks in Engineering and Construction. Springer, Berlin, Heidelberg.

Whitman, D., Gubbels, T., Powell, L., 1999. Spatial Interrelationships between Lake Elevations, Water Tables, and Sinkhole Occurrence in Central Florida: A GIS Approach. Photogramm. Eng. Remote Sensing 65 (10), 1169–1178.

World Bank, 2016. Population growth indicator. date accessed 2016-01-14. https://data.worldbank.org/indicator/sp.pop.grow.

Yechieli, Y., Abelson, M., Baer, G., 2015. Sinkhole formation and subsidence along the Dead Sea coast, Israel. Hydrogeol. J.

CHAPTER 4

Geomechanical modelling of sinkhole development using distinct elements: model verification for a single void space and application to the Dead Sea area

Published on 23 of November 2018 in *Solid Earth* vol. 9 pp. 1341–1373.
https://doi.org/10.5194/se-9-1341-2018

Solid Earth, 9, 1341–1373, 2018
https://doi.org/10.5194/se-9-1341-2018

Solid Earth

Geomechanical modelling of sinkhole development using distinct elements: model verification for a single void space and application to the Dead Sea area

Djamil Al-Halbouni[1], **Eoghan P. Holohan**[2], **Abbas Taheri**[3], **Martin P. J. Schöpfer**[4], **Sacha Emam**[5], **and Torsten Dahm**[1,6]

[1]Helmholtz Centre – German Research Centre for Geosciences (GFZ), Section 2.1, Telegrafenberg, Potsdam, Germany
[2]UCD School of Earth Sciences, University College Dublin, Belfield, Dublin, Ireland
[3]School of Civil, Environmental and Mining Engineering, University of Adelaide, Adelaide, Australia
[4]Department for Geodynamics and Sedimentology, University of Vienna, Athanstrasse 14, Vienna, Austria
[5]Geomechanics and Software Engineer, Itasca Consultants S.A.S, Écully, France
[6]Institute of Earth and Environment, University of Potsdam, Potsdam, Germany

Correspondence: Djamil Al-Halbouni (halbouni@gfz-potsdam.de)

Received: 30 June 2018 – Discussion started: 16 July 2018
Revised: 5 October 2018 – Accepted: 23 October 2018 – Published: 23 November 2018

Abstract. Mechanical and/or chemical removal of material from the subsurface may generate large subsurface cavities, the destabilisation of which can lead to ground collapse and the formation of sinkholes. Numerical simulation of the interaction of cavity growth, host material deformation and overburden collapse is desirable to better understand the sinkhole hazard but is a challenging task due to the involved high strains and material discontinuities. Here, we present 2-D distinct element method numerical simulations of cavity growth and sinkhole development. Firstly, we simulate cavity formation by quasi-static, stepwise removal of material in a single growing zone of an arbitrary geometry and depth. We benchmark this approach against analytical and boundary element method models of a deep void space in a linear elastic material. Secondly, we explore the effects of properties of different uniform materials on cavity stability and sinkhole development. We perform simulated biaxial tests to calibrate macroscopic geotechnical parameters of three model materials representative of those in which sinkholes develop at the Dead Sea shoreline: mud, alluvium and salt. We show that weak materials do not support large cavities, leading to gradual sagging or suffusion-style subsidence. Strong materials support quasi-stable to stable cavities, the overburdens of which may fail suddenly in a caprock or bedrock collapse style. Thirdly, we examine the consequences of layered arrangements of weak and strong materials. We find that these are more susceptible to sinkhole collapse than uniform materials not only due to a lower integrated strength of the overburden but also due to an inhibition of stabilising stress arching. Finally, we compare our model sinkhole geometries to observations at the Ghor Al-Haditha sinkhole site in Jordan. Sinkhole depth / diameter ratios of 0.15 in mud, 0.37 in alluvium and 0.33 in salt are reproduced successfully in the calibrated model materials. The model results suggest that the observed distribution of sinkhole depth / diameter values in each material type may partly reflect sinkhole growth trends.

1 Introduction

Sinkholes are enclosed surface depressions in sediments and rocks. They commonly result from subsidence of overburden into void space that is generated through the physical–chemical removal of material in the underground. In the final stage of a sinkhole process, a sudden collapse of the overburden may occur (Gutiérrez et al., 2014; Waltham et al., 2005). Removal of material and void formation in the underground is usually related to hydraulic flow and to associated dissolution, physical erosion of material or both. Subsidence may occur continuously over a long time depending on the flow conditions and material properties (Goldscheider and Drew,

Published by Copernicus Publications on behalf of the European Geosciences Union.

2007; Parise and Gunn, 2007; Waltham et al., 2005). Depending on the properties of the overburden (cover or caprock) and the evolution stages, different sinkhole morphologies can be described. Typical end-members can be defined (Fig. 1; see Gutiérrez et al., 2008, 2014).

1.1 Sinkhole development at the Dead Sea

The Dead Sea is a hypersaline terminal lake and is one of the world's most active areas of sinkhole development. More than 6000 sinkholes have formed there at an increasing rate over the last 35 years (Abelson et al., 2017). Previous studies relate the sinkhole formation at the Dead Sea to the regression of the lake, which has been ongoing since the 1960s, and to the consequent invasion of evaporite-rich sedimentary deposits around the Dead Sea by relatively fresh groundwater. Evaporitic minerals in the sediments are susceptible to dissolution, while the non-evaporitic sedimentary materials are weak (poorly consolidated or unconsolidated) and can easily be physically eroded by subsurface flow ("piping"). Some studies have highlighted the role of subrosion, i.e. both mechanical and chemical (leaching) erosion of the subsurface (Wadas et al., 2016), in the development of sinkholes (Al-Halbouni et al., 2017; Arkin and Gilat, 2000; Polom et al., 2018), while others have focussed on the role of dissolution only in generating large cavity development in a relatively shallow but thick salt layer (Ezersky and Frumkin, 2013; Taqieddin et al., 2000; Yechieli et al., 2006).

In this paper, we draw upon observations from the sinkhole site of Ghor Al-Haditha (31°18′45″ N, 35°31′52″ E) on the southeastern shore of the Dead Sea in Jordan (Figs. 2, 3). Sinkhole development in the area has been active since 1986 (Sawarieh et al., 2000), with ongoing damage or destruction of infrastructure and agriculture. As of 2018, the cumulative number of sinkholes formed there has passed 1000 (Watson et al., 2018). Photogrammetric datasets have been acquired in 2014, 2015 and 2016 to produce high-resolution and high-accuracy digital surface models and orthophotos for the Ghor Al-Haditha sinkhole site. Although the results for 2015 and 2016 shown below in this paper are new, the methodology of their generation is the same as for the 2014 survey, which is described in detail by Al-Halbouni et al. (2017).

Sinkholes form in the three "end-member" near-surface materials at the Ghor Al-Haditha sinkhole site (Fig. 2): (1) unconsolidated to semi-consolidated lacustrine clayey carbonates ("mud") with interleaved thin evaporite layers; (2) unconsolidated to semi-consolidated alluvial sand–gravel sediments; and (3) rock salt (mainly halite) with interleaved thin mud layers. The main morphological distinction is that narrower and deeper sinkholes occur in the "alluvium" and in the "salt" (Fig. 3b, c), whereas wider and shallower sinkholes occur in the "mud" (Fig. 3a). Many sinkholes in the alluvium and especially in the salt have overhanging sides and/or large marginal blocks and deep (up to several metres) concentric ground cracks. The alluvium and the salt can sustain metre-scale or multi-metre cavities associated with sinkhole development (Al-Halbouni et al., 2017; Closson and Abou Karaki, 2009; Yechieli et al., 2006). The mud sinkholes commonly contain a wide peripheral zone of back-rotated blocks delimited by small faults that down-throw towards the centre. Ground cracks are commonly also well developed around sinkholes in the mud but are not as deep (up to a few tens of centimetres) as in the other materials.

1.2 Numerical modelling of sinkhole development

The numerical simulation of sinkhole development is of interest to understand better the processes of sinkhole formation and the related hazard. Continuum-mechanics approaches (Carranza-Torres et al., 2016; Fazio et al., 2017; Fuenkajorn and Archeeploha, 2010; Parise and Lollino, 2011; Rawal et al., 2016; Salmi et al., 2017) have generally defined a single cavity in an elastic or elastoplastic half space and assessed the static threshold strength of the overburden to predict mechanical failure. This approach is possibly suitable for assessing the factor of safety of an individual, fully developed cave and for deriving a relation between measured surface subsidence and cavern configuration. However, the geometries of voids involved in sinkhole development are often non-singular, irregular and distributed on lots of scales (Abelson et al., 2017; Al-Halbouni et al., 2017; Ezersky et al., 2017; Gutiérrez et al., 2016; Parise et al., 2018; Yizhaq et al., 2017). Alternatively, continuum-based corrosion models have addressed the rock dissolution and void growth in a hydrogeological framework (Kaufmann and Romanov, 2016; Shalev and Lyakhovsky, 2012). This approach has the advantage of accounting for geometrically complex or stochastic void development and the role(s) of material heterogeneity, but it does not account for effects of overburden instability. Both of these past continuum-based approaches have neglected the mechanical consequences of void growth and the explicit simulation of sinkhole collapse.

Distinct element method (DEM) modelling is increasingly used in geoscience for numerical simulation of large-strain and discontinuous rock deformation (Cundall and Strack, 1979; Potyondy and Cundall, 2004). The main advantage of the DEM is its ability to simulate rock samples or rock masses as an assemblage of discrete particles or blocks, which can undergo large displacements and rotations. The method uses a so-called soft contact approach where the particles are rigid but allowed to overlap at contact points. Based on updated particle positions, the contacts between particles are automatically detected or deleted during the simulation. Based on the relative displacement and velocity of the particles in contact, interaction laws are used to update the forces and moments transmitted through the contacts. The resultant forces and moments that accumulated on each particle are subsequently used to solve Newton's second law of motion and to update the particle's position and velocity. Elastoplastic bonds of finite strength can be accounted

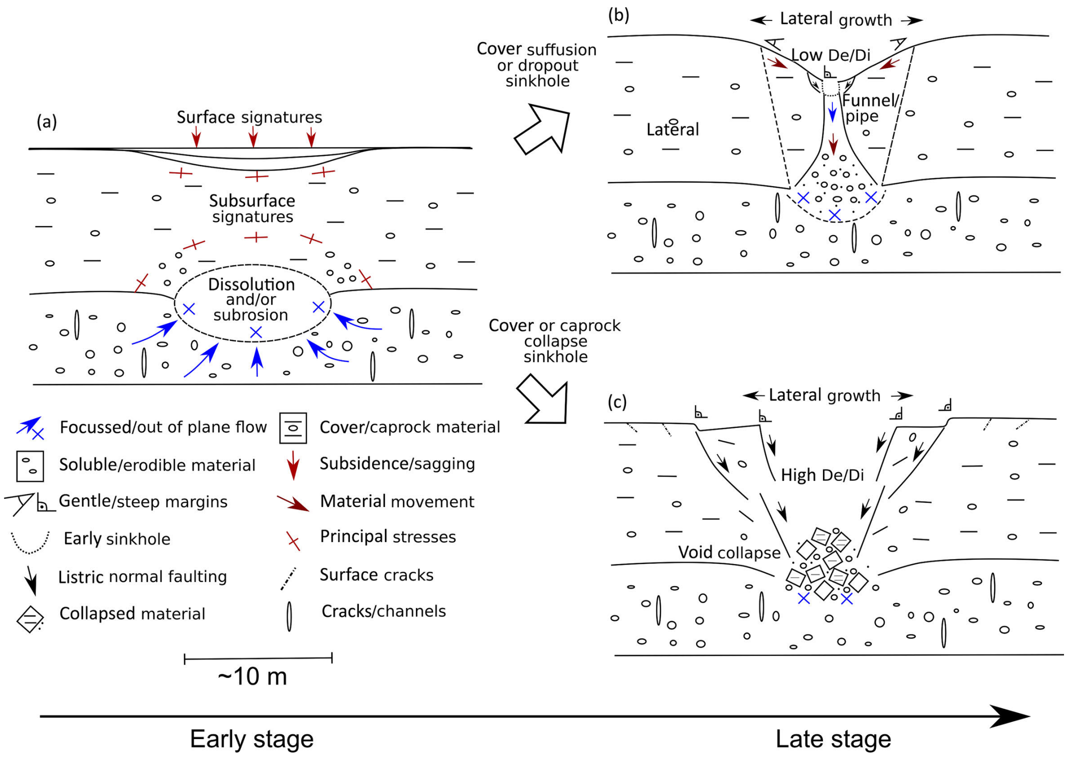

Figure 1. Conceptual models of sinkhole formation. **(a)** Subsurface dissolution and/or subrosion caused by focussed flow in soluble/weak material. **(b)** Cover suffusion or dropout sinkhole that forms by material transport through a pipe or along a funnel. A weak cover material slumps into the voids and creates a sinkhole with low depth / diameter (De / Di) ratio and flat-to-steep margins depending on the material cohesion. **(c)** Cover or caprock collapse sinkhole. Large voids may stay initially stable in a strong material, but their growth leads to a sudden overburden collapse. The formed sinkholes have usually a high De / Di ratio and contain steep margins with large ground cracks. Both sinkhole types represent late-stage end-members and mixtures of both are very common in nature (Fig. 2).

Figure 2. Sinkhole examples from the eastern shoreline of the Dead Sea. **(a)** Sinkhole with De / Di $\sim$ 0.15 formed in semi-consolidated lime-carbonate mud of the former Dead Sea bed. **(b)** Sinkhole with De / Di $\sim$ 0.33, formed in semi-consolidated sandy gravel (alluvial) sediment. Note the deep cracks and tilted blocks marginal to the sinkhole. **(c)** Sinkhole with De / Di $\sim$ 0.33 formed in semi- to well-consolidated salt material. Note the typical overhanging sides and pronounced cracks in the surroundings.

for in the interaction law and enable a quasi-continuum behaviour at assembly scale, which can evolve to highly discontinuous deformation as bonds between particles break and damage develops. In this way, the DEM can overcome limitations of continuum-based numerical simulation of large and highly localised strains in discontinuous media (Jing and Stephansson, 2007). Using the DEM, recent advances have been made in, for example, rock mechanics (Schöpfer et al., 2009), slope stability and mass movements (Thompson et al., 2010), mine or tunnel stability (Bonilla-Sierra et al., 2012), synthetic rock mass modelling (Ivars et al., 2011), fracture growth (Schöpfer et al., 2016), hydrofracture and caldera subsidence analysis (Holohan et al., 2011, 2015, 2017).

For modelling sinkhole collapse, Baryakh et al. (2008, 2009) used the DEM to conduct simple stability tests and mechanical analyses for a single, instantaneously generated cavity of varying geometry, depth and overburden mechanical properties. Other studies have adopted a similar approach but also included discrete fracture networks (DFNs) that represent predefined or empirically determined discontinuities

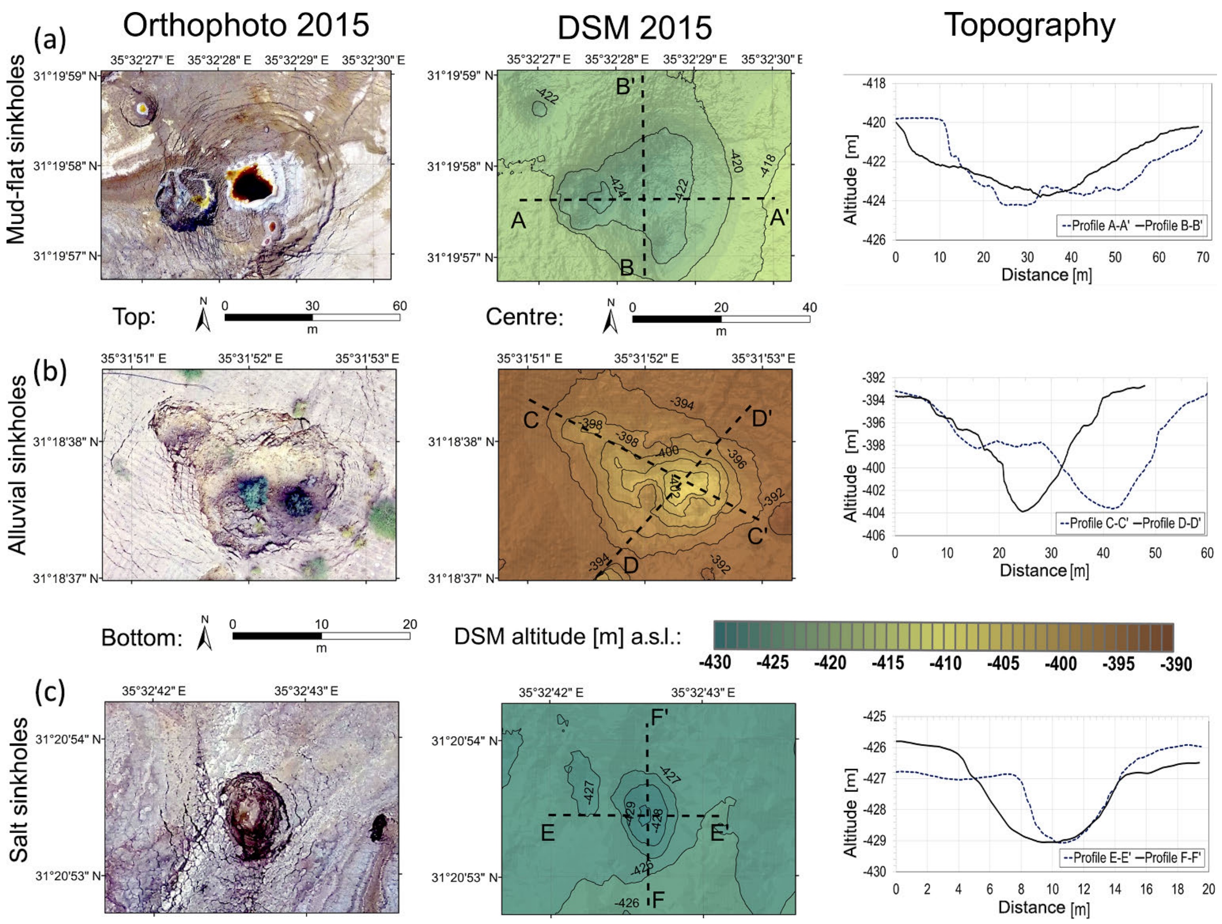

Figure 3. Representative morphological data from single sinkholes at the eastern shoreline of the Dead Sea: **(a)** in the mud flat, **(b)** in the alluvial material and **(c)** in the salt cover. Shown here are orthophotos (left column), digital surface models (DSMs, middle column) and topographic cross-sections (right column) with a resolution of 10 cm and an accuracy of 12 and 17 cm (H and V), respectively. These were created from low-altitude aerial images acquired in 2015 and processed by structure-from-motion photogrammetry. Contours of elevation in metres are indicated for clarity on the DSM, which is plotted in the same colour scale for all materials.

(joints, faults) within rock masses (Hatzor et al., 2010). DEM coupled with finite element modelling (FEM) has been used for simulating mechanical failure above a large salt cavity (Mercerat, 2007), but the DEM part was limited to a single rock layer within the overburden. Again, the main shortcoming of these earlier DEM-based studies is that cavity growth and related mechanical development were not explicitly simulated.

1.3 Contribution of this paper

This paper reports the first two-dimensional DEM simulations of sinkhole formation that explicitly simulate both void growth and overburden collapse. In part, the approach of void growth adopted here is similar to that in a recent work on mine caving (Sainsbury, 2012). Our study builds upon the previous works of Caudron et al. (2006) and Baryakh et al. (2008, 2009) but goes further in calibration of geomechanical behaviour, in complexity of process and in application to natural sinkholes. As in many previous studies, we focus here on the creation, growth and instability of a single void leading to a single sinkhole. We use the general-purpose commercial DEM Particle Flow Code in two dimensions (PFC2D) software, developed by Itasca Consulting Group Inc. (Potyondy, 2014b). Further details of the DEM, as implemented in PFC2D, are covered in Appendix A. Note that, in accordance with PFC2D convention, compressive stress is taken as negative throughout this paper.

Regarding the structure of this paper, we begin by summarising tests on model resolution, model dimensions and void creation procedures, and we show results of benchmarking to continuum-based solutions for displacement around a void. We then show the results of calibration tests that were used to tune the bulk geomechanical behaviours of the DEM particle assemblies. Following this, we analyse the evolution stages of model void growth and sinkhole collapse for uniform and layered materials. We then compare the morphological parameters at the Ghor Al-Haditha survey site to those predicted by our models. In the final part, an outlook to future improvements and applications is given.

2 A distinct element method approach for modelling cavity and sinkhole formation

In this section, we report on convergence and benchmarking tests for the DEM model as pertained to cavity generation. To this end, we firstly simulate a material that behaves elastically by using bond strength and cohesion values at the upper limit of realistic rock strengths (see Table 1). We also report on the material parameter calibration by simulated biaxial compression and tension tests applied to the numerical materials mimicking those common in the Dead Sea region. Finally, we summarise the final procedure for cavity growth that is based on these tests but implemented under conditions in which the DEM model material is weak enough to fail and lead to sinkhole formation.

2.1 Determination of the optimal void space installation and model dimensions

We tested model sensitivity to resolution, dimension and void installation method. In a first test, different void space installation methods were compared in terms of computation time. For this, surface particle displacement was tracked above a cavity of 5 m radius placed at 35 m depth (Fig. 4a), an assumed realistic subrosion zone depth and dimension. Two methods utilised a particle deletion scheme, while two other methods were based on particle radii reduction. No substantial differences in the vertical and horizontal surface displacements were observable; i.e. the methods did not affect the outcome of the elastic solution, but the particle deletion scheme was 1 order of magnitude faster than radii reduction. Hence, the particle deletion scheme was chosen as appropriate for the following tests and the sinkhole models. More details on the results and the set of investigated parameters can be found in Appendix B1.

In a second test, model width, height and particle radii were varied to determine the optimal model dimensions for the problem of a void space in the subsurface. The void installation method based on instantaneous particle deletion was applied. The final results indicates that symmetric boundaries of $H \times W = 400 \times 400\,\mathrm{m}$ with a particle mean radius of 0.32 m yield the best results. These model dimensions and resolution were hence chosen for the main model set reported below. Details on the convergence tests that led to this choice of dimensions and resolution can be found in Appendix B2.

2.2 Benchmarking of the DEM approach against analytical solutions and BEM

We performed a benchmarking of surface displacements in the DEM cavity development models with displacements derived from different continuum-based approaches. Cavity depth and size, model dimensions (Fig. 4a) and the bulk elastic parameters of the DEM material in Table 1 serve as input parameters for two analytical solutions and a boundary element (BEM) numerical model.

The analytical solutions are for a circular cavity in a gravity loaded, infinite, linear elastic full/half space under plane strain conditions (Kirsch, 1898; Verruijt and Booker, 2009). The Kirsch solution is a classical full-space solution for simple excavation shapes but does not include the free-surface effect; mathematical details are provided by Brady and Brown (2006). The Mindlin (1940) solution is for stresses around tunnels and includes free-surface effects; mathematical details are given by Verruijt and Booker (2009). The input values for the Mindlin analytical solution are $d/h = 4$, $E = 5\,\mathrm{GPa}$, $\nu = 0.39$ and $K_0 = 0.26$. The reader is referred to Appendix B3 for more details on the effect of d and E.

The BEM model is based on a code by Nikkhoo and Walter (2015) and simulates the surface displacements along a cross-section above a 3-D cylindrical void space. The void space is simulated as a traction-free, horizontal, north–south-oriented cylinder of 200 m total length. The cylinder's centroid is located exactly beneath the origin; a hydrostatic remote stress is applied equal to the gravitational stress $\sigma_{xx} = \sigma_{yy} = \sigma_{zz} = \rho g h$, where h is the depth to the cylinder centroid.

The DEM model displacements $\left(U_x, U_y\right)$ as well as the displacement differences $\left(\Delta U_x, \Delta U_y\right)$ in Fig. 5 match closely the Kirsch solution and the BEM results. For the Mindlin solution, this is only true for the horizontal components. For the vertical components, the modelled components only match the Mindlin solution in the near field of the subsidence centre, while in the far field a large disagreement is observable, expected from an intrinsic mathematical difficulty in determining the displacement of a stress-loaded half space (Appendix B3).

2.3 Model setup for cavity generation and sinkhole formation

Based on the above-described tests for model resolution, dimensions and cavity generation, a generalised setup for cavity growth with attendant fracturing and sinkhole collapse is presented in Fig. 4c. This setup comprised a $400 \times 400\,\mathrm{m}$ assembly of parallel-bonded particles of 0.32 m radius on average. The assembly is subdivided according to bond and particle contact properties into a cover material sequence that lies over a "soluble" or "mobile" material with a fixed basement rock below. The cavity is grown according to a material removal zone of arbitrary geometry, taken here as a verti-

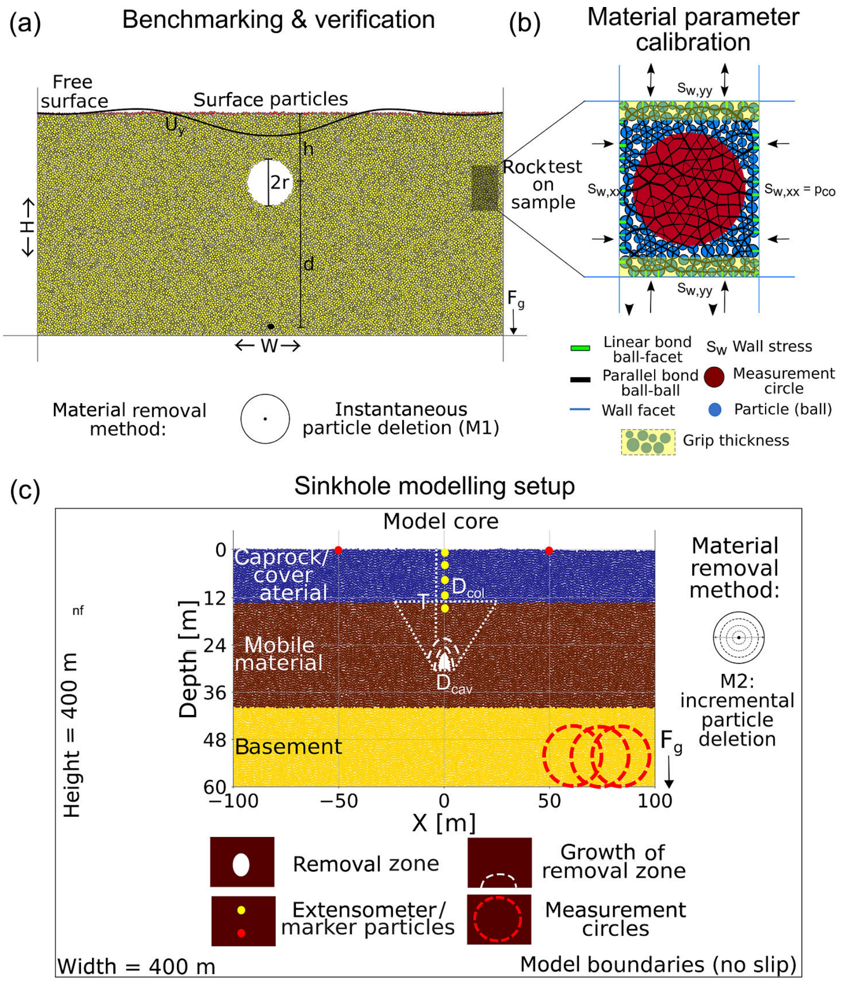

Figure 4. Setups for model benchmarking, calibration and sinkhole simulation. Panel **(a)** indicates model verification and benchmarking. A circular cavity of radius $r = 5$ m is placed instantaneously at a depth $h = 35$ m and a distance $d = H - h$ from a fixed point at the bottom of a box of varying dimensions $H \times W$ and particles of radii R subject to the body force due gravitational acceleration F_g. Panel **(b)** indicates rock tests for material parameter calibration. A sample is contained within walls that are used for applying confining pressure simulating the materials' response at different depth. A servo-mechanism controls the walls' axial velocity. For a tensile test, grips of certain thickness are defined at the bottom and top of the sample and moved outwards. **(c)** Sinkhole simulation by quasi-static incremental single void growth. T/D is referring to the overburden thickness to diameter ratio of either a stable cavity ($D = D_{\mathrm{cav}}$) or an unstable collapse zone ($D = D_{\mathrm{col}}$). Yellow/red circles represent particles that act as extensometers/markers, respectively. Big red circles indicate overlapping measurement circles distributed within an area of interest.

Table 1. Bulk properties of the particle assemblies used in the benchmarking of DEM cavity formation models vs. analytical solutions and BEM.

Bulk parameter (unit)	Symbol	Unit	Value
Porosity	n	–	0.16
Density[1]	ρ_{bulk}	$(\mathrm{kg\,m^{-3}})$	2100
Earth pressure coefficient at rest[1]	K_0	–	0.26
Young's modulus	E	(GPa)	5.337 ± 7^{-3}
Poisson ratio[2]	ν	–	0.39 ± 0.03

[1] Estimation based on measurement circles in five different particle assemblies at a depth of 35 m.
[2] Estimation based on fitting of measurement circle data in 10 different simulated rock tests.
Compare Sect. 2.4.

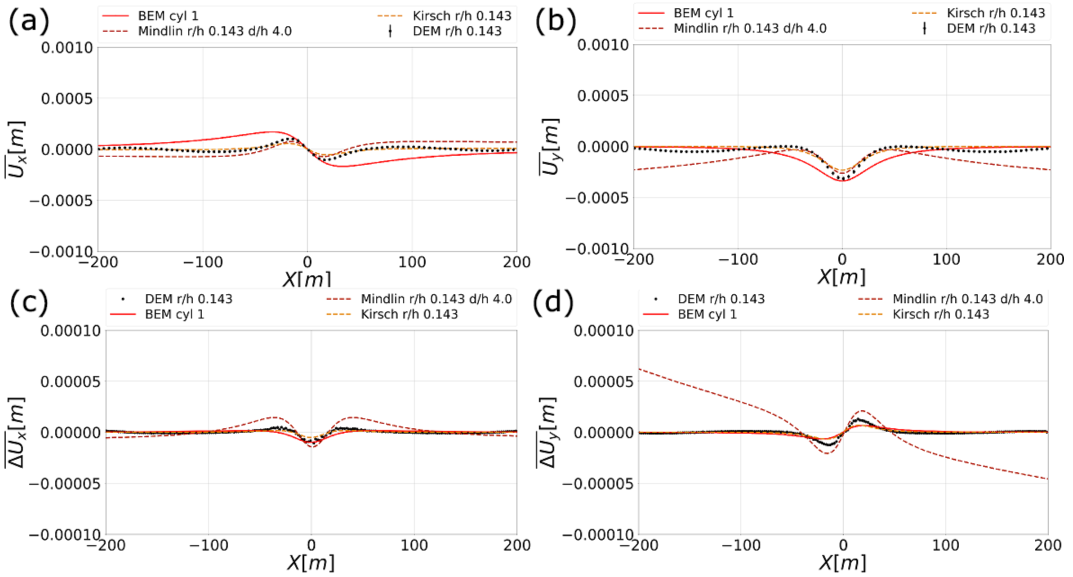

Figure 5. Results of benchmarking of the DEM cavity model against continuum-based cavity models: analytical solutions and modelled displacement curves for model dimensions of 400 × 400 m with particle radius 0.32 m. The reference is a cavity with $r/h = 0.143$, at 35 m depth and with a 5 m radius. **(a)** Horizontal displacement, **(b)** vertical displacement, **(c)** horizontal displacement difference and **(d)** vertical displacement difference.

cally orientated half ellipse, using the incremental deletion approach (M2) described above. For the technical details of the bond installation and void space creation procedure, see Appendix B5.

A key geometric parameter in subsidence studies is the ratio of overburden thickness (T) to width or diameter (D) of the undermined area before the initiation of subsidence or collapse. In the following, T/D refers to (1) thickness of the overburden/diameter of the cavity (T/D_{cav}) if materials can sustain a cavity in or around the material removal zone or (2) thickness of the strong material/diameter of the destabilised zone (T/D_{col}) if materials cannot sustain a cavity. This subsurface destabilised zone is shown arbitrarily as a triangular-shaped area in Fig. 4c. For each model setup, at least two (mostly five) different particle assemblies were run, and the errors in the following are based on these.

2.4 Calibration of the distinct element method approach for modelling sinkhole collapse at the Dead Sea

2.4.1 Bulk parameter estimation of geomaterials adjacent to the Dead Sea

The geotechnical parameters of rocks and soils commonly cover a wide range, as they depend strongly on detailed mineral composition, grain sizes, external stress conditions, fluid saturation and stress histories; cf., e.g. Brady and Brown (2006) and Jaeger et al. (2007). Here, we consider geotechnical parameters for the three main material types involved in sinkhole formation at the Dead Sea region: (1) lacustrine clayey carbonates and evaporites, (2) alluvial sands and gravels and (3) pure rock salt (halite) (Table 2).

For lacustrine mud, friction angle, cohesion, porosity and density parameters from laboratory tests are used (Ezersky et al., 2013, 2017; Frydman et al., 2008, 2014). For the alluvial sediments, upper limits are given by nearby field investigations in firm sandstone rocks (El-Naqa, 2001) and also by published values for medium-grained Quaternary sand–gravel (Carter, 1983; Manger, 1963; Taqieddin et al., 2000). The bulk modulus of alluvial sand–gravel and lacustrine clays were estimated using Poisson's ratio values from the literature (Zhu, 2010) and shear-wave velocities from recent field measurements (Polom et al., 2018), where the latter were reduced by a factor of 1.5 to account for drained conditions.

Elastic parameters and strength values of the field materials have been estimated by using tables from Brown (1981) and Hoek (2007) and by classifying the clayey mud as grade R0 in terms of intact rock consistency and the alluvial sediments as grade R0–R1. The Holocene salt rock of the Dead Sea is considered weaker than typical halite rock salt (Frydman et al., 2008, 2014) and has been classified as grade R1. The cohesion value of salt is strongly depth dependent and has been determined by using depth-normalised results derived from triaxial tests (Frydman et al., 2014) via

$$c = \frac{q \times z}{2 \times N_f}, \qquad (1)$$

where $N_f = \sqrt{\frac{1+\sin\phi}{1-\sin\phi}}$, c the cohesion, z the depth of the rock sample, q the intercept in a principal stress σ_1 (σ_3) plot and ϕ

Table 2. Estimated geomechanical properties of main materials in sinkhole-affected areas at the Dead Sea. References: Ezersky et al. (2017); Ezersky and Livne, (2013); Frydman et al. (2008, 2014); Hoek (2007); Khoury (2002); Manger (1963); Polom et al. (2018); Zhu (2010).

Parameter	Symbol	Unit	Wet lacustrine mud	Alluvial sediment	Holocene salt
Bulk density	ρ_{bulk}	($\text{kg}\,\text{m}^{-3}$)	1500–2100	1500–2300	1400–2200
Porosity	n		0.2–0.3	0.2–0.3	0.05–0.4
Friction angle	ϕ	(°)	2.4 (wet)–34 (saturated)	30–40	53
Young's modulus	E	(MPa)	83	220	300–10 000
Poisson's ratio	ν		0.2–0.4	0.15–0.35	0.2–0.4
Unconfined compressive strength	UCS	(MPa)	-0.243 to -0.053	-5 to -0.1	-5 to -1
Unconfined tensile strength*	T	(MPa)	0.0053–0.0243	0.01–0.5	0.1–0.5
Cohesion	c	(MPa)	0–0.019	0.027–1.33	0.84–1.73 (at 20–40 m depth)

*($T \sim$ UCS/10) after Hoek (1968).

the friction angle. We use a friction angle of $\phi = 54°$, depth $z = 20$–40 m and an intercept of $n = 259$ kPa for a specific rock weight of $18\,\text{kN}\,\text{m}^{-3}$ (Frydman et al., 2014). For the alluvial sediment, we assume a friction angle of $\phi = 34°$ and an UCS of 0.1–5 MPa and calculate the cohesion value by the well-known relation $c = \text{UCS}/(2N_f)$ (Jaeger et al., 2007). Modulus, friction angle and strength hereby depend strongly on the porosity distribution, while Poisson's ratio is quasi-independent of it (Schöpfer et al., 2009).

2.4.2 Calibration of DEM material properties via simulated rock tests

Bulk material parameters are determined by simulated, biaxial compression and tension tests similar to those described by Khanal and Schubert (2005) and Schöpfer et al. (2007) (see Fig. 4b). We generated material "samples" with dimensions of 10×8 m and with a mean particle radius of 0.32 m and an initial porosity of 0.2. Each sample then contains approximately 200 particles. In order to simulate the materials of the Dead Sea region, we used the microproperties listed in Table 3 and the assembly generation scheme outlined in Appendix B5.1. Note that, for the lacustrine mud material, we also implemented a re-bonding ("annealing") scheme to simulate the cohesiveness of that material. Tests were conducted with confining pressures p between 0 and -5 MPa, corresponding for a bulk density of $\sim$ 2000–2200 $\text{kg}\,\text{m}^{-3}$ to depth range of 0–250 m. Measurement circles (averaging regions as described in Potyondy and Cundall, 2004) are installed in the centre of the sample to determine the stress–strain and porosity values.

The sandy gravel and salt materials show brittle failure behaviour (i.e. a sharp post-peak stress drop) at low confining pressures, which changes to brittle–ductile behaviour for larger confining pressures (Fig. 6). Ductile is defined as the state of deformation without significant loss of strength, and the transition to this behaviour is the brittle–ductile transition (Byerlee, 1968). The salty mud material shows a brittle–ductile transition for all tested confining pressures or, more precisely, a brittle-to-cataclastic-flow transition to distinguish it from the brittle-to-crystal-plastic transition (Schöpfer et al., 2013).

Plots of the peak stress data for each confining pressure are used to estimate the bulk strength parameters according to the widely applied Mohr–Coulomb and Hoek–Brown failure criteria (Hoek, 2007; Hoek et al., 2002; Hoek and Brown, 1997) (Fig. 7). The Mohr–Coulomb failure envelopes for the compression tests are shown in Fig. 7a. If tension test results are included, a highly non-linear behaviour of the material is recorded, so that a Mohr–Coulomb envelope is partly not appropriate anymore. Consequently, a non-linear Hoek–Brown envelope is included in Fig. 7b, although it only fits well to all the data for the lacustrine mud material and to low-confining pressure data for the other materials.

The slopes of the elastic parts of the stress–strain curves are used to estimate the bulk elasticity parameters. Figure 7c shows that Young's modulus, E, increases with confining pressure (i.e. depth), while Poisson's ratio, ν, shows no trend. Tensile tests reveal lower elastic moduli and Poisson ratios than in the compression tests. An overview of the bulk material properties resulting from these calibration tests is given in Table 4. At low confining pressures, the failure envelopes for bonded particle models are non-linear – cf. Schöpfer et al. (2013). Further details and examples are found in Appendix B4.

This calibration shows that the model materials mimic the mechanical responses of the natural materials, and it builds the basis for the analysis of the specific sinkhole formation problem at the Dead Sea, as presented in the following section.

Table 3. Particle, contact and bond properties for DEM sinkhole collapse models. Note the geology convention.

Parameter[1]	Symbol	Unit	Lacustrine mud	Alluvial sediment	Holocene salt
Initial material porosity	n	–	0.2	0.2	0.2
Particle density	ρ	(kg m^{-3})	2715	2750	2500
Contact Young's modulus[2]	E_L	(GPa)	0.1	0.2	1
Contact Young's modulus at particle-wall contacts	E_{W}	(GPa)	5	5	5
Bond Young's modulus	E_{Pb}	(GPa)	0.1	0.2	1
Bond tensile strength	σ_c	(MPa]	0.1	0.5	1.0
Bond cohesion	$\acute{c}$	(MPa)	0.02	0.5	1.0
Bond friction angle	ϕ	(°)	2.4	34	54

[1] See Appendix A and Potyondy and Cundall (2004) for a detailed definition of these parameters. [2] A friction coefficient of 0.5 and a normal-to-shear stiffness ratio of 2.5 is chosen for all materials.

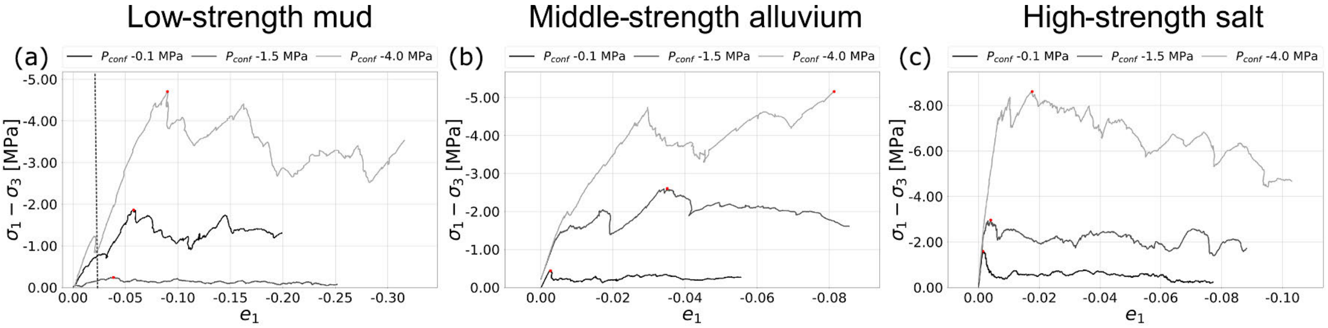

Figure 6. Differential stress vs. vertical strain plots for simulated compression tests. Confining pressures of −0.1, −1.5 and −4.0 MPa are compared that highlight the depth-dependent division into elastic, yielding and post-peak behaviour in all tested materials: **(a)** low-strength lacustrine mud, **(b)** middle-strength alluvial sediment and **(c)** high-strength Holocene salt material. Black dashed line in panel **(a)** marks the cutoff limit at $E_{yy} = -0.02$ for lacustrine mud elastic properties and peak stress estimation.

3 Results of DEM models of void growth and sinkhole collapse

3.1 Development in "end-member" Dead Sea materials

We simulated the effect of continuous material removal from a semi-elliptical subrosion zone at 20, 30 or 40 m depth below the initial surface for all three end-member Dead Sea materials. For brevity, we here report on the evolution of the models with subrosion at 30 m depth only; for the detailed evolution of all simulated configurations, see the electronic Appendix.

As shown in Figs. 8 and 9, the evolution of cavity development strongly depends on the mechanical interaction with the surrounding material. The mud is geomechanically the weakest end-member, and even the initial small cavity is not supported by it; the cavity collapses almost instantly after it is generated. Consequently, a cavity of large size (metre scale) never develops in the mud. As material is progressively removed from the subrosion zone, material from around and above the removal zone subsides gradually toward it. A column of subsiding material develops that is partly fault-bound and is characterised internally by downsagging of the overburden layering. This column grows upward until intersecting the surface, where a sag-like sinkhole forms. With further subrosion, the sinkhole grows deeper and wider as areas marginal to the subsiding column slump inwards.

In contrast, the alluvium is strong enough to sustain the cavity as it grows. The growing cavity interacts mechanically with the surrounding material, as sections of the cavity roof and walls collapse into it. Eventually, the overburden above the cavity fails abruptly, and the cavity is closed by the collapse of the overburden into it. The overburden collapse is also usually partly fault-bound with downsagging or with a more complex internal structure. The resultant model sinkhole margins are characterised initially by large and deep (metre-scale) opening mode fractures (ground cracks), inward-tilted blocks and in part by overhanging sides. With further subsidence, the inward-tilted blocks and overhanging sides tend to slump into the sinkhole's centre. The salt is the strongest end-member geomechanically, and so large stable cavities can develop within it – essentially unaffected by deformation of the surrounding material – until only a thin "bridge" of overburden is left.

The mechanical differences in the structural development are highlighted in Fig. 9. For the low-strength mud, stress

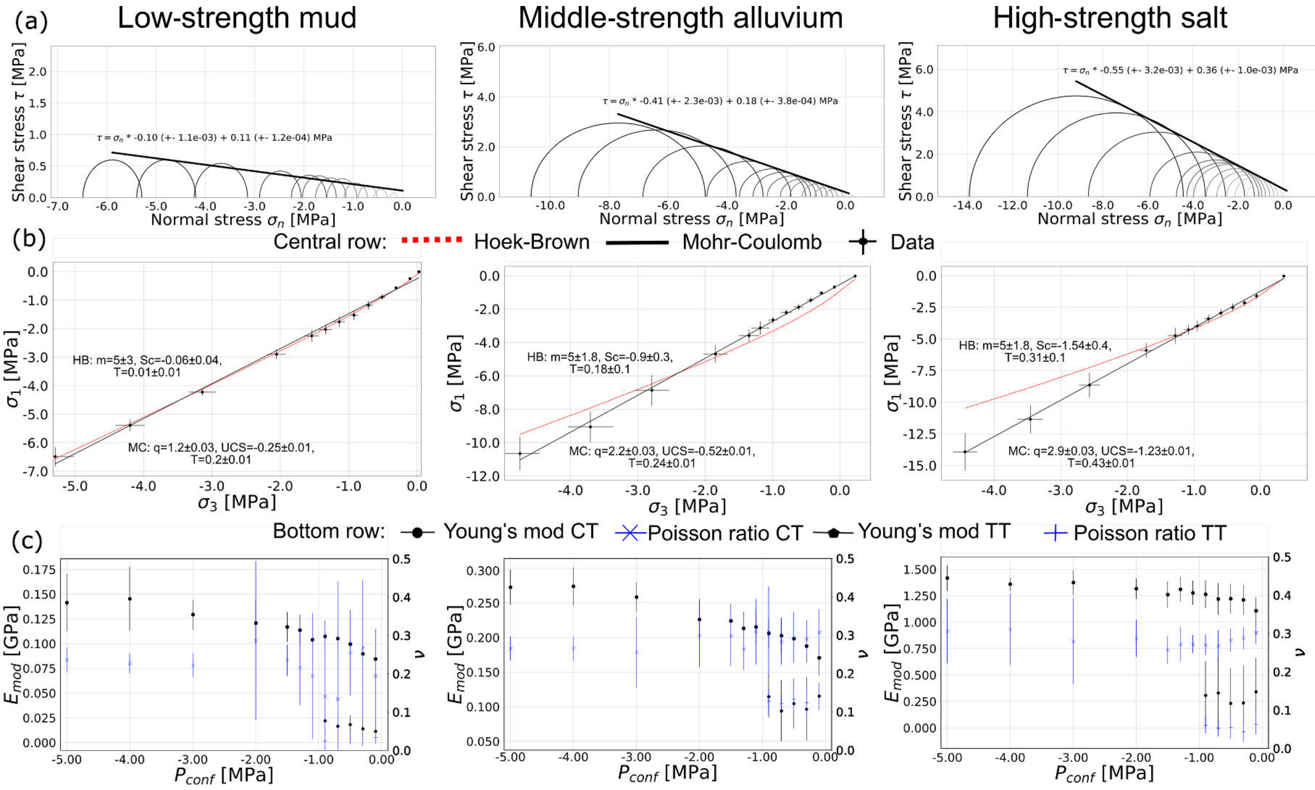

Figure 7. Bulk failure envelopes and elasticity parameters of the simulated Dead Sea materials derived from simulated laboratory tests. **(a)** Mohr–Coulomb failure envelopes, **(b)** Mohr–Coulomb and Hoek–Brown principal stress, **(c)** variation of elastic parameters with confining pressure. Left column: low-strength cohesive lacustrine mud; central column: middle-strength alluvial sandy gravel material; right column: higher-strength Holocene salt. CT indicates compression test data; TT indicates tension test data.

Table 4. Bulk material properties of the three investigated Dead Sea materials as derived by simulated rock tests and measurement circles. All values refer to unconfined conditions (i.e. at or close to the surface). Mohr–Coulomb and Hoek–Brown results are based on compression and tension tests on 10 different particle assemblies for each material.

Parameter	Symbol	Unit	Wet lacustrine mud	Alluvial sediment	Holocene salt
Particle packing porosity	n_{eff}	–	0.21	0.2	0.17
Bulk density	ρ_{bulk}	(kg m^{-3})	2145	2200	2075
Young's modulus	E_{eff}	(GPa)	0.084 ± 1.2^{-2}	0.174 ± 2.5^{-2}	1.106 ± 126^{-3}
Poisson's ratio	ν_{eff}		0.19 ± 0.12	0.31 ± 6^{-2}	0.30 ± 0.03
Mohr–Coulomb: unconfined compressive strength	UCS	(MPa)	-0.25 ± 5^{-3}	-0.52 ± 8^{-3}	-1.23 ± 1.4^{-2}
Mohr–Coulomb: unconfined tensile strength	T	(MPa)	0.2 ± 4^{-3}	0.24 ± 4^{-3}	0.43 ± 5^{-5}
Mohr–Coulomb: cohesion	c	(MPa)	0.11 ± 1.2^{-4}	0.18 ± 5^{-4}	0.36 ± 1^{-3}
Mohr–Coulomb: friction angle	ϕ	(°)	5.7 ± 0.06	22.3 ± 0.17	28.8 ± 0.18
Hoek–Brown: unconfined compressive strength	UCS	(MPa)	-0.06 ± 0.04	-0.92 ± 0.28	-1.54 ± 0.41
Hoek–Brown: unconfined tensile strength	T	(MPa)	0.01 ± 0.01	0.18 ± 9^{-2}	0.31 ± 0.14
Hoek–Brown: ratio compressive/tensile strength	UCS / T	(MPa)	6.0	5.1	5

arching, which tends to stabilise the overburden, is weakly developed around the material removal zone and within the overburden. Stress arching is well developed around and above the cavity in the alluvium, although the absolute values of shear stress are high on the cavity's lateral walls, suggesting that these areas are most susceptible to failure. The stress arch is disrupted upon final failure of the overburden and formation of a sinkhole. In the strong salt, stress arching is best developed and persists even after the thin "bridge" of the remaining overburden fails.

3.2 Development in layered Dead Sea materials

We also simulated the effect of continuous material removal from a semi-elliptical subrosion zone at 20, 30 or 40 m depth below the initial surface for layered combinations of the end-member Dead Sea materials. The models comprise a layer of either alluvial sandy gravel or rock salt (0–13 m depth) overlying a lacustrine mud layer (13–40 m depth), followed by the alluvium/salt as a basement, respectively. For brevity, we again report on the evolution of the models with subrosion at a depth of 30 m only (Figs. 10 and 11); for the detailed evolution of all simulated configurations, see the Supplement.

In general, for layered materials with mud as the subrosion-affected interlayer, the ground tends to fail clearly earlier than for the uniform materials. The mud cannot sustain large cavities and hence fails immediately upon material removal, and the upper mud layers bend. This leads consequently to the development of a cone-shaped underground collapse zone. In alluvium on lacustrine mud, a small subsidence may be noted before collapse and cracks appear even at a certain distance from the main area. Note also the development of ephemeral cavities at the interface with the mud and/or within the alluvium or salt top layers, as deformation migrates upward toward the surface. After the collapse, large and small rotated blocks slump towards the centre, and opening cracks grow downwards to a depth of 12 m around the collapse zone. These blocks define the base of the formed sinkholes. Although salt has double the strength of alluvium, the shapes of the sinkhole for these multilayer models do not differ much, but a small tendency to more overhanging sides is observed. For the condition of lacustrine mud on rock salt, the salt layer sustains large cavity formation, but as soon as the void space reaches ~ 2 m below the mud border, the material collapses. The formed sinkhole is a mixture of typical end-member types mentioned in Sect. 1.

As shown in Fig. 11, the mechanical effect of the weak mud layer is to inhibit the development of stable stress arching in the overburden. Where the weaker layer lies below the stronger layer, the development of a collapse zone is indicated as a zone of low stresses, around and above which a stress arching is weakly developed. Effectively, this subsurface collapse zone is mechanically similar to a large cavity. The lack of support from the weak layer concentrates stress in the stronger layer (note the high magnitude of shear stress there), pushing the strong layer toward failure. Where the weak layer overlies the strong layer, the stress arch is well developed until the cavity growth nears the weaker layer. The weaker layer cannot sustain the stress arch, and so the overburden collapses.

3.3 Effect of subrosion zone depth

As shown in Fig. 12, the variation of depth of the subrosion zone changes the morphology of the sinkholes. For more details, refer to the electronic Appendix. The removed material in the subrosion zone is assigned a removed "volume" ΔV, which is based on the area of the removed disk-shaped particles and its unit thickness; see Appendix A.

In lacustrine salty mud, for all subrosion depths, the sinkhole collapse is gradual with continuous subsidence. The deeper the subrosion zone, the lower the vertical displacement at the surface, and a greater amount of material needs to be removed before an effect is visible at the surface ($\Delta V \sim 80\,\mathrm{m}^3$ for deep vs. $\Delta V \sim 50\,\mathrm{m}^3$ for shallow). For a shallow subrosion zone, the sinkholes are V shaped with partly steep margins. For middle subrosion zones, the sinkholes exhibit a compressed V shape with both flat and steep margins. In contrast, the deep subrosion zone leads to bowl-shaped sinkholes with flat sides.

In the homogeneous alluvium models, the sinkhole collapse process varies between sudden (shallow material removal zone) and partly gradual (deep zone). For a shallow subrosion zone, the collapse occurs relatively late at a removed material volume of $\Delta V \sim 400\,\mathrm{m}^3$. A long-term stable cavity, also asymmetric (see Fig. 8), can reach the immediate subsurface, and no precursory cracks at the surface appear. The final sinkhole is A shaped with overhanging sides. A deep subrosion zone causes cracking in the overlying layers and at the surface together with subsidence before gradual collapse occurs, commencing relatively early at $\Delta V \sim 80\,\mathrm{m}^3$. The final sinkhole is V shaped.

In homogeneous rock salt models, for all subrosion depths, the sinkhole collapse is sudden and occurs after large amounts of material are removed. The sinkholes that form are in all cases A shaped. No surface subsidence can be observed before the collapse, as the void spaces stay stable up to the immediate subsurface. For a shallow subrosion zone, the cavity fails very late at $\Delta V \sim 400\,\mathrm{m}^3$, for a middle subrosion zone at $\Delta V \sim 900\,\mathrm{m}^3$ and for a deep subrosion zone at $\Delta V \sim 1500\,\mathrm{m}^3$. The latter shows pronounced spalling at the sides of the cavity. The shallow model only fails because the material left is of minute thickness.

For the multilayer model alluvium on mud with alluvial basement, the collapse in all cases happens earlier than in pure alluvial material and is sudden. For a shallow subrosion zone, the sinkhole forms at $\Delta V \sim 240\,\mathrm{m}^3$; for middle and deep subrosion zones, it forms at $\Delta V \sim 80$–$100\,\mathrm{m}^3$, with little subsidence before collapse onset. For middle and deep subrosion zones, the formed sinkhole is initially narrower

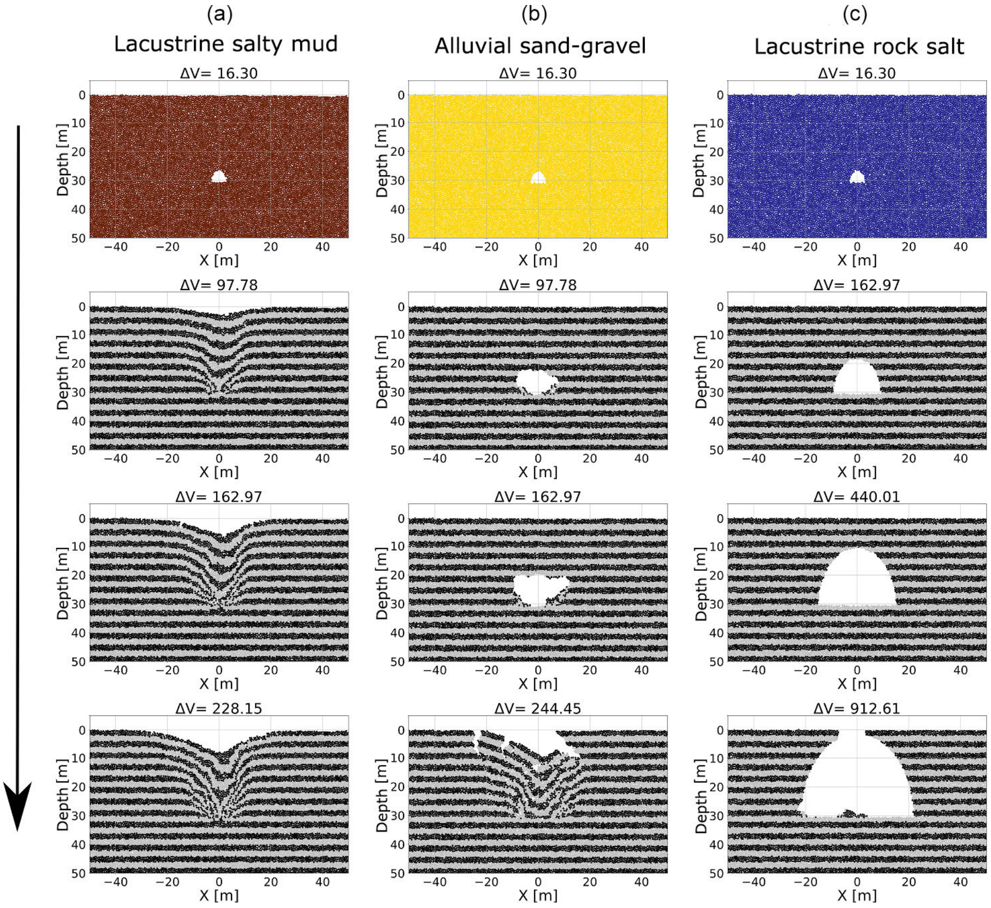

Figure 8. Evolution of DEM model cavity growth and sinkhole collapse in end-member Dead Sea materials. Shown here are selected stages in the development of cavity/sinkhole in salty mud **(a)**, alluvium **(b)** and rock salt **(c)**. The top row shows the initial cavity growth stage for each material. The layering in the other rows defines passive markers and does not represent any change in material properties.

but widens with continued material removal. For the shallow zone, this does not happen due to lack of material.

Similar features are observed for the multilayer model salt on mud; the collapse in all cases happens earlier than in pure salt material and is sudden. The removed volume before collapse is similar to results from alluvium on mud; namely, for a shallow subrosion zone the sinkhole forms at $\Delta V \sim 240\,\mathrm{m}^3$; for middle and deep subrosion zones, it forms at $\Delta V \sim 80$–$120\,\mathrm{m}^3$, with little pre-collapse subsidence and compression ridges. The sinkhole morphologies are similar to the ones for alluvium on mud, but a tendency to larger block size and a more pronounced overhanging is observed.

3.4 Thickness-to-diameter ratio at the onset of collapse

Figure 13a shows the estimated T/D ratios at the onset of the collapse (T/D_{crit}) for all model setups independent of the subrosion zone depth. A collapse hereby is defined when both particle movement at the surface and in the subsurface occurs. A distinction for the different involved materials is found. Pure lacustrine mud models generally fail at higher ratios of $T/D_{\mathrm{crit}} \geq 0.5$ than the majority of the other models. Multilayer models with mud underlying alluvium or salt show low $T/D_{\mathrm{crit}} \leq 0.5$, while pure alluvium or salt models have the highest and lowest measured values, respectively. A collection of the mean values is given in Table 5. The deeper the subrosion zone in both multilayer and uniform material models, the less material needs to be removed to trigger a collapse (Fig. 13b).

4 Comparison with data derived from photogrammetry at Ghor Al-Haditha sinkhole site

4.1 Surface displacement

In Fig. 14, we compare the topographic profiles of sinkholes derived from photogrammetric studies at Ghor Al-Haditha (see Sect. 1, Fig. 3) with our results from DEM sinkhole modelling. In Fig. 14a, we show the simulated sinkhole morphologies for different evolution stages for a subrosion zone with intermediate depth (30 m). To facilitate the comparison,

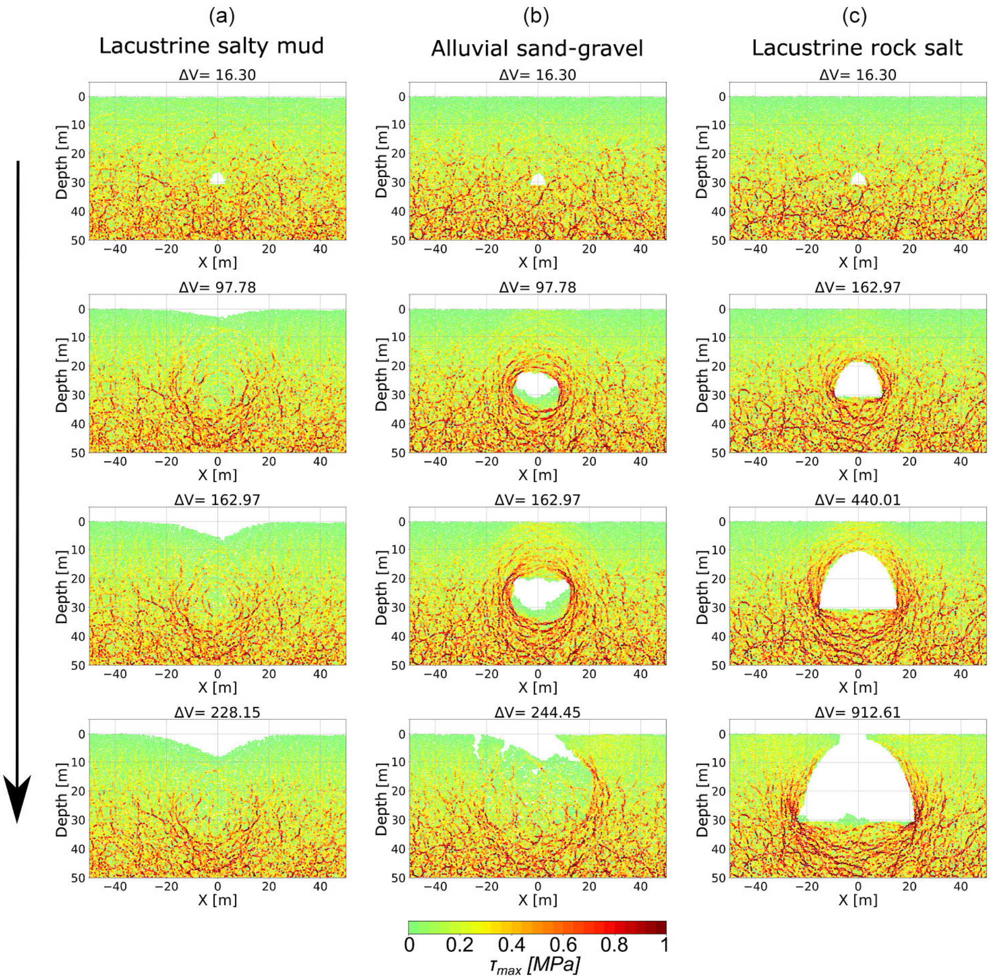

Figure 9. Evolution of maximum shear stress during cavity growth and sinkhole collapse in end-member Dead Sea materials. Shown here are selected stages in the development of cavity/sinkhole in salty mud **(a)**, alluvium **(b)** and rock salt **(c)**. The same model setups as in Fig. 8 are used.

Table 5. Critical thickness to diameter ratios for modelled sinkhole collapse onsets. The error is based on the mean between different particle assemblies for each setting.

Subrosion zone depth/ modelled material setup	Lacustrine mud	Alluvium	Salt	Alluvium on mud	Salt on mud	Mud on salt
Shallow	0.66 ± 0.01	0.06 ± 0.05	0.02 ± 0.01	0.22 ± 0.05	0.17 ± 0.1	–
Middle	0.57 ± 0.05	0.5 ± 0.29	0.03 ± 0.03	0.32 ± 0.08	0.48 ± 0.15	0.43 ± 0.1
Deep	0.57 ± 0.02	0.97 ± 0.1	0.08 ± 0.01	0.27 ± 0.06	0.51 ± 0.03	–

the topographic profiles derived by photogrammetry have been normalised and the axes have been adjusted to the same dimensions as for the models (Fig. 14b). An impressive similarity can be found for these sinkhole end-members both in terms of lateral extent and subsidence amplitude: (1) the mud sinkhole in the field appears to be of an early-stage sinkhole but with a larger extension laterally; (2) the alluvium sinkhole shape is remarkably similar to the late-stage (evolved) modelled sinkholes both laterally and vertically; (3) the salt sinkhole is comparable to the respective simulation result for an early-stage salt sinkhole.

These findings are essentially confirmed by knowledge about the rather recent development of the sinkholes selected in the mud and salt flats and the older, more evolved sinkholes in the alluvial fan of Ghor Al-Haditha (Al-Halbouni et al., 2017). Our models, which are based on realistic material parameter estimation, hence reproduce the topographic features of the sinkholes successfully in the field site. This result

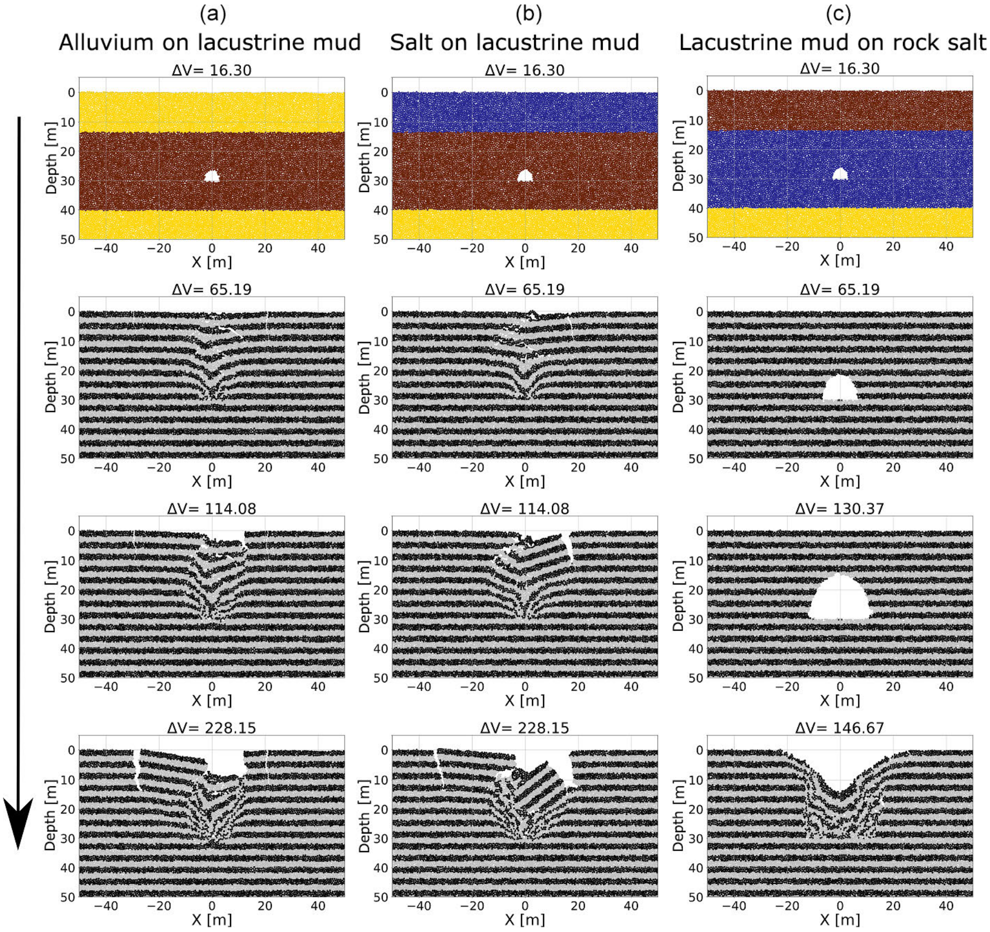

Figure 10. Evolution of DEM model cavity growth and sinkhole collapse in layered configurations of the end-member Dead Sea materials. Shown here are selected stages in the development of cavity/sinkhole in salty mud overlain by alluvium **(a)**, salty mud overlain by rock salt **(b)** and rock salt overlain by salty mud **(c)**. The top row shows the initial cavity growth stage for each material. Note that the initial cavity again closes rapidly in the mud, leading to a broader zone of subsurface instability.

is even better reflected in the De / Di analysis described in the following section.

Sinkhole depth / diameter ratios

In Fig. 15, we compare the sinkhole depth / diameter (De / Di) ratios for the DEM models and for natural equivalents at the Ghor Al-Haditha field site. We use results from the models with uniform lacustrine mud from the layered models of alluvium on mud for different stages of collapse (early, middle and late). Figure 15 does not include data for salt-on-mud layered models, as natural equivalents were not mapped by Al-Halbouni et al. (2017), but the De / Di ratios for these models are given in Table 6 and are generally similar to those in alluvium-on-mud models. Mean values of De / Di are 0.37 ± 0.15 for alluvium, 0.15 ± 0.02 for mud and 0.33 ± 0.11 for salt, and close to the statistical estimates given by Al-Halbouni et al. (2017) and to the examples shown in Fig. 2.

In simulations with uniform mud material, the fit to the De / Di data is good in the early and intermediate stages of collapse (Fig. 15a). For the late stages of these models, the model De / Di ratios are at the outer bound of the natural range. Conversely, in simulations with alluvium-on-mud material, the fit to the De / Di data is better in the intermediate and early stages of collapse (Fig. 15b). For the early stages in alluvium, the results are at the lower margin of the depth.

5 Discussion

5.1 Comparison to previous DEM and non-DEM studies of cavity generation and sinkhole collapse

Baryakh et al. (2008, 2009) used the DEM to investigate the effect of depth, geometry and mechanical properties on the collapsed state in karst. Their approach is to some extent similar to ours; however, essentially only the position of a rectangular or an arched cavity was varied for different uncalibrated

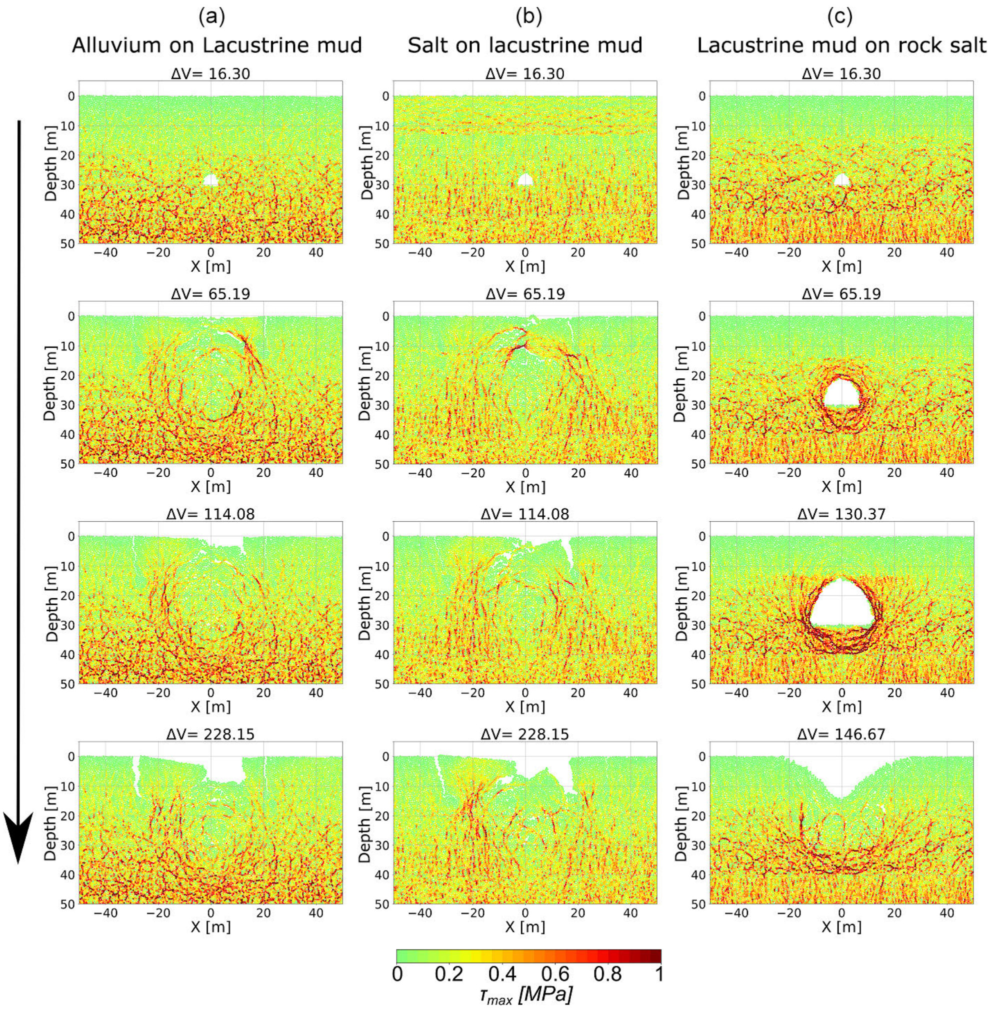

Figure 11. Evolution of maximum shear stress during cavity growth and sinkhole collapse in layered configurations of the end-member Dead Sea materials. Shown here are selected stages in the development of cavity/sinkhole in salty mud overlain by alluvium **(a)**, salty mud overlain by rock salt **(b)** and rock salt overlain by salty mud **(c)**. The same model setups as in Fig. 10 are used.

Table 6. Depth / diameter ratios for modelled sinkhole collapses. A set of five models for each material combination is analysed for a subrosion zone at middle depth (30 m). De / Di ratios for alluvium and salt are generally higher than for mud.

Collapse stage	Removed volume (m^3)	Lacustrine mud	Alluvium on mud	Salt on mud
Early	100	0.09 ± 0.01	0.13 ± 0.06	0.08 ± 0.05
Middle	160	0.13 ± 0.02	0.25 ± 0.1	0.21 ± 0.08
Late	220	0.15 ± 0.02	0.37 ± 0.15	0.33 ± 0.11

materials. In contrast, our numerical simulations allow for a mechanical interaction of a slowly growing void space with the surrounding rock and provide calibrated bulk rock parameters. Consequently, the material removal either creates a cavity or not, leading to variably shaped subsurface collapse zones, details of which are elaborated on later. Hatzor et al. (2010) used jointed blocky rock mass (DFN) modelling to define stability criteria (T/D ratios) for a rectangular cavern in high-strength (UCS > 10 MPa) rocks. One conclusion of their study, namely the conservative $T/D = 1.0$ for large cavity sizes, may also apply to our results for homogeneous, relatively weak rock and cohesive soil models. Nevertheless, the stability depends strongly on the collapse zone geometry, and the well-known stability limit for deep-seated excavation from Terzaghi (1946) does not hold for our shallow collapse zones. A FEM approach from Shalev and Lyakhovsky (2012) addresses sinkhole formation by utilising viscoelastic rheology with a damage model. It is applied to the sinkhole hazard

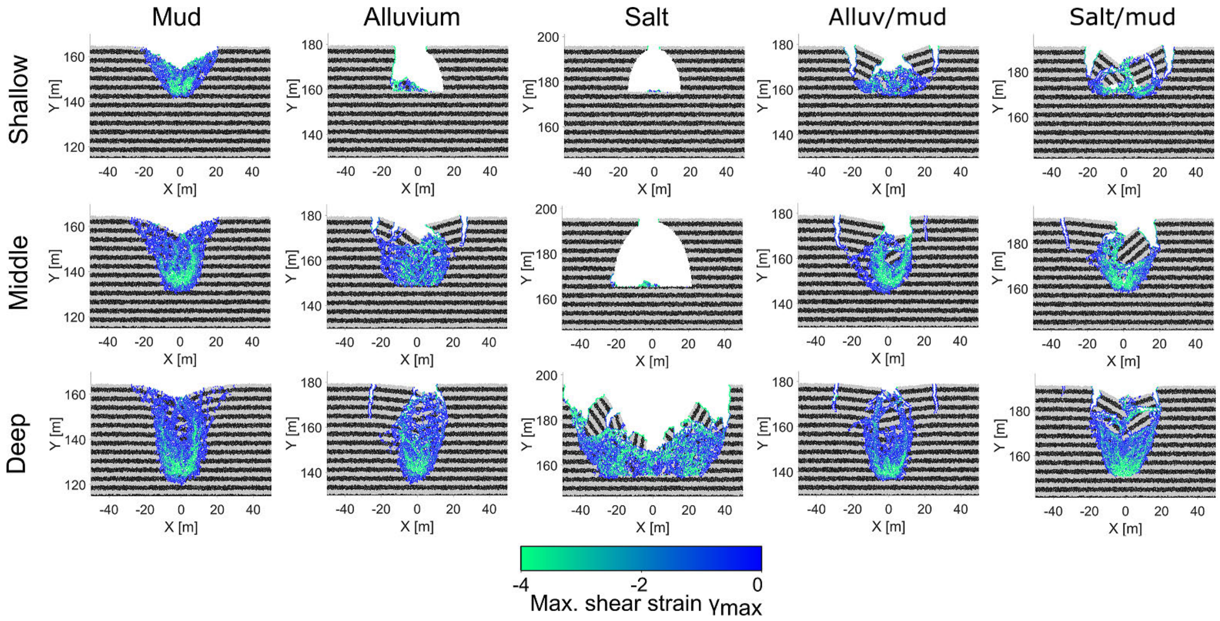

Figure 12. Sinkhole end-members in dependency of the depth of the subrosion zone for all material combinations investigated in this study. The maximum shear strain is used to visualise the collapse zone.

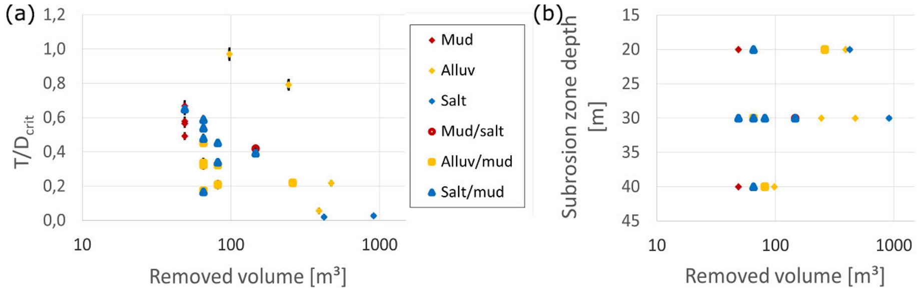

Figure 13. Parameters at the onset of collapse. **(a)** Thickness to diameter ratio vs. removed volume at the onset of collapse. Note that the T/D_{crit} ratio is either referring to the (stable) subsurface cavity or the (instable) subsurface collapse zone. Red colours stand for mud, orange for alluvial material and blue for salt and the respective multilayer models. **(b)** Removed volume at the onset of collapse in dependency of the subrosion zone depth.

at the Dead Sea and relates the different deformation modes (viscoelastic vs. brittle) to the different mechanical properties of the involved materials (mud vs. alluvium) and their common morphological characteristics. However, no field data comparison is given, and sinkhole formation is only simulated using a simplified cavity geometry that does not evolve.

In summary, earlier studies lack a detailed calibration of the model strength parameters to field and laboratory estimates, and quantitative comparisons of model results with measured data are limited or absent. Our study hence fills this important gap and explicitly simulates cavity growth and related sinkhole development and therefore provides a significant advance in this field.

5.2 Model testing, and benchmarking and limitations

Our tests and model benchmarking provide several new insights for undertaking the simulation of karstic void development and sinkhole collapse under gravity with the DEM. As expected, there is a strong sensitivity of model results (displacement) not only to parameters such as model dimensions and resolution but also to model shape, with the best results attained for relatively high-resolution and equidimensional model setups. Our tests also show that the method of cavity generation has only a minor impact on the surface displacement pattern. Cavity generation by particle deletion differs from generation by particle radius reduction mainly in the much longer model runtime for the latter. This is reasonable given the elastic and quasi-static conditions of the DEM test models. By such tests, we infer that the models with non-

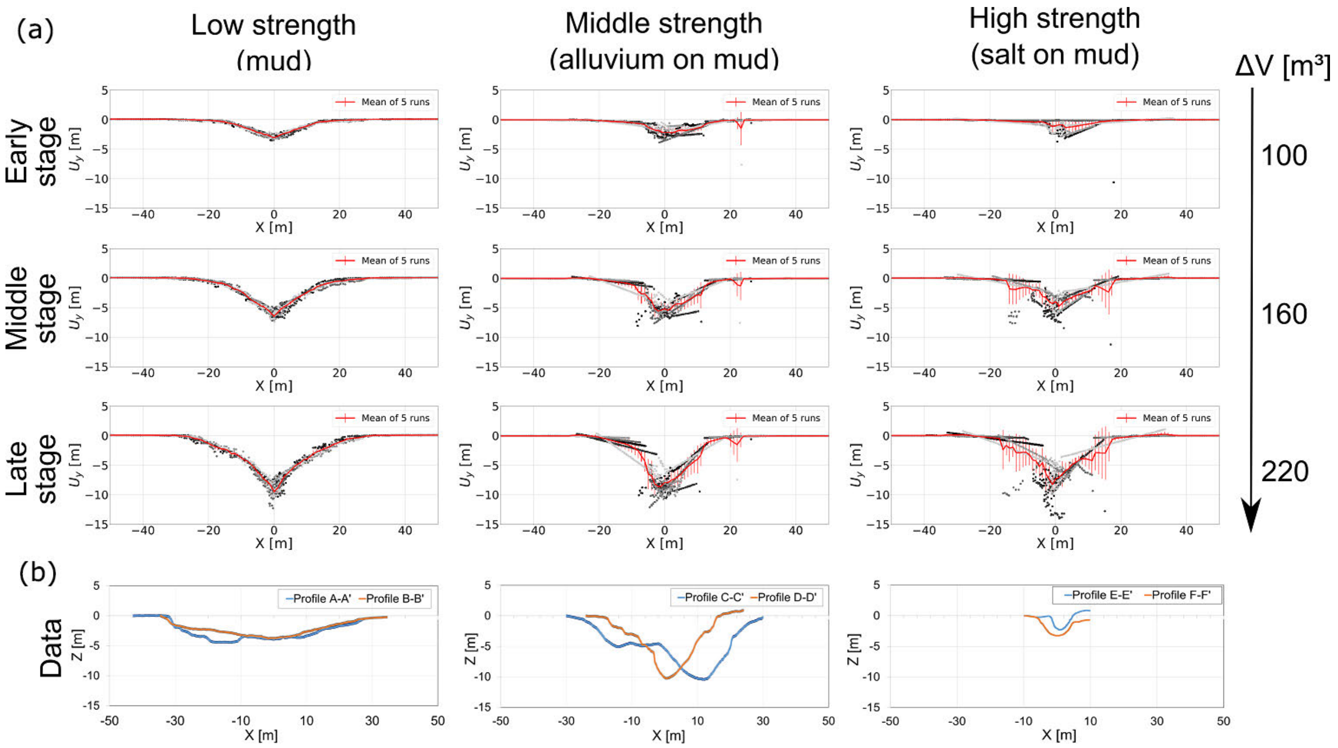

Figure 14. Topographic cross-sections of sinkholes in different cover materials. **(a)** Modelled profiles for subrosion zones in 30 m depth and three different evolution stages. Plotted is the vertical position of the surface particles for five different particle assemblies of each tested model setup. Model sets are pure lacustrine mud (left row), alluvium on mud multilayer (middle row) and salt on mud multilayer (right row). **(b)** Field data replotted topographic profiles of the three different sinkhole morphologies from Fig. 3. The distance and altitude are normalised for better comparison with the models.

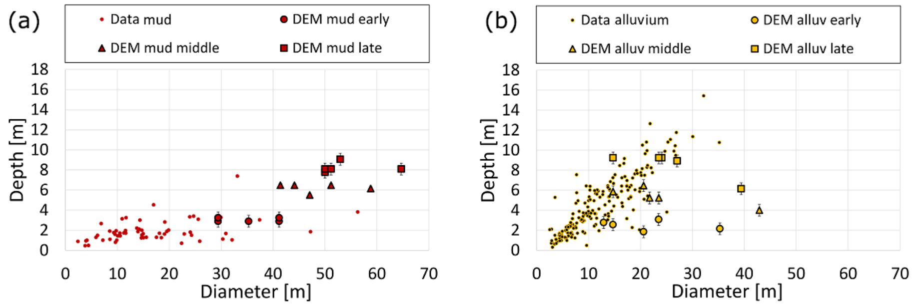

Figure 15. Sinkhole depth / diameter ratios from photogrammetry (Al-Halbouni et al., 2017) and DEM model results of this study. For field data, depth and diameter for the materials alluvium and mud were determined for 237 sinkholes. The mean values are 0.4 ± 0.11 for sinkholes in alluvium and 0.14 ± 0.04 for those in mud. No field data were available for salt at the time of this study. For the models, we distinguish between early collapses (circles), middle collapses (triangles) and late collapses (squares); **(a)** mud-flat sediments and lacustrine mud models, **(b)** alluvial sediments and multilayer alluvium on lacustrine mud model results.

elastic deformation (i.e. cavity wall failure and sinkhole collapse) are also insensitive to cavity generation method as long as they are run under quasi-static conditions, as was the case in our study.

In the benchmarking tests, the DEM surface displacements for a circular cavity in a gravitationally loaded elastic material closely resemble those predicted by the BEM model and the Kirsch solution both in the far and near fields of the subsidence centre (see Fig. 5). A perfect match is not expected, despite our efforts to compare like for like, having in mind the intrinsic differences between these models in terms of material properties and boundary conditions. The Kirsch results nonetheless provide the best match to the DEM results for both vertical displacement and displacement differences. Overall, the DEM and Kirsch curves fit in the near field and behave similarly and realistically (tendency to zero) in the far field. The BEM models offer a plane-strain solution for a hydrostatic remote stress, while the two-dimensional DEM model does not consider out-of-plane stress–strain and additionally has before cavity creation a horizontal to vertical stress ratio K_0 equal to $\sim 1/4$. This leads to the generally narrower vertical and horizontal displacement curves in the DEM models at the centre of the subsidence area. The mismatch to the Mindlin solution is greatest in the far-field displacements; these displacements as predicted by the Mindlin solution seem unrealistic given that they progressively increase away from the cavity. Consequently, for the purposes of this work and in light of the minute differences between the DEM results and the BEM/analytical solutions (sub-millimetre for displacements and micrometer for displacement differences, except for the Mindlin solution in the far field), we consider the DEM model approach here to be a valid numerical approximation of the problem.

The manner of cavity growth and its timing relative to collapse are, of course, simplified approximations to complex processes of dissolution and mechanical erosion of the subsurface as they occur in nature. The model cavity grows by instantaneous and repeated material removal of the same volume within a domain of simplified shape. In reality, cavity growth may occur on extremely long to relatively short timescales, depending on the nature of the materials (e.g. limestone vs. salt) and hydrogeological conditions (e.g. porous flow, conduit flow, dripping, flash floods). The cycling to quasi-static equilibrium during each model growth increment ensures, however, that cavity growth rate is smaller than or equal to collapse rate, as expected in nature. An improvement will be to adjust the cavity area growth function to follow typical dissolution laws (cf. Dreybrodt and Kaufmann, 2007; Kaufmann and Romanov, 2016) and thus to develop more complex and realistic cavity geometries.

5.3 Geomechanical parameter calibration

The outcomes of the simulated compression and tension tests (Table 4) closely agree with literature values and estimations from geotechnical studies and seismic velocity measurements (Table 2), in terms of UCS ranges, bulk densities, Young's modulus and Poisson ratios. The friction angles of the simulated sand–gravel and rock salt materials are slightly lower than the desired values but fit well in the case of the low-strength lacustrine clay material. Low-friction angles are typical for bonded particle models (cf., e.g. Schöpfer et al., 2017), because both sliding and rotation of particles accommodate bulk deformation; with the contact model used in the present study, the latter cannot be inhibited even with large friction coefficients. It is well known from other DEM studies that UCS / T ratios in bonded-particle materials are lower when compared to natural rock (UCS / $T \sim 10$) and soils (UCS / $T \sim 8$; Koolen and Vaandrager, 1984), reflecting the discretisation by means of circular/spherical particles (Schöpfer et al., 2007, 2009).

The Mohr–Coulomb and Hoek–Brown failure envelopes (Fig. 7) fitted to the calibration data serve as guides to the material behaviour. These envelopes were chosen as they are widely used in geomechanics, and so the overall behaviour of the model materials is readily assessed from them. In detail, however, neither envelope provides a perfect fit to the calibration results. This may be a consequence of the timing of confinement of the particle assembly, which is here done before installing the parallel bonds. Our results indicate that this may lead to some stress-path-dependent behaviour that is more complex than can be represented fully by either Mohr–Coulomb or Hoek–Brown envelopes. A thorough exploration of such complexities is well beyond the scope of this paper, but it could be subject of future work.

It is well known that the relationship between field-scale rock parameters and those determined at the laboratory sample scale depends strongly on the degree of fracturing or alteration of the rock mass (Schultz, 1996). Given that the materials we studied are of rather low strength and are weakly consolidated materials (in contrast to hard karst rock in which sinkholes often form), we neglected the effect of pre-existing weaknesses (e.g. tectonic fractures). We hence adopted literature values for salt and mud derived from laboratory-scale measurements. A poorly understood effect in the Dead Sea materials is, however, the influence of water content which may lead to time-dependent geomechanical behaviours (see Shalev and Lyakhovsky, 2012) that is not accounted for in our models. In principle, however, the modelling scheme we developed could be adapted to account for time-dependent (e.g. viscoelastic) material behaviour.

5.4 General implications for cavity and sinkhole formation

5.4.1 Structural or morphological features of sinkholes

The DEM models of sinkhole collapse show a wide range of structural or morphological features that are found at natural sinkholes, and they highlight how these features reflect the mechanical properties of the material in which the sinkholes form. Similar near-surface structural features are found at volcanic collapse calderas and pit craters, and similar explanation in terms of mechanical properties of the near-surface materials have been proposed (Holohan et al., 2011; Poppe et al., 2015).

In relatively weak materials (here the simulated "mud"), the near-surface strain is distributed across many small fractures, such that there is no sharp margin to the sinkhole. Subsidence at the surface develops gradually before the collapse develops (if at all) and the material's response is brittle–ductile. The sinkhole also widens gradually as it deepens. Overall, the sinkhole formation process is similar to classic "cover sagging" or "cover collapse" with partial suffusion (cf. Gutiérrez et al., 2008).

In relatively strong materials (here the simulated "alluvial sand–gravel" and "salt"), the strain is localised on fewer but larger fractures that develop as faults (shear fractures) and/or deep cracks (opening-mode fractures). Structures like compression ridges form in the centre of the subsidence area. Sinkhole margins in such materials are consequently sharp, steep and, at least initially, overhanging. Any subsidence before collapse is slight, although this depends partly on material rigidity (i.e. modulus); the material's response is brittle. The sinkhole also widens as it deepens but in more of a stepwise manner as new marginal fractures form and delimit marginal blocks. Overall, the collapse style is similar to classic "caprock collapse" or "bedrock collapse" (see Gutiérrez et al., 2008). In extremely strong materials, there may be little or no collapse at all – in the limit, the hole may result simply from the intersection of an essentially stable, growing cavity with the ground surface.

5.4.2 Stability of cavities and relationship to sinkhole geometry

The stability of cavities in the DEM models is clearly related to the strength of the material and to the depth of the material removal zone. In general, the cavity stability depends on a combination of material strength (UCS, T, friction coefficient) and geometric properties (cavity geometry, T/D ratio). In principle, larger T/D and stronger materials promote larger void spaces in the underground as stable compression arches build up (Fig. 16; see also Holohan et al., 2015). Thus, for a given T/D, cavities are unstable in the weak "mud" material but are stable in the stronger "sand–gravel" and "rock salt" materials. As the cavity grows, however, the T/D ratio decreases and ultimately the overburden geometry can no longer support its weight. Eventually, the overburden will fail partially or completely and collapse into the cavity.

The gravitational stress field in the models also means that the absolute depth, and not just relative depth as expressed by T/D, is critical, however. The deeper the cavity, inside which stresses are zero, the higher the differential stress immediately around it (Figs. 9, 11 and 16). This accounts for the observation in our models that, for a given material strength, deeper-seated cavities fail earlier than shallow ones in these weakly consolidated materials. Overall, our results indicate that cavity sizes and stability, and hence the style of sinkhole collapse, will depend on the material strength and depth of dissolution. Thus, caprock collapse sinkholes, which form above large cavities (Fig. 1), may be favoured for relatively strong material and/or shallow dissolution levels. Dropout or suffusion sinkholes may be favoured by relatively weak material and/or deep dissolution levels. In the limit, no macro-scale cavities will form below a certain dissolution zone depth in a given material, as in situ stresses become too high for that material to support such cavities.

The DEM models also show how the interaction of material removal and mechanical instability can lead to cavity growth. This is seen mainly in moderately strong DEM material (here the "sand and gravel"), where void spaces usually stay stable until large volumes of material are removed, with typical spalling at the sides rather than from the roof (Fig. 8). This lateral spalling of the cavity is typical of "tunnel breakouts" encountered by engineers and arises from the in situ stress field in the DEM model surrounding the cavity being characterised by a $K_0 < 1$ ($\sigma_{xx} < \sigma_{yy}$). In nature, a feedback mechanism may arise from such spalling, whereby lateral or vertical spalling expose more fresh surfaces to dissolution and reduces the overburden T/D, leading to further cavity growth and instability, leading to more spalling, etc.

Another important result of our DEM models is that multilayer models with a weak (mud) interlayer fail earlier than the models with a uniform material. This is not only because the integrated strength of the overburden is lessened, but also because the rapid failure of any cavities in the weak layer effectively increases the stress concentration in the strong overlying layer, similar to a beam (Fig. 16), leading to bending induced stresses with inner arc contraction and outer arc extension. This is contrary to the higher T/D ratios for the same amount of removed volume in the homogeneous layer models in which a stable cavity develops.

A consequence of such material-controlled cavity stability is that, as is often inferred for nature (e.g. Waltham et al., 2005), the geometric relationship between subsurface cavities and sinkholes is not a straightforward one. In the weak DEM model material, a sinkhole can have little or no geometric relationship to a cavity, because cavities are not sustained at any comparable scale. In the strong DEM model materials, on the other hand, the sinkhole geometry may relate to cavity geometry to a variable degree. This relationship may be especially direct in the case of a shallow removal zone and a very strong material, where a cavity can stably grow upward with little or no collapse until intersecting the ground surface. Overall, our results reinforce the point that the use of continuum-based methods to estimate cavity geometry from sinkhole geometry (i.e. where there are large permanent strains) should be treated with caution (see also Fuenkajorn and Archeeploha, 2010 and Holohan et al., 2017).

Future work will include a variation of lateral (long-wall-mining-like), vertical (tube-like) and multiple void space growth systems. Especially for typical karst simulations, multiple void spaces with different growth functions and geometries are a more suitable, complex approach. Another aspect is the role of hydrostatic (buoyancy) and pore pressure, which is usually an important factor regarding soil liquefaction and landslides due to the reduction of effective stress (cf., e.g. Tharp, 1999; Zeev et al., 2017; Clément et al., 2018) and has been ignored in these simulations for simplicity. A possible DEM approach is to apply forces to the boundary particles of the void space to simulate the pressure inside a water-filled cavity or to apply forces related to the pore spaces between particles to simulate hydrofractures (Yoon et al., 2015). An alternative is the combination of FEM and

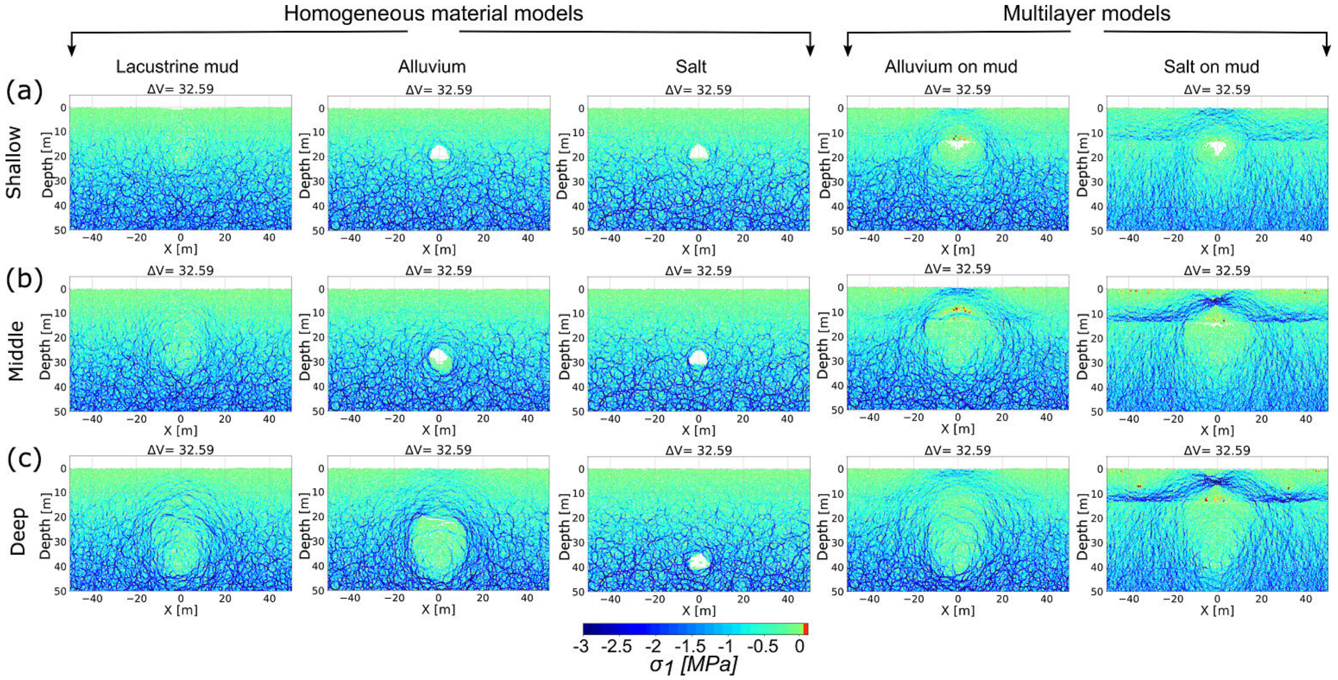

Figure 16. Maximum compressive stress for representative models after the same amount of material removal ($\sim 33\,\mathrm{m}^3$). Different depths of subrosion zones are compared: **(a)** shallow (20 m), **(b)** middle (30 m) and **(c)** deep (40 m). The deeper the zone, the higher the maximum compressive stress above the created void space. The stronger the material, the more pronounced the compression arch. Tensile stresses are observed directly above the removal zone.

DEM with accounting for drag forces due to fluid flow or other combined particle-lattice model schemes (Ghani et al., 2013).

5.5 Implications for sinkhole formation at the Dead Sea

In general, the good fit of model sinkhole geometry with the observed topography of sinkholes at Ghor Al-Haditha (Sect. 4) confirms the suitability of the DEM approach and allows for interpretation of morphological features there. In addition, structures as found in the simulations are visible also in the field, such as sagging layers and distributed marginal fracturing in weak materials, as well as cavities, compression ridges (pop-up structures) and overhanging sides in stronger materials. For a still better fit to the low diameter results of the field (Fig. 15), we would need to use a wider variety of the void space growth functions, geometries and subrosion zone depths, as expected to happen in nature. Due to computational costs, this has not been included in this study. Nonetheless, the already good agreement between the paths of depth / diameter of the existing model sinkholes as subsidence evolves and the distribution of depth / diameter values in the field (Fig. 15) strongly suggests that those distributions represent growth trends of the natural sinkholes that are controlled ultimately by material properties (Fig. 17).

Since material heterogeneity is the rule rather than the exception in nature, and since our simulation results fit well to seismic and photogrammetric studies in the area of Ghor Al-Haditha (Al-Halbouni et al., 2017; Polom et al., 2018), we consider our multilayer models as favourable over uniform models for Ghor Al-Haditha. The exact values of large-scale material strength, however, due to the described material testing procedure with a constant particle packing porosity and the limitations of literature laboratory scale values under the assumption of intact rock, should be rather used carefully. Lower strength for the materials in the field is highly probable, as the observed maximum crack depth in alluvial and salt materials (4 m) is less than in the DEM simulations (up to

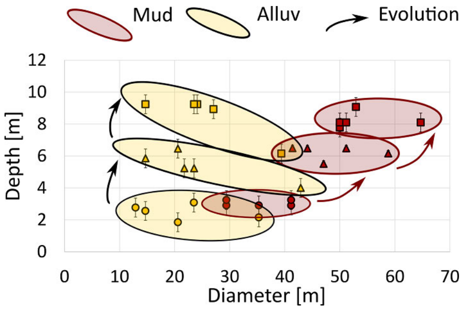

Figure 17. Simulated sinkhole depth / diameter interpretation. The simulations reveal a tendency towards deeper sinkholes in alluvium and both deeper and wider sinkholes in mud, a trend that is able to explain the observations for sinkholes at Ghor Al-Haditha.

12 m). This is probably because in detail "pure" sand–gravel or rock salt is rare on a large scale at the site – usually, there is plenty of muddy material interbedded. However, some general observations for the models with materials and material successions typical at the field site of Ghor Al-Haditha in Jordan can be drawn from the following simulations:

1. A weak lacustrine mud layer beneath a strong cover material favours sinkhole formation. Even high-strength material like the salt would collapse in such a setting.

2. A middle–deep subrosion zone (30–40 m) leads to collapses even for the pure alluvium models, which means that a subrosion acting only in the alluvial sediments can similarly cause sinkhole formations like those with a weak interlayer. Only a higher-volume removal is needed.

3. The pure salt models do not produce typical sinkholes as observed in the field zone. This fact can be related either to a lack of such a thick and strong cover material in nature or a too-high strength assigned in the model. It is perhaps worth noting that at the Lisan Peninsula, close to the field area at the Dead Sea, large (several-metre-scale) cavities and arches were observed here in Holocene Dead Sea salt (Closson et al., 2007). On the other hand, the observed salt exposure at our field site contains rather thin salt layers, interleaved with mud on a centimetre scale, so that the bulk material strength there is expected to be lower than that simulated.

4. The possibility to record surface subsidence before actual sinkhole collapse depends on both the cover material type and the depth of the subrosion zone. A multilayer model of a middle-deep subrosion zone with a large subsurface collapse zone may produce recordable surface signatures in the order of sub cm before the onset of collapse.

Finally, the single void collapse concept explored in this paper may sufficiently explain some individual sinkhole occurrences at Ghor Al-Haditha and elsewhere around the Dead Sea (cf. laboratory experiments by Oz et al., 2016); the coalescence, sequence evolution and sinkhole cluster structures, morphological expressions at the surface and larger sinkhole depression areas may not. For this, a more sophisticated approach of multiple void space growth, testing different geometries and a more realistic subrosion process is necessary and will be addressed in a future paper.

6 Summary and conclusions

In this work, we presented a benchmarked and calibrated 2-D distinct element modelling approach to simulating the process of both cavity growth and sinkhole development. Our principal findings are as follows.

Firstly, we presented a computationally fast DEM approach to simulating sinkhole formation by instantaneous, quasi-static, stepwise material removal in a single void space at a depth of an arbitrarily shaped geometry under gravitational loading. We successfully benchmarked the models with analytical and BEM solutions yielding a sub-millimetre degree of agreement for surface displacements and displacement differences.

Secondly, we performed simulated compression and tension tests to determine microscopic bond strength parameters and moduli calibrated by intact rock literature values and field estimates for the three materials common at the Dead Sea shoreline. The simulated rock tests yield low bulk strength (UCS ~ 0.06–0.25 MPa) for lacustrine mud, middle bulk strength (UCS ~ 0.53–0.92 MPa) for alluvial sandy gravel sediments and high bulk strength (UCS ~ 1.23–1.54 MPa) for rock salt materials, based on Mohr–Coulomb and Hoek–Brown fits.

Thirdly, we simulated a cavity growth until sinkhole collapse in uniform materials. Cavity development is controlled by the interaction of the material strength and the depth of material removal. Weak materials do not support large cavities, and so subsidence is characterised by gradual sagging and suffusion-type collapse into the material removal zone. Stronger materials support the development of large cavities at the material removal zone, leading to sinkhole formation by the sudden collapse of the overburden (caprock or cover collapse type sinkholes). At one end of the spectrum, near the Earth's surface, very strong materials may support cavity growth until the intersection with the ground surface, giving rise to sinkholes with little or no collapse. At the other end of the spectrum, below sufficient depth and for a given material strength, the development of cavities on a significant scale is inhibited as gravitational stresses are too high.

Fourthly, we simulated a cavity growth until the sinkhole collapse in multilayered materials. We show with the inclusion of weak layers, either as cover material or as subroded bedrock material, results in sinkhole development with less volume of removed material than in the case of uniform model material. Such development is not only due to an integrated weakening of the overburden but also due to the growth of a subsurface collapse zone in the weak material that geometrically destabilises the overburden.

Lastly, we compare the developed morphologies from a set of models for all three materials with photogrammetric analysis from the sinkhole area of Ghor Al-Haditha in Jordan. Our approach produces physically realistic sinkhole shapes and successfully reproduces typically measured sinkhole depth / diameter ratios of 0.15 in mud-flat material, 0.37 for sinkholes in alluvium and 0.33 in salt. The field distribution appears hereby to be related to evolution stages of the sinkholes between early and late collapses. A weak (mud) interlayer and/or a deeper lying subrosion zone enhances formation of sinkholes in materials typical of the Dead Sea margins.

Appendix A: The distinct element method and its use for simulating geomaterials

The DEM is a specific scheme of undeformable particles and deformable contacts developed by (Cundall, 1971). In the PFC2D v5.035 software, the DEM is used to implement Newton–Euler equations of motion and rotation on disk-shaped particles (Itasca Cooperation Group, 2014; Potyondy, 2014a; Potyondy and Cundall, 2004) (Fig. A1a). In PFC, the resolution scheme is an explicit second-order velocity Verlet algorithm (Verlet, 1967). The particles are assigned a mass and a radius, are initially unbonded and are free to move and rotate depending on external forces. Particles interact only at contact points between particles and wall facets, where the mechanical interaction is treated in terms of a frictional contact with a set of linear elastic springs that are assigned normal and shear stiffness (Fig. A1b). The “rigidity” of the particles is defined by setting the elastic Young constant in accordance to the spring stiffness. An additional bonding of the elements can be performed, whereby many different bond types can be specified. Here, we use the parallel-bond model (Potyondy and Cundall, 2004), which is defined in terms of a set of linear elastic springs in parallel to the linear contact bond. The parallel bonds allow for tensile forces and bending moments between the bonded particles, and they break once their strength is exceeded. Here, we set the bonds to have the same material constants (microproperties) as the particles, like stiffness and elastic modulus, but since bond strength is defined similar to a Mohr–Coulomb failure criterion, the bonds are also assigned a cohesion, tensile strength and friction angle (Fig. A1c).

A1 Mathematical details of the DEM method implemented in the PFC software

The Newton–Euler equations are solved in a finite difference explicit time-stepping algorithm involving dynamic relaxation (Cundall, 1971; Jing and Stephansson, 2007). During the procedure, Newton’s second law and the force-displacement law is solved for each of the particles and its contacts (Potyondy and Cundall, 2004). For a 2-D system of coupled rigid elements, the differential equations solved by the explicit time-marching relaxation scheme for a particle of mass m are (Jing and Stephansson, 2007)

$$\begin{aligned} m\ddot{u}_x^t + \alpha m\dot{u}_x^t &= F_x m\ddot{u}_y^t + \alpha m\dot{u}_y^t = F_y, \\ I\ddot{\theta}^t + \alpha I\dot{\theta}^t &= M, \end{aligned} \tag{A1}$$

with F as force, u as displacement, $\dot{u}$ as velocity, $\ddot{u}$ as acceleration, α as damping, M as moment of force, I as inertia, θ as Euler rotation angle, $\dot{\theta}$ as Euler rotation velocity and $\ddot{\theta}$ as Euler rotation acceleration at a certain time t.

It is assumed that (1) velocities and accelerations within one time step are constant and (2) that the step chosen is small enough that disturbances, which occur due to external or body forces, particle or boundary wall movement, propagate only to the neighbours of the particles. The resulting velocity and acceleration components for both the translational and rotational motion of one particle are determined via a finite difference scheme successively for each time step t (Jing and Stephansson, 2007):

$$\begin{aligned} \ddot{u}_i^t &= \frac{1}{(\Delta t)^2}\left(u_i^{t+1} - 2u_i^t + u_i^{t-1}\right) \\ \dot{u}_i^t &= \frac{1}{2\Delta t}\left(u_i^{t+1} - u_i^{t-1}\right), \end{aligned} \tag{A2}$$

with i as x or y and the equations for $\dot{\theta}$ and $\ddot{\theta}$ accordingly. The displacement calculation is generally one time step ahead of velocities’/accelerations’ calculation, and constitutive laws of arbitrary complexity (Jing and Stephansson, 2007) can be added between the contacts without numerical instability. The kinematic critical time step $\Delta t_{\text{crit}} = \min\left(\sqrt{\frac{m_i}{k_i}}\right)$ is determined for an infinite multiple set of masses m_i and springs with stiffness k_i to allow for the above constraints and solution of the equations.

The equilibrium is defined by a convergence criterion, where the ratio between the “out-of-balance” forces to the overall forces is below a defined threshold (solve ratio, SR) of usually 1^{-5} or lower. This “solving” can be performed for the mean (SR_{mean}) or maximum (SR_{max}) forces that appear in the model. A problem can occur when absolute normal force calculation during material gravity settling is used: interlocked forces due to the particle overlap may not be released during further simulation. This issue has been overcome by introducing an incremental normal force calculation (Fakhimi, 2004) which is implemented in PFC2D v5 (Itasca Cooperation Group, 2014; Potyondy, 2014b).

A2 Creating a gravitationally loaded synthetic rock mass in the DEM

Creation of a bonded particle assembly in this study followed that of Holohan et al. (2011) and involved the following chain of steps:

1. *Creation of an unbonded particle assembly of defined particle sizes, porosity and geometrical distribution.* A uniform distribution of particles between a defined minimum and maximum radius is placed randomly in the model box of size $H \times W$. The unbonded material is limited by three walls with low-friction (0.01) elastic interaction. The radii distribution in this study is chosen to be equal between the minimum and maximum assigned radius (Table B1) according to the defined porosity.

2. *Assignment of material domains.* The mechanical properties are distributed in the assembly according to the desired model setup, e.g. layering. The linear contact model is installed between each two entities at a distance smaller than or equal to the surface gap.

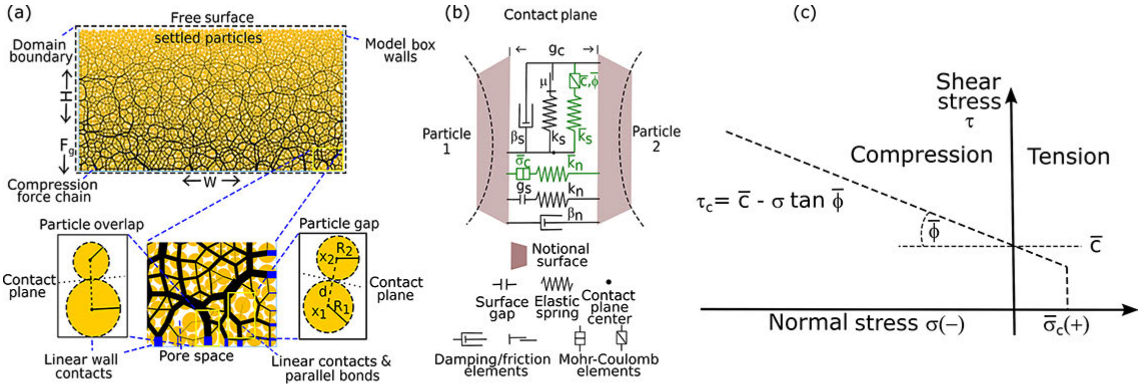

Figure A1. Schematic description of 2-D DEM modelling with PFC2D v5. **(a)** Inter-particle and particle-wall force chains developed after gravity settling of an assembly of balls in a box of dimension $H \times W$. The close-ups below show the pore space, contact planes and nomenclature. Particles, although undeformable, are allowed to overlap slightly or have a small gap g_c. In both cases, linear contacts and optional parallel bonds are active. These bonds act additionally to the linear contacts. **(b)** Close-up of the notional and contact planes with all elements necessary for the physical definition of the contact and bond interactions. **(c)** Failure criterion for parallel bonds. Compression in this study is considered as negative.

3. *Gravity settling.* Gravity acts as the main body force. A settling criterion is applied; i.e. the material is considered as settled when a certain threshold, here $\mathrm{SR}_{\mathrm{mean}} = 1^{-6}$, of the velocity and displacement change of the particles between two time steps is reached. The material is settled under low friction until the defined solve ratio.

4. *Particle bonding.* The created assembly contains, as real rock, interlocked forces. Now the particle bonding is applied according to a chosen bond type (parallel) and the model is cycled into equilibrium. Linear contact friction is set to the defined value.

At each step, the material assembly is cycled until a static equilibrium is reached. The behaviour of a DEM model depends strongly on the material packing assembly (Schöpfer et al., 2009), and so a spectrum of solutions is usually obtained by performing multiple realisations for different assemblies. The above chain is thus repeated to produce many random particle assemblies that may be used to obtain a statistical mean of packing-dependent model outcomes. In this study, the procedure was repeated generally for 5–10 random assemblies of the particles.

Appendix B: Details on model convergence tests, benchmarking, material calibration and the final sinkhole model implementation

The following section gives an overview over the performed DEM model convergence, void space installation and benchmarking tests that were performed to determine the optimal sinkhole formation modelling setup. Table B1 summarises the main DEM model parameters used for the tests.

B1 Comparison of cavity generation methods

Several methods have been tested in order to determine the optimal void installation procedure for reasonable simulation time and realistic surface displacement curves. These are instantaneous material removal by particle deletion (M1), incremental material removal by particle deletion (M2), whole cavity particle radii reduction (M3) and incremental particle radii reduction (M4). The radius ($r = 5$ m) and centre depth ($h = 35$ m) of the circular material removal zone was chosen to match the expected sizes of cavities at the area of application. In M1, particles inside the cavity are instantaneously removed, while M2 allows for 15 steps of incremental particle deletion. For the other two methods, parallel bonds are first removed and then we use particle radii reduction in 50 steps to 7.7 % of the original size, each step meaning 5 % reduction. The difference between both is again a complete (M3) vs. incremental (M4) approach. In all methods, the assembly is cycled to $\mathrm{SR}_{\mathrm{max}} = 1e-6$.

M3 and M4 show similar results for the horizontal displacement U_x but a slightly lower vertical displacement U_y compared with M1 and M2 (Fig. B1). A crucial finding is that M3 and M4 reveal a longer calculation time by 1–2 orders of magnitude. As a result of this test, we consider methods M1 and M2 as generally suitable to simulate a realistic material removal under acceptable calculation time. For the following model verification tests, we rely on method M1 as the simplest option to implement a cavity, and M2 will serve for the final sinkhole models.

B2 Convergence tests on model dimensions and resolution

We performed model resolution tests to determine the optimal size for the mechanical problem of a shallow cavity

Table B1. Dimensions of the model and contact and particle properties used in development and testing of DEM cavity formation models.

Geometric parameter or microparameter	Symbol	Unit	Value range (common)
Model height	H	(m)	100–500 (400)
Model width	W	(m)	100–500 (400)
Material porosity	n		0.2
Minimum particle radius	R_{min}	(m)	4.98–0.17 (0.24)
Mean particle radius	$\overline{R}$	(m)	6.65–0.23 (0.32)
Particle radius factor	R_{f}		1.66
Particle density	ρ	(kg m^{-3})	2500
Solve ratio unbalanced/balanced forces	SR		1^{-6}
Cavity centre depth	h	(m)	35
Cavity radius	r	(m)	5
Boundary walls Young's modulus	E_{W}	(GPa)	−5
Parallel bond Young's modulus	E_{Pb}	(GPa)	−5
Parallel bond tensile strength	$\overline{\sigma}_c$	(MPa)	1000
Parallel bond cohesion	$\overline{c}$	(MPa)	1000
Parallel bond friction angle	ϕ	(°)	30
Parallel bond ratio normal/shear stiffness	$\overline{k}_{\mathrm{n}}/\overline{k}_{\mathrm{s}}$		2.5
Linear contact Young's modulus	E	(GPa)	−5
Linear contact friction coefficient	μ		0.01–0.5 (0.5)
Linear contact normal/shear stiffness ratio	$k_{\mathrm{n}}/k_{\mathrm{s}}$		2.5
Linear contact normal/shear damping	$\beta_{\mathrm{n}}/\beta_{\mathrm{s}}$		0.7/0.0
Surface gap	g_{S}	(m)	$2.1^{-2} \times R_{\mathrm{min}} (= 5.04^{-3})$
Gravitational acceleration	G	(m s^{-2})	9.81

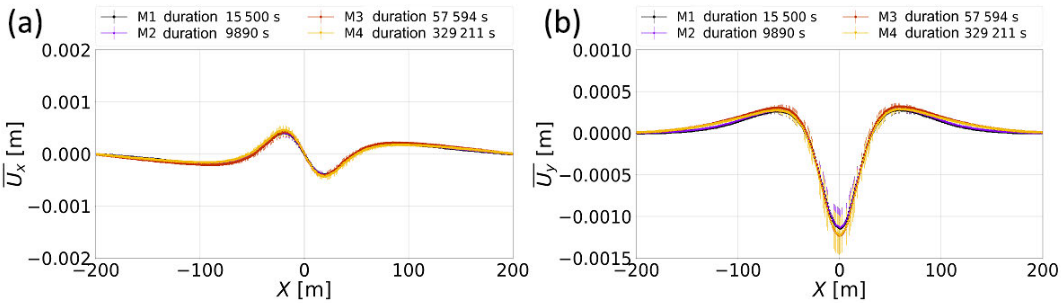

Figure B1. Displacement plots for different void installation methods. **(a)** Horizontal and **(b)** vertical model setup with size 400 × 400 m using a coarse particle distribution (mean radius 0.74 m). Indication of needed simulation time is given in the legend. M1–M4 refer to the installation methods described in the text.

in a bonded rock assembly. The cavity is installed by instantaneous (quasi-static) particle removal (M1 as shown in Fig. 4a). We varied the width W and height H of the model box from 100 to 800 m while keeping the particle radii constant at 0.74 m for a cavity installation in 35 m depth with a radius of 5 m and track the horizontal and vertical surface displacement.

In Fig. B2, we see the horizontal and vertical displacement curves for all model dimensions. Boundary effects in such a setting close to the free surface make the judgement of the optimal size demanding, but the expected behaviour for the vertical displacement is a subsidence roughly 9/10 and an uplift roughly 1/10 of the total vertical displacement (see model benchmarking in Sect. 2.2).

We observe the most stable results for symmetric model dimensions and define the optimal model size to height (H) × width (W) $= 400 \times 400$ m to account for later possible growth of such a void space. In relation to the cavity size, this means the optimal model is 40 times the cavity diameter. In another expression, the optimal model dimension / cavity depth ratio is 10, a typical value in engineering problems (see Sect. B3). In detail, asymmetric or small model sizes lead to instable results with tails not reaching the expected zero line.

The influence of the particle radii on the displacement curves is shown in Fig. B3 for the above-determined favourable model dimensions. A convergence is observed for particles with mean radius around 0.32 m. Model dimensions of $H \times W = 400 \times 400$ m with a mean particle radius of

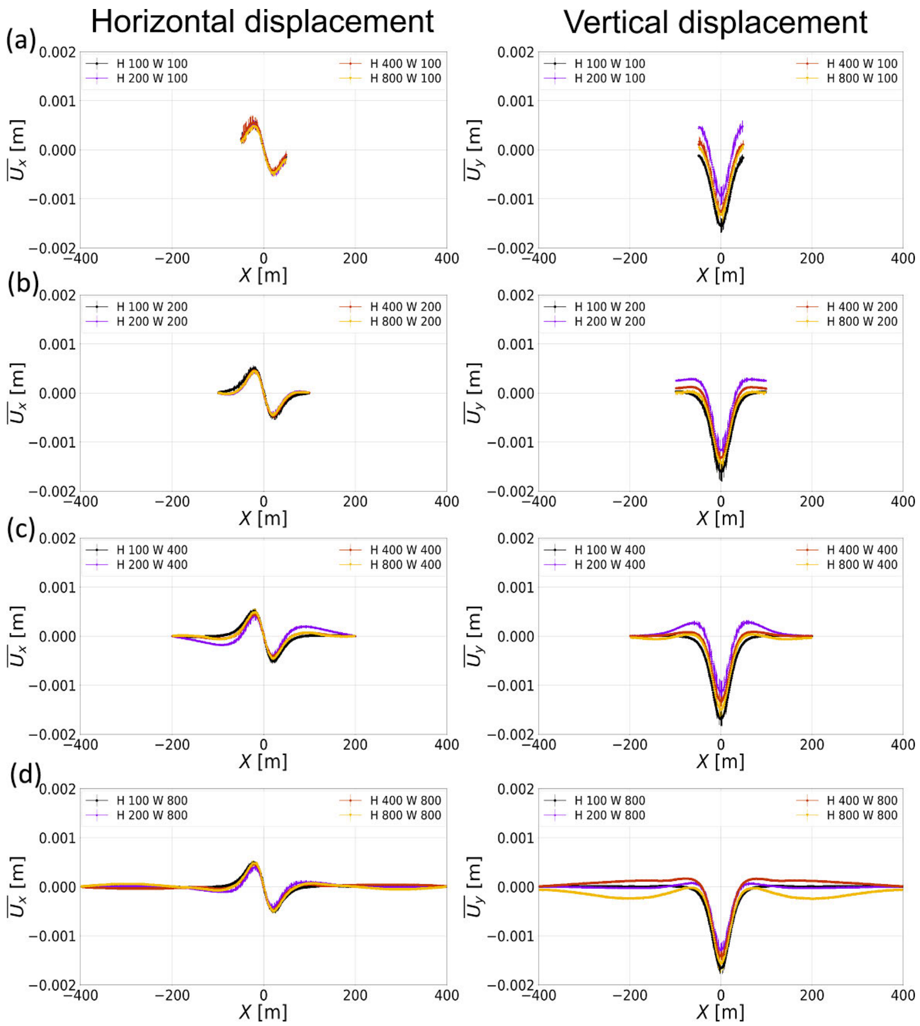

Figure B2. Convergence test results for model assembly dimensions: cavity of radius of 5 m and depth of 35 m created in each case by method M1. Mean particle radius is 0.74 m. Left and right columns show horizontal and vertical displacement profiles, respectively. Each plot shows results for varying model height (H) from 100 to 800 m for a given width (W): **(a)** $W = 100$ m; **(b)** $W = 200$ m; **(c)** $W = 400$ m; **(d)** $W = 800$ m. A convergence is observed for larger model dimensions and a minimum height of 400 m is favoured. Symmetric boundaries (400 × 400 m) give the most stable results.

$\overline{R} = 0.32$ m are thus the optimum parameters to account for converging results, model boundary effects and minimising simulation times.

B3 Detailed of continuum-based solutions for displacements around a gravitationally loaded cavity in 2-D

The first analytical solution used, the Kirsch solution, a classical solution for simple excavation shapes, does not include the free-surface effect, and the mathematical details are depicted, e.g. in Brady and Brown (2006). The radial and tangential displacements at a point $a = a(a, \theta)$ at the surface for an average vertical stress P, the horizontal stress $K \times P$ and the shear modulus G are

$$u_r(a\theta) = \frac{Pr^2}{4G\,|a|}\left[(1+K)-(1-K)\times\left(4\times(1-\upsilon)-\frac{r^2}{|a|}\right)\cos 2\Theta\right] \tag{B1}$$

$$u_t(a\theta) = \frac{Pr^2}{4G\,|a|}\left[(1-K)\times\left(2\times(1-2\times\upsilon)+\frac{r^2}{|a|}\right)\sin 2\Theta.\right] \tag{B2}$$

With translation into Cartesian coordinates, this yields the surface displacements:

$$u_{xx}\,(y=0) = u_r\cos 2\Theta - u_t\sin 2\theta \tag{B3}$$

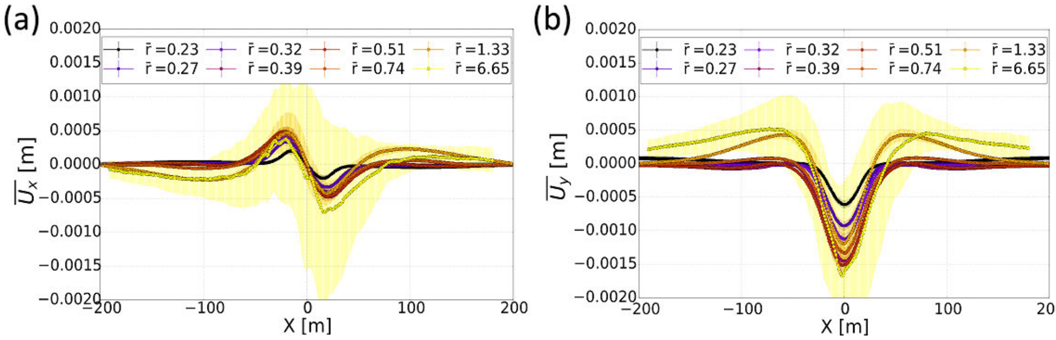

Figure B3. Results of convergence tests of for influence of particle size: horizontal **(a)** and vertical displacement **(b)** profiles for method M1 with in a 400 × 400 m sized box. We observe a convergence of the displacement curves for mean radii around 0.32 m, but for decreasing particle sizes, we observe further diminishing of the amplitudes.

$$u_{yy}\,(y=0) = u_r \sin 2\theta + u_t \cos 2\Theta. \tag{B4}$$

The second analytical solution used is from Verruijt and Booker (2009) and includes the free-surface effect and is based on the analytical solution of stresses from Mindlin (1940). Verruijt and Booker (2009) added the displacement calculation to the original 2-D Mindlin solution. It is determined via the complex variable method (Muskhelishvili, 1953) and consists of three partial solutions. The second and third partial solutions are relevant for displacement calculation. The second is based on Melan's solution for a concentrated vertical force in a semi-infinite medium and the third involves a balance of the stresses at the cavity boundary. The reader is referred to Verruijt and Booker (2000, 2009) for mathematical details.

The equation for normal displacements as derived by the second solution for an elastic half space $(x,\ y)$ under the action of normal line surface load P (Melan's solution) is (Davis and Selvadurai, 1996; Jaeger et al., 2007)

$$u_{yy}(xy) = \frac{(1-\upsilon)\,P}{G\pi}[[\ln(x+a)]]_{x=0}^{x=\infty}, \tag{B5}$$

with G the Lamé parameter (shear modulus), υ the Poisson ratio and a the distance to the point of interest.

As known well from linear elastic material theory (Muskhelishvili, 2013; Timoshenko and Goodier, 1973), the integration of the stress formulae is such that a setting of a loaded material (Flamant's problem), which is similar to material removal in the underground, leads to the logarithmic term in the equation above. This leads to infinite vertical displacements along the x surface and a singularity at the centre point $(xy = 0)$.

As a workaround for calculation of finite displacements around the cavity, Verruijt and Booker (2009) defined a value d where displacements are set to zero, $u_{yy}(y=d,\ x=0) = 0$, a so-called fixed point at depth. This constant d can be arbitrarily defined; in engineering, it is usually set to 10 times the depth of the cavity $(d = 10 \times h)$.

Thus, displacements are considered as not physically realistic in the far field of a load (or cavity), but relative displacement differences are (cf. Davis and Selvadurai, 1996 and Verruijt and Booker, 2009). For the above-stated problem, the relative vertical displacements $\Delta u_{yy} = u_{yy}(x_1) - u_{yy}(x_2)$ between two points x_1 and x_2 at the surface are (Davis and Selvadurai, 1996)

$$\Delta u_{yy} = \frac{(1-\upsilon)\,P}{G\pi}\ln\frac{x_1}{x_2}. \tag{B6}$$

Figure B4 highlights the effect of a variation in Young's modulus and the fixed point depth on the fit between modelled vertical displacements and the analytical Mindlin solution described above. A general finding is that E determines the amplitude of the curve and one can gain even better fits of the DEM results when using a higher elasticity module than determined by the simulated rock tests. Furthermore, setting the d/h value to a more realistic value such as 11.43 which corresponds to a cavity central depth of 35 m and a model height of 400 m, shifts the entire vertical displacement curve. The displacement difference is not affected by this integration constant. Hence, when considering the final "best-fit" solution with a low $d/h = 4$ and high elastic modulus $E > 10$ GPa, the difficulty in cancelling out the integration constant of the analytical displacement solution leaves a still poor fit of the DEM results in the far field but a reasonable fit in the near field of the installed cavity. We use this approach to determine the near field at the surface as approximately $-8r \le x \le 8r$ with r the radius of the cavity. In our case, this means that the surface near-field limits are ±40 m from the centre of the depression.

B4 Details on Mohr–Coulomb and Hoek–Brown rock test analysis

The bulk behaviour of particle assemblies emerges from the interaction of the particle according to the mechanical rules imposed at the contact and bond scale. Therefore, and unlike for continuum-based approaches, the bulk behaviour in DEM models must be calibrated by simulated rock or soil mechanics tests (Potyondy and Cundall, 2004). Here, biax-

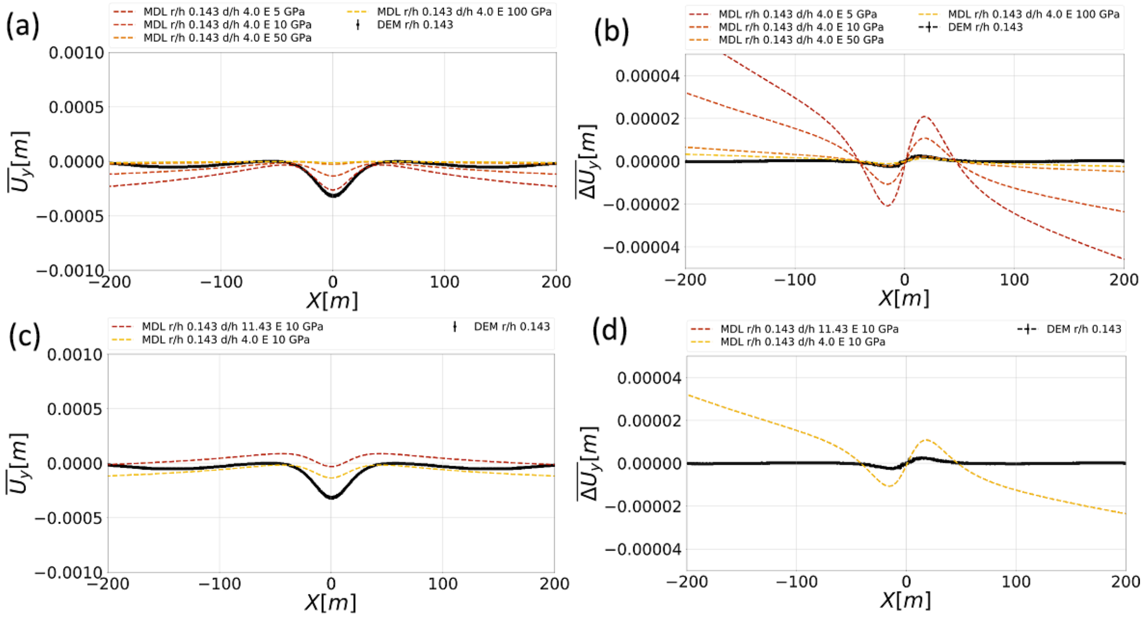

Figure B4. The effect of Young's modulus E and fixed depth point d/h on the vertical displacement **(a, c)** and displacement difference **(b, d)** of the Mindlin (MDL) analytical solution as calculated by Verruijt and Booker (2009). Panels **(a)** and **(b)** show the scaling effect of the elastic modulus which affects both U_y and ΔU_y. Panels **(c)** and **(d)** show the effect of d/h for $E = 10$ GPa which shifts the U_y curve but has no effect on ΔU_y.

ial compression and tension tests are used to determine the bulk elastic properties of the medium, i.e. the Poisson ratio ν and Young's elastic modulus E. By fitting of the peak stress data upon failure in such tests to, e.g. Mohr–Coulomb or Hoek–Brown failure envelopes, one can also determine bulk strength properties (tensile strength T, unconfined compressive strength UCS, coefficient of internal friction ϕ).

A typical stress vs. strain curve contains three parts: (1) a non-linear or linear elastic behaviour, (2) a non-linear yielding behaviour as cracks appear in the material and (3) a non-linear post-peak behaviour after material failure. The peak of the stress–strain curve defines the maximum and minimum principal stresses (σ_1, σ_3) at failure. For the compression test, the axial stress is the maximum compressive stress σ_1 (most negative value in the convention used here) and the transversal stress is the minimum compressive stress σ_3 (least negative). For the tension test, it is vice versa: the transversal stress is the maximum tensile stress σ_1 (most positive) and the axial stress is the minimum tensile stress σ_3 (least positive).

The mean peak stresses can be determined for each confining pressure and plotted against each other. In a linear (Mohr–Coulomb) fit of $\sigma_1(\sigma_3)$, the UCS is determined by the intercept at $\sigma_3 = 0$ and the unconfined tensile strength (T) by the intercept at $\sigma_1 = 0$. The slope $q = \tan^2\beta$ can be used to fit the Mohr failure envelope as shown in Fig. 7:

$$\sigma_1 = C + \sigma_3 \tan^2\beta, \tag{B7}$$

with $C = \text{UCS} = 2c_0 \tan\beta$ and $\beta = 45° + \phi/2$. For a Hoek–Brown fit in a $\sigma_1(\sigma_3)$ plot, a function of the following form is used:

$$\sigma_1 = \sigma_3 + \sqrt{m\sigma_0\sigma_3 + s{\sigma_0}^2}, \tag{B8}$$

with m and s as the empirical rock parameters. For the assumption of intact rock, $s = 1$, $\sigma_0 = C$, the UCS and $T \sim \frac{C}{m}$. Hence, the fit parameters m and C are used to derive the strength properties of the tested materials. Figure B5 provides exemplary stress vs. strain plots at a confining pressure of -0.1 MPa for all tested materials.

B5 Technical details of implementation of cavity growth and sinkhole collapse in Dead Sea materials in PFC2D v5.0

B5.1 A PFC- and Python-based code to simulate sinkhole formation

A graphical description of the implemented Python/PFC2D-Fish sinkhole modelling code is depicted in Fig. B6. Here, Fish code parts are marked in yellow and Python code in grey colour. A typical sinkhole simulation follows the following scheme:

1. Model dimensions, particle parameters and a function $f(i)$ for the material removal is defined at the beginning of each set. An unbonded assembly of particles with a fixed porosity of 0.2 is generated at once for the whole

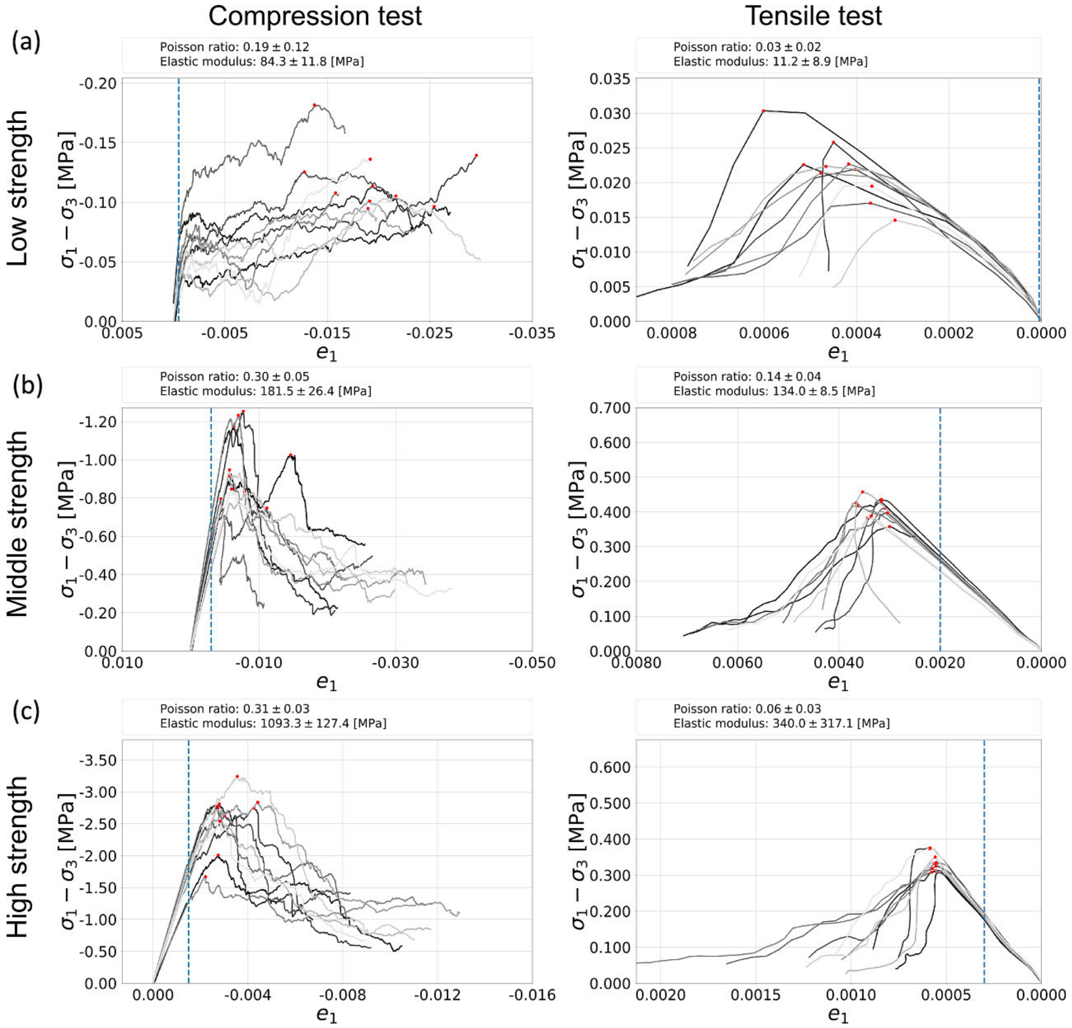

Figure B5. Differential stress vs. vertical strain for CC and DT tests for a confining pressure of 0.1 MPa: **(a)** lacustrine mud; **(b)** alluvium sediments; **(c)** holocene salt rock. The dashed line indicates elastic limit which was used to determine elastic parameters displayed above the graphs. Red dots mark the peak stresses.

assembly at the initial void space growth round ($i = 0$, no material removal yet).

2. Similar to the material generation procedure for the model verification material (see Appendix A2), we settle and bond the assembly with a parallel bond model according to the desired material properties. It has to be noted that for low-strength material a bond-reinstallation procedure has been applied, a so-called annealing; i.e. failed bonds can be re-established by contact with other particles of the same material, accounting for, e.g. cohesive mud behaviour. For the other materials, a failed PB is not activated again. We then install the desired tracking functions (measurement circles, marker particles, histories) and group the initial void spaces defined in the model control file.

3. This material removal loop acts on each defined cavity growth round i. If the area of the particles in the void space zones matches the definition by function $f(i)$, the loop is broken and important tracked parameters are recorded.

4. Step 3 is repeating with increasing material removal round i, and after each, the desired tracked results are output via Python code. When a predefined maximum void space growth is reached, the model is finished and a new random assembly starts at step 1.

To avoid another degree of freedom in the calibration of micro- vs. macroproperties, the initial porosity only changes due to the compression by the gravity settling scheme. We have refrained from using either post-settling particle removal to adjust the porosities to specific values or layer-wise

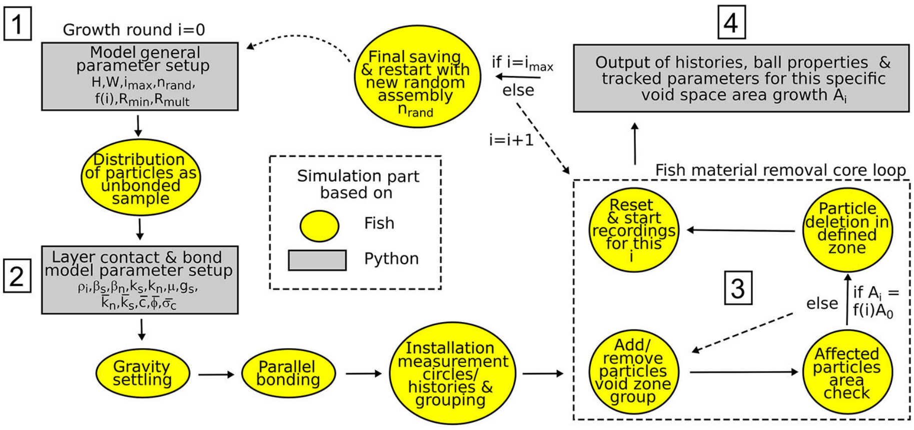

Figure B6. Graphical description of the PFC2D-based sinkhole modelling code. Yellow colours indicate PFC-Fish language-based code; grey colours are Python control connections. Solid arrows indicate time step cycling. Each model set consists of n_{rand} random assemblies of particles to account for statistical variation of the DEM sinkhole collapse via arbitrary material removal function in single voids.

gravity deposition with different porosities because of the high amount of calculation time needed.

The Fish material removal core loop (no. 3 in Fig. B6) provides the technical implementation of a quasi-static void space growth. A simple law between the particle area A_i that is supposed to be removed during the void space growth round i and the initial area A_0 has been chosen with arbitrarily definable function $f(i)$:

$$A_i = f(i)A_0. \tag{B9}$$

The void space area is defined by a major and a minor axis. This enables both semi-elliptical, elliptical and circular void space growth. For the results presented in this paper, a slow, constant void space growth $f(i) = 1.0^i$ with $A_0 = 16.3\,\text{m}^2$ and a linear eccentricity of $e = 2.64$ was chosen. This avoids the triggering of dynamic effects if too many particles are deleted at once. Other options may include a doubling void space each round ($f(i) = 2.0^{i-1}$ or an exponential increase $f(i) = e^{(i-1)}$ for $i \geq 1$. For this purpose, a computationally rather cost-intensive static equilibrium procedure is available in PFC2D v5, which sets the bond strengths high before particle deletion, cycles to a stable limit after particle deletion and then resets the bond strengths to the original value.

The pure runtime for a full simulation of an alluvium on mud setup on an Intel Xeon 3.7 GHz processor with 64 GB RAM needs roughly 2 weeks for one particle assembly without tracking geophysical parameters. The tracking would increase the runtime by a factor of ~ 1.5. A possible improvement in future will be the introduction of focus regions with an increasing particle radius with distance from the centre of the model.

B5.2 Details on the implemented parameter tracking

A tracking of pre-, syn- and post-collapse geodetic and geophysical parameters has been implemented in the modelling code (no. 4 in Fig. B6). The technical details are listed as follows.

Porosity, stress and strain rate are recorded using the distribution of so-called measurement circles of area A^{m} throughout the model domain (Itasca Cooperation Group, 2014; Potyondy and Cundall, 2004).

Porosity is calculated via $n = \frac{V_{\text{void}}}{V_{\text{m}}} = 1 - \frac{V_{\text{mat}}}{V_{\text{m}}}$ with V_{void} as the volume of the void and V_{mat} the approximated volume of the particles of amount N_b in the measurement circle.

The average stress tensor is calculated in static conditions via $\overline{\sigma} = -\frac{1}{V_{\text{m}}} \sum_{N_c} F^{(\text{c})} \otimes L^{(\text{c})}$ where $\otimes$ is the dyadic product of two tensors, N_{c} is the number of contacts, $F^{(\text{c})}$ is the contact force vector and $L^{(\text{c})}$ the branch vector that joins the centroids of two entities. From this, the maximum compression principal stress σ_1, the minimum compression principal stress σ_3 and the maximum shear stress $T_{\text{max}} = \frac{(\sigma_3 - \sigma_1)}{2}$ are calculated, which is always positive in the convention used here, where compression is negative.

The strain rate tensor $\dot{e}$ (velocity gradient tensor) is calculated via a least-squares best-fit approach of the predicted vs. the measured relative velocities $\widetilde{V}_i^{(p)} = V_i^{(p)} - \overline{V}_i$ between each two entities p during a time step i, with $V_i^{(p)}$ as the translational velocity and $\overline{V}_i = \frac{\sum_{N_p} V_i^{(p)}}{N_p}$ as the mean velocity in the circle area.

The strain tensor in the measurement region is then calculated by multiplying strain rate components with the simulation time step and summing over the desired period.

Alternatively, strain is calculated via simulated extensometers. For these, pairs of particles which lie either horizontally or vertically next to each other are defined. By registering the displacement of each particle, a pairwise calculation of the horizontal and vertical strains is achieved at low computational cost in comparison to the measurement circle distribution (Itasca Cooperation Group, 2014).

Data availability. A full set of metadata is available upon request. For photogrammetric surveys, raw images, DSMs and orthophotos are available upon consultation with the authors. For DEM models, data and results are available upon request.

Supplement. The supplement related to this article is available online at: https://doi.org/10.5194/se-9-1341-2018-supplement.

Author contributions. DAH led the production of figures, data analysis and numerical modelling. DAH and EPH led the writing of the manuscript. DAH, EPH, AT, MPJS and SE developed the calibration of the materials and discussed technical issues. All authors reviewed and commented on the manuscript, and they contributed to discussions of the data and interpretation.

Competing interests. The authors declare that they have no conflict of interest.

Special issue statement. This article is part of the special issue "Environmental changes and hazards in the Dead Sea region (NHESS/ACP/HESS/SE inter-journal SI)". It is not associated with a conference.

Acknowledgements. We would like to thank the two reviewers and the editor for the fruitful discussion. We very gratefully acknowledge fieldwork support from Ali Sawarieh, Hussam Alrshdan and their colleagues at the Ministry of Energy and Mineral Resources of the Hashemite Kingdom of Jordan. Acknowledgements go to Emad Talafheh and Zayad Mansour from the Arab Potash Company, as well as to Michael Ezersky of the Geophysical Institute of Israel, for their support regarding geotechnical parameters. Also, we thank Arnold Verruijt for the comments regarding the analytical solution, as well as Daniel Woodell and Mehdi Nikhoo for the technical advice of the DEM and BEM modelling, respectively, and Marc Elmouttie for facilitating the research stay at CSIRO (Brisbane). Special thanks go to Damien Closson and Thomas R. Walter for continuous support and material provision. Particular thanks go to Itasca Consulting Group for providing the license of PFC2D v5.0 in the framework of the Itasca Education Partnership program and the German Academic Exchange Service (DAAD) for a short-term doctorate research grant. Last, but not least, thanks go to the projects DESERVE and SIMULTAN and the involved colleagues for their kind support and funding opportunities.

The article processing charges for this open-access
publication were covered by a Research
Centre of the Helmholtz Association.

Edited by: Amotz Agnon
Reviewed by: Renaud Toussaint and one anonymous referee

References

Abelson, M., Yechieli, Y., Baer, G., Lapid, G., Behar, N., Calvo, R., and Rosensaft, M.: Natural versus human control on subsurface salt dissolution and development of thousands of sinkholes along the Dead Sea coast, J. Geophys. Res.-Earth, 122, 1262–1277, https://doi.org/10.1002/2017JF004219, 2017.

Al-Halbouni, D., Holohan, E. P., Saberi, L., Alrshdan, H., Sawarieh, A., Closson, D., Walter, T. R., and Dahm, T.: Sinkholes, subsidence and subrosion on the eastern shore of the Dead Sea as revealed by a close-range photogrammetric survey, Geomorphology, 285, 305–324, https://doi.org/10.1016/j.geomorph.2017.02.006, 2017.

Arkin, A. and Gilat, Y.: Dead Sea sinkholes – an ever-developing hazard, Environ. Geol., 39, 711–722, 2000.

Baryakh, A. A., Stazhevskii, S. B., Timofeev, E. A., and Khan, G. N.: Strain state of a rock mass above Karst cavities, J. Min. Sci., 44, 531–538, 2008.

Baryakh, A. A., Rusin, E. P., Stazhevsky, S. B., Fedoseev, A. K., and Khan, G. N.: Stress-strain state of Karst areas, J. Min. Sci., 45, 3–10, 2009.

Bonilla-Sierra, V., Donzé, F. V, Scholtès, L., and Elmouttie, M. K.: The use of photogrammetry and 3D Discrete Element Models to better assess Rock Slope Stability, Laboratoire 3sr, Grenoble, France, 2012.

Brady, B. H. G. and Brown, E. T.: Rock Mechanics for underground mining, 3rd ed., Springer, 2006.

Brown, E. T.: Rock characterization, testing & monitoring: ISRM suggested methods, Pergamon Press, Oxford and New York, 1981.

Byerlee, J. D.: Brittle-ductile transition in rocks, J. Geophys. Res., 73, 4741–4750, https://doi.org/10.1029/JB073i014p04741, 1968.

Carranza-Torres, C., Fosnacht, D., and Hudak, G. J.: Analytical and numerical study of the stability of shallow underground openings for mining and compressed air energy storage applications, edited by: Ranjith, P. G. and Zhao, J., IC3G Int. Conf. Geomech. Geoenergy Georesources, 2016.

Carter: Geotechnical Handbook, Pentech Press, London, Plymouth, UK, 1983.

Caudron, M., Emeriault, F., Kastner, R., and Al Heib, M.: Numerical modeling of the soil structure interaction during sinkholes, in Numerical methods in geotechnical engineering?, proceedings of the 6th European conference, 6–8 September 2006, Graz, Austria, 267–273, 2006.

Clément, C., Toussaint, R., Stojanova, M., and Aharonov, E.: Sinking during earthquakes: Critical acceleration criteria control drained soil liquefaction, Phys. Rev. E, 97, 0–19, https://doi.org/10.1103/PhysRevE.97.022905, 2018.

Closson, D. and Abou Karaki, N.: Salt karst and tectonics: sinkholes development along tension cracks between parallel strike-slip faults, Dead Sea, Jordan, Earth Surf. Proc. Land., 34, 1408–1421, https://doi.org/10.1002/esp.1829, 2009.

Closson, D., LaMoreaux, P. E., Abou Karaki, N., and Al-Fugha, H.: Karst system developed in salt layers of the Lisan Peninsula, Dead Sea, Jordan, Environ. Geol., 52, 155–172, https://doi.org/10.1007/s00254-006-0469-9, 2007.

Cundall, P. A.: A computer model for simulating progressive large scale movements in blocky rock systems, Proc. Symp.

Rock Fract. (ISRM), Nancy, available at: citeulike-article-id:11887443, 1971.

Cundall, P. A. and Strack, O. D. L.: A discrete numerical model for granular assemblies, Géotechnique, 29, 47–65, available at: citeulike-article-id:11888085, 1979.

Davis, R. O. and Selvadurai, A. P. S.: Elasticity and geomechanics, Cambridge University Press, England, 1996.

Dreybrodt, W. and Kaufmann, G.: Physics and chemistry of dissolution on subaerialy exposed soluble rocks by flowing water films, Acta Carsologica, 36, 357–367, 2007.

El-Naqa, A.: Application of RMR and Q geochemical classification systems along the proposed Mujib Tunnel route, Central Jordan, B. Eng. Geol. Environ., 60, 257–269, https://doi.org/10.1007/s100640100112, 2001.

Ezersky, M. and Frumkin, A.: Fault – Dissolution front relations and the Dead Sea sinkhole problem, Geomorphology, 201, 35–44, https://doi.org/10.1016/j.geomorph.2013.06.002, 2013.

Ezersky, M. and Livne, E.: Mo P 13 Geotechnical and Geophysical Properties of Soils in the Dead Sea Sinkhole Problem, in: Near Surface Geoscience, Bochum, Germany, 2013.

Ezersky, M., Keydar, S., Al-Zoubi, A., and Eppelbaum, L.: Middle East Regional Cooperation Program Jordan – Sinkhole Hazard Assessment of the Dead Sea area in Israel and Jordan: Multidisciplinary study, Washington, D.C., 2013.

Ezersky, M. G., Legchenko, A., Eppelbaum, L., and Al-zoubi, A.: Overview of the geophysical studies in the Dead Sea coastal area related to evaporite karst and recent sinkhole development, Int. J. Speleol., 46, 277–302, https://doi.org/10.5038/1827-806X.46.2.2087, 2017.

Fakhimi, A.: Application of slightly overlapped circular particles assembly in numerical simulation of rocks with high friction angles, Eng. Geol., 74, 129–138, https://doi.org/10.1016/j.enggeo.2004.03.006, 2004.

Fazio, N. L., Perrotti, M., Lollino, P., Parise, M., Vattano, M., Madonia, G., and Di Maggio, C.: A three-dimensional back-analysis of the collapse of an underground cavity in soft rocks, Eng. Geol., 228, 301–311, https://doi.org/10.1016/j.enggeo.2017.08.014, 2017.

Frydman, S., Charrach, J., and Goretsky, I.: Geotechnical properties of evaporite soils of the Dead Sea area, Eng. Geol., 101, 236–244, https://doi.org/10.1016/j.enggeo.2008.06.003, 2008.

Frydman, S., Charrach, J., and Goretsky, I.: A geotechnical study of evaporitic, lacustrine sediments in the saline environment of the Dead Sea area, Eng. Geol., 181, 309–322, https://doi.org/10.1016/j.enggeo.2014.08.028, 2014.

Fuenkajorn, K. and Archeeploha, S.: Prediction of cavern configurations from subsidence data, Eng. Geol., 110, 21–29, https://doi.org/10.1016/j.enggeo.2009.10.003, 2010.

Ghani, I., Koehn, D., Toussaint, R., and Passchier, C. W.: Dynamic Development of Hydrofracture, Pure Appl. Geophys., 170, 1685–1703, https://doi.org/10.1007/s00024-012-0637-7, 2013.

Goldscheider, N. and Drew, D. (Eds.): Methods in Karst Hydrogeology, Taylor and Francis, London, UK, 2007.

Gutiérrez, F., Guerrero, J., and Lucha, P.: A genetic classification of sinkholes illustrated from evaporite paleokarst exposures in Spain, Environ. Geol., 53, 993–1006, https://doi.org/10.1007/s00254-007-0727-5, 2008.

Gutiérrez, F., Parise, M., De Waele, J., and Jourde, H.: A review on natural and human-induced geohazards and impacts in karst, Earth-Sci. Rev., 138, 61–88, https://doi.org/10.1016/j.earscirev.2014.08.002, 2014.

Gutiérrez, F., Fabregat, I., Roqué, C., Carbonel, D., Guerrero, J., García-Hemroso, F., Zarroca, M., Linares, R., García-Hermoso, F., Zarroca, M., and Linares, R.: Sinkholes and caves related to evaporite dissolution in a stratigraphically and structurally complex setting, Fluvia Valley, eastern Spanish Pyrenees. Geological, geomorphological and environmental implications, Geomorphology, 267, 76–97, https://doi.org/10.1016/j.geomorph.2016.05.018, 2016.

Hatzor, Y. H., Wainshtein, I., and Bakun Mazor, D.: Stability of shallow karstic caverns in blocky rock masses, Int. J. Rock Mech. Min. Sci., 47, 1289–1303, https://doi.org/10.1016/j.ijrmms.2010.09.014, 2010.

Hoek, E.: Brittle Fracture of Rock, Rock Mech. Eng. Pract., 1–30, 1968.

Hoek, E.: Practical Rock Engineering, Rocscience, North Vancouver, Canada, 2007.

Hoek, E. and Brown, E. T.: Practical Estimates of Rock Mass Strength, Int. J. Rock. Min. Sci., 34, 1165–1186, 1997.

Hoek, E., Carranza-Torres, C., and Corkum, B.: Hoek-brown failure criterion – 2002 edition, 5th North., University of Toronto, Ontario, Canada, 2002.

Holohan, E. P., Schöpfer, M. P. J., and Walsh, J. J.: Mechanical and geometric controls on the structural evolution of pit crater and caldera subsidence, J. Geophys. Res., 116, B07202, https://doi.org/10.1029/2010JB008032, 2011.

Holohan, E. P., Schöpfer, M. P. J., and Walsh, J. J.: Stress evolution during caldera collapse, Earth Planet. Sc. Lett., 421, 139–151, https://doi.org/10.1016/j.epsl.2015.03.003, 2015.

Holohan, E. P., Sudhaus, H., Walter, T. R., Schöpfer, M. P. J., and Walsh, J. J.: Effects of Host-rock Fracturing on Elastic-deformation Source Models of Volcano Deflation, Sci. Rep., 7, 10970, https://doi.org/10.1038/s41598-017-10009-6, 2017.

Itasca Cooperation Group, I.: PFC 5.0 Manual, Itasca, 2014.

Ivars, D. M., Pierce, M. E., Darcel, C., Reyes-Montes, J., Potyondy, D. O., Paul Young, R., and Cundall, P. A.: The synthetic rock mass approach for jointed rock mass modelling, Int. J. Rock Mech. Min. Sci., 48, 219–244, https://doi.org/10.1016/j.ijrmms.2010.11.014, 2011.

Jaeger, J. C., Cook, N. G. W., and Zimmerman, R.: Fundamentals of rock mechanics, 4th ed., Wiley – Blackwell, 2007.

Jing, L. and Stephansson, O.: Fundamentals of Discrete Element Methods for Rock Engineering I, Elsevier, 2007.

Kaufmann, G. and Romanov, D.: Structure and evolution of collapse sinkholes?, Combined interpretation from physico-chemical modelling and geophysical field work, J. Hydrol., 17, 2958, https://doi.org/10.1016/j.jhydrol.2016.06.050, 2016.

Khanal, M. and Schubert, W.: DEM simulation of diametrical compression test on particle compounds, Granul. Matter, 7, 83–90, https://doi.org/10.1007/s10035-005-0200-7, 2005.

Khoury, H. N.: Clays and clay minerals in Jordan, Amman, Jordan, 2002.

Kirsch, E. G.: Die Theorie der Elastizität und die Bedürfnisse der Festigkeitslehre, Z. Ver. Dtsch. Ing., 42, 797–807, 1898.

Koolen, A. J. and Vaandrager, P.: Relationships between soil mechanical properties, J. Agr. Eng. Res., 29 313–319, https://doi.org/10.1016/0021-8634(84)90086-6, 1984.

Manger, E. G.: Porosity and Bulk Density of Sedimentary Rocks, edited by: Udall, S. and Nolan, T., US Government Printing Office, Washington, D.C., 1963.

Mercerat, E. D.: Évaluation de l'endommagement dans le recouvrement d'une cavité saline par une approche numérique couplée continue-discrète, in XXVèmes Rencontres Universitaires de Genie Civil, Nancy, France, 2007.

Mindlin, R. D.: Stress distribution around a tunnel, T. Am. Soc. Civ. Eng., 2082, 1117–1153, 1940.

Muskhelishvili, N. I.: Singular Integral Equations: Boundary Problems of Functions Theory and Their Application to Mathematical Physics, P. Noordhoff, 1953.

Muskhelishvili, N. I.: Some basic problems of the mathematical theory of elasticity, Springer Science & Business Media, 2013.

Nikkhoo, M. and Walter, T. R.: Triangular dislocation: an analytical, artefact-free solution, Geophys. J. Int., 201, 1119–1141, https://doi.org/10.1093/gji/ggv035, 2015.

Oz, I., Eyal, S., Yoseph, Y., Ittai, G., Elad, L., and Haim, G.: Salt dissolution and sinkhole formation: Results of laboratory experiments, J. Geophys. Res.-Earth, 121, 1–17, https://doi.org/10.1002/2016JF003902, 2016.

Parise, M. and Gunn, J.: Natural and anthropogenic hazards in karst areas: recognition, analysis and mitigation, Geological Society of London, 2007.

Parise, M. and Lollino, P.: A preliminary analysis of failure mechanisms in karst and man-made underground caves in Southern Italy, Geomorphology, 134, 132–143, https://doi.org/10.1016/j.geomorph.2011.06.008, 2011.

Parise, M., Gabrovsek, F., Kaufmann, G., and Ravbar, N.: Recent advances in karst research: from theory to fieldwork and applications, Geol. Soc. London, Spec. Publ., SP466.26, https://doi.org/10.1144/SP466.26, 2018.

Polom, U., Alrshdan, H., Al-Halbouni, D., Holohan, E. P., Dahm, T., Sawarieh, A., Atallah, M. Y., and Krawczyk, C. M.: Shear wave reflection seismic yields subsurface dissolution and subrosion patterns: application to the Ghor Al-Haditha sinkhole site, Dead Sea, Jordan, Solid Earth, 9, 1079–1098, https://doi.org/10.5194/se-9-1079-2018, 2018.

Poppe, S., Holohan, E. P., Pauwels, E., Cnudde, V., and Kervyn, M.: Sinkholes, pit craters, and small calderas: Analog models of depletioninduced collapse analyzed by computed X-ray microtomography, B. Geol. Soc. Am., 127, 281–296, https://doi.org/10.1130/B30989.1, 2015.

Potyondy, D.: Material-Modeling Support in PFC, Minneapolis, Minnesota, USA, 2014a.

Potyondy, D. O.: The bonded-particle model as a tool for rock mechanics research and application: current trends and future directions, Geosystem Eng., 17, 342–369, 2014b.

Potyondy, D. O. and Cundall, P. A. A.: A bonded-particle model for rock, Int. J. Rock Mech. Min. Sci., 41, 1329–1364, https://doi.org/10.1016/j.ijrmms.2004.09.011, 2004.

Rawal, K., Wang, Z.-M., and Hu, L.-B.: Exploring the Geomechanics of Sinkholes: A Numerical Study of Sinkhole Subsidence and Collapse, in: 4th Geo-China International Conference, Shandong, China, https://doi.org/10.1061/9780784480007.001, 2016.

Sainsbury, B.: A model for cave propagation and subsidence assessment in jointed rock masses, University of South Wales, 2012.

Salmi, E. F., Nazem, M., and Giacomini, A.: A Numerical Investigation of Sinkhole Subsidence Development over Shallow Excavations in Tectonised Weak Rocks: The Dolaei Tunnel's Excavation Case, Geotech. Geol. Eng., 35, 1685–1716, https://doi.org/10.1007/s10706-017-0202-3, 2017.

Sawarieh, A., Al Adas, A., Al Bashish, A., and Al Seba'i, E.: Sinkholes Phenomena At Ghor Al Haditha Area – Internal Report No. 12, Amman, Jordan, 2000.

Schöpfer, M. P. J., Childs, C., and Walsh, J. J.: Two-dimensional distinct element modeling of the structure and growth of normal faults in multilayer sequences: 1. Model calibration, boundary conditions, and selected results, J. Geophys. Res., 112, B10401, https://doi.org/10.1029/2006JB004902, 2007.

Schöpfer, M. P. J., Abe, S., Childs, C., and Walsh, J. J.: The impact of porosity and crack density on the elasticity, strength and friction of cohesive granular materials: Insights from DEM modelling, Int. J. Rock Mech. Min. Sci., 46, 250–261, https://doi.org/10.1016/j.ijrmms.2008.03.009, 2009.

Schöpfer, M. P. J., Childs, C., and Manzocchi, T.: Three-dimensional failure envelopes and the brittle-ductile transition, J. Geophys. Res.-Sol. Ea., 118, 1378–1392, https://doi.org/10.1002/jgrb.50081, 2013.

Schöpfer, M. P. J., Childs, C., Manzocchi, T., and Walsh, J. J.: Three-dimensional Distinct Element Method modelling of the growth of normal faults in layered sequences, Geol. Soc. London, Spec. Publ., 439, SP439.17, https://doi.org/10.1144/SP439.17, 2016.

Schöpfer, M. P. J., Childs, C., Manzocchi, T., Walsh, J. J., Nicol, A., and Grasemann, B.: The emergence of asymmetric normal fault systems under symmetric boundary conditions, J. Struct. Geol., 104, 159–171, https://doi.org/10.1016/j.jsg.2017.10.006, 2017.

Schultz, R. A.: Relative scale and the strength and deformability of rock masses, J. Struct. Geol., 18, 1139–1149, https://doi.org/10.1016/0191-8141(96)00045-4, 1996.

Shalev, E. and Lyakhovsky, V.: Viscoelastic damage modeling of sinkhole formation, J. Struct. Geol., 42, 163–170, https://doi.org/10.1016/j.jsg.2012.05.010, 2012.

Taqieddin, S. A., Abderahman, N. S., and Atallah, M.: Sinkhole hazards along the eastern Dead Sea shoreline area, Jordan: a geological and geotechnical consideration, Environ. Geol., 39, 1237–1253, https://doi.org/10.1007/s002549900095, 2000.

Terzaghi, K.: Rock Defects and loads on Tunnel Supports, Harvard Univ. PP – Massachusetts, 1946.

Tharp, T. M.: Mechanics of upward propagation of cover-collapse sinkholes, Eng. Geol., 52, 23–33, https://doi.org/10.1016/S0013-7952(98)00051-9, 1999.

Thompson, N., Bennett, M. R., and Petford, N.: Development of characteristic volcanic debris avalanche deposit structures: New insight from distinct element simulations, J. Volcanol. Geoth. Res., 192, 191–200, https://doi.org/10.1016/j.jvolgeores.2010.02.021, 2010.

Timoshenko, S. P. and Goodier, J. N.: Theory of Elasticity, Internatio, Kogakusha Company Ltd., Tokyo, 1973.

Verlet, L.: Computer "Experiments" on Classical Fluids. I. Thermodynamical Properties of Lennard-Jones Molecules, Phys. Rev., 159, 98–103, 1967.

Verruijt, A. and Booker, J. R.: Complex variable analysis of Mindlin's tunnel problem, Dev. Theor. Geomech., 1–20, 2000.

Verruijt, A. and Booker, J. R.: Complex Variable Solution of Mindlin's Problem of an Excavated Tunnel (background material of the publication by Verruijt & Booker, 2000), Dev. Theor. Geomech., 2009.

Wadas, S. H., Polom, U., and Krawczyk, C. M.: High-resolution shear-wave seismic reflection as a tool to image near-surface subrosion structures – a case study in Bad Frankenhausen, Germany, Solid Earth, 7, 1491–1508, https://doi.org/10.5194/se-7-1491-2016, 2016.

Waltham, T., Bell, F., and Culshaw, M. G.: Sinkholes and subsidence: Karst and Cavernous Rocks in Engineering and Construction, Springer, Berlin, Heidelberg, 2005.

Watson, R. A., Holohan, E. P., Al-Halbouni, D., Saberi, L., Sawarieh, A., Closson, D., Alrshdan, H., Abou Karaki, N., Siebert, C., Walter, T. R., and Dahm, T.: Sinkholes, stream channels and base-level fall: a 50-year record of spatio-temporal development on the eastern shore of the Dead Sea, Solid Earth Discuss., https://doi.org/10.5194/se-2018-105, in review, 2018.

Yechieli, Y., Abelson, M., Bein, A., Crouvi, O., and Shtivelman, V.: Sinkhole “swarms” along the Dead Sea coast: Reflection of disturbance of lake and adjacent groundwater systems, Geol. Soc. Am. B., 118, 1075–1087, https://doi.org/10.1130/B25880.1, 2006.

Yizhaq, H., Raz, E., Ashkenazy, Y., Cohen, C., Raz, E., and Ashkenazy, Y.: Scale-free distribution of Dead Sea sinkholes?: Observations and modeling, Geophys. Res. Lett., 44, 1–9, https://doi.org/10.1002/2017GL073655, 2017.

Yoon, J. S., Zimmermann, G., and Zang, A.: Numerical Investigation on Stress Shadowing in Fluid Injection-Induced Fracture Propagation in Naturally Fractured Geothermal Reservoirs, Rock Mech. Rock Eng., 48, 1439–1454, https://doi.org/10.1007/s00603-014-0695-5, 2015.

Zeev, S. Ben, Goren, L., Parez, S., Toussaint, R., Clement, C., and Aharonov, E.: The Combined Effect of Buoyancy and Excess Pore Pressure in Facilitating Soil Liquefaction, in Poromechanics VI, 107–116, 2017.

Zhu, T.: Some useful numbers on the engineering properties of materials (geologic and otherwise), available at: https://www.jsg.utexas.edu/tyzhu/files/Some-Useful-Numbers.pdf (last access: 23 February 2018), 2010.

CHAPTER 5

Distinct element geomechanical modelling of the formation of sinkhole clusters within large-scale karstic depressions.

Published on 29 of July 2019 in *Solid Earth* vol. 10 pp. 1219–1241.
https://doi.org/10.5194/se-10-1219-2019

Solid Earth, 10, 1219–1241, 2019
https://doi.org/10.5194/se-10-1219-2019

Solid Earth
Open Access

Distinct element geomechanical modelling of the formation of sinkhole clusters within large-scale karstic depressions

Djamil Al-Halbouni[1,2], **Eoghan P. Holohan**[3], **Abbas Taheri**[4], **Robert A. Watson**[3], **Ulrich Polom**[5], **Martin P. J. Schöpfer**[6], **Sacha Emam**[7], **and Torsten Dahm**[1,2]

[1]Helmholtz Centre – German Research Centre for Geosciences (GFZ), Physics of Earthquakes and Volcanoes, Telegrafenberg, Potsdam, Germany
[2]University of Potsdam, Institute of Geosciences, P.O. Box 601553, Potsdam–Golm, Germany
[3]UCD School of Earth Sciences, University College Dublin, Belfield, Dublin, Ireland
[4]School of Civil, Environmental and Mining Engineering, University of Adelaide, Adelaide, South Australia, Australia
[5]Department S1 – Seismics, Gravimetry, and Magnetics, Leibnitz Institute for Applied Geophysics (LIAG), Stilleweg 2, Hanover, Germany
[6]Department for Geodynamics and Sedimentology, University of Vienna, Athanstrasse 14, Vienna, Austria
[7]Geomechanics and Software Engineer, Itasca Consultants S.A.S, Écully, France

Correspondence: Djamil Al-Halbouni (halbouni.etal@posteo.de)

Received: 26 January 2019 – Discussion started: 29 January 2019
Revised: 24 May 2019 – Accepted: 19 June 2019 – Published: 29 July 2019

Abstract. The 2-D distinct element method (DEM) code (PFC2D_V5) is used here to simulate the evolution of subsidence-related karst landforms, such as single and clustered sinkholes, and associated larger-scale depressions. Subsurface material in the DEM model is removed progressively to produce an array of cavities; this simulates a network of subsurface groundwater conduits growing by chemical/mechanical erosion. The growth of the cavity array is coupled mechanically to the gravitationally loaded surroundings, such that cavities can grow also in part by material failure at their margins, which in the limit can produce individual collapse sinkholes. Two end-member growth scenarios of the cavity array and their impact on surface subsidence were examined in the models: (1) cavity growth at the same depth level and growth rate; (2) cavity growth at progressively deepening levels with varying growth rates. These growth scenarios are characterised by differing stress patterns across the cavity array and its overburden, which are in turn an important factor for the formation of sinkholes and uvala-like depressions. For growth scenario (1), a stable compression arch is established around the entire cavity array, hindering sinkhole collapse into individual cavities and favouring block-wise, relatively even subsidence across the whole cavity array. In contrast, for growth scenario (2), the stress system is more heterogeneous, such that local stress concentrations exist around individual cavities, leading to stress interactions and local wall/overburden fractures. Consequently, sinkhole collapses occur in individual cavities, which results in uneven, differential subsidence within a larger-scale depression. Depending on material properties of the cavity-hosting material and the overburden, the larger-scale depression forms either by sinkhole coalescence or by widespread subsidence linked geometrically to the entire cavity array. The results from models with growth scenario (2) are in close agreement with surface morphological and subsurface geophysical observations from an evaporite karst area on the eastern shore of the Dead Sea.

1 Introduction

Karstification occurs worldwide in rocks like limestone, dolomite, gypsum, anhydrite and salt primarily by chemical dissolution (BGR et al., 2017). While subsurface-solution-based drainage networks and connected void spaces resulting from karstification are hydrologically important for groundwater provision (Chen et al., 2017), such features reduce the mechanical stability of the geologic material and so may

Published by Copernicus Publications on behalf of the European Geosciences Union.

pose a significant hazard to humans and infrastructure. Sinkholes, also termed dolines, are the prominent karst landforms (Waltham et al., 2005). They form enclosed small- to large-scale depressions that are commonly considered to be morphological expressions of material removal in the underground and subsequent collapse of the overburden (Gutiérrez et al., 2014; De Waele et al., 2011; Waltham, 2016). Often, systems develop into agglomerations of closely spaced or coalesced dolines and elongated valley-like depressions, potentially revealing linear patterns of drainage (Waltham et al., 2005). Such sinkhole cluster development can be highly dynamic and partly accelerating, and may affect large areas in short times (e.g. Abelson et al., 2017). Understanding their development and, where possible, their precursory signals is of utmost importance to mitigate their hazard and to promote sustainable land and water usage.

The main problem for unravelling the geometric and genetic relationships between sinkhole cluster development and larger-scale depressions in limestone karst areas, where such landforms have historically been best described, is that the landform evolution is controlled by the relatively slow dissolution kinetics of carbonate minerals. Consequently, the development of these karstic landform types is not directly observable in such areas, and furthermore, it is susceptible to long-term influences from climate change and tectonic activity. Indeed, the areas in which dolines and other karstic depressions have been historically best documented have been modified not only by karst processes but also by fluvial and/or glacial processes (compare Ćalić, 2011).

An opportunity to shed new light on such relationships has arisen in an evaporite karst setting at the margins of the shrinking Dead Sea (Yechieli et al., 2016). There, clusters of tens to over a hundred sinkholes (1–75 m diameter) that are surrounded by larger-scale (100–800 m diameter) depressions have rapidly developed over the last 40 years (Al-Halbouni et al., 2017; Atzori et al., 2015; Filin et al., 2011). In particular, recent studies by (Al-Halbouni et al., 2017; Watson et al., 2019) involving field work, remote sensing and photogrammetric surveying enabled the detailed documentation of spatiotemporal relationships between sinkhole and depression development at Ghor Al-Haditha, on the eastern shore of the Dead Sea (Fig. 1a). The area exhibits mature karst landforms comprising individual and compound sinkholes. The term "compound sinkhole" here means the nested or non-nested coalescence of individual sinkholes. Sinkhole clusters or aggregations commonly comprise multiple individual sinkholes and/or compound sinkholes in close proximity. Such clusters commonly lie within gentler, larger-scale (uvala-like) depressions of up to several hundreds of metres in diameter, as depicted in Fig. 1b and c.

Initially, these karst landforms develop as small localised subsidence zones, with single sinkholes that form in heterogeneous material made of Dead Sea mud, alluvial fan sediments and salt (Watson et al., 2019). Wider-scale subsidence and sinkhole clustering follow, with ground fracture systems developing that are geometrically related to the larger-scale depression rather than to the individual sinkholes or sinkhole clusters (Fig. 2).

In this paper, we test the hypothesis that the driving process for the geomorphological and structural development of such large-scale karst features is a widespread, differential subsidence above an array of subsurface cavities, with temporally and spatially variable patterns of material removal driven by base-level fall associated with the shrinking of the Dead Sea.

To test our hypothesis, we use a novel 2-D distinct element method (DEM) numerical modelling. We examine two end-member growth scenarios of model cavity arrays, and we look at the surface morphologies, subsurface structure and stress patterns developed by subsidence of the overburden as those cavity arrays grow. The numerical results are discussed with respect to both surface and subsurface data from the Dead Sea evaporite karst. Interpretation of shear wave reflection data indicates that the subsurface under the alluvial fan sediments at the Ghor Al-Haditha site is characterised by inclined layering typical of a prograding Gilbert-type delta, superimposed on which are zones of disrupted seismic reflectors, as well as bowls and depression structures (Polom et al., 2018). We provide in this work both a qualitative and quantitative comparison of the results from the seismic survey and from the numerical modelling. We show that our more complex end-member modelling scenario is able to explain complementary observations from surface morphology to subsurface hydrology and subsurface geophysics.

2 Numerical approach

2.1 Distinct element method numerical modelling

The mechanical interaction of a single void space with its surrounding rock mass has been investigated previously by analytical methods (e.g. Tharp, 1999) and numerical modelling studies (e.g. Al-Halbouni et al., 2018; Baryakh et al., 2009; Fazio et al., 2017; Hatzor et al., 2010; Parise and Lollino, 2011). Little is known, however, about the mechanical interactions between multiple actively evolving void spaces in the subsurface and about how these interactions may lead to the development of sinkhole clusters and large-scale depressions. Moreover, commonly used continuum numerical simulation methods are usually not appropriate to simulate rotation, detachment and non-continuous deformation found in rocks or semi-consolidated materials that have been subject to large strains, which are characteristic of sinkhole collapses. Discontinuous medium simulation methods, on the other hand, allow for complex behaviours like spontaneous crack formation and block rotation (Jing and Stephansson, 2007). The distinct element method (Cundall, 1971) is a subset of discrete element modelling (Cundall and Strack, 1979; Jing and Stephansson, 2007), whereby a ma-

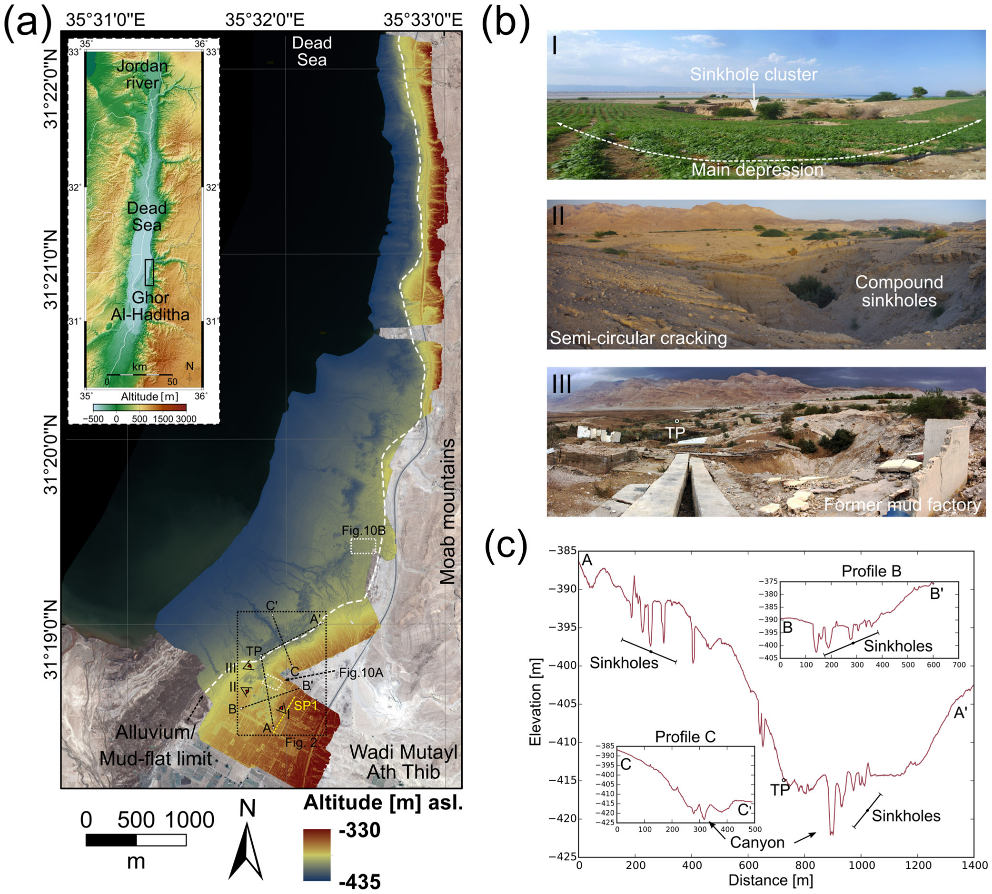

Figure 1. Topography of the Ghor Al-Haditha sinkhole area. **(a)** Digital surface model (DSM) from 2016 on Pleiades satellite image from 2015 for the sinkhole area at the Dead Sea (inset). The DSM has a resolution of 10 cm px^{-1} and accuracy of 37 and 31 cm (H and V), respectively. The main zone affected by sinkholes extends from the south towards the NNE along the contact zone between alluvial fans and the mud flat (dashed white line) and comprises several partly connected large depression zones, of which the main area is indicated by the square. SP1 is a section of seismic profile 1 of Polom et al. (2018). **(b)** Typical examples of sinkhole formations in the main depression. (I) View from the stable agricultural area towards the centre of the depression. (II) Nested sinkholes and ground cracks from the opposite view. (III) Destroyed "Numeira" mud factory at the turning point (TP) of the depression. **(c)** N–S and E–W topographic profiles across the several-hundred-metre depression, derived from the DSM of 2016.

terial is represented as an assembly of non-deformable particles in the shape of disks of unit thickness (2-D, Fig. 3) or spheres (3-D). The particles are assigned a density, radius and elastic contact modulus. They are assembled with a certain porosity and follow a defined size distribution. The particles follow the Newton–Euler laws of motion and the linear force-displacement law as they interact elastically at each contact point. The assembly is generated via a randomised particle-packing scheme and a gravitational settling scheme (Al-Halbouni et al., 2018), after which particles can be bonded with their neighbours (Potyondy and Cundall, 2004). In this study, we used the parallel-bond model (PBM) in the commercially available PFC2D software (Potyondy, 2014), which sets a second pair of elastic springs that incorporate moments and can fail either in shear or tension, allowing for a complex elasto-plastic rheology (Al-Halbouni et al., 2018; Holohan et al., 2011; Potyondy and Cundall, 2004; Schöpfer et al., 2009). The resulting differential equations are solved via a finite-difference explicit time-stepping algorithm (Jing and Stephansson, 2007). Each model requires multiple realisations as the outcomes generally depend on the randomised particle packing. For more mathematical details on the calculations and modelling scheme, refer to Al-Halbouni et al. (2018), Itasca (2014), Jing and Stephansson (2007), Potyondy (2014) and Wang et al. (2018).

2.2 Cavity growth in a DEM model

Al-Halbouni et al. (2018) simulated the growth of a single cavity in a DEM model, and they conducted a detailed calibration and verification procedure to determine the optimal model geometry, resolution and material removal technique. We here adopt the same setup parameters and conditions: i.e. a 2-D box of model height $H \times$ width $W = 400 \times 400$ m, a

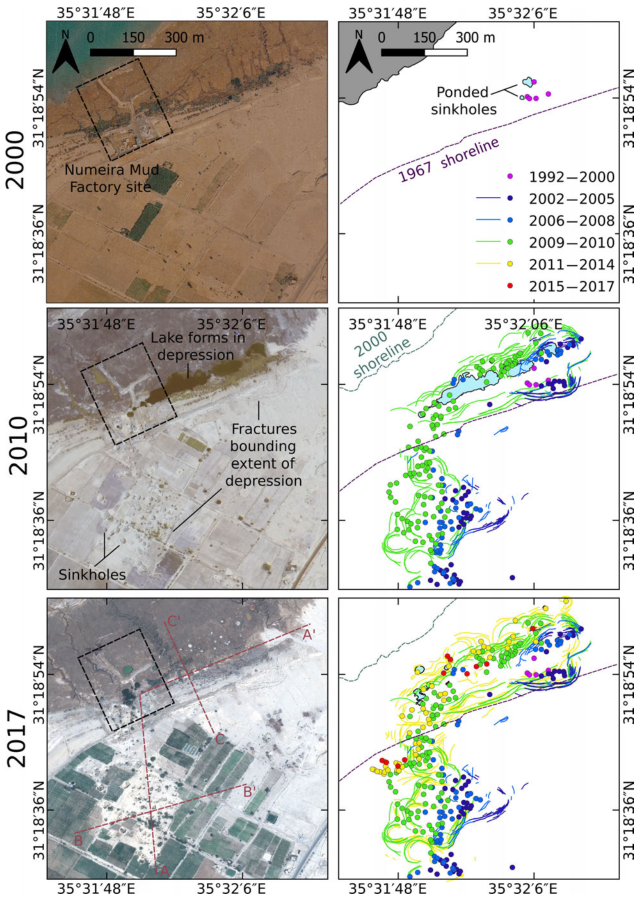

Figure 2. Remote sensing analysis of the evolution of sinkholes, cracks and large depressions at the main depression of Ghor Al-Haditha, Dead Sea. Small single sinkholes appear in 2000 at the former "Numeira" mud factory site ($0.6\,\mathrm{m\,px^{-1}}$ aerial photo from Royal Jordanian Geographic Centre). Up to 2010, lakes, sinkhole clusters and large fractures have appeared around a depression zone spanning over both alluvium and the mud flat ($0.5\,\mathrm{m\,px^{-1}}$ GeoEye-1 satellite image). Up to today, the number of fractures and sinkholes as well as the depth of the depression has increased ($0.5\,\mathrm{m\,px^{-1}}$ Pleiades satellite image). Red lines in lower left image mark the locations of the profiles shown in Fig. 1c.

uniform particle distribution between a minimum ($R_{\mathrm{min}} = 0.24\,\mathrm{m}$) and maximum particle radius ($R_{\mathrm{max}} = 0.4\,\mathrm{m}$); an initial porosity of the unsettled assembly of $n = 0.2$; no-slip boundary conditions; and a fixed wall elastic modulus of $E_{\mathrm{w}} = 5\,\mathrm{GPa}$. Instead of simulating material removal in a single cavity as in Al-Halbouni et al. (2018), here, we implemented an array of multiple cavities of arbitrary shape (Fig. 3a; see Appendix A1). The adopted procedure is an incremental particle removal that mimics subrosion, i.e. the removal of subsurface material by chemical leaching and/or physical erosion. Our 2-D model thus represents a flow-perpendicular cross-section through a groundwater conduit network, which we envisage to result from dissolution that rapidly localises through a feedback mechanism of enhanced fluid flow with increasing dissolution (Weisbrod et al., 2012) and which in turn can also promote conduit growth by physical erosion.

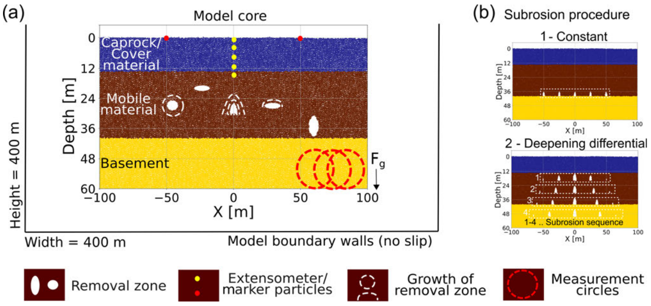

Figure 3. Generic setup for multiple cavity modelling with DEM. **(a)** The core of the model and the specific setup of the void zone and implemented features. Arbitrary material removal zones can be defined and associated with different removal functions activated at arbitrary removal zone growth increments. **(b)** The subrosion procedures for (1) models with deep constant subrosion and (2) models with deepening and differential cavity growth are highlighted.

We test two end-member growth scenarios of the cavity array and their impact on surface subsidence in the models (Fig. 3b): (1) cavity growth at the same depth level and at the same individual growth rate; (2) cavity growth at progressively deepening levels with varying individual growth rates. The quasi-static growth is simulated by incremental particle removal and details can be found in Appendix A1 and A2. In the first scenario, five semi-elliptical cavities begin to grow at the same time, at the same constant rate, and at the same depth of 40 m. The latter has been chosen according to tests on single cavities in Al-Halbouni et al. (2018) and similar tests on cavity arrays as presented in Appendix A2. In the second scenario, the five cavities start to grow simultaneously, but the initial cavity area is largest in the centre and decreases laterally. In addition, the cavity growth rate is largest for the central cavity and smallest for the outermost cavities. This represents the energy distribution of a progressively focussed flow within the growing conduit system. Furthermore, the array geometry changes as new cavity sets develop at progressively increasing depths from 20 to 50 m at 10 m increments. The growth in the shallower cavity set stops when the new set initiates. The area of removed particles multiplied by a unit thickness is considered as the total removed volume, ΔV. A 30 m deep cavity set only initiates after a total volume removal of $\Delta V \sim 400\,\mathrm{m}^3$, a 40 m deep set starts after $\Delta V \sim 800\,\mathrm{m}^3$, and a 50 m deep set starts after $\Delta V \sim 1200\,\mathrm{m}^3$. The width of the array also increases slightly from $\sim 110\,\mathrm{m}$ in the shallow part to $\sim 150\,\mathrm{m}$ in the deep part. This progressive initiation of newer and deeper sets of cavities represents a vertical evolution of a dissolution front during base-level fall, the main hydrogeological boundary condition at the shrinking Dead Sea (Abelson et al., 2017; Bartov, 2002; Watson et al., 2019).

2.3 Material parameters

The bonded particle assembly's bulk material properties, which emerge from the properties defined on the particle scale, were constrained by simulated geomechanical tests on material samples (Schöpfer et al., 2007; Al-Halbouni et al., 2018). Parallel-bond tensile strength, modulus and friction, cohesion and friction angle, as well as contact modulus and friction, are hence transferred to corresponding bulk values of unconfined compressive strength (UCS) and tensile strength (T), Poisson's ratio (ν) and Young's modulus (E). This calibration procedure has been done for three materials representing those in which sinkholes form at the Dead Sea shoreline: (1) low-strength marl (mud) of the former Dead Sea lake bed, (2) middle-strength sandy-gravel alluvial fan sediments and (3) relatively high-strength Holocene rock salt of the Dead Sea (Table 1). For (1), a bond-healing procedure has been implemented to account for a more realistic recombination behaviour of naturally wet muddy material. For each material, the calibration was run on 10 subsamples of $H \times W = 10 \times 8$ m size, with approximately 200 particles of a mean radius $\overline{R} = 0.32$ m. See Al-Halbouni et al. (2018) for details on the procedure.

2.4 Geophysical parameter tracking

Distributed measurement circles of 10 m diameter (area $A^{\mathrm{m}} = 78.5\,\mathrm{m}^2$) are used to record stresses, strain rates, positions and porosity of the particle assemblies (see Al-Halbouni et al., 2018, for details). From recording of the stress components ($\sigma_{xx}\sigma_{xy}, \sigma_{yx}, \sigma_{yy}$) and particle areas, we calculate the principal stresses, σ_1 (most compressive, i.e. most negative) and σ_3 (least compressive) The maximum shear stress is calculated via half the differential stress (e.g. Holohan et al., 2015):

$$\tau_{\max} = \frac{(\sigma_3 - \sigma_1)}{2}. \tag{1}$$

For strain calculation, the displacement gradient tensor is calculated for particles inside the 50 % overlapping measurement circles between two simulation stages (e.g. Schöpfer et al., 2006). The maximum in-plane shear strain is determined via the principal strains (ε_1, ε_3) and the shear strain (γ_{xy}):

$$\gamma_{\max} = 2\sqrt{\frac{(\varepsilon_1 - \varepsilon_3)^2}{2} + \frac{\gamma_{xy}^2}{2}}. \tag{2}$$

We use porosity-tracking results to determine apparent elastic moduli, which can then be translated via bulk density into apparent bulk seismic velocities. In general, for a homogeneous, linearly elastic, isotropic medium, compression wave velocities (v_p) and shear wave velocities (v_s) are estimated by

$$v_\mathrm{s} = \sqrt{\frac{G}{\rho}} \tag{3}$$

$$v_\mathrm{p} = \sqrt{\frac{K + \frac{4}{3}\nu}{\rho}} = \sqrt{\frac{2G(1-\nu)}{\rho\,(1-2\nu)}}. \tag{4}$$

KG are the bulk/shear modulus, respectively. $E = 2G\,(1+\nu)$ is Young's elastic modulus for homogeneous, isotropic materials, with ν as the Poisson ratio. ρ is the bulk density calculated by $\rho = \rho_{\mathrm{particle}}(1-n)$, with n as the particle-packing porosity. A correction factor is needed to account for the differences between static and dynamic moduli to enable a comparison of numerical simulation with field data. Dynamic field methods like seismic reflection profiling measure at small strains and therefore reveal high values of the shear modulus. E and ν of the model materials are known from simulated large-strain compression tests for a variation of confining pressures and porosities (Al-Halbouni et al., 2018). We here use $G_{\mathrm{dyn}} \sim 1.5 \times G_{\mathrm{stat}}$, the dynamic shear modulus, approximated as a minimum scaling of the static shear modulus determined for unconsolidated sand in a cycling loading/unloading and shearing test (Soldal and Mondol, 2015). The factor depends on the applied static technique in laboratory experiments and on the cycles; the difference arises mainly from the strain amplitude (Hammam and Eliwa, 2013; Wichtmann and Triantafyllidis, 2009). Furthermore, from the simulated compression tests, conservative values for moduli and Poisson ratio are taken at limits where few or no cracks have appeared in the sample. For a more realistic approach, the values are further adjusted by accounting for the crack (broken bond) density in the model, following Dahm and Becker (1998). For the adjustment to the DEM, crack density is defined as $c = k\pi\overline{R}/A^{\mathrm{m}}$, with k as the number of cracks, A^{m} the area of the measurement circle and $\overline{R}$ the mean particle radius, which is a proxy to the parallel-bond (crack) half length (see Al-Halbouni et al., 2018, for details). Cracks, i.e. broken parallel bonds in DEM, are recorded by using an intrinsic "fishcall" procedure (Hazzard, 2014; Hazzard and Young, 2004) and distributed onto the according measurement circles. With increasing crack density, ν and the apparent (effective) shear modulus G_{eff} are expected to change by

$$\nu(c) = \frac{(1-\nu_0)\,e^{\frac{fc}{2}} + 2\nu_0 - 1}{2\,(1-\nu_0)\,e^{\frac{fc}{2}} + 2\nu_0 - 1} \tag{5}$$

$$G(c)_{\mathrm{eff}} = G_0/(2\,(1-\nu_0)\,e^{\frac{fc}{2}} + 2\nu_0 - 1). \tag{6}$$

For randomly oriented cracks, the mean of the shear tractions on the cracks is one-half of the maximum shear stress in the body (compare Dahm and Becker, 1998), for which a factor of $f = 0.5$ can be estimated. Furthermore, $\nu_0 = 0.5$ is the Poisson ratio when the bulk modulus is larger than G_0,

Table 1. Estimated mean bulk geomechanical properties of the main materials in sinkhole-affected areas at the Dead Sea. The variation of the bulk strength values is related to analysis by both Mohr–Coulomb and Hoek–Brown failure criteria assuming intact rock (Al-Halbouni et al., 2018). Note the geotechnical engineering convention of compressive stress being taken as negative.

Parameter	Symbol	Unit	Wet lacustrine mud	Alluvial sediment	Holocene salt
Particle-packing porosity	n_{eff}	–	0.21	0.2	0.17
Bulk density	ρ_{bulk}	$[\mathrm{kg\,m^{-3}}]$	2145	2200	2075
Young's modulus	E_{eff}	[GPa]	0.084 ± 0.02	0.174 ± 0.025	1.106 ± 0.126
Poisson's ratio	ν_{eff}	–	0.19 ± 0.12	0.31 ± 0.6	0.30 ± 0.03
Unconfined compressive strength	UCS	[MPa]	-0.25 to -0.06	-0.92 to -0.52	-1.54 to -1.23
Unconfined tensile strength	T	[MPa]	0.01–0.2	0.18–0.24	0.31–0.43
Cohesion	c	[MPa]	0.11	0.18	0.36
Friction angle	ϕ	[°]	5.7	22.3	28.8

the shear modulus of a homogeneous, isotropic rock mass (Dahm and Becker, 1998).

3 Modelling results

In this section, we present outcomes of both end-member cavity growth scenarios, while focussing on a final model setup that most closely reproduces the natural karst landforms (Sect. 1). For both end-member cavity growth scenarios, we also show the results of models for layered combinations of weak and strong materials common at the Dead Sea shoreline. Note that for certain model conditions (weak material and/or deep subrosion; see also Al-Halbouni et al., 2018) the cavity walls and overburden tend to collapse immediately, and so cavities may remain small during a model evolution or may exist only instantaneously for each increment of material removal.

In Fig. 4, we compare the outcomes of both end-member cavity growth scenarios for four different material setups representing weak and strong overburden configurations: (I) alluvium-on-lacustrine mud (Fig. 4a), (II) a thin salt layer above lacustrine mud and alluvium (Fig. 4b), (III) pure lacustrine mud (Fig. 4c) and (IV) a mud layer above a salt and alluvium succession (Fig. 4d). In this overview, a clear difference between the cavity growth scenario (1), constant medium-depth (40 m) subrosion, and scenario (2), a differential deepening subrosion, can be seen. While scenario (1) results in block-wise subsidence or large-scale sagging over the entire array, scenario (2) reproduces the observed pattern of multiple sinkholes in a large-scale depression zone. The main structural and morphological features that relate to differences in material and in subrosion scenario are marked in each individual plot.

In Fig. 5, we show the main evolutionary stages (I–VI) of sinkhole/depression development for cavity growth scenario (2), i.e. the deepening differential cavity growth scenario. Detailed animations of the evolution can be found in the Supplement.

For all combinations of material type, the large-scale depression is deepest throughout the evolution above the central and fastest growing cavity in each array (as per definition in the model setup).

In general, for the material combination of a strong or weak overburden above a weak cavity-hosting material (Fig. 5a–c), individual sinkholes form synchronously with, or just before, the development of a larger-scale synclinal depression that initially spans several central cavities and eventually spans the cavity array as a whole. The formation of the sinkholes more clearly predates the array-scale depression where the overburden is weak. The margins of the array-scale synclinal depression are commonly delimited, especially in the strong overburden, by fractures and/or faults. These marginal fractures geometrically relate to subsidence across several cavities or to subsidence across the entire array, rather than to collapses into individual cavities. In weaker overburden, the margins of the main depression are defined by inward bending (sagging) of the overburden layers (although in detail there are many small-scale fractures here).

For the material combination of a weak overburden above a strong cavity-hosting material (Fig. 5d), large cavities can develop before the overburden collapses into them. This produces deeper and wider sinkholes in the later stages of the model evolution. Also in this case, the strong cavity-hosting material does not deform so easily around the cavity array as a whole; therefore, synclinal bending of the overburden across the cavity array is much less pronounced. Consequently, a larger-scale depression forms in this case mainly by nesting and coalescence of the sinkholes.

For individual sinkholes in strong overburden materials (Fig. 5a, b), the collapsed overburden is commonly delimited by faults near the surface, but at depth the structure takes a synclinal form (V-shaped) on the same scale as the individual cavities. For individual sinkholes in weak overburden material (Fig. 5c, d), the collapsed overburden shapes are synclinal at all depths. In the strong cavity-hosting material (Fig. 5d), the deep levels of the individual collapse zones are again in part fault bounded but also take in part a syn-

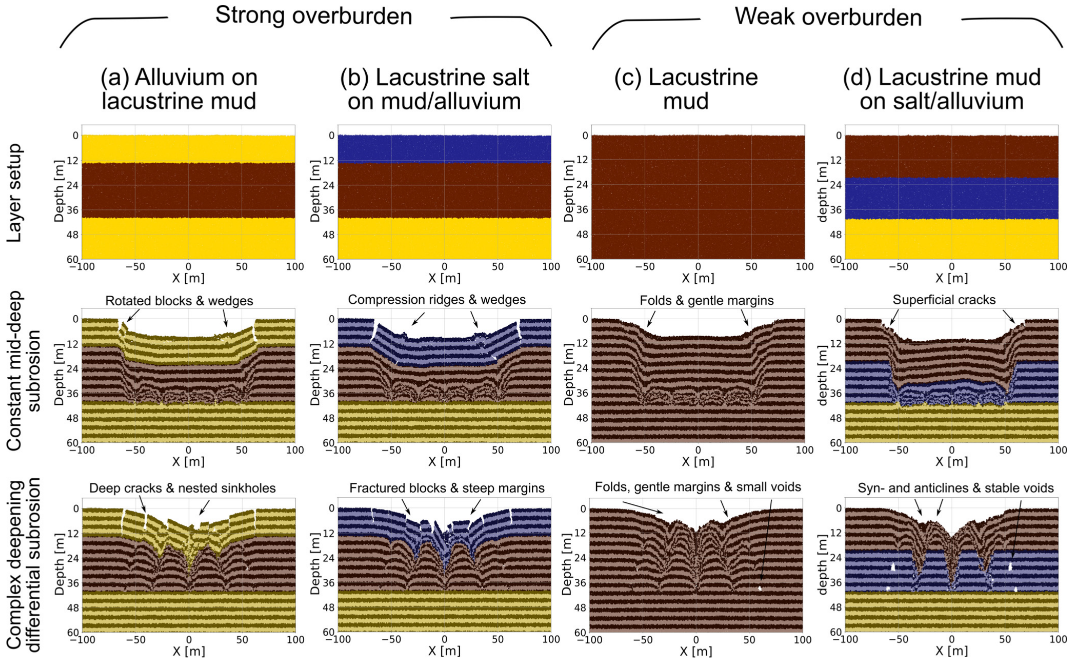

Figure 4. Comparison between final results for two cavity growth end-members and different material compositions common at the Dead Sea shoreline. The removed volume at the shown stages is approximately 900 m^3. Strong overburden: **(a)** alluvium/mud succession and **(b)** salt-on-mud/alluvium succession. Weak overburden: **(c)** pure lacustrine mud and **(d)** mud-on-salt/alluvium succession. Note that passive marker layers are applied to highlight structural features.

clinal form. These cavity-scale synclinal structures represent the downward flow of the weak material into the cavities or, where cavity formation is inhibited, into the zones of material removal.

Depth-to-diameter (De / Di) ratios of simulated sinkholes and depressions are given in Table 2 as mean values of five model assemblies of each material combination. The dimensions of depressions at the scale of the entire cavity array range from ∼ 65 to 190 m across and ∼ 2 to 18 m deep, while individual sinkholes have dimensions of ∼ 1.5–36 m across and ∼ 0.5–12 m deep. Higher De / Di ratios of 0.48–0.64 for sinkholes are generally recorded for cover material of higher strength (alluvium, salt), while lower De / Di ratios of 0.22–0.24 are found for low-strength cover material (mud). The De / Di ratios of 0.08–0.14 of the larger-scale depressions are many times lower (in some cases, nearly an order of magnitude lower) than those of the sinkholes.

The evolution of depth and diameter of large-scale depressions (Fig. 6) shows the influence of the material strength on their geometries. A clear divergence can be observed between mud subsurface and salt subsurface models. A mechanically weak subsurface (mud) enables a lateral widening of the depression at the expense of deepening. A mechanically strong (salt) subsurface inhibits the synclinal bending at the margins of the main depression, leading to deepening of the depressions and preventing their widening.

The influences of different positions and different speeds of material removal zones have also been tested thoroughly (see Appendix A for details). In all material cases for scenario (1), i.e. the constant cavity growth level and rate, and regardless of the depth of the array, only large, array-scale depressions occur and no sinkholes form in relation to the individual cavities. A shallower cavity array leads only to faulting/segmentation of the sinking block and/or fracturing of the margins. Varying the speed of array-wide subrosion produces no discernible difference in model outcome, as expected for the quasi-static approach.

Clearly, a differential cavity growth is essential for development of sinkholes within a larger-scale depression. This is even more pronounced with accelerating growth of the central cavities. Additionally, and importantly, for reproducing the morphological features and the order of appearance of sinkholes relative to the larger-scale depression, as observed in the Dead Sea examples, a simulated deepening of the karstification/subrosion level, i.e. cavity growth scenario (2), is necessary. From comparison of numerical simulations of all tested scenarios and setups in the previous section and in Appendix A1 and A2, we conclude also that the inter-cavity distance has an influence on the sinkhole clustering and generation of larger-scale depressions. In the limit, if the inter-cavity distance is wide enough, no clusters or large-scale depressions would form but only individual sinkholes.

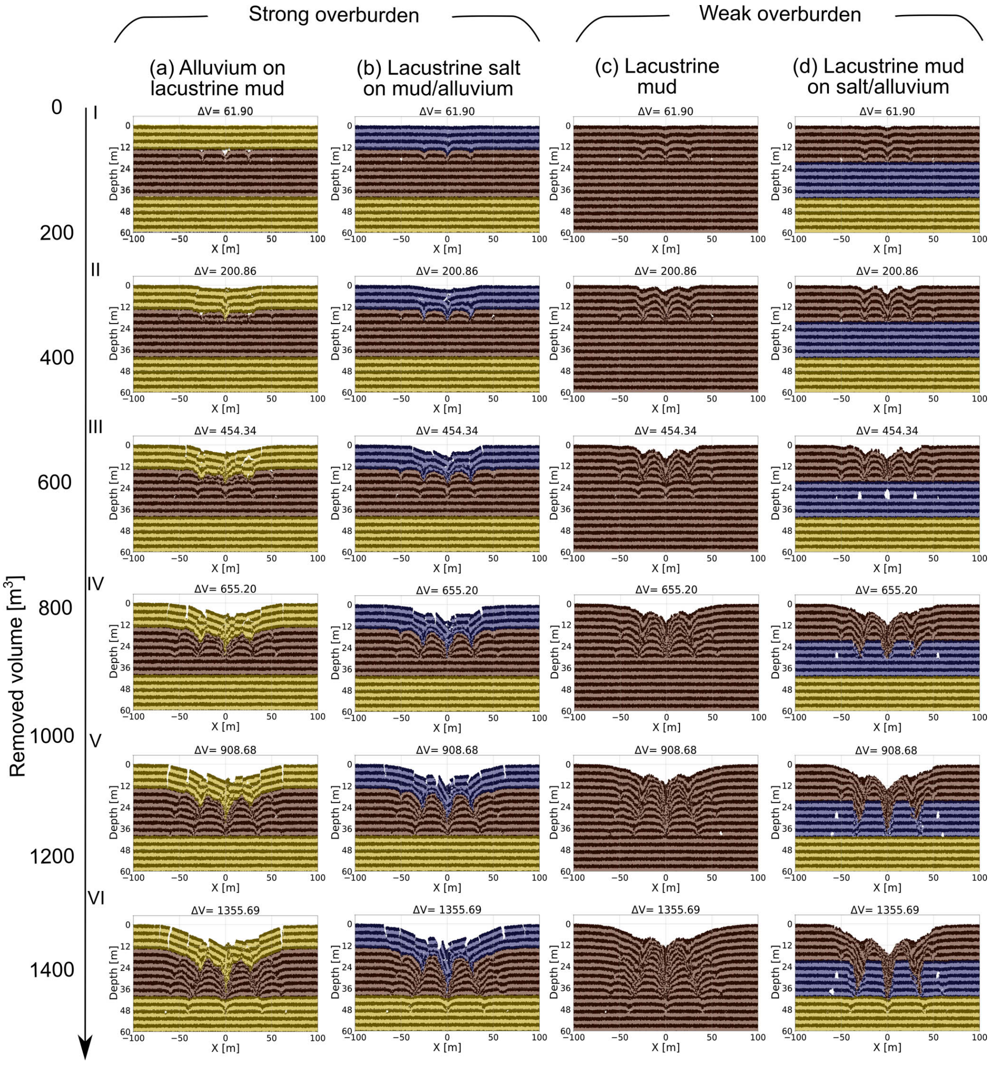

Figure 5. Final model sinkhole evolution results for four different material combinations common at the Dead Sea shoreline. Strong overburden: **(a)** alluvium/mud succession and **(b)** salt-on-mud/alluvium succession. Weak overburden: **(c)** pure lacustrine mud and **(d)** mud-on-salt/alluvium succession. The removed volume [m^3] is shown above the plots. Note that passive marker layers are applied to highlight structural features.

3.1 Stresses and strains in a multiple void space system

The differences in model outcome depending on the cavity growth scenario are better understood when looking at the stress and strain distribution patterns. The maximum shear stress $\tau_{\max}$ around the cavity arrays in model cavity growth scenarios (1) and (2) is shown in Fig. 7. We here compare two different material setups: strong alluvium on weak mud and weak mud on strong salt and alluvium. Each model has the same particle assembly and comprises five void spaces at ~ 40 m depth at stages immediately before or exactly during the collapse of the overburden. The differential subrosion scheme here uses the same setup as in the model (Fig. 14g) in Appendix A2, which is without a deepening of the subrosion zone, to avoid effects of remnant stress distributions.

Regarding the mechanical development, cavity growth scenario (1) produces a stress arch spanning the whole array of cavities, best visible in the alluvium-on-mud combination of Fig. 7a. For cavity growth, scenario (2) produces a more complex pattern of more localised stress concentrations and arches appearing around or between individual cavities. The setup of a constant cavity growth rate hence leads to a block-wise subsidence, while for differential cavity growth rate, the interaction of stresses around and between the cavities leads to multiple sinkhole development in a large-scale depression. Appendix A3 shows similar results for principal stresses.

For the same scenarios, the maximum shear strain $\gamma_{\max}$ is shown in Fig. 8. It highlights the different subsidence styles: block-wise subsidence for a constant subrosion scenario (1), and fragmented, individual overburden failure with fault-

Table 2. Depth-to-diameter ratios of simulated array-scale depressions. The average results for the four different material setups and different stages of depression development are given. The depth of a depression is hereby considered the deepest point that might coincide with the deepest point of a sinkhole within the depression. The diameter goes as far as a vertical surface displacement of ∼ 10 cm amplitude can be observed. A total of five realisations were done for each material combination.

Type/model setup	Lacustrine mud	Alluvium on mud	Salt on mud/alluvium	Mud on salt/alluvium
Depression – early stage	0.05 ± 0.003	0.03 ± 0.009	0.04 ± 0.003	0.07 ± 0.006
Depression – middle stage	0.08 ± 0.004	0.07 ± 0.013	0.08 ± 0.006	0.12 ± 0.010
Depression – late stage	0.08 ± 0.004	0.09 ± 0.004	0.11 ± 0.007	0.14 ± 0.005
Sinkholes – final stage	0.22 ± 0.12	0.48 ± 0.36	0.64 ± 0.3	0.24 ± 0.08

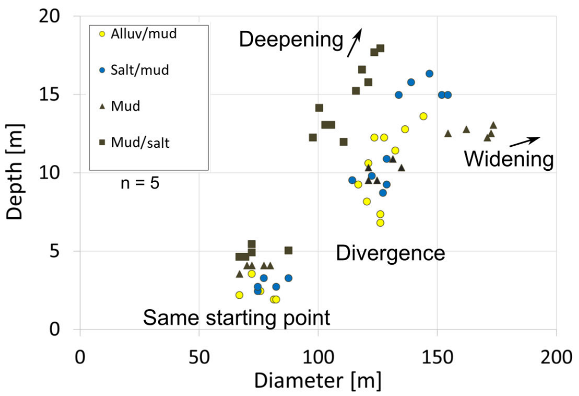

Figure 6. Depth versus diameter for different stages of the final model large-scale depressions for different material combinations. A clear divergence can be observed between mud-rich subsurface and salt-rich subsurface models at the late stage of the simulation. The number of realisations of each model is $n = 5$.

ing/segmentation for the differential subrosion scenario (2), with stable areas of low strain in between the subsiding blocks. In comparison to the shear stress images, this representation more clearly illustrates cracking and fracture development. These observations are complemented by the incremental strain and maximum shear stress evolution as presented in Appendix A4 and A5.

3.2 Generic geophysical parameters

Figure 9 shows the synthetic geophysical parameters that characterise the model underground. As we consider a non-elastically deformed underground, all derived elastic parameters must be regarded as apparent. We concentrate on a snapshot of the final stage of the alluvium-on-mud model simulating cavity growth scenario (2); see Fig. 5a at a removed volume of $\Delta V = 1355\,\mathrm{m}^3$ for the most important structural features. A deep and large depression zone with sinkholes has formed already. At this stage, the actively growing cavity set (or active subrosion zone) lies at ∼ 50 m depth. The initial porosities lie between 0.2 and 0.1 depending on the depth (Fig. 9a). We consider areas of porosities over 0.5 as "empty" space with a zero modulus/seismic velocity. Initial values of the shear wave velocity in "stable" ground are 100–150 $\mathrm{m\,s^{-1}}$ for mud and 200–450 $\mathrm{m\,s^{-1}}$ for alluvium (Fig. 9b).

The porosity distribution at the final stage can be seen in Fig. 9c. The number of cracks is depicted in Fig. 9d. Note that cracks in alluvium are counted in a cumulative way, while cracks in mud are calculated per stage, due to the healing procedure for broken bonds in mud (see Sect. 2 and Al-Halbouni et al., 2018). These cracks cause, in addition to the porosity, further changes of the apparent shear modulus (Eq. 6) and Poisson ratio (Eq. 5) and hence reduce the effective apparent elastic modulus of the underground (Fig. 9e). This is also expressed in the apparent shear wave velocity (Eq. 3) for the same stage (Fig. 9f). We observe strong changes in the central deep part of the model, where the largest void space growth rate exists. Remnants of earlier subrosion at shallower depths are nicely reflected in the apparent modulus and shear wave velocity distribution. More stable parts of the alluvium layers have higher values of $E > 500\,\mathrm{MPa}$ and $v_\mathrm{S} > 275\,\mathrm{m\,s^{-1}}$ (HVZ – high-velocity zone). The lowest values of $E < 100\,\mathrm{MPa}$ and $v_\mathrm{S} < 100\,\mathrm{m\,s^{-1}}$ occur in the mud layer close to the zones with highest porosity and most cracks in the currently active area cavity growth (very-low-velocity zone – VLVZ). In between lies the low-velocity subrosion-affected part both in the mud and alluvium layers (low-velocity zone – LVZ), corresponding to the areas of earlier cavity growth and overburden disruption. The model shows up to 75 % shear wave velocity reduction in the central subrosion-affected parts of the mud in comparison to the initial values and up to 50 % for the alluvial overburden or contact zone between mud and alluvium.

4 Discussion

In this section, we discuss how realistic our numerical modelling results are in comparison to natural observations and what can be deduced in terms of process understanding. We first make some general points about the relationship between sinkholes and larger-scale depression in different karst settings. We then concentrate our comparison on results from remote sensing and geophysics for the very active sinkhole formation area at Ghor Al-Haditha at the Dead Sea. As a reminder, our model should be able to explain the following

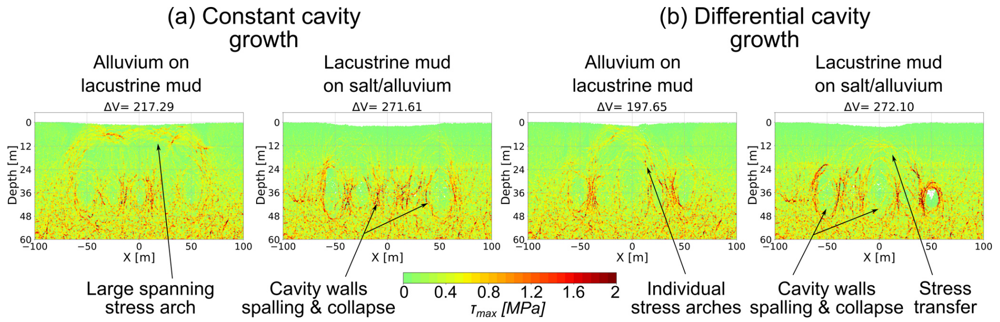

Figure 7. Maximum shear stress around void spaces for **(a)** constant and **(b)** differential cavity growth scenarios models. Chosen are two material combinations where the subrosion-affected layer differs in strength: alluvium-on-mud multilayer and mud-on-salt/alluvium succession. Shown are critical stages after void space installation followed by or exactly during overburden collapse for the same particle assembly. The removed volume [m^3] is shown above the plots.

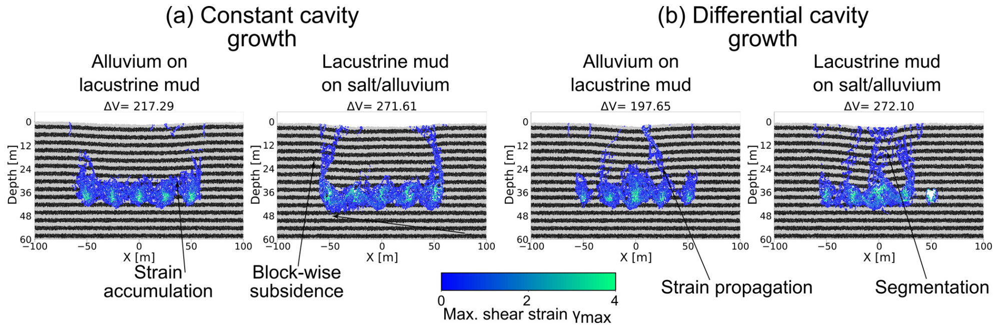

Figure 8. Maximum finite shear strain for **(a)** constant and **(b)** differential cavity growth scenarios models. Chosen are two material combinations where the subrosion-affected layer differs in strength: alluvium-on-mud multilayer and mud-on-salt/alluvium succession. Shown are the same critical stages after void space installation as in Fig. 7. The removed volume [m^3] is shown above the plots.

features of the karst landform evolution typical in that area (Figs. 1, 2; compare Al-Halbouni et al., 2018; Watson et al., 2019):

- In all materials, multiple sinkholes have formed with many clustered, coalesced and/or nested.
- Larger-scale depression zones with pronounced marginal cracks have also developed around the sinkholes and sinkhole clusters. Formation of sinkholes began before, or at the same time as, the appearance of the first marginal cracks of the depression zones. Lateral expansion of the depression occurs in tandem with sinkhole formation.
- Morphological differences depend in which material the sinkholes form: low depth/diameter (De / Di) ratio for mud-flat sinkholes; high De / Di for alluvium sinkholes. Sinkholes in high-strength materials have partly overhanging sides.
- The De / Di ratios of the larger-scale depressions are an order of magnitude lower than those of the sinkholes within them.

4.1 Implications for karst landforms of clustered sinkholes and large-scale depressions

As discussed by Ćalić (2011), for limestone karst areas, differences between enclosed depression types in karst regions occur in regard to scale, inter-relationship and morphometry. Sinkhole (or doline) diameters occur on a sub-100 m scale, uvalas typically occur on a several-hundred-metre to kilometre scale in limestone karst and so-called poljes on even a larger scale. A single uvala typically includes numerous dolines within it, which led to the concept of uvala formation by doline coalescence (Gutiérrez et al., 2014; Waltham et al., 2005). The further development of dolines to uvalas and ultimately to poljes, is regarded by most workers as erroneous, and some do not consider uvalas to evolve by doline coalescence either (Ćalić, 2011). Although our simulations are purely mechanical and hence lack some important hydrological aspects for comparison to areas of limestone or evaporite karst, they nonetheless yield some new insights into the potential controlling factors on the inter-relationship between these different depression types.

Our models generally show that a differential subrosion pattern is necessary to achieve clustered sinkhole formation within a larger-scale depression. A spatially constant growth

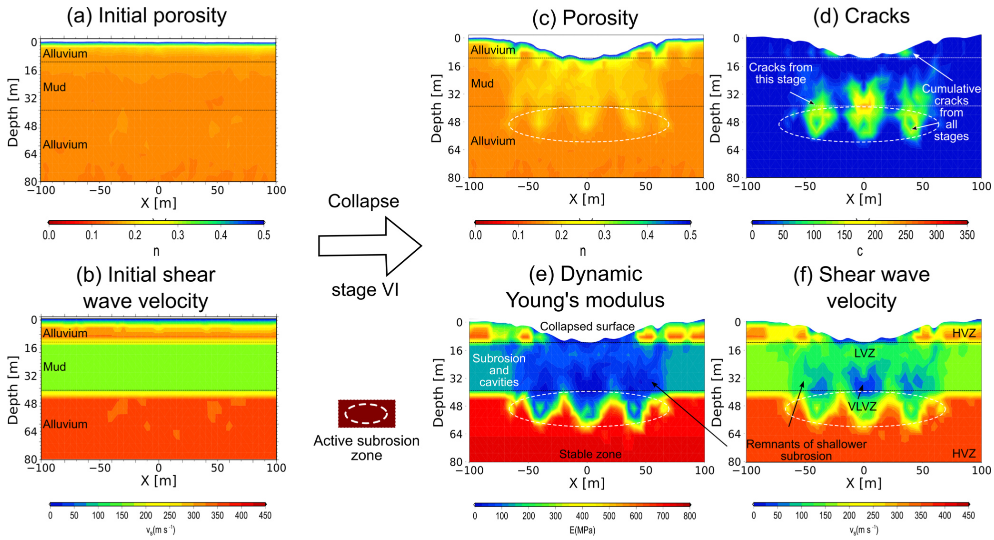

Figure 9. Geophysical characterisation of the underground. Derived generic parameters for the initial and final models of alluvium on mud shortly before stage VI (see Fig. 5a). **(a)** Porosity and **(c)** distribution. Panels **(b)** and **(f)** indicate apparent shear wave velocities. **(d)** Number of cracks in the vicinity of the subrosion zone. Note that the cracks in the mud layer arise from the current stage of material removal (due to rebonding), whereas those in alluvium layers are accumulated throughout the model evolution. **(e)** Apparent dynamic elastic (Young's) modulus. Black lines mark the initial limits of the mud horizon. The surface has collapsed partly into a depression plus sinkholes.

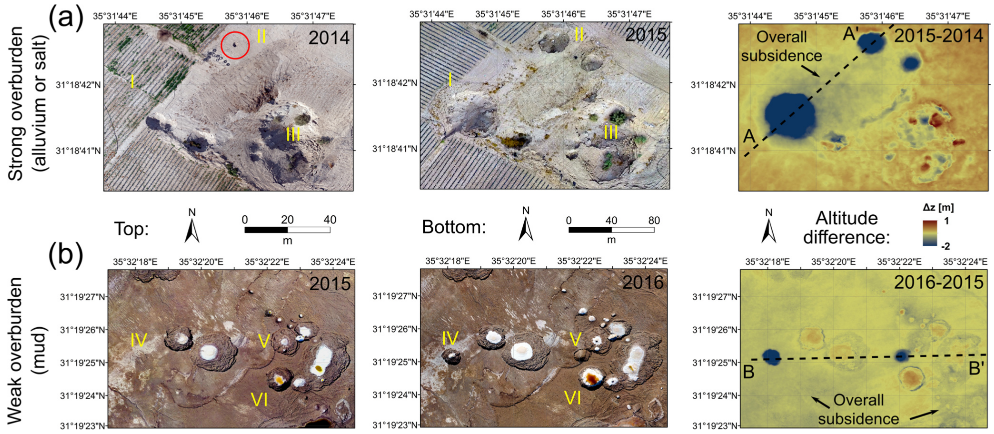

Figure 10. Examples for subsidence and sinkhole formation at Ghor Al-Haditha from orthophotos and DSM difference maps. All orthophotos and DSMs have the same resolution (10 cm px^{-1}) and the accuracies (horizontal, vertical) are as follows: 2014 (10, 11 cm), 2015 (12, 17 cm) and 2016 (37, 31 cm). **(a)** Vertical displacement between 2014 and 2015 in the alluvium. Large sinkholes have formed in the alluvium (I, II) with slight overall subsidence along cross-section A–A' from SW to NE. The red circle marks a small precursory hole at (II). Vegetation growth may cover subsidence effects in coalesced sinkholes (III). **(b)** Vertical displacement changes between 2015 and 2016 in the mud flat. Precursory information (reactivated sinkholes) may exist (IV) or not be visible (V). Nests of sinkholes exist (VI) in an area of pronounced overall subsidence of 0.5 m ±0.2 m determined for cross-section B–B' from W to E. Compare topographic profiles in Fig. 11.

rate across the cavity array alone is not sufficient to generate sinkhole clusters, even if the interacting cavities were at different depths. This is due to the resultant stress system, whereby a well-developed stress arch spans the entire constant-growth cavity array, which acts mechanically as a single entity. A differential cavity growth, on the other hand, produces more localised stress concentrations and arches above individual cavities in the array, leading to localised overburden failure and collapse into those cavities. The progressive deepening of subrosion is particularly important to account for the observation at the Ghor Al-Haditha site of initiation of larger-scale depression synchronously with or shortly after sinkhole development.

Our models also highlight conditions under which uvala-like depressions may or may not develop by sinkhole coalescence. In models with a relatively strong soluble layer, sinkhole coalescence is a mechanism for formation of a larger-scale uvala-like depression (Fig. 5d). This is because the relatively strong cavity-hosting layer inhibits deformation beyond the immediate cavity surroundings and promotes the formation of relatively large sinkholes that coalesce. In models with a relatively weak soluble layer, however, the uvala-like depression develops as a spatially and temporally distinct feature from the sinkholes within it. Rather than forming by sinkhole coalescence, the uvala-like depression reflects a wider-scale subsidence into the cavity array (or subrosion zone) as a whole that results from more widely distributed deformation in the weak cavity-hosting layer (Fig. 5a, b and c). The results of this latter model setup are consistent with observations of the spatiotemporal relationships between sinkholes and uvalas in the evaporite karst examples at Ghor Al-Haditha (Fig. 2).

In our model results, we also reproduce the main relative morphometric attributes of sinkholes and uvala-like depressions as observed at the Ghor Al-Haditha study area. As shown by Al-Halbouni et al. (2018), sinkhole depth/diameter ratios in the models and nature are dependent on overburden material properties, especially strength. Sinkholes in strong alluvium overburden have De / Di ~ 0.48 in the models compared with De / Di ~ 0.40 in nature; sinkholes in weak mud overburden have De / Di ~ 0.22 in the models compared with De / Di ~ 0.10 in nature (Watson et al., 2019). The uvala-like depressions at Ghor Al-Haditha have a De / Di ~ 0.016–0.042 (Watson et al., 2019), which, as seen also for limestone karst settings (Ćalić, 2011), is about an order of magnitude less than the sinkholes. A similar relationship is seen in our models in which the larger-scale depressions have De / Di ~ 0.07–0.14; this ratio could have been made even lower simply by having a wider cavity array.

4.2 Detailed comparison with temporal development of subsidence at the Dead Sea sinkhole area

We analysed data from repeated photogrammetry of 3 consecutive years of the sinkhole area of Ghor Al-Haditha, at the eastern side of the Dead Sea (Fig. 1a and Al-Halbouni et al., 2017). The datasets have been used to derive DSM difference maps between the consecutive years via GIS software.

Figure 10 shows the spatiotemporal evolution of recent sinkhole formations and patterns of holes, drainage channels, cracks and depression structures as observed in all cover materials in and around the main depression zone of the area (see Figs. 1 and 2). In the relatively strong alluvial sandy-gravel cover material (Fig. 10a), we observe a cluster of rather deep and narrow sinkholes forming between 2014 and 2015. Small conical holes are precursors to the development of larger conical sinkholes (I and II). A typical coalescence and partial overprinting of large and small holes can be seen at the lower right (III). The DSM difference in Fig. 10a depicts the new sinkholes and lateral sinkhole growth. We observe a small overall subsidence between the new sinkholes but a rather stable surrounding.

In the relatively weak clayey limestone carbonate material (Fig. 10b), we observe the development of a cluster of typical wide and shallow sinkholes formed between 2015 and 2016. Similar to the alluvium, coalescence of individual holes into larger ones as well as the alignment of a series of different sized holes are observed. The development of new collapses during 1 year in this material can either show possible precursory structures (IV) or not (V). The scarps are generally not stable in time (VI) due to the weak material, as seen in the DSM difference map. An overall wider-scale subsidence of approximately $0.5\,\mathrm{m} \pm 0.2\,\mathrm{m}$ is observed in the mud and between the sinkholes in the alluvium.

For qualitative comparison with our models, Fig. 11 shows the profiles across the DSM and vertical surface displacement for different stages of our models for weak and strong overburden. Although a precise matching is not intended, we clearly observe similar features in the modelled topographic profiles in comparison to the ones of the sinkholes/depression system at the Dead Sea. In weak material in the field, slight subsidence at the early stage is visible, revealing the contours of the future sinkhole (imprints), which were also observed in the model. In strong material, early collapse sinkholes may be a precursor for further large-scale collapses and nesting, both in nature and in the models. Sinkhole development is usually accompanied by fracturing at the margins of the larger-scale depression (see Figs. 2, 5a, c and 11c). Large, deep fractures occur in strong material, while small, shallow fractures in the cohesive weak material (see also Holohan et al., 2011). In general, the fractures indicate a widening of the depression zone. Finally, because of the prescribed geometry of the subrosion zone, which is expected to be more complex in natural karst systems, and the limitation to 2-D modelling, we cannot infer conclusions about the observed migration of such sinkhole clusters in nature (Fig. 2).

4.3 Subsurface patterns of sinkhole clusters and subrosion

From shear wave reflection seismics, zones with low reflectivity and velocity inversion anomalies in the S-wave velocity field are indicators for zones of material depletion or faults (Wadas et al., 2016). In the central part of the sinkhole-affected alluvial fan system at Ghor Al-Haditha, a deep-seated (≥ 60 m depth) main subrosion zone based on the determined top of a lacustrine mud layer has been identified by comparison of shear wave reflection profiles with borehole logs (Polom et al., 2018). In several profiles of that work, shallower subrosion zones can also be identified, and a general dip tendency of the deeper layers towards the NW is observed, indicating a Gilbert-type alluvial fan foreset/topset system. We picked a section of profile 1 (see Fig. 1) of Polom et al. (2018) as an example, and we present an interpreted version of the shallower part in Fig. 12a.

A layered system of alluvial fan sediments with stronger reflections can be seen to the SW, while the central and NE

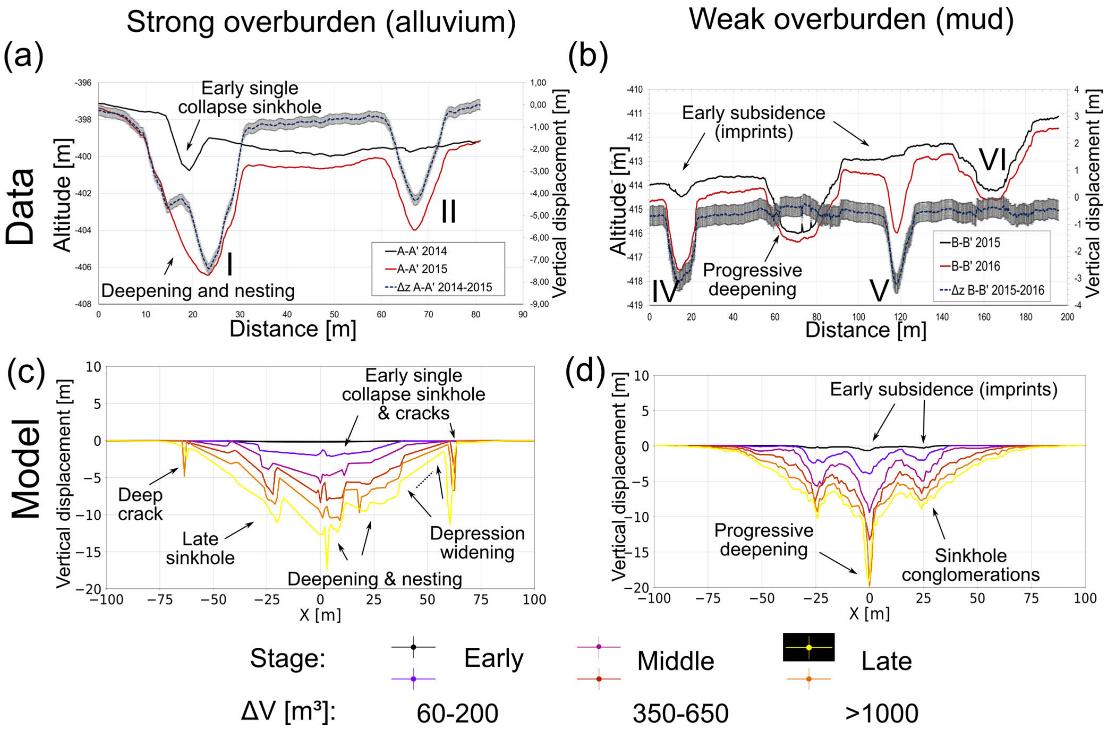

Figure 11. Topographic profiles data as indicated in Fig. 10 and corresponding models. Top row: topography and vertical displacement. Figure 10 of **(a)** cross-section A–A' from SW to NE in the alluvium and **(b)** cross-section B–B' from W to E in the mud flat. Bottom row: representative topographic profiles across final models for **(c)** high-strength alluvium on mud and **(d)** low-strength lacustrine mud.

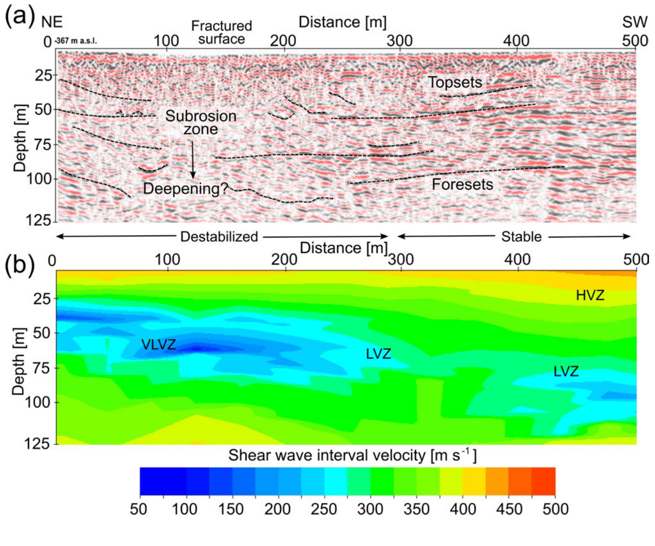

Figure 12. Subrosion-affected parts of shear wave reflection seismic profile 1 at the sinkhole site of Ghor Al-Haditha. **(a)** Modified and interpreted first 500 m of profile 1 after Polom et al. (2018). **(b)** Shear wave interval velocity versus depth with marked very-low- (VLVZs), low- (LVZs) and high-velocity zones (HVZs).

parts, close to the main depression zone, are affected by downsagging of up to several metres, by disturbed layers, and by bowl- or cone-shaped features in the upper 50 m. Near-surface uneven reflectors may indicate local fracturing of the layers. Locally, more stable parts, i.e. stronger reflections, exist. This is comparable to the subsurface structure as found in the final stages of the alluvium-on-mud model (Fig. 5a). The stable blocks are especially clearly visible in the incremental strain evolution plots (see Fig. 17 in Appendix A4). An indication of a deepening subrosion zone can be inferred from the change in the transparency of the reflectors.

Figure 12b shows the 2-D field of shear wave interval velocities in depth of the same profile section. It was derived after Dix (1955), based on the 2-D root mean square (rms) mean velocity field in time resulting iteratively from interactive velocity analysis of the hyperbola move-outs for the common midpoint (CMP) stacking procedure, which was subsequently iteratively evaluated and optimised by migration velocity analysis. The velocity field reflects the general survey situation of a relatively high velocity of 400–425 $\mathrm{m\,s^{-1}}$ close to the surface caused by the road construction (asphalt surface over a compacted man-made gravel infill) and reduced velocities of 300–375 $\mathrm{m\,s^{-1}}$ below for the natural alluvial sediments. The lateral structure mainly correlates with the structure image in Fig. 12a. Low-velocity values of 275 $\mathrm{m\,s^{-1}}$ down to approximately 100 $\mathrm{m\,s^{-1}}$ (light

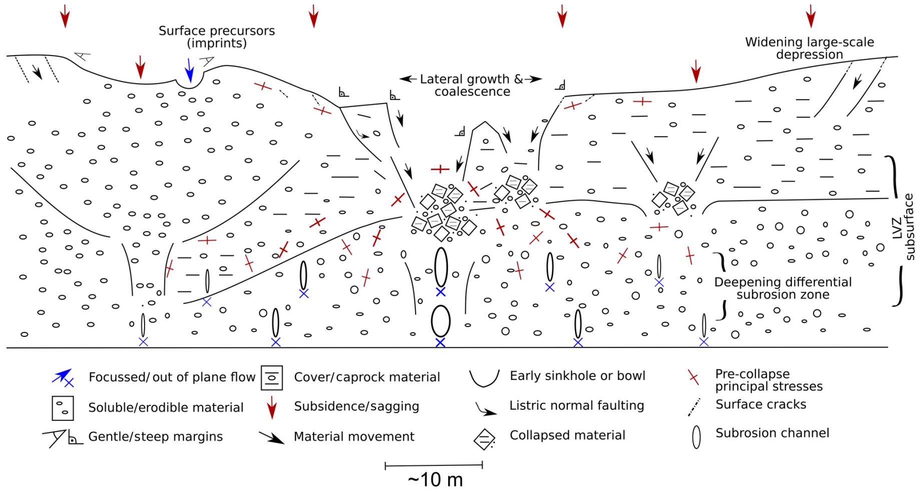

Figure 13. Conceptual model of sinkhole cluster and large-scale depression development. Several sinkholes of different stages, types and varying subrosion depths are indicated in this sketch (centre – caprock sinkholes; left – suffosion sinkhole).

blue to blue zones) indicate either subsurface zones of true low velocities due the specific lithologic formation, i.e. soft sediments, or zones of disturbed formations where the shear modulus is reduced due to mechanical stress of the formation by disruptions, caused by an upward-propagating deformation process. Very low values below $100\,\mathrm{m\,s^{-1}}$ may indicate areas where the shear wave could not propagate the area by a straight ray path and turned around it, e.g. in the case of a cavity ($G_{\mathrm{dyn}} = 0$) or a collapsed zone of very low shear modulus. In this case, the resulting elongated propagating paths compared to the regular straight paths lead to zones of apparently very low interval velocities of less than $100\,\mathrm{m\,s^{-1}}$, partly close to zero, which are not realistic for true lithologic units.

The decrease in apparent seismic shear wave velocity has been attributed by Polom et al. (2018) to diminished grain coupling (either by pore pressure effects or enhanced fracturing of the rocks) and to the influence of a high-velocity surface layer (e.g. asphalt). The simulated apparent velocity values of Sect. 3.2 lie in the range of the field estimates with a strong reduction in the simulated mud layer during cracking and collapse. We consider the presented simulation stage of Fig. 9 as most appropriate to explain the observed shear wave velocity reduction, which we interpret to be caused by enhanced fracturing, i.e. crack density increase, porosity increase and consequent modulus reduction in a deepening differential subrosion zone. As such, our final model qualitatively and quantitatively aids the interpretation of the subsurface geophysical patterns for the material combination as found at the Ghor Al-Haditha field site.

A conceptual model in Fig. 13 summarises the main findings of this study and how they relate to the complex, dynamic karst systems in nature. A large-scale depression builds up due to distributed material removal in the underground by subrosion in a karstic drainage network. Nested and/or clustered sinkholes may appear with relatively stable blocks in between. Lateral material heterogeneities may cause different sinkhole morphologies and surface expressions of cracks/fractures that surround the large-scale depression. Depending on the material strength, large-scale depressions may build up either by sagging, block-wise brittle failure, lateral widening or coalescence of sinkholes. The subsurface shows strong layering disturbances and porosity and modulus changes leading to a low seismic velocity zone (LVZ). The pre-collapse principal stress system is divided into individual stress arches due to the differential subrosion pattern. Water infiltration generally may cause additional superficial dissolution structures.

5 Summary and conclusions

In this study, we presented a physically realistic 2-D distinct element numerical modelling approach to simulate the growth of a system (array) of karstic cavities with the subsequent formation by subsidence of multiple (clustered) sinkholes within a larger-scale (uvala-like) depression. Two end-member growth scenarios of the multiple cavity array were tested with the following main outcomes:

1. Cavity growth at the same depth level and growth rate yields a stable compression arch around the entire cavity array. This scenario hinders individual sinkhole collapses but favours a simple block-wise subsidence spanning the whole cavity array.

2. Cavity growth at progressively deepening levels with varying growth rates is characterised by a heterogeneous, interacting stress pattern in the cavity array and overburden. This scenario favours the more complex formation by subsidence of individual sinkholes and

sinkhole clusters within a larger-scale, gentler (uvala-like) depression.

The influences of geomechanical variation in growth scenario (2) were further investigated by simulating four different layered combinations of low- and high-strength materials representing the cavity-hosting medium and its overburden. The model results were also compared with surface morphologies from remote sensing and with subsurface structures from geophysical studies at the active sinkhole formation area near Ghor Al-Haditha at the Dead Sea. We found that

- For models with a weak cavity-hosting material, cavities remain small throughout, and wide-scale deformation in the cavity-hosting material and the overburden is promoted. This leads to development of a large-scale depression formed by subsidence that is structurally distinct from the individual sinkholes and is geometrically linked to the cavity array as a whole.
- For models with a strong cavity-hosting material, large cavities can develop before the overburden collapses into them and wider-scale deformation is inhibited. Consequently, a larger-scale depression forms in this case mainly by coalescence of sinkholes.
- Deepening of the differentially growing cavity array in model scenario (2) leads to sinkholes forming synchronously with, or just before, the development of a larger-scale synclinal depression. This order of appearance of sinkholes relative to the larger-scale depression is observed at the Ghor Al-Haditha sinkhole area. The modelling condition of deepening cavity growth is representative of a base-level fall, the main hydrogeological boundary condition occurring at the Dead Sea shoreline.
- Morphometric relations (depths and diameters) for both sinkholes and large-scale depressions as observed in nature are successfully reproduced in the models.
- Subsurface structures and calculated shear wave velocities match to a high degree those inferred from field estimations in shear wave seismic data. A low seismic velocity zone (100–275 $\mathrm{m\,s^{-1}}$) is imaged and simulated, compatible with the existence of a deepening subrosion zone at the Ghor Al-Haditha field site.

Finally, we conclude that the presented numerical modelling approach of multiple cavity growth has proven to be successfully applicable to sinkhole–depression systems and that it provides a basis for enhanced geomechanical understanding of karst development and hazard assessment.

Data availability. A full set of metadata is available upon request. For photogrammetric surveys, raw images, DSMs and orthophotos are available upon consultation with the authors. For DEM models, data and results are available upon request.

Appendix A: Numerical simulation of multiple void spaces with DEM

A1 Cavity growth implementation

The cavity growth function, $f(i)$, which relates the initial removed area A_0 to the area increment to be removed A_i (Al-Halbouni et al., 2018), has been updated to account for multiple voids that can start and stop growing at defined intervals (i_0, $i_{\max}$). The function hence depends on each single void of index j and the formula becomes

$$A_i = f_j(i,)\,A_0, i \in [i_0, i_{\max}]. \tag{A1}$$

The linear void space growth function relating initial void space area with the removed area at further intervals stands as an approximation for real fracture or void growth by physio-chemical processes in karst aquifers. Pure chemical dissolution of limestone or gypsum versus fracture widening shows a linear behaviour as long as the concentration of the under-saturated incoming fluid is lower than 90 % of the equilibrium concentration for that mineral (Dreybrodt et al., 2005; Kaufmann and Dreybrodt, 2007; Romanov et al., 2010).

A2 Optimal model development

For finding the optimal model, we generally define five individual semi-elliptical voids with a distance of 25–40 m from each other. They belong to one of three initial size groups and one of three void space growth function classes. Initial areas of set 1 (small) are $A_{0,1} = 2.7$–$6\,\mathrm{m}^3$ and linear eccentricity $e_1 = 1.7$–2.2 of set 2 (mid-sized) $A_{0,2} = 10$–$14\,\mathrm{m}^3$ and $e_2 = 3.5$–4.0 and of set 3 (big) $A_{0,3} = 24.5\,\mathrm{m}^3$ and $e_3 = 5$–5.5. Material removal of set A (slow) has an incremental function of $f_{j=1}(i) = 1.0^i$, set B (mid-speed) $f_{j=2}(i) = 1.05$-1.075^i and set C (fast) $f_{j=3}(i) = 1.1^i$. The subrosion zone is defined in different depth below the surface: set I (shallow) is for 20 m depth, set II (middle) for 30 m depth, set III (mid-depth) for 40 m depth, set IV (deep) for 50 m depth and set V (very deep) for 60 m depth. Representative of different material combinations, all results of the tests are shown in Fig. 14 for the alluvium-on-mud layer setup. The following table summarises the different tested void space setups. The results for the final model are shown in Sect. 3.

Constant void space growth (test scenario 1). Figure 14a shows the evolution of a growing void space system of five voids of set A until surface collapse for multiple layers of alluvium and mud. It shows cracks at the margins of the collapse zone and gradual sinking of a whole block. Individual smaller-scale sinkholes do not form. See the main text of the paper for the description of the results for this test scenario.

Constant void space growth with shallower inner voids. Figure 14b shows the evolution of a growing void space system of five voids of set A with two inner voids 10 m higher than the others. It shows cracks at the margins of the collapse zone and gradual sinking of the whole block but with a division of the block into segments. Real individual smaller-scale sinkholes do not form but are only an effect of the segmentation by the higher-lying voids.

Constant void space growth with shallower outer voids. Figure 14c shows the evolution of a growing void space system of five voids of set A with the two outer voids 10 m higher than the others. It shows cracks at the margins of the collapse zone and gradual sinking of the whole block and toppled blocks at the margins. Real individual smaller-scale sinkholes do not form – only a large and rather flat depression.

Accelerating growth of outer voids. Figure 14d shows the evolution of a growing void space system of three inner voids of set A with the two outer voids of set B, which leads effectively to an accelerated growth of the outer voids. We observe cracks and toppled blocks at the margins of the collapse zone, a gradual sinking of the whole block and first individual but very large sinkholes. The deepest part of the depression is one of the sinkholes. The convex-shaped bending of the middle part is not observed in our field study.

Differential growth with same initial areas. Figure 14e shows the evolution of a growing void space system of the two outer voids of set A, the two inner voids of set B and the central void of set C, effectively an accelerating growth for the inner voids. We find cracks and toppled blocks at the margins of the collapse zone, a gradual sinking of the whole block. A large-scale, more steep-sided depression forms.

Constant growth with variable initial areas. In Fig. 14f, the same effect as in the previous model can be produced by larger initial areas of the inner void spaces, with the largest material removal zone in the centre. The growth rate is constant for each individual void space leading but the initial sizes differ. Here, we produce a compression ridge at the centre of the depression zone.

Differential void space growth with variable initial areas. In Fig. 14g, a combination of a larger starting area with the fastest growing rate in the centre as in Fig. 14e and f is used to achieve an accelerating differential void space growth. We can see the same effect as in the previous models but with a first formation of a small-scale sinkhole in the centre of the depression.

Deepening differential void space growth (test scenario 2). Figure 14h is a pre-final model accounting for the base-level fall affecting the subrosion zone depth. A combination of a larger starting area and deepening from levels I (20 m) to III (40 m) to V (60 m) is implemented, halting the previous subrosion when the new one is activated. We can see already complex structure of individual nested sinkholes in a large-scale depression. This process is refined for the final model shown in Fig. 14i, using a more complex combination and intermediate steps of subrosion zone deepening from levels I to IV. This leads to clearer development of multiple nested sinkholes that subside into a large depression zone the deeper the subrosion zone lies. See the main text of the paper for a detailed description of the outcomes of this test scenario.

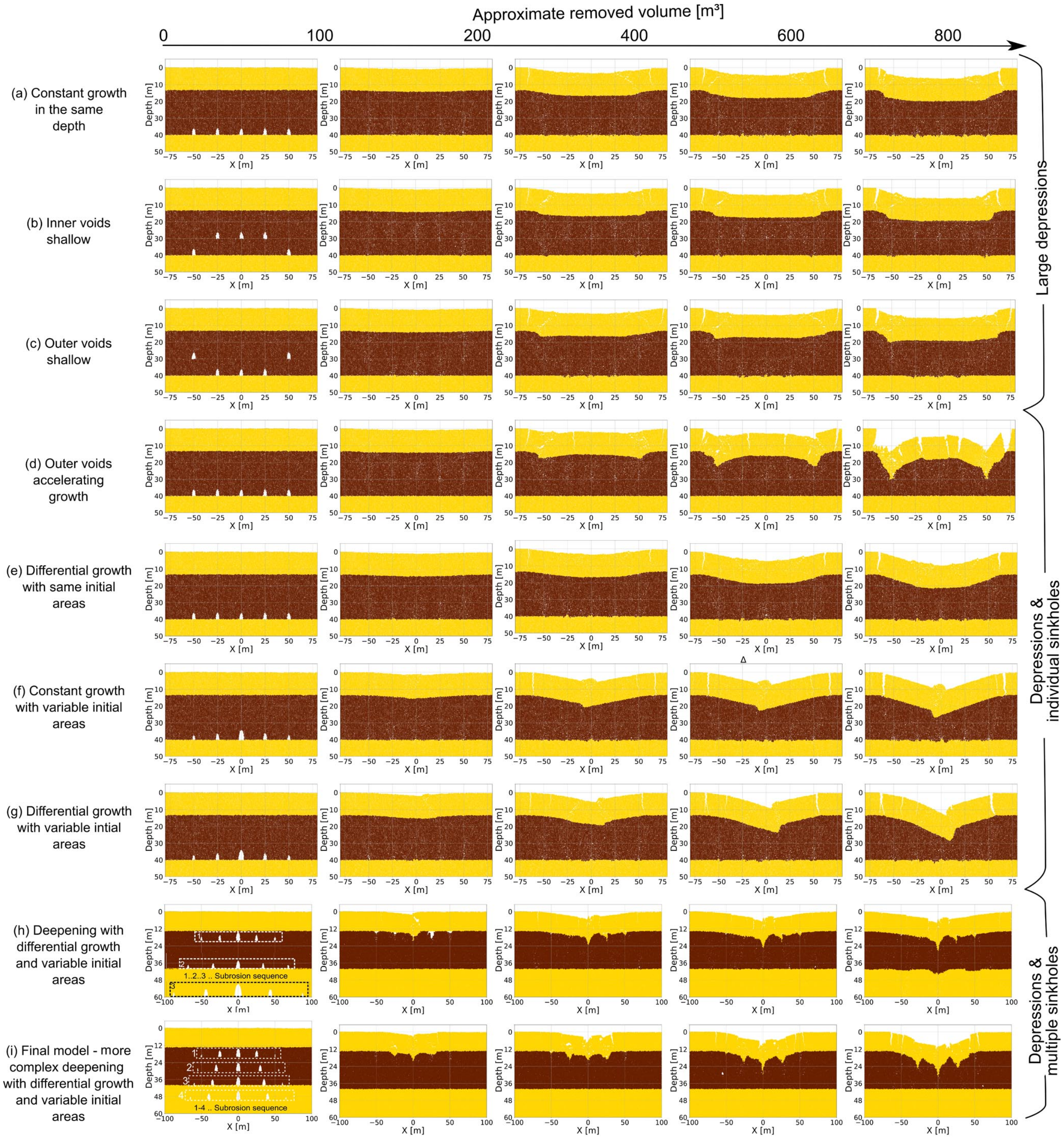

Figure A1. The influence of void space geometry (sizes and positions) and material removal speed in an alluvium-on-mud layered system. These simulations **(a)**–**(i)** are essential to determine, step by step, the optimal model setup to achieve multiple sinkhole collapses in a large depression zone. Shown are only the core zones of the models at different stages of removed volume indicated above each plot. Note the slightly different size of plots **(h, i)** in order to account for the widening and deepening subrosion zone. For simplicity, no passive markers are applied in these images.

Table A1. Tested sets of void spaces for the DEM models. All of them were applied to the material settings common at the Dead Sea shoreline. The model set combination is given in the terminology: initial area set/void space growth class/subrosion depth set. So, e.g. 1/A/I would stand for small-sized, shallow-seated void spaces growing at a constant rate.

Removal zone (void space)/ model set name	A: all voids the same ($A_{0,2}$)	B: three inner voids shallower ($A_{0,2}$)	C: two outer voids shallower ($A_{0,2}$)	D: two outer voids accelerating growth ($A_{0,2}$)	E: all voids differential but same initial areas ($A_{0,2}$)	F: all voids same but variable initial areas ($A_{0,2}, A_{0,3}$)	G: all voids voids growth rate and variable initial areas ($A_{0,1}, A_{0,2}, A_{0,3}$)	H: deepening differential growth rate and variable initial areas ($A_{0,1}, A_{0,2}, A_{0,3}$)	I: final model: deepening differential growth rate and variable initial areas ($A_{0,1}, A_{0,2}, A_{0,3}$)
Central Central	2/A/III	2/A/II	2/A/III	2/A/III	2/C/III	3/A/III	3/C/III	1: 3/C/I 2: 3/C/III 3: 3/C/V	1: 3/C/I 2: 3/C/II 3: 3/C/III 4: 3/C/IV
Two Inner	2/A/III	2/A/II	2/A/III	2/A/III	2/B/III	2/A/III	2/B/III	1: 2/B/I 2: 2/B/III 3: 2/B/V	1: 2/B/I 2: 2/B/II 3: 2/B/III 4: 2/B/IV
Two Outer	2/A/III	2/A/III	2/A/II	2/B/III	2/A/III	1/A/III	1/A/III	1: 1/A/I 2: 1/A/III 3: 1/A/V	1: 1/A/I 2: 1/A/II 3: 1/A/III 4: 1/A/IV

A3 Principal stresses in a multiple void space system

Figures 15 and 16 show the developed maximum σ_1 and minimum and σ_3 compressive stress for the constant subrosion versus differential subrosion setups (scenarios 1 and 2) and two different material combinations. A large compression arch spanning the cavity array develops in scenario (1) but is more fragmented in scenario (2). For the weak overburden, rather individual stabilising compressive arches build up in the strong interlayer and hardly translate upward. The minimum compressive stress plots for both setups show similar behaviour. Tensile stresses are recorded near the surface for strong overburden material. In contrast, the strong interlayer beneath the weak material leads to strong tensile stresses lined up at the edges of the cavities with spalling phenomena for both subrosion schemes. This line is centrally broken in the differential subrosion scheme. Shear stress observations are discussed in Sect. 3.1.

A4 Incremental shear strain evolution

Figure 17 shows the incremental shear strain evolution for all simulated material combinations for the differential deepening subrosion scenario (2). The different mechanical response to material removal in the subsurface is nicely illustrated by these images. Strong strain localisation occurs in all models in the material removal zones, at the boundaries of the depressions and at the margins of formed fractures. The continuous evolution of cracks into long fractures is nicely imaged as well.

A5 Maximum shear stress evolution

Figure 17 shows the maximum shear stress evolution for all simulated material combinations for the differential deepening subrosion scenario (2). The stress is best imaged prior to collapse, i.e. the snapshots refer to unstable moments except for the strong cavity-hosting material. Localised and fragmented stress patterns can be observed in all models, with maxima for the mechanically strong overburden and cavity-hosting materials (salt and alluvium) and delamination patterns due to the modulus contrasts.

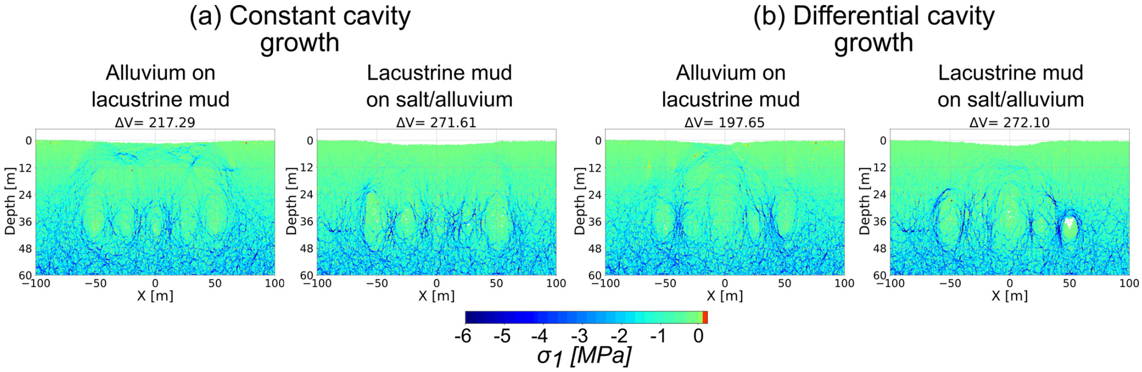

Figure A2. Maximum principal stress around void spaces for **(a)** constant and **(b)** differential cavity growth scenarios models. Chosen are two material combinations where the subrosion-affected layer differs in strength: alluvium-on-mud multilayer and mud-on-salt/alluvium succession. Shown are critical stages after void space installation followed by or exactly during overburden collapse for the same particle assembly. The removed volume [m^3] is shown above the plots.

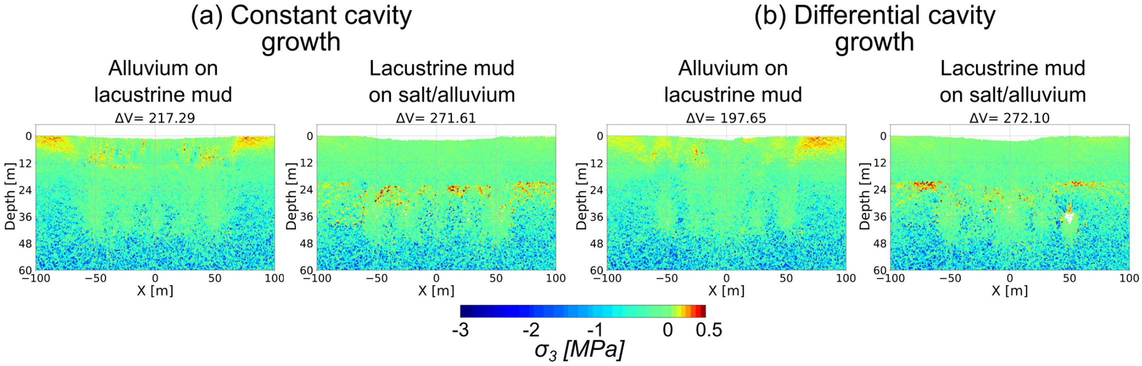

Figure A3. Minimum principal stress around void spaces for **(a)** constant and **(b)** differential cavity growth scenarios models. Chosen are two material combinations where the subrosion-affected layer differs in strength: alluvium-on-mud multilayer and mud-on-salt/alluvium succession. Shown are critical stages after void space installation followed by or exactly during overburden collapse for the same particle assembly. The removed volume [m^3] is shown above the plots.

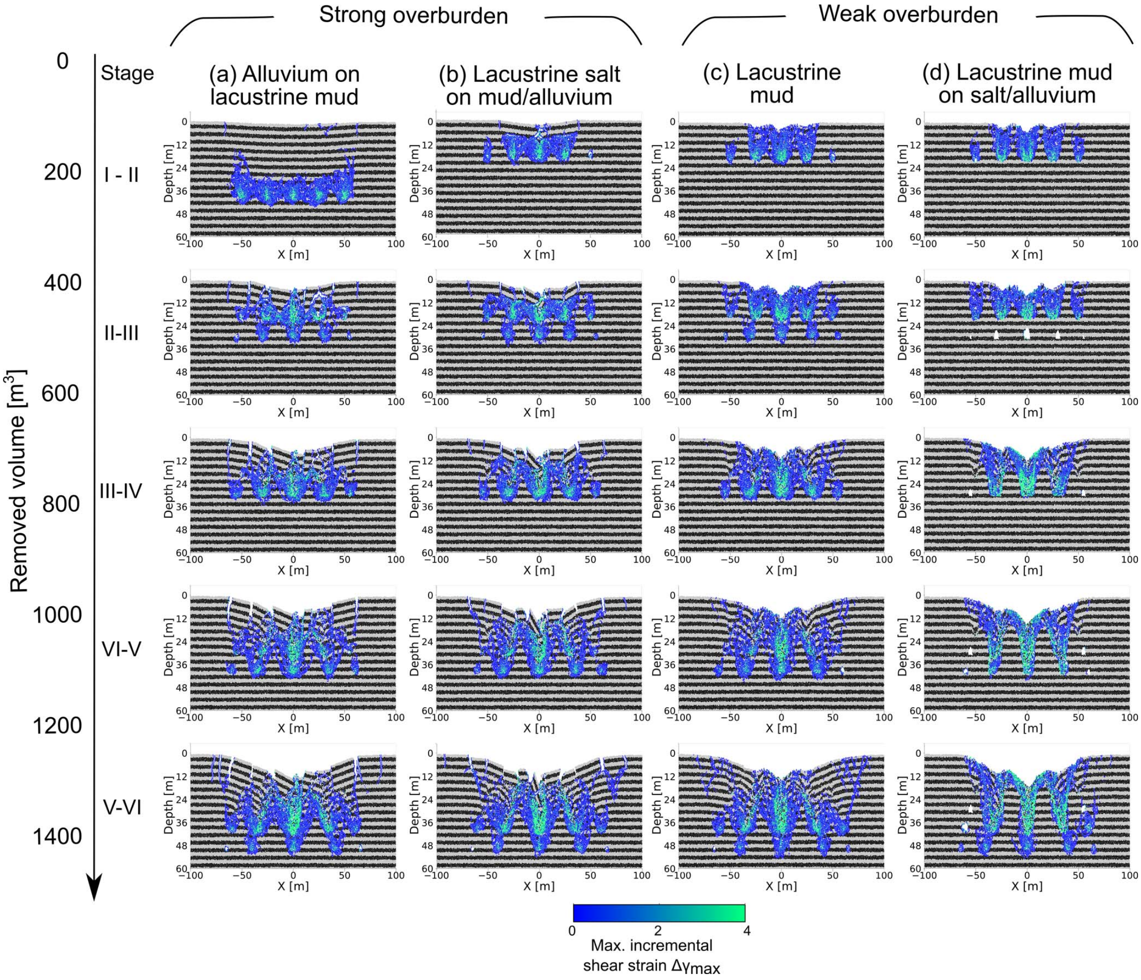

Figure A4. Incremental shear strain evolution in between the simulation stages for four different material combinations common at the Dead Sea shoreline. Strong overburden: **(a)** alluvium/mud succession and **(b)** salt-on-mud/alluvium succession. Weak overburden: **(c)** pure lacustrine mud and **(d)** mud-on-salt/alluvium succession. The plots refer to the difference of maximum strains between two simulation stages indicated to the left. Refer to Fig. 5 for individual stages. Note that passive marker layers are applied to highlight structural features.

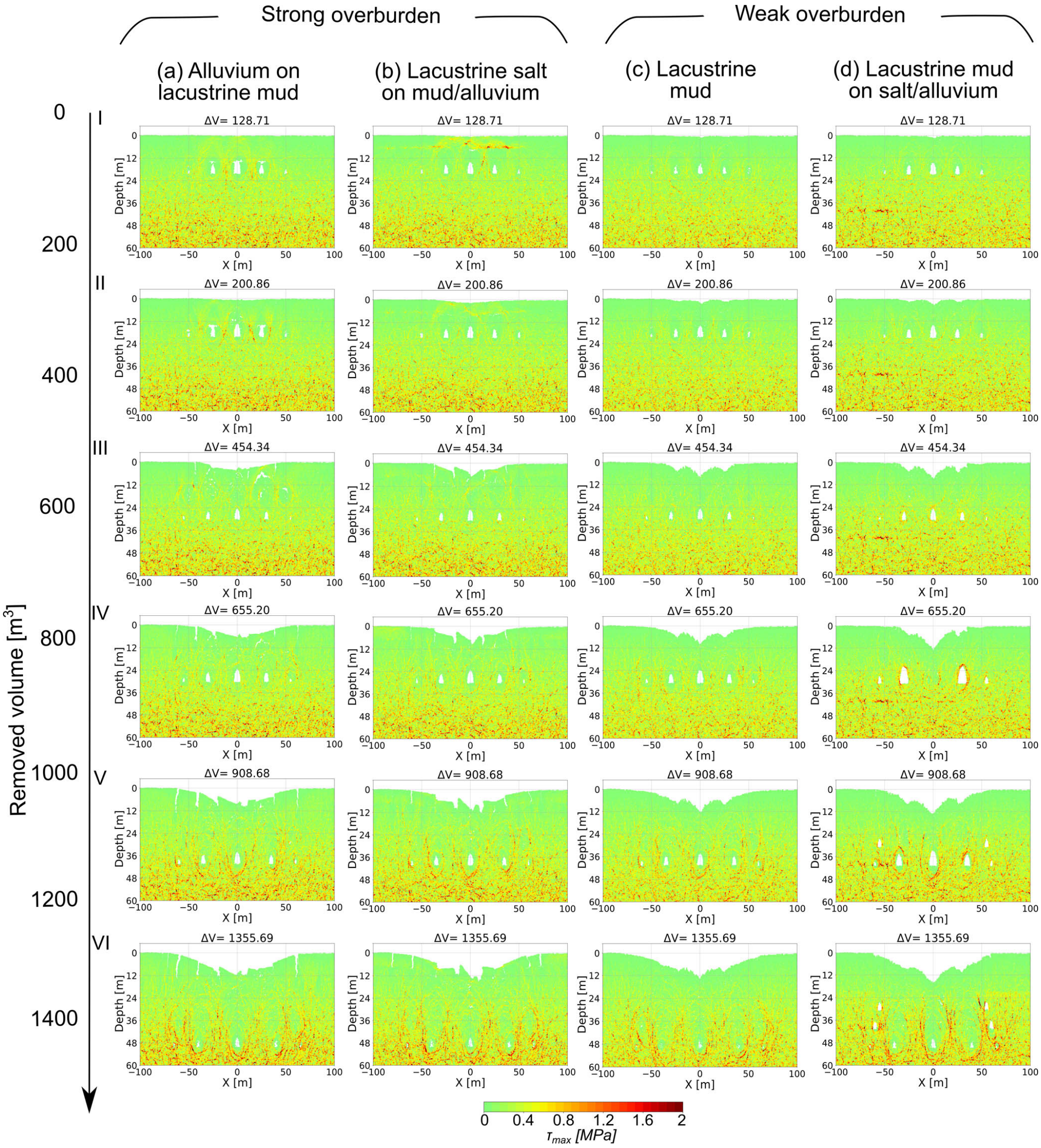

Figure A5. Maximum shear stress evolution for four different material combinations common at the Dead Sea shoreline. Strong overburden: **(a)** alluvium/mud succession and **(b)** salt-on-mud/alluvium succession. Weak overburden: **(c)** pure lacustrine mud and **(d)** mud-on-salt/alluvium succession. Note that snapshots show unstable stages before cavity collapse except partly for salt-cavity-hosting material.

Supplement. The supplement related to this article is available online at: https://doi.org/10.5194/se-10-1219-2019-supplement.

Author contributions. DAH and EPH led the production of figures and writing of the manuscript. DAH undertook the majority of the data analysis associated with the DSMs and modelling. EPH, DAH, RAW and UP undertook the field studies and close-range photogrammetric surveys in 2014–2016. UP and RAW contributed with satellite image and seismic data analysis. All authors reviewed and commented on the manuscript, and they contributed to discussions of the data.

Competing interests. The authors declare that they have no conflict of interest.

Acknowledgements. We would like to acknowledge our colleagues from MEMR, namely Ali Sawarieh and Hussam Alrshdan, for their continuous support. Particular thanks go to Damien Closson, Thomas R. Walter, Marc K. Elmouttie and Charlotte M. Krawczyk. We would additionally like to thank the reviewers and the editor for the fruitful discussion. Finally, particular thanks go to Itasca for providing the license of PFC-V5 in the framework of the IEP and the German Academic Exchange Service (DAAD) for a short-term doctorate research grant.

Financial support. This research has been supported by the Federal Ministry of Education and Research of Germany (grant no. 03G0843) and the Helmholtz DESERVE Virtual Institute (grant no. VH-VI-527).

The article processing charges for this open-access
publication were covered by a Research
Centre of the Helmholtz Association.

Review statement. This paper was edited by Federico Rossetti and reviewed by Renaud Toussaint and Nestor Cardozo.

References

Abelson, M., Yechieli, Y., Baer, G., Lapid, G., Behar, N., Calvo, R., and Rosensaft, M.: Natural versus human control on subsurface salt dissolution and development of thousands of sinkholes along the Dead Sea coast, J. Geophys. Res.-Earth, 122, 1262–1277, https://doi.org/10.1002/2017JF004219, 2017.

Al-Halbouni, D., Holohan, E. P., Saberi, L., Alrshdan, H., Sawarieh, A., Closson, D., Walter, T. R., and Dahm, T.: Sinkholes, subsidence and subrosion on the eastern shore of the Dead Sea as revealed by a close-range photogrammetric survey, Geomorphology, 285, 305–324, https://doi.org/10.1016/j.geomorph.2017.02.006, 2017.

Al-Halbouni, D., Holohan, E. P., Taheri, A., Schöpfer, M. P. J., Emam, S., and Dahm, T.: Geomechanical modelling of sinkhole development using distinct elements: model verification for a single void space and application to the Dead Sea area, Solid Earth, 9, 1341–1373, https://doi.org/10.5194/se-9-1341-2018, 2018.

Atzori, S., Antonioli, A., Salvi, S., and Baer, G.: InSAR-based modeling and analysis of sinkholes along the Dead Sea coastline, Geophys. Res. Lett., 42, 8383–8390, https://doi.org/10.1002/2015GL066053, 2015.

Bartov, Y.: Lake Levels and Sequence Stratigraphy of Lake Lisan, the Late Pleistocene Precursor of the Dead Sea, Quaternary Res., 57, 9–21, https://doi.org/10.1006/qres.2001.2284, 2002.

Baryakh, A. A., Rusin, E. P., Stazhevsky, S. B., Fedoseev, A. K., and Khan, G. N.: Stress-strain state of Karst areas, J. Min. Sci., 45, 3–10, 2009.

BGR, IAH, KIT and UNESCO: World Karst Aquifer Map, 1:40000000, Berlin, Reading, Karlsruhe, Paris, 2017.

Ćalić, J.: Karstic uvala revisited: Toward a redefinition of the term, Geomorphology, 134, 32–42, https://doi.org/10.1016/j.geomorph.2011.06.029, 2011.

Chen, Z., Auler, A. S., Bakalowicz, M., Drew, D., Griger, F., Hartmann, J., Jiang, G., Moosdorf, N., Richts, A., Stevanovic, Z., Veni, G., and Goldscheider, N.: The World Karst Aquifer Mapping project: concept, mapping procedure and map of Europe, Hydrogeol. J., 25, 771–785, https://doi.org/10.1007/s10040-016-1519-3, 2017.

Cundall, P. A.: A computer model for simulating progressive large scale movements in blocky rock systems, Proc. Symp. Rock Fract, (ISRM), Nancy, 1, 1971.

Cundall, P. A. and Strack, O. D. L.: A discrete numerical model for granular assemblies, Géotechnique, 29, 47–65, 1979.

Dahm, T. and Becker, T.: On the elastic and viscous properties of media containing strongly interacting in-plane cracks, Pure Appl. Geophys., 151, 1–16, https://doi.org/10.1007/s000240050102, 1998.

De Waele, J., Gutiérrez, F., Parise, M., and Plan, L.: Geomorphology and natural hazards in karst areas: A review, Geomorphology, 134, 1–8, https://doi.org/10.1016/j.geomorph.2011.08.001, 2011.

Dix, C. H.: Seismic velocities from surface measurements, Geophysics, 20, 68–86, 1955.

Dreybrodt, W., Gabrovšek, F., and Romanov, D.: Processes of a Speleogenessis: A Modeling Approach, Založba ZRC, 2005.

Fazio, N. L., Perrotti, M., Lollino, P., Parise, M., Vattano, M., Madonia, G., and Di Maggio, C.: A three-dimensional back-analysis of the collapse of an underground cavity in soft rocks, Eng. Geol., 228, 301–311, https://doi.org/10.1016/j.enggeo.2017.08.014, 2017.

Filin, S., Baruch, A., Avni, Y., and Marco, S.: Sinkhole characterization in the Dead Sea area using airborne laser scanning, Nat. Hazards, 58, 1135–1154, https://doi.org/10.1007/s11069-011-9718-7, 2011.

Gutiérrez, F., Parise, M., De Waele, J., and Jourde, H.: A review on natural and human-induced geohazards and impacts in karst, Earth-Sci. Rev., 138, 61–88, https://doi.org/10.1016/j.earscirev.2014.08.002, 2014.

Hammam, A. H. and Eliwa, M.: Comparison between results of dynamic and static moduli of soil determined by different methods, HBRC J., 9, 144–149, https://doi.org/10.1016/j.hbrcj.2013.05.002, 2013.

Hatzor, Y. H., Wainshtein, I., and Bakun Mazor, D.: Stability of shallow karstic caverns in blocky rock masses, Int. J. Rock Mech. Min. Sci., 47, 1289–1303, https://doi.org/10.1016/j.ijrmms.2010.09.014, 2010.

Hazzard, J. F.: Acoustic Emission Calculation in PFC5.0, Minneapolis, Minnesota, USA, 2014.

Hazzard, J. F. and Young, R. P.: Dynamic modelling of induced seismicity, Int. J. Rock Mech. Min. Sci., 41, 1365–1376, https://doi.org/10.1016/j.ijrmms.2004.09.005, 2004.

Holohan, E. P., Schöpfer, M. P. J., and Walsh, J. J.: Mechanical and geometric controls on the structural evolution of pit crater and caldera subsidence, J. Geophys. Res., 116, B07202, https://doi.org/10.1029/2010JB008032, 2011.

Holohan, E. P., Schöpfer, M. P. J., and Walsh, J. J.: Stress evolution during caldera collapse, Earth Planet. Sc. Lett., 421, 139–151, https://doi.org/10.1016/j.epsl.2015.03.003, 2015.

Itasca: PFC 5.0 Manual, Itasca International, Inc., Technical Documentation, 2014.

Jing, L. and Stephansson, O.: Fundamentals of Discrete Element Methods for Rock Engineering, Elsevier, 2007.

Kaufmann, G. and Dreybrodt, W.: Calcite dissolution kinetics in the system $CaCO_3$-H_2O-CO_2 at high undersaturation, Geochim. Cosmochim. Ac., 71, 1398–1410, https://doi.org/10.1016/j.gca.2006.10.024, 2007.

Parise, M. and Lollino, P.: A preliminary analysis of failure mechanisms in karst and man-made underground caves in Southern Italy, Geomorphology, 134, 132–143, https://doi.org/10.1016/j.geomorph.2011.06.008, 2011.

Polom, U., Alrshdan, H., Al-Halbouni, D., Holohan, E. P., Dahm, T., Sawarieh, A., Atallah, M. Y., and Krawczyk, C. M.: Shear wave reflection seismic yields subsurface dissolution and subrosion patterns: application to the Ghor Al-Haditha sinkhole site, Dead Sea, Jordan, Solid Earth, 9, 1079–1098, https://doi.org/10.5194/se-9-1079-2018, 2018.

Potyondy, D. O.: The bonded-particle model as a tool for rock mechanics research and application: current trends and future directions, Geosystem Eng., 17, 342–369, 2014.

Potyondy, D. O. and Cundall, P. A.: A bonded-particle model for rock, Int. J. Rock Mech. Min. Sci., 41, 1329–1364, https://doi.org/10.1016/j.ijrmms.2004.09.011, 2004.

Romanov, D., Kaufmann, G., and Hiller, T.: Karstification of aquifers interspersed with non-soluble rocks: From basic principles towards case studies, Eng. Geol., 116, 261–273, https://doi.org/10.1016/j.enggeo.2010.09.008, 2010.

Schöpfer, M. P. J., Childs, C., and Walsh, J. J.: Localisation of normal faults in multilayer sequences, J. Struct. Geol., 28, 816–833, https://doi.org/10.1016/j.jsg.2006.02.003, 2006.

Schöpfer, M. P. J., Childs, C., and Walsh, J. J.: Two-dimensional distinct element modeling of the structure and growth of normal faults in multilayer sequences: 1. Model calibration, boundary conditions, and selected results, J. Geophys. Res., 112, B10401, https://doi.org/10.1029/2006JB004902, 2007.

Schöpfer, M. P. J., Abe, S., Childs, C., and Walsh, J. J.: The impact of porosity and crack density on the elasticity, strength and friction of cohesive granular materials: Insights from DEM modelling, Int. J. Rock Mech. Min. Sci., 46, 250–261, https://doi.org/10.1016/j.ijrmms.2008.03.009, 2009.

Soldal, M. and Mondol, N. H.: Dynamic to static relationships of shear modulus for sand and sandstones, in: Thrid international Workshop on Rock Physics, Perth, Australia, 2015.

Tharp, T. M.: Mechanics of upward propagation of cover-collapse sinkholes, Eng. Geol., 52, 23–33, https://doi.org/10.1016/S0013-7952(98)00051-9, 1999.

Wadas, S. H., Polom, U., and Krawczyk, C. M.: High-resolution shear-wave seismic reflection as a tool to image near-surface subrosion structures – a case study in Bad Frankenhausen, Germany, Solid Earth, 7, 1491–1508, https://doi.org/10.5194/se-7-1491-2016, 2016.

Waltham, T.: Control the drainage: the gospel accorded to sinkholes, Q. J. Eng. Geol. Hydroge., 49, 5–20, https://doi.org/10.1144/qjegh2015-088, 2016.

Waltham, T., Bell, F., and Culshaw, M. G.: Sinkholes and subsidence: Karst and Cavernous Rocks in Engineering and Construction, Springer, Berlin, Heidelberg, 2005.

Wang, C., Deng, A., and Taheri, A.: Three-dimensional discrete element modeling of direct shear test for granular rubber-sand, Comput. Geotech., 97, 204–216, https://doi.org/10.1016/j.compgeo.2018.01.014, 2018.

Watson, R. A., Holohan, E. P., Al-Halbouni, D., Saberi, L., Sawarieh, A., Closson, D., Alrshdan, H., Abou Karaki, N., Siebert, C., Walter, T. R., and Dahm, T.: Sinkholes and uvalas in evaporite karst: spatio-temporal development with links to base-level fall on the eastern shore of the Dead Sea, Solid Earth Discuss., https://doi.org/10.5194/se-2018-105, in review, 2019.

Weisbrod, N., Alon-Mordish, C., Konen, E. and Yechieli, Y.: Dynamic dissolution of halite rock during flow of, diluted saline solutions, Geophys. Res. Lett., 39, 1–7, https://doi.org/10.1029/2012GL051306, 2012.

Wichtmann, T. and Triantafyllidis, T.: On the correlation of “static” and “dynamic” stiffness moduli of non-cohesive soils, Bautechnik, 86, 28–39, https://doi.org/10.1002/bate.200910039, 2009.

Yechieli, Y., Abelson, M., and Baer, G.: Sinkhole formation and subsidence along the Dead Sea coast, Israel, Hydrogeol. J., 24, 601–612, https://doi.org/10.1007/s10040-015-1338-y, 2016.

CHAPTER 6

Summary and discussion of major findings

Complementary methods consisting of satellite image analysis, photogrammetry and distinct element modelling provided important constraints for a more concise picture of subsidence and rock failure in areas of distributed subrosion and dissolution. In this chapter, answers to the overall research questions (1-4) are provided. I focus the discussion on causal relationships and theoretical, conceptional aspects, as a general comparison and literature review is discussed extensively in my papers in the previous chapters. My discussion integrates the findings of individual papers and covers the broader view of the studies integrated in the PhD thesis.

6.1 Spatio-temporal development and morphometrics of sinkholes and ground features in an active karst area

Detailed information about sinkhole and other ground feature development in the study area of Ghor Al-Haditha has been derived by a photogrammetric survey conducted in 2014 (Chap. 3). A 0.45 km^2 sized, sinusoidal main depression, bound partly by non-tectonic faults, and orientated NNW with a shift to NE at the mud/alluvium contact, has been identified at the field site. It contains 85 % of the 300 sinkholes in the studied area. From GIS analysis, the minimum volume loss of the surveyed area has been estimated to $2.5e^6$ m^3 in 25 years, leading to an average subsidence rate of 0.21 m yr^{-1}. The minimum erosion rate lies at 16-40 mm yr^{-1}, comparable to results for other salt dominated terrains (Mottershead et al., 2007, 2008; Bruthans et al., 2008). Important morphological features have been derived: The morphology of sinkholes in the depression area is related to the type of the overburden material they formed in. In mud, wide and shallow sinkholes develop with low depth to diameter values (0.14), in alluvium, deep and narrow sinkholes develop (0.4). Overall, sinkholes are basically elliptical with eccentricities of 1.31 and strike of the long-axis between NNW-N for alluvium and NNE-NE for mud, and significantly clustered with a nearest neighbour ratio of 0.69. Mixtures of the morphological endmembers mentioned in Chap. 1.2 exist at the field site.

From field work and analysis of satellite images and orthophotos, evidence of the background driving hydro(geo)logical process could be derived. A conceptual model summarizing these findings, main sinkhole types and the general formation processes is sketched in Fig. 6.1. Actively evolving, partly artesian springs, and channelized, highly mobile, sediment-laden groundwater flows form at the contact between the mud and alluvium sequences, sketched as a simplified layered alluvial fan system in Fig. 6.1A-C. The evaporite rich Dead Sea mud hereby acts as an aquitard, locally penetrated by solution-driven water channels, which dynamically form new canyon and subsurface channel systems. These conduits in the soluble/erodible material are schematically indicated as ellipses in Fig. 6.1. Consequently, sinkhole formation and subsidence at Ghor Al-Haditha is related to karstification by both chemical dissolution and mechanical subrosion along a channelized subterranean flow network in interbedded evaporite and mud/alluvium deposits.

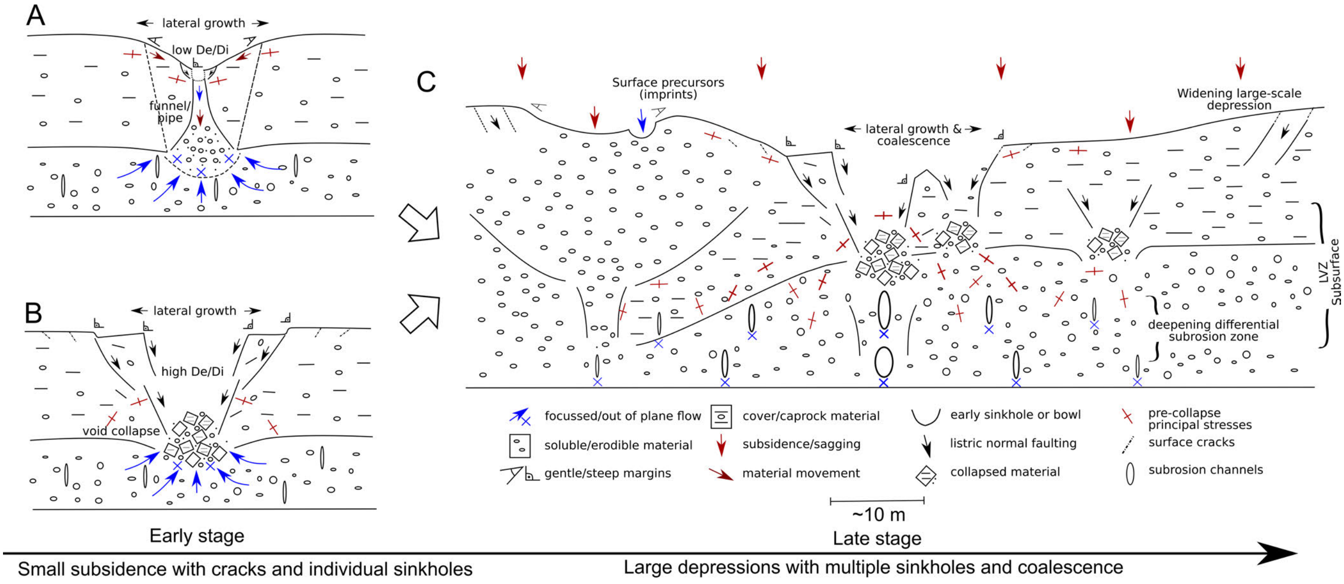

Figure 6.1: Generic model of karst landform development with focus on sinkholes and large-scale depression formation. Indicated are typical surface and subsurface features and the principal stress system. (**A**) cover suffosion or dropout sinkhole endmember. (**B**) cover or caprock collapse sinkhole endmember. (**C**) large depression formation with mixtures of multiple and nested sinkholes and indications of precursory structures.

From analysis of repeated DSMs (Chap. 5), little or no subsidence or crack formation is observed before a collapse in strong materials. Rather often precursory small holes grow with time. In the weak cover material, small subsidence may indicate a subrosion in depth. This development and growth of individual sinkholes is highlighted in Fig. 6.1A and B. With further development, multiple nested and coalesced sinkholes in large depression zones bound by deep cracks form in all materials (Fig. 6.1C), characteristic for a mature karst system. Remote sensing images covering the last 50 years of a larger part of the study area ($25\,\mathrm{m}^2$) have been analysed recently (Watson et al., 2019). Highlight is the appearance order in the evolution of sinkholes and depressions: Individual sinkholes often appear before or at the same time as cracks around major depression zones. While the large-scale depression-zone deepens, sinkhole clusters and alignments form, building aggregations, indicated by the overall subsidence in Fig. 6.1C. These depressions show generally De/Di ratios of one order of magnitude lower than for sinkholes. The extended study in Watson et al. (2019), also emphasizes the role of the base-level fall in the formation of the sinkhole and stream channel system. Our remote sensing studies of the sinkhole area hence provide essential findings about the background driving processes and local conditions as well as morphological characteristics which build the basis for our numerical modelling.

6.2 A distinct element modelling approach to simulate large-scale ground subsidence

A novel, 2D distinct element modelling approach with the software PFC2D-V5 to simulating individual and multiple cavity growth and sinkhole/depression formation has been developed (Chapters 4 and 5). The approach uses a stepwise material removal technique in void spaces of arbitrarily shaped geometries under gravitational loading, simulating a network of subsurface groundwater conduits growing by chemical/mechanical erosion. Such a network is sketched in Fig. 6.1C. A feedback loop between material removal and mechanical failure of the material with porosity increase develops. The approach has been benchmarked successfully by analytical and boundary element method solutions for a growing circular cavity. For application to the Dead Sea sinkhole phenomenon, simulated compression and tension tests have been used to derive realistic bulk rock properties from microscopic bond-strength parameters and moduli. Tests yielded relatively low bulk strength values for lacustrine mud (UCS $\approx$ 0.06-0.25 MPa), middle values for alluvial sandy-gravel sediments (UCS $\approx$ 0.53-0.92 MPa) and high values for lacustrine salt(UCS $\approx$ 1.23-1.54 MPa).

Morphological data derived from photogrammetry at the karst area of Ghor Al-Haditha are, both qualitatively and quantitatively, in close agreement with numerical modelling results. The DEM approach produces physically realistic sinkhole shapes, and successfully reproduces typically measured sinkhole and depression De/Di ratios for the Dead Sea materials, also comparable with other studies and regions (see discussion in Chap. 3). Vertical displacement profiles across the surface of either individual sinkholes or large-scale depressions with nested sinkhole clusters are in close agreement to field results. The field distribution appears to be related to evolution stages of the sinkholes between early and late stage collapses. With continuous material removal, future developments may be anticipated: Large basins may develop, with a flat bottom for weak material and a scattered ground for strong materials.

The developed DEM approach has therefore been successfully benchmarked and calibrated to address the simulation of collapse processes and the evolution of (sub)surface features. The detailed mechanical characteristics of such process are discussed in the following.

6.3 Mechanical development of sinkhole clusters and depressions

The most important result of the modelling study (Chapters 4 and 5) is that cavity and sinkhole/depression evolution are controlled by:

- material strength of the overburden and cavity host material,
- the depth and relative speed of the cavity growth process,
- and the developed stress pattern in the subrosion zone and near the surface.

In the summarizing Fig. 6.1 these aspects are indicated in a simplified way: Different overburden and host materials stand for variable mechanical parameters and produce different morphological features; a deepening differential subrosion zone (indicated by channels of variable elliptic shape) and the stress systems at depth and at the surface are sketched. It is important to mention that these controlling factors are not independent from each other, and their relation is discussed under the aspect of the mechanical development of karstic features. Major findings hereby include:

1. Low-strength materials do not support large cavities in the material removal zone, and subsidence is characterised by gradual sagging into the material removal zone and lateral widening, both for sinkholes and large-scale depressions, as sketched in Fig. 6.1A and C (left and right part). Synclinal bending structures develop and the margins show gentle slopes for low strength overburden and fractures for high strength overburden. The material behaviour is brittle-ductile.

2. High-strength materials support large cavity formation, leading to sinkhole formation by sudden collapse of the overburden, as sketched in Fig. 6.1B and C (central part). The margins of sinkholes and depression in high strength overburden are steep due to fracturing and can be partly overhanging. Large-scale depression formation happens by coalescence of holes if high strength material is covered by low strength material. The material behaviour is brittle.

3. A constant subrosion in a multiple cavity array yields a stable compression stress arch spanning over the whole subrosion zone. It hinders sinkhole collapse into individual cavities and favours block-wise large-scale subsidence.

4. A deepening differential subrosion, highlighted in Fig. 6.1C, yields a more fragmented stress pattern. Local stress interaction around individual cavities generates more stress peaks that lead to cracks that destabilize the subground. This favours multiple sinkhole collapses by shear and tensile failure and nesting within large-scale depressions.

5. The inclusion of weak layers in multilayer models results generally in earlier sinkhole development, i.e. less amounts of removed volume at depth are needed for a collapse in comparison to the case of uniform model material. This is related to both integrated weakening and geometrical destabilisation of the overburden.

6. A strong interlayer leads to stabilizing individual compressive stress arches and focussing shear stresses near the edges of the cavities, with subsequent spalling, a typical phenomenon observed e.g. in boreholes, mines or tunnels (Karatela et al., 2016; Zang and Stephansson, 2010; Potyondy and Cundall, 2004).

Cavities can further be destabilized and grow in a feedback mechanism. Such feedback mechanism depends on all mentioned controlling aspects: material strength and distribution, depth and relative speed of the cavity growth and stress pattern development. The DEM method hereby proved to be explicitly suitable to investigate the influence of each aspect and their relation, due to the intrinsic spontaneous crack and void space formation based on particle bond failure. Although the mechanical aspects of collapse processes are well described and simulated with the presented DEM approach, further complexities may be introduced due to e.g. lateral material variations or thinly layered systems, which resemble more heterogeneous materials in nature (see Chap. 7).

6.4 Relation of the sinkhole formation process to geophysical parameters of the subsurface

Generic tracking of geodetic and geophysical parameters has been implemented successfully in the DEM approach, such as porosity, stress, strain, surface displacement and microseismicity. The latter is described more in detail for synthetic examples in the following Chap. 7 and in Appendix A.

Porosity tracking, simulated rock testing and crack density is used to derive apparent elastic moduli and shear wave velocities comparable to field survey results from Polom et al. (2018) at the Ghor Al-Haditha sinkhole site. Reflection seismics with a shear wave vibrator and landstreamer device were performed there between 2014 - 2016. The seismic study from Polom et al. (2018) nicely revealed the geologic structures of intercalated, dipping alluvial fan and mud-flat sediment layers. The 30-

60 m deep lying mud and alluvium layers show hereby a reduced apparent shear wave velocity of $\leq$ 275 m/s, while more stable parts at the surface have higher values. Such a low-velocity layer is also indicated in Fig. 6.1C. The propagation of shear wave velocities depends on grain size coupling. After Polom et al. (2018) velocity reduction can occur due to different reasons: (1) Diminished grain size coupling due to less cementation or pore-pressure increase, (2) High-velocity layers at the surface (e.g. asphalt roads) and (3) mechanical damage of the subsurface material. The effect of (2) is documented for parts of the survey area in Polom et al. (2018). However, it does not explain the larger scale reduction in areas without a high-velocity top layer. The favoured explanation for the sinkhole area of Ghor Al-Haditha is (3), shear wave velocity reduction related to fracturing of the rock mass, as also the numerical simulations with DEM in Chap. 5 support this hypothesis. Both simulated and well-calibrated material types, alluvium and mud, are affected by cracking and void space formation, which leads to enhanced porosities and reduced seismic velocities of the same order like derived from field data. The effects of this subrosion process can be seen in the seismic profiles of Polom et al. (2018), where subsurface features like depressions, bowl-shaped zones and areas of low reflectivity are documented. However, the effect of the pore-pressure increase with depth has not been tested in our mechanical models and should be addressed in future work (see Chap. 7).

Supportive results from related geophysical studies

For sinkhole sites along the western shore of the Dead Sea, seismic refraction, surface-wave dispersion, electric and electromagnetic methods as well as borehole drillings revealed a complex setting of a thick Holocene salt layer in a system of sandy-gravel aquifer and Dead Sea mud deposits, and the existence of faults, buried sinkholes, void spaces and synforms at the salt layer edge (Ezersky and Livne, 2013; Ezersky et al., 2013; Ezersky and Frumkin, 2017; Ezersky et al., 2017; Frumkin et al., 2011). At our study area on the eastern side of the Dead Sea, however, neither such a thick salt layer, nor the existence of tectonics related fault zones are found by the detailed shear wave reflection survey from Polom et al. (2018). Moreover, recent near-surface geophysics in the area support our findings of a deepening subrosion system in poorly cemented sediments and are presented in the following.

Fig. 6.2A shows an interesting and important anomaly that was found in an old, coloured satellite image (see Chap. 3). Vegetation and water is coloured by red and at the indicated location, a former surface channel fork is observed in 1970. In 2016, a profile with shear wave reflection was conducted along the main road on the eastern boundary of the sinkhole area, crossing the marked anomaly. The preliminary analysis of the seismic data of the profile, based on the same technique from Polom et al. (2018), is presented in Fig. 6.2B. The interpretation in part C of the figure reveals the structure of a deepening channel system, an important finding as in 1970 the water was still flowing superficially. Nowadays, the water follows subsurface channels as indicated in Fig. 6.1C, and creates the deepening subrosion zone in weak materials due to groundwater flow, with the subsequent consequences of sinkhole formation within large-scale depressions that develop above such dynamic channel system.

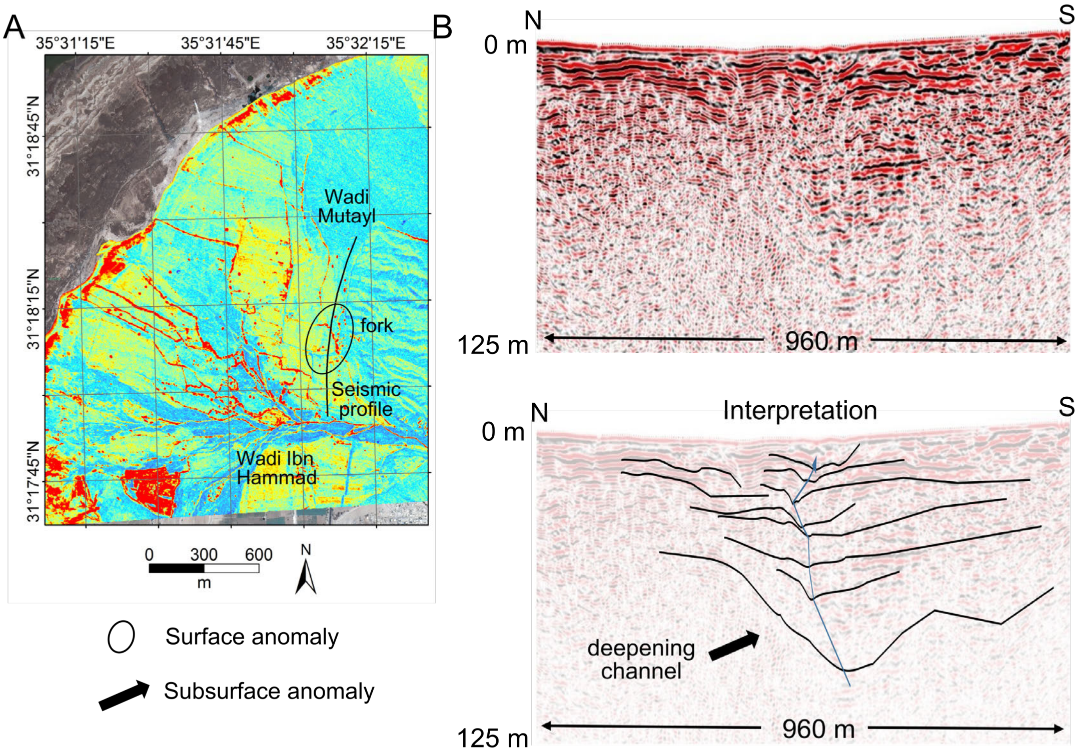

Figure 6.2: Water conduit anomaly in aerial photos and seismics. (**A**) highlights the former surface channel fork on a coloured Corona satellite image from 1970 (resolution of 1.8 m px^{-1}). Water content and vegetation appears in reddish color (see Chap. 3). (**B**) shear wave reflection seismics profile 6 and its preliminary interpretation after analysis performed like in Polom et al. (2018) and Wadas et al. (2016). A deepening channel system can be recognized in the central part.

Technically, water-bearing layers and flow patterns, both horizontal and vertical movement on different scales can be resolved by electromagnetic (Jackisch et al., 2017) and electric methods (Jardani et al., 2007; Kaufmann and Romanov, 2016). Variations of resistivity or electromagnetic wave velocity derived from ERT and ground penetrating radar (GPR), respectively, are often related to complex porosity and water saturation distribution in the underground (Billi et al., 2016; Ezersky, 2008; Kaufmann, 2014; Sevil et al., 2017).

Exemplary application of ERT and SP, performed during fieldwork in 2018 near the main canyon system of the field site, is shown in Fig. 6.3. The canyon developed by retrogressive, upslope erosion and connected several sinkholes (Watson et al., 2019). These recent electric measurements revealed an extremely low resistivity layer (interpreted as salty mud) beneath resistive alluvial gravel and sand cover (Fig. 6.3B). These data also highlight low resistivity areas of possible groundwater flow connected to the spring system. Complementary results are achieved from a 2D SP array with local, strong negative potentials indicating sub-horizontal groundwater flow in the upslope part of the canyon mouth (Fig. 6.3A, cf. e.g. Jardani et al., 2007; Revil, 2005; Richards et al., 2010).

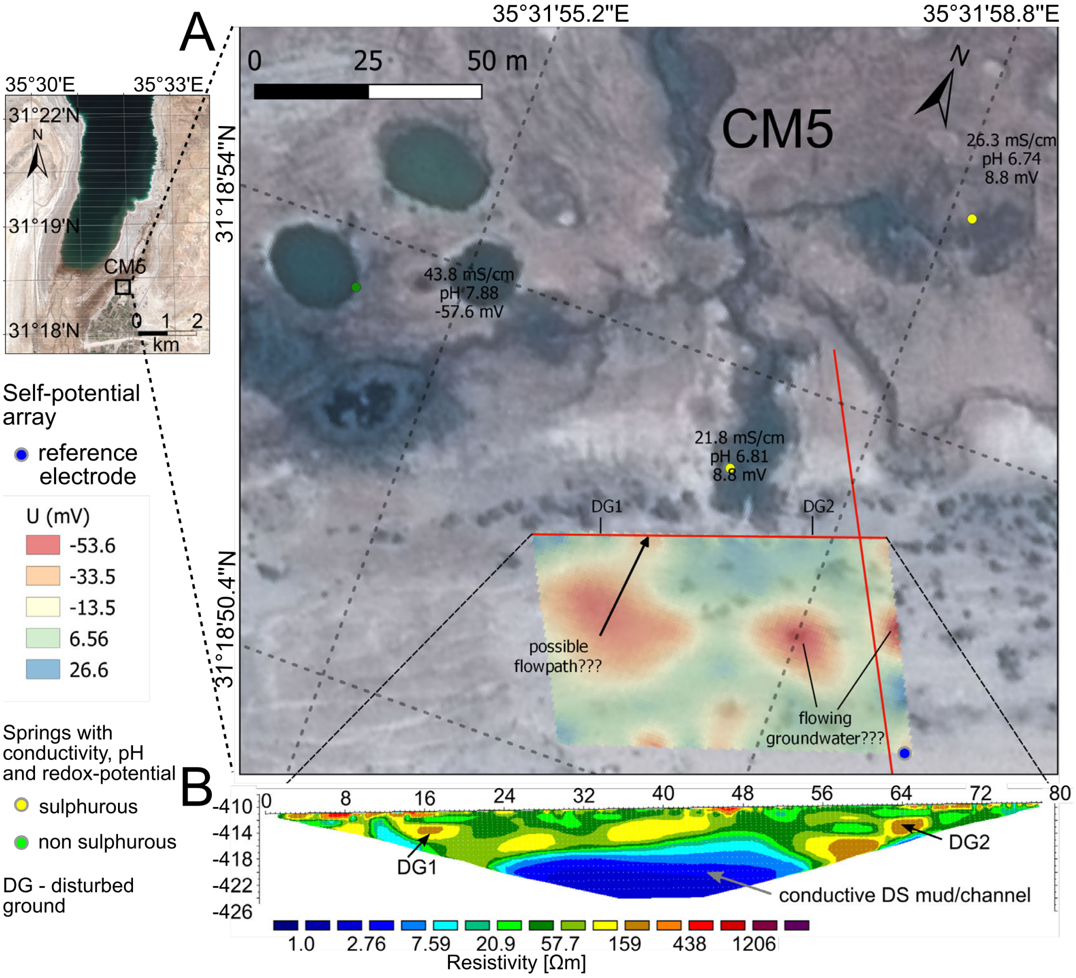

Figure 6.3: Electric resistivity tomography and self-potential at the main spring area CM5. (**A**) Pleiades satellite image from April 2018 of the still-evolving head of the 'main channel' CM5 showing the profile location and the SP array results acquired by unpolarizable Ag-AgCl electrodes. The error on SP data has been estimated by repeated measurements to 4.5 %. Circles indicate water sampling points. (**B**) electric resistivity distribution along the profile achieved by inversion of apparent resistivities. A Wenner spread of steel electrodes, the Lippmann ERT device '4point light 10W' (Grinat et al., 2010) and the software Geotomo Res2DInv (Loke and Dahlin, 2002) were used. The RMS is 4.4 % after 8 iterations.

Overall, all methods of this work yield complementary findings on the detailed development of an active karst system. The deepening subrosion related to preferential flow paths in an intercalated alluvial fan/mud-flat system creates void spaces, subsurface conduits and subsequently leads to hazardous subsidence, and sinkholes within large-scale depressions. The versatilely applicable DEM based numerical modelling approach presented in this thesis is suitable to simulate such collapse processes under different background conditions and resulted in a deeper understanding of the mechanical system of subsidence related phenomena. It gives an important link to measurable geodetic and geophysical parameters. In simple terms, the existence of multiple void spaces, their deepening and variable growing speed, lead to destabilization of the subground. This is characteristic for a system with base-level fall, such as observed at the Dead Sea shoreline, but also for other karst areas.

CHAPTER 7

Perspectives

A key question that remains, is to identify and quantify the links between the time dependent natural hazards of sinkhole and subsidence formation to collapse triggering mechanism. Such potential triggers are for example earthquakes, natural or man-made changes in the groundwater flow, hydraulic transients in fault zones, flash floods related to strong meteorological events and combinations of these. Here, the perspective of a combined, interdisciplinary approach of geophysical methods and numerical modelling to improve the understanding of the time-dependent small-scale formation mechanism, the interplay of the mentioned triggering processes and the relevance for accurate hazard assessment and early warning potential is discussed.

7.1 Advanced modelling

Improvements of DEM based numerical modelling techniques are possible in regards of several terms. Further ideas and directions that are important for a model scenario based geodetic and geophysical monitoring system, are elaborated in the following.

Firstly, although bulk rock parameters are well calibrated for the application of our DEM approach to materials common at the Dead Sea, rocks and sediments are heterogeneous in nature. Especially the former Dead Sea lakebed consists of a mud/salt-flat, a layered mixture of clay and silt minerals with evaporites like gypsum, calcite and halite. In the simulations, this has been simply represented by the material mud, with an implemented bond healing procedure accounting for the brittle-ductile mud behaviour. For future work, the material composition of mud could be adjusted to thin alternating layers between a strong and weak compound. Also, a different, non-linear particle contact scheme (e.g. hysteretic contact model, cf. Itasca Cooperation Group, 2014) could be used for the purpose of simulating viscoelastic rheology, as done successfully in sinkhole formation simulations with FEM (Shalev and Lyakhovsky, 2012; Baer et al., 2018). More complex model setups with lateral material variation, pre-fracturing or fault inclusion have also not been scope of this work. Particularly, DEM is able to simulate the deformation patterns in fault systems (Schöpfer et al., 2007a,b), using a different particle-bonding scheme (e.g. smooth or flat joints, cf. Itasca Cooperation Group, 2014).

Secondly, such faults are however often the nucleation points where dissolution and material removal in the underground start, as a result of fluid movement. For more realistic simulation of the material removal process in karst, it is possible to include dissolution kinetics and fluid mechanics more thoroughly (for calcite see e.g. Kaufmann and Dreybrodt, 2007). In FEM based studies, coupled chemo-mechanical modelling has been investigated by Khadka and Hu (2019), while pure chemical dissolution in karst has been addressed by e.g. Kaufmann et al. (2012). Mechanically, drag-forces on particles due to fluid movement or pore-fuid pressure effects have a strong impact on the stress limits in the system before rock failure. Both could be simulated by external forces purely by DEM

(Yoon et al., 2015; Ghani et al., 2013). But this is computationally intensive[1] and, additionally, correct boundary conditions for simulated flow are needed. For the latter, FEM could be used for the extended model domain, and DEM could be limited to the fracturing affected model core, effectively reducing the computation costs. These costs are the main reason why an early-warning aspect is currently not possible with pure DEM modelling. The coupling of FEM with DEM, so called hybrid FDEM modelling (Lisjak and Grasselli, 2014), e.g. the codes FLAC and PFC-V6 from Itasca, could serve as the basis for this purpose.

Thirdly, simulation of fluid flow in rocks may lead to a completely new aspect in DEM modelling, the consideration of the electric double layer (Grahame, 1947). Simulation of electric potential differences have been successfully applied to small-scale swelling clay phenomena (Anandarajah and Amarasinghe, 2012), but not yet on large-scale rock and flow systems. Technically, if electrokinetic forces between the particles are considered and thoroughly added, the proposed coupled FEM-DEM modelling would also be able to simulate electric potential differences.

Forthly, micro earthquakes can occur related to fracturing, collapses and material movement in the underground (Dahm et al., 2011; Kinscher et al., 2014; Wust-Bloch and Joswig, 2006; Abelson et al., 2018). In DEM, breakage of bonds between particles lead to crack formation. Acoustic emission/microseismicity and moment tensor calculation based on the forces and displacements during cracking have been provided for PFC2D and 3D by Hazzard and Young (2002, 2004) and Hazzard (2014). The physics behind the implementation is explained in Appendix A.1. As an example, Fig. 7.1 shows the cumulative microseismicity at final collapse stage. They are recorded for several material combinations in the complex deepening differential subrosion scheme presented in Chap. 5.

The events are coloured by simulation time (cycles). Their size relate to the moment magnitude. Most of the events appear closely spaced around the defined subrosion zones or relate to crack and fracture zone growth at the surface. Larger events appear mainly in the horizon between 20 and 30 m. Different stages of subsurface cavity growth and fracture propagation can be imaged by this way. A different pattern of event distribution is also visible for weak (Fig. 7.1A-C) and strong cavity host material (Fig. 7.1D). The latter is affected by fracturing beside the active subrosion zone.

---

[1] For pure DEM simulations using the developed approach, depending on which parameters are tracked, the time needed for computation on an up to date workspace computer to produce a well-developed mature collapse structure is 2-5 weeks, for one model assembly only.

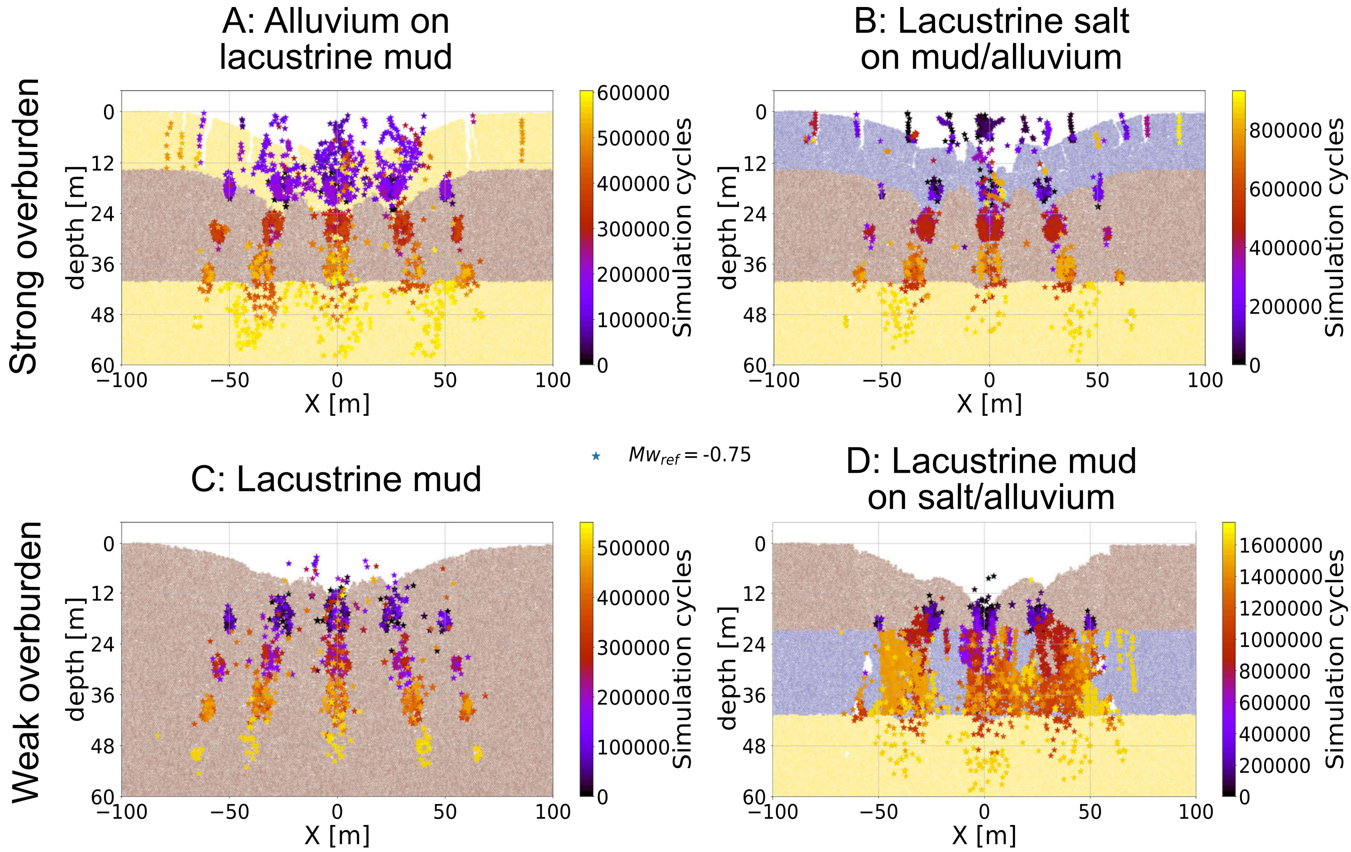

Figure 7.1: Cumulative microseismicity coloured by time for simulations of four material setups common at the Dead Sea with the multiple cavity growth scenario by deepening differential subrosion. Note that transparent background represents post-collapse layers at the final stage of the model. Star size represents magnitudes and reference magnitude is indicated. Setup are (**A**) Alluvium on mud, (**B**) lacustrine salt on mud, (**C**) pure lacustrine mud and (**D**) lacustrine mud on salt and alluvium.

In the following, the potential of this microseismicity and strain recording procedure is highlighted for future analysis and comparison with real data during fracturing and collapse processes on large scales. An exemplarily tracked simulation of a single void growth starting in 30 m depth and subsequent sinkhole collapse in an alluvium on mud multilayer model is presented in Fig. 7.2. A focus is given on stresses, microseismicity, extensometer strains and marker particle displacement. Their locations are indicated in Fig. 7.2A. We observe that both compressive and shear stress accumulate in an arch form around the material removal zone (A). Most events are either in the subrosion zone or clustered in the roof of the cavity, before the actual collapse. The moment magnitudes are clipped to $M_w \geq -2.5$ according to typically measurable values in field experiments (Kinscher et al., 2016; Wust-Bloch and Joswig, 2006; Dahm et al., 2011). Although the seismicity keeps increasing in the early stages, the maximum subsidence does not, related to further cracking in the subsurface after subsidence (B and C). The extensometer record is only shown for the timeframe before the collapse (D). The deeper extensometer (no. 5) reacts first, recording vertical strain, but immediately afterwards the superficial extensometers (no. 1 and 2) react, indicating subsidence. In parts E and F of Fig. 7.2, the stable zone marker particle, 50 m away from the centre of the collapse zone, records a dynamic particle movement before the collapse actually happens, related to the cracking of the subsurface and the appearance of seismic waves. For completeness, the whole record of stress, displacements, porosity and microseismicity of this model is shown in Fig. A.2.1.

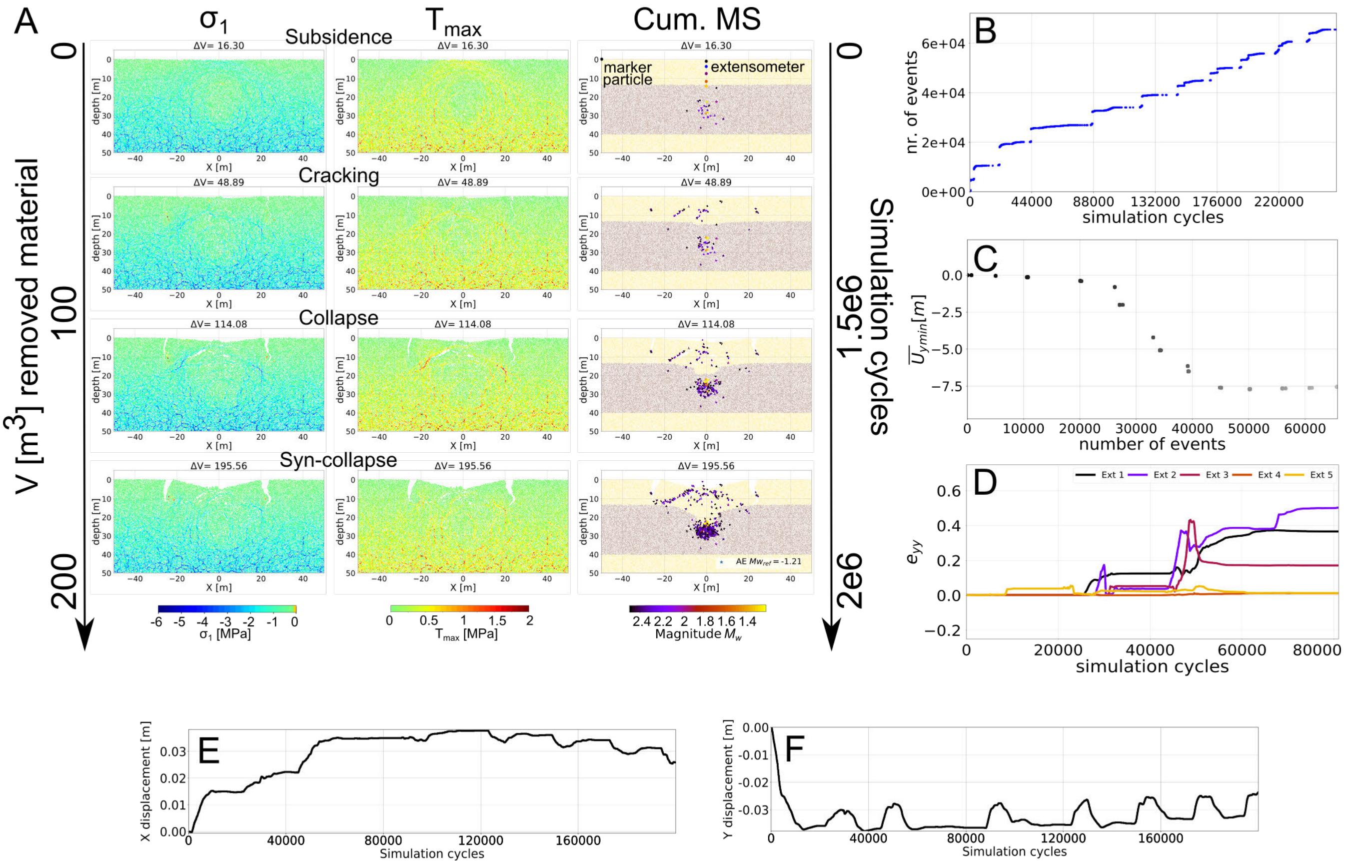

Figure 7.2: Microseismicity vs. stress patterns tracked with PFC2D-V5. (**A**) principal stress σ_1, maximum shear stress τ_{max} and the cumulative microseismic events for the early pre- and syn-collapse states of the alluvium on mud multilayer models with a subrosion zone in 30 m depth. Events are scaled by magnitude and the reference maximum magnitude is given in the legend. Mean moment magnitude is $\bar{M_w} = -3.17$, but note that event magnitudes are clipped for $M_w = -2.5$ for clarity. (**B**) cumulative number of events versus simulation cycles. Note that semi-transparent background represents layers at the current stage of the model. (**C**) surface subsidence $U_{y,min}$ versus the number of events. (**D**) vertical strain e_{yy} of extensometers put in the cover material above the centre of the active zone at depths $2, 4, 8, 12$ and 15 m from the surface. (**E**) record of the horizontal displacement and (**F**) the vertical displacement of a marker particle located 50 m away from the centre of the collapse zone.

This proposed advanced modelling approach will allow for a direct comparison of the different methods in one setup, and offer new options for joint interpretation and analysis of the time-dependent collapse process. An application of this coupled modelling scheme would not be limited to sinkholes, but applicable also to other natural hazard phenomena that involve the influence of fluids on mechanical strength and stability, e.g. hydro-fracturing, landslides, rock-falls or related volcano hazards. In case the detailed hydro- and geological background (boundary conditions), as well as rock mechanical parameters for an investigation area are well-known, this approach may lead to scenario-based model sets, which can be used for quick assessment of a hazard. For this, the provision of geodetic and geophysical data is essential. The composition of such a monitoring system is explained below.

7.2 Monitoring systems and early warning

Satellite/aerial based monitoring or well-equipped ground monitoring systems are commonly used for large-scale surveillance of natural hazards, e.g. volcanoes (Amoroso et al., 2018; Sigmundsson et al., 2018; Sparks et al., 2012). However, for shallow and local hazard like the sinkhole formation, researchers often focus on one technique that addresses the effect but not the cause, e.g. mostly deformation studies with InSAR or laser scanning, seismic activity as well as gravity monitoring (Benito-Calvo et al., 2018; Kersten et al., 2016; Intrieri et al., 2015; Lebert et al., 2011; Abelson et al., 2018). Only recently, the combination of different methods for monitoring of the deeper processes that lead to sinkhole formation has been applied (Krawczyk, 2018), although not intended for long-term installation. The most important aspect for monitoring the ground-scale sinkhole hazard, is the relation of both, subsurface water-flow and rock failure processes, as supported by the main findings of this thesis.

Cost-effective near-surface geophysical methods have shown generally a high potential to investigate processes, fluid flow systems and the potential impact and precursory information of sinkhole and subsidence development (Baer et al., 2018; Wust-Bloch and Joswig, 2006; Jardani et al., 2007; Krawczyk et al., 2012; Malehmir et al., 2016; Krawczyk, 2018, and references therein). For surveying sinkhole affected areas like the field-site of Ghor Al-Haditha, I suggest the installation of a combined geodetic and geophysical monitoring system. The installation of the ground devices should be around relevant areas identified as susceptible to subsurface flow and future material failure, for example near the main canyon/spring system at Ghor Al-Haditha. As the first preparative step, available geodetic data, e.g. from high accuracy InSAR studies like in Baer et al. (2018) and Nof et al. (2019), should be used to identify zones that have shown strong ground movement in the last years. Lately, semi-automatic delineation methods for geological structures prove very promising for fast processing of such remote sensing data (Yeomans et al., 2018; Hofierka et al., 2018). The identified areas could be confirmed by the experience of local inhabitants and experts. As a second preparative step, electric resistivity tomography (ERT) and self-potential (SP) should be used to identify zones of distribution and flow of fresh and salt water in shallow depth of the underground, which represent possible subrosion horizons. At these areas, the ground monitoring system could be installed and may consists of the following:

- Buried unpolarizable electrodes and data logger for SP electric monitoring.
- Buried seismometers and data logger for acoustic emission/microseismicity monitoring.
- Fixed Differential GPS stations to record horizontal and vertical ground movement.
- Installed time-lapse cameras at buildings or telephone posts nearby, and ground-control points, to record images that can be processed directly via photogrammetric software to see immediate changes of the surface, e.g. cracks and subsidence.
- Data transfer system via wireless satellite links.

The combination of the proposed cost-effective methods, electrics, seismics and deformation recording, will therefore offer unique chances to identify relations between the causes and effects, i.e. the different mechanical processes and the areas prone to failure. The key and novel point is hereby the integration of a locally well calibrated FDEM advanced modelling scheme, as described above. This may provide the background scenario database for such a system and new means for identifying and evaluating hazard and pre-collapse early warning possibilities for near-surface processes.

7.3 Fault control on sinkhole formation

Another still open question specifically for the Dead Sea area is related to possible tectonic control on regional-scale sinkhole formation (see Fig. 1.3). Studies on the western shore relate the sinkhole formation to fault-controlled groundwater flow in contact with dissolvable, thick salt layers from the Holocene (Ezersky and Frumkin, 2013; Shalev et al., 2006). The sinkhole lineaments hereby show similarity to the N340-350 ° and N10-30 ° strike of major tectonic rift faults of the Dead Sea transform system (Yechieli et al., 2016), their deviation is explained by the variation of the salt-edge dissolution front (Ezersky et al., 2016), which has also been proposed to be the origin of salt-cavern collapse based seismic events (Abelson et al., 2018). Similar observations on tectonic controls are drawn about the eastern Dead Sea. There, 'en-echelon' lineaments, i.e. closely-spaced, sub-parallel structural features oblique to the overall trend, are typical for left-lateral rift basins (Smit et al., 2008). Closson and Abou Karaki (2009) compared these observations with sinkhole lineaments at Ghor Al-Haditha and recent studies confirm the similarity of the sinkhole lineament trends of N10-24 ° with main regional faults (Watson et al., 2019). Such tensile fracture systems and related damage zones may provide enhanced groundwater percolation by increased hydraulic conductivity (cf. e.g. Kim and Sanderson, 2010). This may lead to fresh water contact with dissolvable and erodible material and the evolution of artesian, even submarine springs. However, as the existence of a thick salt-layer beneath Ghor Al-Haditha is unclear (see Chap. 3 and Polom et al., 2018) and no tectonic surface-faults have been observed directly in the area, further investigations about the origin and control of groundwater flow systems beneath the area are necessary.

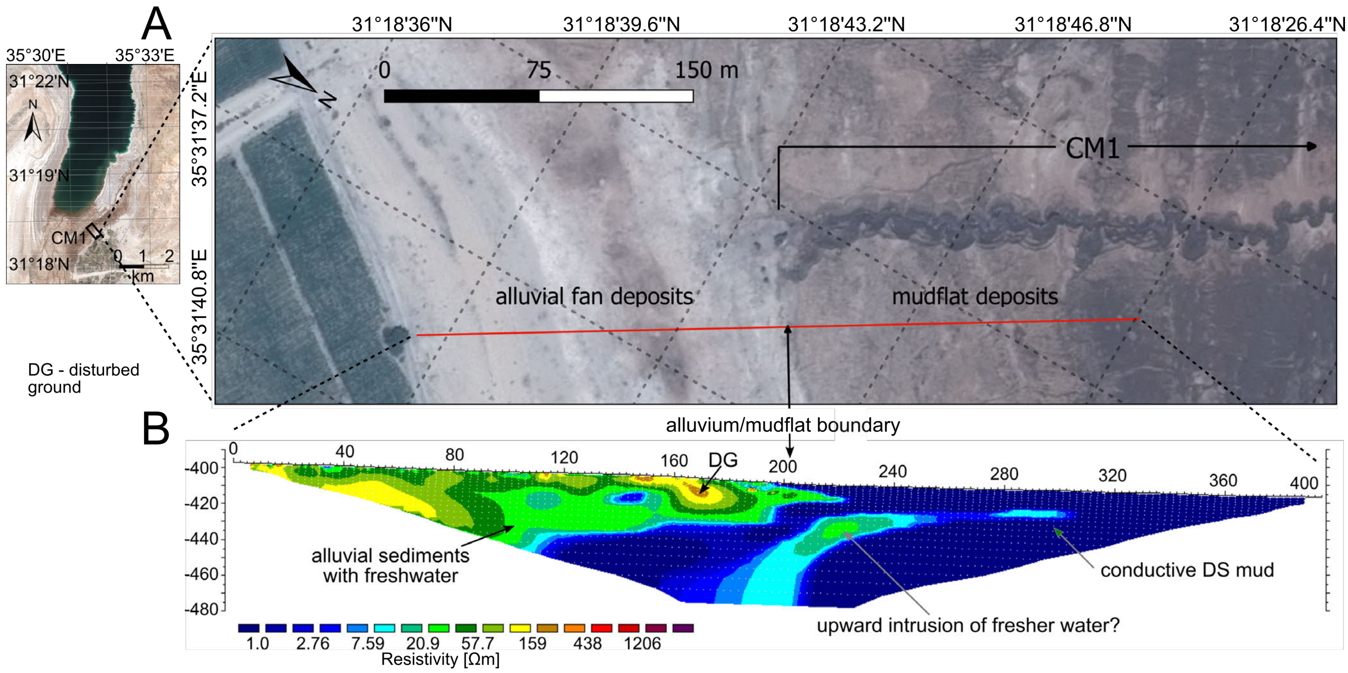

Figure 7.3: Electric resistivity tomography at the interface between mud and alluvium. (**A**) Pleiades satellite image from April 2018 near canyon CM1 showing the profile location. (**B**) electric resistivity distribution along the profile achieved by inversion of apparent resistivities. A Wenner spread of steel electrodes, the Lippmann ERT device '4point light 10W' (Grinat et al., 2010) and the software Geotomo Res2DInv (Loke and Dahlin, 2002) were used. The RMS is 8.3 % after 10 iterations.

Presented in Fig. 7.3 is an ERT survey from our most recent fieldwork at the Ghor Al-Haditha sinkhole site. It shows the 2D resisitivity pseudo-section from a profile close to a stream channel emerging at the alluvium-mud-flat boundary. At time of the measurement the channel was dry. The resistivity contour graph nice reveals the salt-fresh water interface and an upward intrusion like structure, originating at the lower centre of the profile. One possible interpretation of this vertically rising and then horizontally striking structure, is a subsurface, relatively fresh water conduit (resistivity 5-30 Ωm) that intruded into the conductive mud-flat deposits (resisitivity $< 5\,\Omega m$). This is the first geophysically-imaged evidence of > 80 m deep groundwater flow in the area of the Dead Sea. It may relate to concealed faults between the different aquifer levels (Kurnub and Um Ishrin Sandstone aquifers) on the eastern Dead Sea shore, which have been nicely imaged by magnetotelluric measurements of Meqbel et al. (2013). These examples shall emphasize of how relevant electric geophysical measurements in this setting are and can be used to derive more information about the important fault control on groundwater flow patterns and sinkhole formation in future studies.

CHAPTER 8

Conclusion

In the presented thesis, the topic of sinkhole and large-scale depression formation has been successfully addressed by a combined, cross-disciplinary approach consisting of geodetic, geophysical and numerical simulation techniques. By repeated photogrammetric and geologic field surveys as well as satellite image analysis, the morphology, morphological changes and structural features of sinkholes and depressions have been investigated at a field-site at the Dead Sea. Geophysical methods helped to reveal structural features in the underground and the role of water in the formation process. By using a novel, well calibrated, distinct element based mechanical modelling approach to simulate subsurface void space growth and large-scale subsidence, important connections between surface observations and detailed subsurface mechanical development have been derived. This thesis has consequently offered significant advances in several terms:

- Detailed estimation of the extent and consequences of the sinkhole hazard in the area.
- Methodological development in large-scale subsidence simulation with the DEM method.
- Conceptual understanding of general hydro-mechanical karst formation processes.

Essential major aspects of sinkhole and karstic depression formation, which are of relevance to determine the potential hazard of such a system, were derived in this thesis and include:

1. A progressively deepening subrosion zone with variable growth speed of the associated voids leads to the formation of multiple, partly nested sinkholes in large-scale depressions.
2. Subsidence in low-strength materials is characterised by gradual sagging and development of synclinal bending structures.
3. Subsidence in high-strength materials is characterised by sudden collapse of the overburden with pronounced and deep crack formation.
4. Depending on the material combination and cavity growth scenario, larger depressions may form either by coalescence of sinkholes, block-wise brittle failure or by gradual, large-scale sagging with lateral widening.

More specifically, this work has achieved a detailed understanding of the sinkhole formation process at the Ghor Al-Haditha sinkhole area. The development of a fresh and very active karst system has been documented and the evolution pattern of sinkholes and large-scale depressions more thoroughly investigated. The process in the study area is based on dynamic physio-chemical processes in the underground, i.e. subrosion of weak material of different composition (mud, sandy-gravel alluvium and salt) by high-gradient groundwater flow in preferential channel systems, with subsequent void space creation and collapse.

The detailed conceptual comprehension of this process helps not only to estimate impacts for the local community and decision makers in the area, but has also much wider implications applicable to similarly active karstification regions. For example, these findings may offer complementary information for researchers and stakeholders on the eastern side of the Dead Sea, where a dominating mechanism of salt dissolution has been postulated. Furthermore, the developed versatile numerical modelling approach and derived conceptual model are applicable to karst formation areas worldwide, regardless if the process runs on geologic (long) or human (short) time scale.

The outlook of this work highlights important suggestions and ideas for the installation of geodetic/geophysical monitoring systems combined with an advanced modelling scheme. This will not only improve our knowledge about hazardous collapse triggers, but also provide means to address natural hazards based on similar hydro-mechanical mechanism (i.e. landslides), in order to mitigate their effects. Finally, and most importantly, this thesis has shown the high relevance and success of combined, interdisciplinary approaches to investigate natural hazard phenomena.

Bibliography

Abelson, M., Y. Yechieli, G. Baer, G. Lapid, N. Behar, R. Calvo, and M. Rosensaft. “Natural versus human control on subsurface salt dissolution and development of thousands of sinkholes along the Dead Sea coast”. In: *Journal of Geophysical Research: Earth Surface* 122.6 (2017), pp. 1262–1277. DOI: 10.1002/2017JF004219.

Abelson, M., T. Aksinenko, I. Kurzon, V. Pinsky, G. Baer, R. Nof, and Y. Yechieli. “Nanoseismicity forecasts sinkhole collapse in the Dead Sea coast years in advance”. In: *Geology* 46.1 (2018), pp. 1–4. DOI: 10.1130/G39579.1.

Abou Karaki, N., S. Fiaschi, and D. Closson. “Sustainable development and anthropogenic induced geomorphic hazards in subsiding areas”. In: *Earth Surface Processes and Landforms* 41.15 (2016), pp. 2282–2295. DOI: 10.1002/esp.4047.

Al-Halbouni, D., E. P. Holohan, L. Saberi, H. Alrshdan, A. Sawarieh, D. Closson, T. R. Walter, and T. Dahm. “Sinkholes, subsidence and subrosion on the eastern shore of the Dead Sea as revealed by a close-range photogrammetric survey”. In: *Geomorphology* 285 (2017), pp. 305–324. DOI: 10.1016/j.geomorph.2017.02.006.

Al-Halbouni, D., E. P. Holohan, A. Taheri, M. P. J. Schöpfer, S. Emam, and T. Dahm. “Geomechanical modelling of sinkhole development using distinct elements : model verification for a single void space and application to the Dead Sea area”. In: *Solid Earth* 9 (2018), pp. 1341–1373. DOI: 10.5194/se-2018-62.

Al-Halbouni, D., E. P. Holohan, A. Taheri, R. Watson, U. Polom, M. P. J. Schöpfer, S. Emam, and T. Dahm. “Distinct element geomechanical modelling of the formation of sinkhole clusters within large-scale karstic depressions”. In: *Solid Earth* 10 (2019), pp. 1219–1241.

Amoroso, O., G. Festa, P. P. Bruno, L. D’Auria, G. De Landro, V. Di Fiore, S. Gammaldi, S. Maraio, M. Pilz, P. Roux, G. Russo, V. Serlenga, M. Serra, H. Woith, and A. Zollo. “Integrated tomographic methods for seismic imaging and monitoring of volcanic caldera structures and geothermal areas”. In: *Journal of Applied Geophysics* 156 (2018), pp. 16–30. DOI: 10.1016/j.jappgeo.2017.11.012.

Anandarajah, A. and P. M. Amarasinghe. “Behaviour of Swelling Clays: A Discrete Element Study”. In: *Journal of the Physical Society of Japan.* Oakland, California, US, 2012.

Andriani, G. F. and M. Parise. “On the applicability of geomechanical models for carbonate rock masses interested by karst processes”. In: *Environmental Earth Sciences* 74.12 (2015), pp. 7813–7821. DOI: 10.1007/s12665-015-4596-z.

Baer, G., Y. Magen, R. N. Nof, E. Raz, V. Lyakhovsky, and E. Shalev. “InSAR Measurements and Viscoelastic Modeling of Sinkhole Precursory Subsidence: Implications for Sinkhole Formation, Early Warning, and Sediment Properties”. In: *Journal of Geophysical Research: Earth Surface* 123.4 (2018), pp. 678–693. DOI: 10.1002/2017JF004594.

Baryakh, A. A., S. B. Stazhevskii, E. A. Timofeev, and G. N. Khan. “Strain state of a rock mass above Karst cavities”. In: *Journal of Mining Science* 44.6 (2008), pp. 531–538.

Baryakh, A. A., E. P. Rusin, S. B. Stazhevsky, A. K. Fedoseev, and G. N. Khan. “Stress-strain state of Karst areas”. In: *Journal of Mining Science* 45.6 (2009), pp. 3–10.

Benito-Calvo, A., F. Gutiérrez, A. Martínez-Fernández, D. Carbonel, T. Karampaglidis, G. Desir, J. Sevil, J. Guerrero, I. Fabregat, and Á. García-Arnay. “4D monitoring of active sinkholes with a Terrestrial Laser Scanner (TLS): A Case study in the evaporite karst of the Ebro Valley, NE Spain". In: *Remote Sensing* 10.4 (2018), p. 571. DOI: 10.3390/rs10040571.

Bender, F. *Geologie von Jordanien.* Gebrüder Bornträger - Berlin - Stuttgart, 1968.

BGR, IAH, KIT, and UNESCO. *World Karst Aquifer Map, 1 : 40 000 000.* Tech. rep. Berlin, Reading, Karlsruhe, Paris, 2017.

Billi, A., L. De Filippis, P. P. Poncia, P. Sella, and C. Faccenna. "Hidden sinkholes and karst cavities in the travertine plateau of a highly-populated geothermal seismic territory (Tivoli, central Italy)". In: *Geomorphology* 255 (2016), pp. 63–80. DOI: 10.1016/j.geomorph.2015.12.011.

Bonilla-Sierra, V., L. Scholtès, F. V. Donzé, and M. K. Elmouttie. "Rock slope stability analysis using photogrammetric data and DFN-DEM modelling". In: *Acta Geotechnica* 10.4 (2015), pp. 497–511. DOI: 10.1007/s11440-015-0374-z.

Brinkmann, R., M. Parise, and D. Dye. "Sinkhole distribution in a rapidly developing urban environment: Hillsborough County, Tampa Bay area, Florida". In: *Engineering Geology* 99.3-4 (2008), pp. 169–184. DOI: 10.1016/j.enggeo.2007.11.020.

Bruthans, J., N. Asadi, M. Filippi, Z. Vilhelm, and M. Zare. "A study of erosion rates on salt diapir surfaces in the Zagros Mountains, SE Iran". In: *Environmental Geology* 53.5 (2008), pp. 1079–1089. DOI: 10.1007/s00254-007-0734-6.

Bym, T., G. Marketos, J. B. Burland, and C. O'Sullivan. "Use of a two-dimensional discrete-element line-sink model to gain insight into tunnelling-induced deformations". In: *Géotechnique* 63.9 (2013), pp. 791–795. DOI: 10.1680/geot.12.T.003.

Carranza-Torres, C., D. Fosnacht, and G. J. Hudak. "Analytical and numerical study of the stability of shallow underground openings for mining and compressed air energy storage applications". In: *IC3G International Conference on Geomechanics, Geoenergy and Georesources* (2016). Ed. by P. G. Ranjith and J. Zhao.

Chapman, C. H. and W. S. Leaney. "A new moment-tensor decomposition for seismic events in anisotropic media". In: *Geophysical Journal International* 188.1 (2012), pp. 343–370.

Chapman, C. H. and W. S. Leaney. "Erratum: A correction to 'A new moment-tensor decomposition for seismic events in anisotropic media'". In: *Geophysical Journal International* 199.3 (2014), pp. 1808–1810. DOI: 10.1093/gji/ggu366.

Closson, D. and N. Abou Karaki. "Salt karst and tectonics: sinkholes development along tension cracks between parallel strike-slip faults , Dead Sea , Jordan". In: *Earth Surface Processes and Landforms* 34 (2009), pp. 1408–1421. DOI: 10.1002/esp.1829.

Cundall, P. A. and O. D. L. Strack. "A discrete numerical model for granular assemblies". In: *Géotechnique* 29.1 (1979), pp. 47–65.

Dahm, T., S. Heimann, and W. Bialowons. "A seismological study of shallow weak micro-earthquakes in the urban area of Hamburg city, Germany, and its possible relation to salt dissolution". In: *Natural Hazards* 58.3 (2011), pp. 1111–1134. DOI: 10.1007/s11069-011-9716-9.

Diabat, A. A. "Sinkholes related to Tectonic Factor at Ghor Al Haditha Area, Dead Sea/Jordan". In: *Hydrogeologie und Umwelt* 33.17 (2005), p. 4.

El-Isa, Z., O. Rimawi, G. Jarrar, N. Abou Karaki, S. Taqieddin, M. Atallah, N. Seif El-Din, and A. Al Saed. *Assessment of the hazard of subsidence and sinkholes in Ghor Al-Haditha area.* Tech. rep. University of Jordan, Center for consultation, technical services and studies, 1995.

Ezersky, M. G., L. V. Eppelbaum, A. S. Al-Zoubi, S. Keydar, A. Abueladas, E. Akkawi, and B. Medvedev. "Geophysical prediction and following development sinkholes in two Dead Sea areas, Israel and Jordan". In: *Environmental Earth Sciences* 70.4 (2013), pp. 1463–1478. DOI: 10.1007/s12665-013-2233-2.

Ezersky, M. G. and A. Frumkin. "Fault - Dissolution front relations and the Dead Sea sinkhole problem". In: *Geomorphology* 201 (2013), pp. 35–44. DOI: 10.1016/j.geomorph.2013.06.002.

Ezersky, M. G. and E. Livne. “Mo P 13 Geotechnical and Geophysical Properties of Soils in the Dead Sea Sinkhole Problem”. In: *Near Surface Geoscience.* Bochum, Germany, 2013.

Ezersky, M. G., A. Legchenko, L. Eppelbaum, and A. S. Al-Zoubi. “Dead Sea evaporite karst – I. Origin”. In: *Speleology* 1 (2016), pp. 1–44.

Ezersky, M. G. and A. Frumkin. “Evaluation and mapping of Dead Sea coastal aquifers salinity using Transient Electromagnetic (TEM) resistivity measurements”. In: *Comptes Rendus Geoscience* 349 (2017), pp. 1–11.

Ezersky, M. G., A. Legchenko, L. Eppelbaum, and A. S. Al-Zoubi. “Overview of the geophysical studies in the Dead Sea coastal area related to evaporite karst and recent sinkhole development”. In: *Int. J. Speleol.* 46.May (2017), pp. 277–302. DOI: 10.5038/1827-806X.46.2.2087.

Ezersky, M. G. “Geoelectric structure of the Ein Gedi sinkhole occurrence site at the Dead Sea shore in Israel”. In: *Journal of Applied Geophysics* 64.3-4 (2008), pp. 56–69. DOI: 10.1016/j.jappgeo.2007.12.003.

Fakhimi, A. and T. Villegas. “Application of Dimensional Analysis in Calibration of a Discrete Element Model for Rock Deformation and Fracture”. In: *Rock Mechanics and Rock Engineering* 40.2 (2007), pp. 193–211. DOI: 10.1007/s00603-006-0095-6.

Fazio, N. L., M. Perrotti, P. Lollino, M. Parise, M. Vattano, G. Madonia, and C. Di Maggio. “A three-dimensional back-analysis of the collapse of an underground cavity in soft rocks”. In: *Engineering Geology* 228 (2017), pp. 301–311. DOI: 10.1016/j.enggeo.2017.08.014.

Frumkin, A., M. G. Ezersky, A. S. Al-Zoubi, E. Akkawi, and A.-R. Abueladas. “The Dead Sea sinkhole hazard: Geophysical assessment of salt dissolution and collapse”. In: *Geomorphology* 134.1-2 (2011), pp. 102–117. DOI: 10.1016/j.geomorph.2011.04.023.

Fuenkajorn, K. and S. Archeeploha. “Prediction of cavern configurations from subsidence data”. In: *Engineering Geology* 110.1-2 (2010), pp. 21–29. DOI: 10.1016/j.enggeo.2009.10.003.

Garfunkel, Z. and Z. Ben-Avraham. “The structure of the Dead Sea basin”. In: *Tectonophysics* 266 (1996), pp. 155–176.

Ghani, I., D. Koehn, R. Toussaint, and C. W. Passchier. “Dynamic Development of Hydrofracture”. In: *Pure and Applied Geophysics* 170.11 (2013), pp. 1685–1703. DOI: 10.1007/s00024-012-0637-7.

Grahame, D. C. “The Electrical Double Layer and the Theory of Electrocapillarity”. In: *Chemical Reviews* 41.3 (1947), pp. 441–501. DOI: 10.1021/cr60130a002.

Grinat, M., W. Südekum, D. Epping, T. Grelle, and R. Meyer. “An automated electrical resistivity tomography system to monitor the freshwater/saltwater zone on a North Sea Island”. In: *Near Surface 2010-16th EAGE European Meeting of Environmental and Engineering Geophysics.* 2010.

Gudmundsson, M. T., K. Jonsdottir, A. Hooper, E. P. Holohan, S. A. Halldorsson, B. G. Ofeigsson, S. Cesca, K. S. Vogfjörd, F. Sigmundsson, T. Högnadottir, P. Einarsson, O. Sigmarsson, A. H. Jarosch, K. Jonasson, E. Magnusson, S. Hreinsdottir, M. Bagnardi, M. M. Parks, V. Hjörleifsdottir, F. Palsson, T. R. Walter, M. P. J. Schöpfer, S. Heimann, H. I. Reynolds, S. Dumont, E. Bali, G. H. Gudfinnsson, T. Dahm, M. J. Roberts, M. Hensch, J. M. C. Belart, K. Spaans, S. Jakobsson, G. B. Gudmundsson, H. M. Fridriksdottir, V. Drouin, T. Dürig, G. Adalgeirsdottir, M. S. Riishuus, G. B. M. Pedersen, T. van Boeckel, B. Oddsson, M. A. Pfeffer, S. Barsotti, B. Bergsson, A. Donovan, M. R. Burton, and A. Aiuppa. “Gradual caldera collapse at Bardarbunga volcano, Iceland, regulated by lateral magma outflow”. In: *Science* 353 (2016). DOI: 10.1126/science.aaf8988.

Gutiérrez, F., J. P. Galve, P. Lucha, C. Castaneda, J. Bonachea, and J. Guerrero. “Integrating geomorphological mapping, trenching, InSAR and GPR for the identification and characterization of sinkholes: A review and application in the mantled evaporite karst of the Ebro Valley (NE Spain)”. In: *Geomorphology* 134.1-2 (2011), pp. 144–156. DOI: 10.1016/j.geomorph.2011.01.018.

Gutiérrez, F., M. Parise, J. De Waele, and H. Jourde. “A review on natural and human-induced geohazards and impacts in karst”. In: *Earth-Science Reviews* 138 (2014), pp. 61–88. DOI: 10.1016/j.earscirev.2014.08.002.

Gutiérrez, F., I. Fabregat, C. Roque, D. Carbonel, J. Guerrero, F. García-Hemroso, M. Zarroca, R. Linares, F. Garcia-Hermoso, M. Zarroca, and R. Linares. “Sinkholes and caves related to evaporite dissolution in a stratigraphically and structurally complex setting, Fluvia Valley, eastern Spanish Pyrenees. Geological, geomorphological and environmental implications”. In: *Geomorphology* 267.June (2016), pp. 76–97. DOI: 10.1016/j.geomorph.2016.05.018.

Gutenberg, B. and C. F. Richter. “Magnitude and energy of earthquakes”. In: *Annals of Geophysics* 53.1 (1956).

Hanks, T. C. and H. Kanamori. “A moment magnitude scale”. In: *Journal of Geophysical Research* 84.B5 (1979), p. 2348. DOI: 10.1029/JB084iB05p02348.

Hatzor, Y. H., I. Wainshtein, and D. Bakun Mazor. “Stability of shallow karstic caverns in blocky rock masses”. In: *International Journal of Rock Mechanics and Mining Sciences* 47.8 (2010), pp. 1289–1303. DOI: 10.1016/j.ijrmms.2010.09.014.

Hazzard, J. F. and R. P. Young. “Moment tensors and micromechanical models”. In: *Tectonophysics* 356.1-3 (2002), pp. 181–197. DOI: 10.1016/S0040-1951(02)00384-0.

Hazzard, J. F. and R. P. Young. “Dynamic modelling of induced seismicity”. In: *International Journal of Rock Mechanics and Mining Sciences* 41.8 (2004), pp. 1365–1376. DOI: 10.1016/j.ijrmms.2004.09.005.

Hazzard, J. F. *Dynamic Numerical Modelling Seismicity and Velocity Interferometry.* Tech. rep. University of Toronto, 2004.

Hazzard, J. F. *Acoustic Emission Calculation in PFC5.0.* Tech. rep. Itasca. Minneapolis, Minnesota, USA: Itasca Consulting Group, Inc., 2014, pp. 1–16.

Hermosilla, R. G. “The Guatemala City sinkhole collapses”. In: *Carbonates and Evaporites* 27.2 (2012), pp. 103–107. DOI: 10.1007/s13146-011-0074-1.

Hofierka, J., M. Gallay, P. Bandura, and J. Sasak. “Identification of karst sinkholes in a forested karst landscape using airborne laser scanning data and water flow analysis”. In: *Geomorphology* 308 (2018), pp. 265–277. DOI: 10.1016/j.geomorph.2018.02.004.

Holohan, E. P., M. P. J. Schöpfer, and J. J. Walsh. “Mechanical and geometric controls on the structural evolution of pit crater and caldera subsidence”. In: *Journal of Geophysical Research* 116.B07202 (2011). DOI: 10.1029/2010JB008032.

Holohan, E. P., M. P. J. Schöpfer, and J. J. Walsh. “Stress evolution during caldera collapse”. In: *Earth and Planetary Science Letters* 421 (2015), pp. 139–151. DOI: 10.1016/j.epsl.2015.03.003.

Holohan, E. P., H. Sudhaus, T. R. Walter, M. P. J. Schöpfer, and J. J. Walsh. “Effects of Host-rock Fracturing on Elastic-deformation Source Models of Volcano Deflation”. In: *Scientific Reports* 7.1 (2017), p. 10970. DOI: 10.1038/s41598-017-10009-6.

Intrieri, E., G. Gigli, M. Nocentini, L. Lombardi, F. Mugnai, F. Fidolini, and N. Casagli. “Sinkhole monitoring and early warning: An experimental and successful GB-InSAR application”. In: *Geomorphology* 241 (2015), pp. 304–314. DOI: 10.1016/j.geomorph.2015.04.018.

Intrieri, E., K. Fontanelli, F. Bardi, F. Marini, T. Carlà, V. Pazzi, M. Di Filippo, and R. Fanti. “Definition of sinkhole triggers and susceptibility based on hydrogeomorphological analyses”. In: *Environmental Earth Sciences* 77.1 (2018). DOI: 10.1007/s12665-017-7179-3.

Itasca Cooperation Group, I. *PFC 5.0 Manual.* Itasca Consulting Group Inc., Minneapolis, Minnesota, USA, 2014.

Jackisch, C., L. Angermann, N. Allroggen, M. Sprenger, T. Blume, J. Tronicke, and E. Zehe. “Form and function in hillslope hydrology: In situ imaging and characterization of flow-relevant structures”. In: *Hydrology and Earth System Sciences* 21.7 (2017), pp. 3749–3775. DOI: 10.5194/hess-21-3749-2017.

Jardani, A., A. Revil, F. Santos, C. Fauchard, and J. P. Dupont. "Detection of preferential infiltration pathways in sinkholes using joint inversion of self-potential and EM-34 conductivity data". In: *Geophysical prospecting* 55.5 (2007), pp. 749–760. DOI: 10.1111/j.1365-2478.2007.00638.x.

Jing, L. and O. Stephansson. *Fundamentals of Discrete Element Methods for Rock Engineering*. Elsevier, 2007.

Karatela, E., A. Taheri, C. Xu, and G. Stevenson. "Study on effect of in-situ stress ratio and discontinuities orientation on borehole stability in heavily fractured rocks using discrete element method". In: *Journal of Petroleum Science and Engineering* 139 (2016), pp. 94–103. DOI: 10.1016/j.petrol.2015.12.016.

Kaufmann, G. and W. Dreybrodt. "Calcite dissolution kinetics in the system CaCO3-H2O-CO2 at high undersaturation". In: *Geochimica et Cosmochimica Acta* 71.6 (2007), pp. 1398–1410. DOI: 10.1016/j.gca.2006.10.024.

Kaufmann, G., D. Romanov, and W. Dreybrodt. "Modeling of Karst Aquifers". In: *Encyclopedia of caves*. Ed. by D. C. B. T. Culver. 2nd ed. Amsterdam: Academic Press, 2012, pp. 508–512. DOI: 10.1016/B978-0-12-383832-2.00073-6.

Kaufmann, G. and D. Romanov. "Structure and evolution of collapse sinkholes : Combined interpretation from physico-chemical modelling and geophysical field work". In: *Journal of Hydrology* 17 (2016), p. 2958. DOI: 10.1016/j.jhydrol.2016.06.050.

Kaufmann, G., D. Romanov, T. Tippelt, T. Vienken, U. Werban, P. Dietrich, F. Mai, and F. Börner. "Mapping and modelling of collapse sinkholes in soluble rock: The Münsterdorf site, northern Germany". In: *Journal of Applied Geophysics* 154 (2018), pp. 64–80. DOI: 10.1016/j.jappgeo.2018.04.021.

Kaufmann, G. "Geophysical mapping of solution and collapse sinkholes". In: *Journal of Applied Geophysics* 111 (2014), pp. 271–288. DOI: 10.1016/j.jappgeo.2014.10.011.

Kersten, T., L. Timmen, S. Schön, M. Kobe, G. Gabriel, and D. Vogel. "On Integrated Geodetic Monitoring for Sinkhole- Induced Surface Deformation and Mass Dislocation". In: *JISDM*. 2016, pp. 1–8.

Khadka, S. and L.-b. Hu. *New Solutions for Challenges in Applications of New Materials and Geotechnical Issues*. Springer International Publishing, 2019. DOI: 10.1007/978-3-319-95744-9.

Kim, Y. S. and D. J. Sanderson. "Inferred fluid flow through fault damage zones based on the observation of stalactites in carbonate caves". In: *Journal of Structural Geology* 32.9 (2010), pp. 1305–1316. DOI: 10.1016/j.jsg.2009.04.017.

Kinscher, J., P. Bernard, I. Contrucci, A. Mangeney, J. P. Piguet, and P. Bigarre. "Location of microseismic swarms induced by salt solution mining". In: *Geophysical Journal International* 200.1 (2014), pp. 337–362. DOI: 10.1093/gji/ggu396.

Kinscher, J., S. Cesca, P. Bernard, I. Contrucci, A. Mangeney, J. P. Piguet, and P. Bigarré. "Resolving source mechanisms of microseismic swarms induced by solution mining". In: *Geophysical Journal International* 206.1 (2016), pp. 696–715. DOI: 10.1093/gji/ggw163.

Kottmeier, C., A. Agnon, D. Al-Halbouni, P. Alpert, U. Corsmeier, T. Dahm, A. Eshel, S. Geyer, M. Haas, E. P. Holohan, N. Kalthoff, P. Kishcha, C. M. Krawczyk, J. Lati, J. B. Laronne, F. Lott, U. Mallast, R. Merz, J. Metzger, A. Mohsen, E. Morin, M. Nied, T. Rödiger, E. Salameh, A. Sawarieh, B. Shannak, C. Siebert, and M. Weber. "New perspectives on interdisciplinary earth science at the Dead Sea : the DESERVE project". In: *Science of the Total Environment* 544 (2016), pp. 1045–1058.

Krawczyk, C. M., U. Polom, S. Trabs, and T. Dahm. "Sinkholes in the city of Hamburg—New urban shear-wave reflection seismic system enables high-resolution imaging of subrosion structures". In: *Journal of Applied Geophysics* 78 (2012), pp. 133–143. DOI: 10.1016/j.jappgeo.2011.02.003.

Krawczyk, C. M. "Joint project SIMULTAN - Sinkhole characterization and monitoring with supplementing geophysical methods". In: *NCKRI Symposium 7 - 15th multidisciplinary conference* *on sinkholes and the engineering and environmental impacts of Karst.* Ed. by I. D. Sasowsky, M. J. Byle, and L. Land. Shepherdstown, 2018, pp. 315–321.

Kwiatek, G., K. Plenkers, M. Nakatani, Y. Yabe, G. Dresen, and JAGUARS-Group. “Frequency-magnitude characteristics down to magnitude -4.4 for induced seismicity recorded at Mponeng Gold Mine, South Africa”. In: *Bulletin of the Seismological Society of America* 100.3 (2010), pp. 1165–1173. DOI: 10.1785/0120090277.

Lebert, F., S. Bernardie, and G. Mainsant. “Hydroacoustic monitoring of a salt cavity: an analysis of precursory events of the collapse”. In: *Natural Hazards and Earth System Science* 11.9 (Sept. 2011), pp. 2663–2675. DOI: 10.5194/nhess-11-2663-2011.

Lisjak, A. and G. Grasselli. “A review of discrete modeling techniques for fracturing processes in discontinuous rock masses”. In: *Journal of Rock Mechanics and Geotechnical Engineering* 6.4 (2014), pp. 301–314. DOI: 10.1016/j.jrmge.2013.12.007.

Loke, M. and T. Dahlin. “A comparison of the Gauss–Newton and quasi-Newton methods in resistivity imaging inversion”. In: *Journal of Applied Geophysics* 49.3 (2002), pp. 149–162. DOI: 10.1016/S0926-9851(01)00106-9.

Maghsoudi, S., S. Hainzl, S. Cesca, T. Dahm, and D. Kaiser. “Identification and characterization of growing large-scale en-echelon fractures in a salt mine”. In: *Geophysical Journal International* 196.2 (2014), pp. 1092–1105. DOI: 10.1093/gji/ggt443.

Malehmir, A., L. V. Socco, M. Bastani, C. M. Krawczyk, A. A. Pfaffhuber, R. D. Miller, H. Maurer, R. Frauenfelder, K. Suto, S. Bazin, K. Merz, and T. Dahlin. “Near-Surface Geophysical Characterization of Areas Prone to Natural Hazards: A Review of the Current and Perspective on the Future”. In: *Advances in Geophysics* 57 (2016), pp. 51–146. DOI: 10.1016/bs.agph.2016.08.001.

MediaSH. *List of websites of media covered sinkholes:* 2019.

Meqbel, N. M. M., O. Ritter, and D. Group. “A magnetotelluric transect across the Dead Sea Basin: electrical properties of geological and hydrological units of the upper crust”. In: *Geophysical Journal International* 193.3 (2013), pp. 1415–1431. DOI: 10.1093/gji/ggt051.

Mercerat, E. D. “Sismicité induite et modélisation numérique de l ’ endommagement dans un contexte salin”. PhD thesis. Nancy-Universite, 2007.

Mottershead, D. N., J. S. Wright, R. J. Inkpen, and W. J. Duane. “Bedrock slope evolution in saltrock terrain”. In: *Zeitschrift für Geomorphologie, Supplementary Issues* 51.1 (2007).

Mottershead, D. N., W. J. Duane, R. J. Inkpen, and J. S. Wright. “An investigation of the geometric controls on the morphological evolution of small-scale salt terrains, Cardona, Spain”. In: *Environmental Geology* 53.5 (2008), pp. 1091–1098. DOI: 10.1007/s00254-007-0736-4.

Nof, R., M. Abelson, E. Raz, Y. Magen, S. Atzori, S. Salvi, and G. Baer. “SAR Interferometry for Sinkhole Early Warning and Susceptibility Assessment along the Dead Sea, Israel”. In: *Remote Sensing* 11.1 (2019), p. 89. DOI: 10.3390/rs11010089.

Pan, Z., X. Jiang, M. Lei, J. Dai, Y. Wu, and Y. Gao. “Review of Monitoring and Early Warning Technologies for Cover Collapse sinkholes”. In: *NCKRI Symposium 6 - 15th sinkhole conference.* Shepherdstown, West Virginia, USA, 2018.

Parise, M. and P. Lollino. “A preliminary analysis of failure mechanisms in karst and man-made underground caves in Southern Italy”. In: *Geomorphology* 134.1-2 (2011), pp. 132–143. DOI: 10.1016/j.geomorph.2011.06.008.

Parise, M. and C. Vennari. “A Chronological Catalogue of Sinkholes in Italy: the First Step Toward a Real Evaluation of the Sinkhole Hazard”. In: *NCKRI Symposium 2.* 2013, pp. 383–392.

Parise, M., F. Gabrovsek, G. Kaufmann, and N. Ravbar. “Recent advances in karst research: from theory to fieldwork and applications”. In: *Geological Society, London, Special Publications* 466.1 (2018), pp. 1–24. DOI: 10.1144/SP466.26.

Polom, U., H. Alrshdan, D. Al-Halbouni, T. Dahm, A. Sawarieh, M. Y. Atallah, and C. M. Krawczyk. “Shear wave reflection seismics yields subsurface dissolution and subrosion patterns:

application to the Ghor Al-Haditha sinkhole site, Dead Sea, Jordan". In: *Solid Earth* 9 (2018), pp. 1079–1098. DOI: 10.5194/se-9-1079-2018.

Potyondy, D. O. and P. A. Cundall. "A bonded-particle model for rock". In: *International Journal of Rock Mechanics and Mining Sciences* 41.8 (2004), pp. 1329–1364. DOI: 10.1016/j.ijrmms.2004.09.011.

Potyondy, D. O., P. A. Cundall, and C. Lee. *Modeling of notch formation in the URL mine-by tunnel - Phase I - Micromechanical experiments.* Tech. rep. Itasca, 1995.

Potyondy, D. O. "The bonded-particle model as a tool for rock mechanics research and application: current trends and future directions". In: *Geosystem Engineering* 17.6 (2014), pp. 342–369.

Rawal, K., Z.-M. Wang, and L.-B. Hu. "Exploring the Geomechanics of Sinkholes: A Numerical Study of Sinkhole Subsidence and Collapse". In: *4th Geo-China International Conference.* Shandong, China, 2016. DOI: 10.1061/9780784480007.001.

Revil, A. "Self-potential signals associated with preferential ground water flow pathways in a buried paleo-channel". In: *Geophysical Research Letters* 32.7 (2005), pp. 4–7. DOI: 10.1029/2004GL022124.

Richards, K., A. Revil, A. Jardani, F. Henderson, M. Batzle, and A. Haas. "Pattern of shallow ground water flow at Mount Princeton Hot Springs, Colorado, using geoelectrical methods". In: *Journal of Volcanology and Geothermal Research* 198 (2010), pp. 217–232.

Sainsbury, B.-a. "A model for cave propagation and subsidence assessment in jointed rock masses". PhD thesis. University of South Wales, 2012.

Salmi, E. F., M. Nazem, and A. Giacomini. "A Numerical Investigation of Sinkhole Subsidence Development over Shallow Excavations in Tectonised Weak Rocks: The Dolaei Tunnel's Excavation Case". In: *Geotechnical and Geological Engineering* 35.4 (2017), pp. 1685–1716. DOI: 10.1007/s10706-017-0202-3.

Sawarieh, A., A. Al Adas, A. Al Bashish, and E. Al Seba'i. *Sinkholes Phenomena At Ghor Al Haditha Area - Internal Report No. 12.* Tech. rep. Amman, Jordan: Natural Resources Authority, 2000.

Schöpfer, M. P. J., C. Childs, and J. J. Walsh. "Two-dimensional distinct element modeling of the structure and growth of normal faults in multilayer sequences: 1. Model calibration, boundary conditions, and selected results". In: *Journal of Geophysical Research* 112.B10401 (2007). DOI: 10.1029/2006JB004902.

Schöpfer, M. P. J., C. Childs, and J. J. Walsh. "Two-dimensional distinct element modeling of the structure and growth of normal faults in multilayer sequences: 2. Impact of confining pressure and strength contrast on fault zone geometry and growth". In: *Journal of Geophysical Research* 112.B10404 (2007). DOI: 10.1029/2006JB004903.

Schöpfer, M. P. J., C. Childs, J. J. Walsh, and T. Manzocchi. "Evolution of the internal structure of fault zones in three-dimensional numerical models of normal faults". In: *Tectonophysics* 666 (2016), pp. 158–163. DOI: 10.1016/j.tecto.2015.11.003.

Schöpfer, M. P. J., C. Childs, T. Manzocchi, J. J. Walsh, A. Nicol, and B. Grasemann. "The emergence of asymmetric normal fault systems under symmetric boundary conditions". In: *Journal of Structural Geology* 104.May 2016 (2017), pp. 159–171. DOI: 10.1016/j.jsg.2017.10.006.

Sevil, J., F. Gutiérrez, M. Zarroca, and G. Desir. "Sinkhole investigation in an urban area by trenching in combination with GPR, ERT and high-precision leveling. Mantled evaporite karst of Zaragoza city, NE Spain". In: *Engineering Geology* 231.October (2017), pp. 9–20. DOI: 10.1016/j.enggeo.2017.10.009.

Shalev, E., V. Lyakhovsky, and Y. Yechieli. "Salt dissolution and sinkhole formation along the Dead Sea shore". In: *Journal of Geophysical Research* 111.B3102 (2006), pp. 1–12. DOI: 10.1029/2005JB004038.

Shalev, E. and V. Lyakhovsky. "Viscoelastic damage modeling of sinkhole formation". In: *Journal of Structural Geology* 42 (2012), pp. 163–170. DOI: 10.1016/j.jsg.2012.05.010.

Siebert, C., T. Rödiger, U. Mallast, A. Gräbe, J. Guttman, J. B. Laronne, Y. Storz-Peretz, A. Greenman, E. Salameh, M. Al-Raggad, D. Vachtman, A. B. Zvi, D. Ionescu, A. Brenner, R. Merz, and S. Geyer. “Challenges to estimate surface- and groundwater flow in arid regions: The Dead Sea catchment”. In: *Science of the Total Environment* 485-486 (2014), pp. 828–841. DOI: 10.1016/j.scitotenv.2014.04.010.

Sigmundsson, F., M. Parks, R. Pedersen, K. Jónsdóttir, B. G. Ófeigsson, R. Grapenthin, S. Dumont, P. Einarsson, V. Drouin, E. R. Heimisson, Á. R. Hjartardóttir, M. Guðmundsson, H. Geirsson, S. Hreinsdóttir, E. Sturkell, A. Hooper, Þ. Högnadóttir, K. Vogfjörð, T. Barnie, and M. J. Roberts. “Magma Movements in Volcanic Plumbing Systems and their Associated Ground Deformation and Seismic Patterns”. In: *Volcanic and Igneous Plumbing Systems*. Ed. by S. B. T. .-.-. V. Burchardt and I. P. Systems. Elsevier, 2018, pp. 285–322. DOI: 10.1016/B978-0-12-809749-6.00011-X.

Smit, J., J.-P. Brun, X. Fort, S. Cloetingh, and Z. Ben-Avraham. “Salt tectonics in pull-apart basins with application to the Dead Sea Basin”. In: *Tectonophysics* 449 (2008), pp. 1–16. DOI: 10.1016/j.tecto.2007.12.004.

Souley, M., G. Armand, K. Su, and M. Ghoreychi. “Modeling the viscoplastic and damage behavior in deep argillaceous rocks”. In: *Physics and Chemistry of the Earth, Parts A/B/C* 36.17-18 (2011), pp. 1949–1959. DOI: 10.1016/j.pce.2011.10.012.

Sparks, R. S. J., J. Biggs, and J. W. Neuberg. “Geophysics. Monitoring volcanoes.” In: *Science* 335.6074 (2012), pp. 1310–1. DOI: 10.1126/science.1219485.

Taqieddin, S. a., N. S. Abderahman, and M. Atallah. “Sinkhole hazards along the eastern Dead Sea shoreline area, Jordan: a geological and geotechnical consideration”. In: *Environmental Geology* 39.11 (2000), pp. 1237–1253. DOI: 10.1007/s002549900095.

Thompson, N., M. R. Bennett, and N. Petford. “Development of characteristic volcanic debris avalanche deposit structures: New insight from distinct element simulations”. In: *Journal of Volcanology and Geothermal Research* 192.3 (2010), pp. 191–200. DOI: 10.1016/j.jvolgeores.2010.02.021.

Tihansky, A. B. *Sinkholes, west-central Florida.* Tech. rep. 1999, pp. 121–140.

USGS. *Karst Topography - Teacher’s Guide and Paper Model.* 2000.

USGS. *Landsat images from USGS.* 2017.

Vey, S., F. Alshawaf, D. Al-Halbouni, J. Vüllers, A. Güntner, G. Dick, M. Ramatschi, J. Wickert, and M. Weber. “Interplay of climate, water and Solid Earth - Subsidence of the Dead Sea shore - under review”. In: *Scientific Reports* (2019).

Wadas, S. H., U. Polom, and C. Krawczyk. “High-resolution shear wave reflection seismics as a tool to image near-surface subrosion structures - a case study in Bad Frankenhausen, Germany”. In: *Solid Earth* 7 (2016), pp. 1491–1508. DOI: 10.5194/se-7-1491-2016.

Waltham, T., F. Bell, and M. G. Culshaw. *Sinkholes and subsidence: Karst and Cavernous Rocks in Engineering and Construction.* Berlin, Heidelberg: Springer, 2005.

Warren, J. K. *Evaporites: Sediments, resources and hydrocarbons.* 2006, pp. 1–1035. DOI: 10.1007/3-540-32344-9.

Watson, R. A., E. P. Holohan, D. Al-Halbouni, L. Saberi, A. Sawarieh, D. Closson, H. Alrshdan, N. Abou Karaki, T. R. Walter, and T. Dahm. “ Sinkholes and uvalas in evaporite karst: spatio-temporal development with links to base-level fall on the eastern shore of the Dead Sea”. In: *Solid Earth Discussions* (2019). DOI: 10.5194/se-2018-105.

Wust-Bloch, G. H. and M. Joswig. “Pre-collapse identification of sinkholes in unconsolidated media at Dead Sea area by nanoseismic monitoring (graphical jackknife location of weak sources by few, low-SNR records)”. In: *Geophysical Journal International* 167.3 (2006), pp. 1220–1232. DOI: 10.1111/j.1365-246X.2006.03083.x.x.

Yechieli, Y., M. Abelson, and G. Baer. “Sinkhole formation and subsidence along the Dead Sea coast, Israel”. In: *Hydrogeology Journal* 24.3 (2016), pp. 601–612. DOI: 10.1007/s10040-015-1338-y.

Yeomans, C. M., M. Middleton, R. K. Shail, and P. A. J. Lusty. “Integrated Object-Based Image Analysis for semi-automated geological lineament detection in SW England”. In: *Computers and Geosciences* 123 (2018). DOI: 10.1016/j.cageo.2018.11.005.

Yizhaq, H., E. Raz, Y. Ashkenazy, C. Cohen, E. Raz, and Y. Ashkenazy. “Scale-free distribution of Dead Sea sinkholes: Observations and modeling”. In: *Geophys. Res. Lett.* 44.00940v1 (2017), pp. 1–9. DOI: 10.1002/2017GL073655.Received. arXiv: 1611.00940.

Yoon, J. S., G. Zimmermann, and A. Zang. “Numerical Investigation on Stress Shadowing in Fluid Injection-Induced Fracture Propagation in Naturally Fractured Geothermal Reservoirs”. In: *Rock Mechanics and Rock Engineering* 48.4 (2015), pp. 1439–1454. DOI: 10.1007/s00603-014-0695-5.

Zang, A. and O. Stephansson. *Stress Field of the Earth’s Crust.* Dordrecht: Springer Netherlands, 2010. DOI: 10.1007/978-1-4020-8444-7.

APPENDIX A

Supplementary information on parameter tracking

A.1 Implementation of acoustic emission tracking in PFC

Acoustic emission (AE) and microseismicity (MS) recording in mines, tunnels or cavities is very important to address stability issues and determine possible geological risks (Maghsoudi et al., 2014; Kinscher et al., 2016; Mercerat, 2007; Kwiatek et al., 2010). As DEM is particularly useful to simulate fracture initiation and propagation on a high resolution (sub-particle)-scale, development to simulate seismicity in this area is of great relevance. Several methods to derive seismic events in PFC have been proposed in literature. For example, kinetic energy of the particles has been used by Potyondy et al. (1995) to calculate magnitudes and forces at the time of bond breakages (cracks) around the particles. Hazzard and Young (2002, 2004) showed that force changes due to bond breakages in PFC can be used to derive AE and MS, and magnitude from the moment tensor matrix. This approach is sketched in Fig. A.1.1 and described in the following.

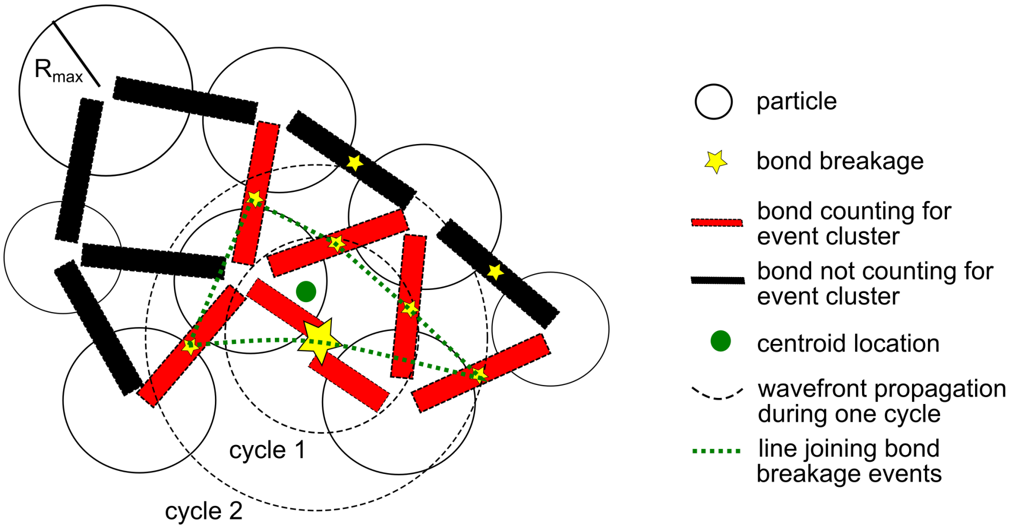

Figure A.1.1: Sketch of acoustic emission and microseismicity tracking as implemented in PFC by Hazzard and Young (2002).

The moment tensor components M_{ij} are calculated by summing all force changes ΔF_i from contact and parallel-bonds multiplied by the distance R_j from a centroid of the event around a closed surface S.

$$M_{ij} = \sum_S \Delta F_i R_j \tag{A.1}$$

In PFC this works under the assumption of angular moment conservation, leading to equal offdiagonal components calculated by averaging (Hazzard, 2004). Summing multiple (small) cracks into one (larger) MS event is needed to account for realistic conditions of a magnitude power law distribution (Gutenberg and Richter, 1956). Hazzard and Young (2002) introduced the shear-fracture propagation velocity, which has to be given by the user. If a new crack forms within the source area of the first crack, determined by duration of and area passed by the shear-wave, both cracks are considered of the same MS event (see Fig. A.1.1).

This approach has been tested in PFC2D-V4 simulations, also in early stages of this work, and two main disadvantages were raised by Hazzard, 2014: large non-tensile components of tensile cracks and generally too large magnitudes. Therefore, more recent implementations by Hazzard, 2014 have been used in the PFC2D-V5 sinkhole modelling approach of this work. Every bond breakage here is considered as one single seismic event (AE) occurring around the source, which is the contact between two particles (see Fig. A.1.1). The relative displacement Δu of two particles involved is recorded for 25 timesteps and the maximum is taken for calculation of the moment tensor after the biaxial, potency decomposition from Chapman and Leaney (2012). The first term is due to volume change ΔV in a spherical cavity and the second term represents the opening and slip across a displacement discontinuity:

$$\mathbf{M} = \Delta V \kappa_{emb} \begin{pmatrix} 1 & 0 & 0 \\ 0 & 1 & 0 \\ 0 & 0 & 1 \end{pmatrix} + \frac{1}{2} A \Delta u \mathbf{c_S} : (\hat{\mathbf{u}}\hat{\mathbf{n}} + \hat{\mathbf{n}}\hat{\mathbf{u}}) \tag{A.2}$$

with the embedded bulk modulus $\kappa_{emb} = \lambda + 2G = M_p$ for isotropic media, λ, G the 1st and 2nd Lamé-constants, M_p the (longitudinal) P-wave modulus, $\hat{\mathbf{n}}$ the unit normal vector, $\hat{\mathbf{u}}$ the unit displacement vector, A the area of the fracture (here the contact area of two parallel bonded particles), $\mathbf{c_S}$ the elastic stiffness tensor and : the double dot product of dyadic tensors.

Bulk and shear modulus are taken from the contact moduli while the Poisson ratio is dependent on a user input. For the details of the calculation see Chapman and Leaney (2012, 2014) and Hazzard (2014). Microcracks occurring close together in space (distance of one R_{max}) and time were used to define a macro event, i.e. moments are summed representing a fracture growth by microcracking (Fig. A.1.1). They form a MS event whose location is the average location of all AE. This is similar to the shear-fracture propagation approach from Hazzard and Young (2002) described above, with more exact moduli values and Poisson ratios that can e.g. be determined by simulated rock tests (see Chap. 4). The scalar moment is then calculated via:

$$M = \frac{1}{2} (m_1 + m_2 + m_3) \tag{A.3}$$

with m_i as the ith principal component of the moment tensor. The moment magnitude is finally calculated after Hanks and Kanamori (1979):

$$M_w = \frac{2}{3} M_o - 6 \tag{A.4}$$

This described approach has been tested by Hazzard (2014) and has shown more realistic magnitude distributions. We used it hence for tracking the microseismicity in the sinkhole models.

A.2 Example of a tracked single void simulation

The potential of the implemented geophysical and geodetic tracking procedure can best be evaluated with the help of Fig. A.2.1. The parameters at each detailed step of the simulation are shown for an alluvium on mud single void space growth model as presented in Chap. 4.

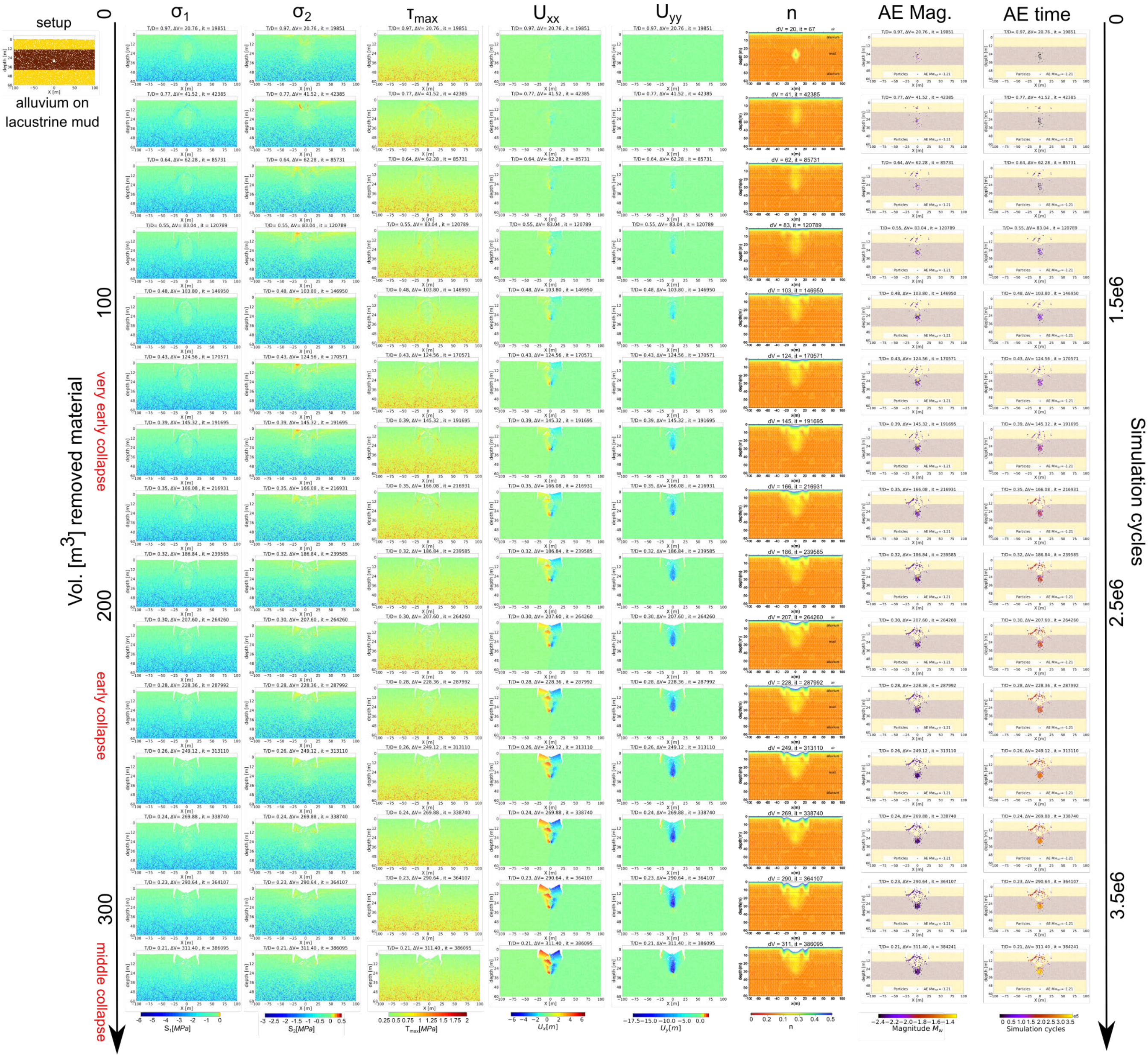

Figure A.2.1: Tracked simulation of a typical sinkhole formation in layered alluvial/mud models with a subrosion zone at 30 m depth. From left to right are plotted the removed material volume at depth versus principal stresses σ_1 and σ_2 , maximum shear stress τ_{max}, displacements U_{xx} and U_{yy}, porosity n, cumulative acoustic emissions coloured by magnitude (above $M_w = -2.5$) and time. T/D stands for thickness to diameter ratio of the overburden, ΔV for the removed volume at depth in m^3, and *it* for the iteration (cycle) of the simulation.

The following is generally observable:

Stress and displacement:

- Shear stress is high at locations where at later simulation stages failure occurs.
- The highest compressive stress occurs in arch like structures around the material removal zone. Similarly, the highest shear stresses also form such an arch.
- Tensile stresses are high in a broad zone directly underneath the surface.
- Surface subsidence and surface tilting is nicely reflected in the vertical and horizontal displacement plots, respectively.

Porosity:

- The collapse happens early when around $100\,\mathrm{m}^3$ of volume has been removed, with large side cracks developing of approximately $6\,\mathrm{m}$ depth. Porosity tracking reflects these changes in the near surface. A compression ridge appears at the later stage and as the subsided zone deepens, also the cracks do up to $12\,\mathrm{m}$, revealing the border of the developing sinkhole.

Microseismicity:

- The highest MS event magnitudes $M_w = -1.21$ are found at early stages directly above the subrosion zone. Later, the caprock is cracking and MS events starts in a broad zone above the subrosion base.
- The main events above $M_w = -2.5$ follow mainly the cracks that form in the subsurface at the early collapse state
- Most of the seismicity comes from small events with mean magnitude of $M_w = -3.17$, which are difficult to record in the field and therefore not shown for clarity of the images.

Acknowledgements

This thesis has been conducted at the University of Potsdam and, most of the time, at the German Research Centre for Geosciences (GFZ). My acknowledgements go to all involved people, especially I would like to thank my supervisors Torsten Dahm and Eoghan Holohan for their continuous support and at the same time, enough freedom to develop this work. Furthermore I would like to thank Charlotte Krawczyk, Michael Weber, Susanne Köster and all other colleagues at GFZ and UP. All colleagues involved in the fieldwork, logistics and data analysis are mentioned in the papers and here I would simply say thank you again for such a great, professional time.

The support of many more people was important for the successful realization of the research and writing of this thesis. A big thank you goes to Rena for her patience, good advices and generally the time together. Also my family (Mama, Papa, Mila) deserves thanks for their patience, support and distraction.

Friends and colleagues who helped me withstand difficult times should not be forgotten. Specifically I would like to mention Nima, Peter, Marius, Gesa, Toño, Sreeram, Ayleen, Friedemann, Jens, Anne V., Anne S., Konrad, Anna-Lena, Laura, Sini, Harm-Friedrich, Simão, David, Joana, Ana B., Azahara, Alberto, Domi, Nadine, Naseem, Murhaf and Wassem with families and more.

I'd also like to express my deepest gratitude to my relatives (Mohsen, Leila, Hussein, Nour, Hassan, Ahmad, Aya, Ammar, Maschadi and more), who reminded me always that different time and space exist(ed).

شكراً لكم على ألوجود.

Finally, financial and logistical support is important and my thanks go to all colleagues and institutions involved, as there are: GFZ and the GFZ expedition funding, DESERVE (Helmholtz Virtual Institute grant VH-VI-527) and SIMULTAN (BMBF grant 03G0843) projects, Ministry of Energy and Mineral Resources in Amman, DAAD, the University of Adelaide and CSIRO, as well as the Itasca Educational Program for the multiple software license extensions.